From the magma chamber to microhabitats : dynamics of diffuse hydrothermal circulations at mid-ocean ridges

Benjamin Wheeler

Thèse préparée à l'Institut de Physique du Globe de Paris
Université de Paris

École doctorale Sciences de la Terre et de l'environnement
et physique de l'Univers STEP'UP n°560

IPGP - Équipe de Géosciences marines

De la chambre magmatique aux microhabitats : dynamique des circulations hydrothermales diffuses aux dorsales médio océaniques

par

Benjamin Wheeler

Thèse de doctorat de Sciences de la Terre et de l'environnement
dirigée par Mathilde Cannat
co-encadrée par Fabrice Fontaine

présentée et soutenue publiquement le
20 décembre 2021

devant un jury composé de

Kim Juniper Directeur de recherche, ONC, Canada	Rapporteur
Lars Rüpke Professeur, GEOMAR, Allemagne	Rapporteur
Thibaut Barreyre Chercheur, UiB, Norvège	Membre
Susan Humphris Professeur, WHOI, Etats-Unis	Membre
Bénédicte Ménez Professeur, PR1, IPGP, France	Membre
Mathilde Cannat Directrice de recherche, IPGP, France	Directrice de thèse
Fabrice Fontaine Chargé de recherche, OVPF-IPGP, France	Co-encadrant de thèse
Valérie Chavagnac Directrice de recherche, GET, France	Membre invité

Thesis prepared at the Institut de Physique du Globe de Paris
Université de Paris

Earth and Environment Science and Physics of
the Universe in Paris STEP'UP doctoral school n°560

IPGP – Marine Geosciences

From the magma chamber to microhabitats: dynamics of diffuse hydrothermal circulations at mid-ocean ridges

by

Benjamin Wheeler

PhD thesis of Earth and environment Sciences
supervised by Mathilde Cannat
Co-supervised by Fabrice Fontaine

presented and publicly defended on
December 20 2021

In front of a jury composed of

Kim Juniper Professor, ONC, Canada	Rapporteur
Lars Rüpke Professor, GEOMAR, Germany	Rapporteur
Thibaut Barreyre Research Scientist, UiB, Norway	Examiner
Susan Humphris Senior Scientist, WHOI, United States	Examiner
Bénédicte Ménez Professor, PR1, IPGP, France	Examiner
Mathilde Cannat Senior Researcher, IPGP, France	PhD advisor
Fabrice Fontaine Researcher, OVPF-IPGP, France	PhD co-advisor
Valérie Chavagnac Senior Researcher, GET, France	Guest member

In memory of Audrey Kathleen Wheeler
et à la mémoire de Henri Jean Ravier

Résumé

Le champ hydrothermal de Lucky Strike présent sur une surface de ~1 km^2 est l'un des plus larges observés au niveau des dorsales océaniques. Un observatoire sous-marin est présent au niveau de ce champ hydrothermal pour étudier les processus en lien avec la faune hébergée au niveau des sites hydrothermaux. L'activité hydrothermale se manifeste sous la forme de cheminées hydrothermales évacuant des fluides de haute température connus sous le nom « fumeurs noirs » mais aussi via des fluides diffus de plus basse température évacués sur de plus larges surfaces. Il existe toutefois relativement peu de données sur les différents mécanismes de formation et la dynamique de circulation des fluides diffus dans le sous-sol malgré leur rôle majeur pour la faune hydrothermale.

Durant cette thèse nous avons étudié les fluides diffus lors d'observations réalisées sur 3 ans au niveau de 2 sites du champ hydrothermal de Lucky Strike (Tour Eiffel and White Castle). Nous avons répertorié la variabilité temporelle et spatiale de la température et chimie des fluides diffus ; l'effet de la charge tidale et des courants marins ; la formation des fluides par mélange, refroidissement ou réchauffement des fluides hydrothermaux ou de l'eau de mer associée à la précipitation et dissolution de minéraux. Sur la base de nos observations, nous avons développé un modèle géologique conceptuel pour la dynamique de circulation hydrothermale à l'échelle du site à Lucky Strike. Ce modèle confirme le rôle joué par la fine couche volcanoclastique déposée sur la couche sous-jacente de basaltes bréchifiés pour le contrôle de la dynamique de circulation et l'évacuation des fluides diffus. Nous avons proposé l'hypothèse que les fluides qui découlent des basaltes au niveau d'un réseau de fissures sont relativement chauds (> 80°C) et comportent une composante notable de fluides hydrothermaux (> 9%). Ces fluides génèreraient un flux de chaleur estimé à 7.5 MW à White Castle et 28.9 MW à Tour Eiffel.

Nous utilisons ces observations pour contraindre un modèle 2D thermo-hydraulique de circulation de fluides chauds dans un milieu poreux, afin de prédire la géométrie de la circulation des fluides dans le sous-sol peu profond et la formation de fluides diffus à proximité des fumeurs noirs, en fonction de paramètres physiques clés. Nous explorons également l'effet de la précipitation de sulfates à partir de l'eau de mer circulant dans la croute océanique. Pour contraindre ces modèles, nous utilisons des observations telles que la dimension des zones de sorties de fluides à l'échelle du site ou leur température. Nos résultats montrent qu'une faible perméabilité ou une grande vitesse pour les fluides hydrothermaux sont nécessaires afin de former des fluides à haute température > 300°C. Pour pouvoir avoir des fluides diffus latéraux >20°C, une précipitation d'anhydrite pour changer la perméabilité locale et l'écoulement du fluide est nécessaire.

Abstract

The 1km^2 Lucky Strike hydrothermal field is one of the largest found at mid-ocean ridges. In this field, a submarine observatory has been established to investigate both the links between geological, physical and chemical processes and with the hosted fauna at hydrothermal sites for different spatial and temporal scales. The hydrothermal activity is visible at the seafloor through chimney edifices called "black smokers" but also through diffuse fluids of lower temperature that are scattered on larger surfaces. Very little is known about the different mechanisms of formation and the dynamics of circulation of diffuse fluids in the subseafloor despite their important role for the hydrothermal fauna.

We studied diffuse fluids during a 3 years monitoring at 2 hydrothermal vent sites from the Lucky Strike hydrothermal field (Tour Eiffel and White Castle). We documented the time and space variability of diffuse venting temperature and chemistry, the effect of tidal loading and currents, fluid formation by mixing, cooling or heating of end-member hydrothermal fluids and seawater associated with minerals precipitation/dissolution. Based on these results, we developed a conceptual geological model for the dynamics of vent site scale hydrothermal circulations at the Lucky Strike field. This model confirms the role of the thin volcaniclastic formation deposited on the brecciated basalt substratum of both sites to control the dynamic of circulation and of venting of diffuse fluids. We propose that fluids that actually flow out of the basalts underneath are relatively hot (> 80°C) and end-member rich (> 9%) fluids, coming out of a network of meter-spaced permeable cracks in the basalt substratum, up to 25 m from the black smokers at both vent sites. These fluids would generate a diffuse heat flow estimated as about 7.5 MW at White Castle, and 28.9 MW at Tour Eiffel.

We use these observations to constrain a 2D thermo-hydraulic model of hot fluid circulation in a porous media, in order to predict the geometry of fluid circulation in the shallow subseafloor and the formation of diffuse fluids close to black smokers, as a response to changes in key physical parameters such as the width of the upflow zone, and the velocity of hydrothermal fluids at the base of the system. We also explore the effect of sulfate precipitation from entrained seawater. To test these models, we use observations on the dimensions of the venting domains at the seafloor, and the temperature of hydrothermal effluents. Our results show that low permeability for the porous media or high velocity for the upflowing hydrothermal fluids are necessary in order to have high-temperature fluids >300°C vents. To be able to have close lateral diffuse fluids >20°C, anhydrite precipitation to change local permeability and fluid flow is necessary.

Remerciements

Il y a quelques années, j'ai poussé la porte du bureau 344 de l'IPGP à la recherche d'un stage de master après avoir découvert le monde de l'hydrothermalisme grâce à l'aide de Muriel Andreani que je remercie chaleureusement pour m'avoir dévoilé ce monde géologique sous-marin. Ce stage m'a alors emmené sur ce grand chemin qu'est la thèse, à travers des aventures inoubliables au large des Açores, des rencontres qui marquent une vie et des obstacles qui bousculent vos principes.

Je souhaite d'abord remercier les membres de mon jury de thèse d'avoir accepté de juger ces 4 ans de travail, pour avoir assisté à la soutenance et pour les passionnantes discussions qui ont suivies : Bénédicte Ménez, Kim Juniper, Lars Rüpke, Thibaut Barreyre, Susan Humphris and Valérie Chavagnac.

La réalisation de cette thèse n'aura jamais été possible sans l'encadrement de Mathilde Cannat. Mathilde je te remercie infiniment pour ton soutient infaillible tout le long de la thèse malgré les difficultés rencontrées et pour tout ce que tu m'as apporté personnellement et professionnellement. Merci énormément pour toutes ces opportunités à travers ces conférences dans le monde entier, ces échanges avec les différents observatoires sous-marins et l'ensemble des missions en mer réalisé ensemble. Tes enseignements m'ont permis de construire une rigueur et une éthique scientifique qui me suivront dans les années à venir.

Je souhaite aussi remercier Fabrice Fontaine pour son aide précieuse pour le travail sur les modèles numériques. Merci beaucoup Fabrice pour ta patience et toutes tes explications qui m'auront permis de découvrir le monde de la modélisation qui m'impressionnait tant avant de mettre les pieds dans le plat. Et encore merci pour m'avoir accueilli à la Réunion pendant ces nombreuses semaines qui ont été si productives pour faire décoller le projet Comsol et pour ton aide précieuse pour la rédaction du manuscrit.

Un grand merci aussi à Valérie Chavagnac pour ce travail réalisé ensemble sur la chimie des fluides hydrothermaux et pour l'aide pour interpréter ce jeu de données si complexe. Merci aussi pour les encouragements en fin de thèse et pour ces bons moments à bord dans le labo humide avec Christine et Alain. Merci à toutes les équipes avec qui nous avons pu travailler à bord des différentes missions Momarsat et plus particulièrement aux chefs de mission Pierre-Marie Sarradin et Julien Legrand. Je garde des souvenirs inoubliables partagés avec tout le monde à bord, des barbecues au milieu de l'Atlantique jusqu'à l'alerte incendie en pleine chasse aux flotteurs de Borel ! Merci à tous mes collègues et amis avec qui j'ai pu m'amuser à exploiter les sondes de température : Mathilde, Fabrice, Simon, Tom, Daniel, Stéphane, Jie, Océane, Soumya, Alister et ceux avec qui j'ai explorer les abysses à travers les écrans du Victor 6000 Julien, Fanny, Loïc, Marjolaine, Ana, Celine, Jozée, David, Anne, Françoise, Bruno, Christian, Bertrand, Philippe, Damien, Nicolas, Laurent, Romain et tout le reste de l'équipe. Un grand merci à l'équipage Genavir du Pourquoi Pas ? et de l'Atalante pour leur travail acharné pour nous aider dans nos études et à toute la team des ROVmen, Julien, Luc, Loïc, Maxime, Luca et tous les autres pour leur précision sans faille pour poser ces satanés sondes de température et pour m'avoir permis de réaliser mon rêve de plonger voir ce monde des abysses.

Je souhaite aussi remercier tous les scientifiques avec qui j'ai pu travailler au cours de ces dernières années. Big thanks to the MuHS team of Geomar, Anne-Cathrin, Nico, Stephan, Froukje, Colin, Jo-Anne, Martine and the other for their warm welcome in Kiel and for my English improved during our Splishy Splashy. Merci à Aline Peltier et l'ensemble de l'équipe de l'OVPF pour leur accueil à l'observatoire et de m'avoir permis de réaliser ces mesures au sommet du Piton de la Fournaise mais aussi à Kim Juniper et Steven Mihaly pour leur accueil au sein de l'ONC malgré l'arrivée en trombe du Covid-19. Merci à Thibaut Barreyre pour son aide lors de mon stage au sein de l'IPGP pour comprendre l'analyse des données temporelle et pour m'avoir accompagné lors de ma première conférence internationale à l'AGU. Merci à Javier Escartin et Jean-Arthur Olive pour les différentes discussions au cours de ces 4 ans de thèse. Merci bien sûr à tout l'équipe de Géosciences marines et particulièrement à Martine Prudent, Florence Rouillé et Marie-Dominique Rocheron pour leur aide indéfectible. Une pensée pour les doctorants et post-doc avec qui j'ai passé de supers moments, ces discussions sans fin dans le bureau 350 avec Aline, Hanjin, Venkata and Jie; les grandes sœurs Océane et particulièrement Manon pour ce soutient tout au long de la thèse, ces soirées trop arrosées, ton introduction au monde de la plongée et du hockey et bien sûr tous nos moments dans le bureau 352 ; merci au reste de la Cannat Family, Jie, Soumya et Souradeep, et tous ceux avec qui j'ai partagé ces repas et soirées Valentine, Zhikai, Emma, Alex, Aude, Gaëlle, Matilde, Pierre, Aurélie Muriel, Gabriel, Antoine, et Kévin.

Il y a aussi tous les copains que j'ai rencontré au cours de ces années avec qui j'ai trinqué aux beer parties et dans les bars du V^{e}, Thaïs, Mathilde, Marie, Guillaume, Mouloud, Pauline, Martin, Marine, Nobu, Robin, Alister, Chloé, Mathurin, Maxime, Apolline, Laura, Juliette, Yvan mais aussi l'Hekla avec Sarah, Edith, Tara, Martin, Matthieu et la meilleure présidente ever Laeti. Gros big up au groupe ClimbIPG avec qui j'ai pu partager ma passion de l'escalade, Delphine, Tara, Matthieu et Matthieu, et les autres ! Mes pensées vont aussi à ma famille d'accueil du Canada, Ryan, Margaret and Sue, thanks for those wonderful weeks in Brentwood Bay during this troubling time. Un profond merci aussi à tous les trois, Cécile, Tanner et Rusty pour ces apéros devant la switch ou The Expanse, ces calvaires de rédaction de thèse, ces soirées déjantés sur l'ile d'Aix ou ces bières sur les quais de Paris, des moments que j'ai hâte de vivre de nouveau dans les décennies qui viennent de Paris jusqu'au Texas !

Enfin, merci à mes vieux amis qui me suivent depuis le Benjamin ado; Jérémie, Jordane, Juliette, Adrien, Julia, Willie, Lulu, Valentin, Alice, Gabin, Roxanne, Aude et Coline, mais aussi Jérémy, Sylvain, Thibaud, Fanny, Paul, Emma, Antho, Antoine; le Benjamin géologue ; Lucia, Auguste, Thomas, Kevin, Théo, Thomas et Cédric; au Benjamin breton de cœur ; Édith que je remercie pour tous ses moments et le soutient ces 5 dernières années, Dimitri, Fab, Lucile, Clément, Nathan, Clément, Marin et tout le reste de la bolée.

Finalement, merci à ma famille qui ne m'a pas lâché jusque dans les périodes les plus difficiles et qui m'ont permis d'avancer. Maintenant que c'est fini, je n'ai plus qu'à vous remercier en profitant de la vie avec vous et soutenir notre futur second docteur de la famille.

Bonne lecture à tous !

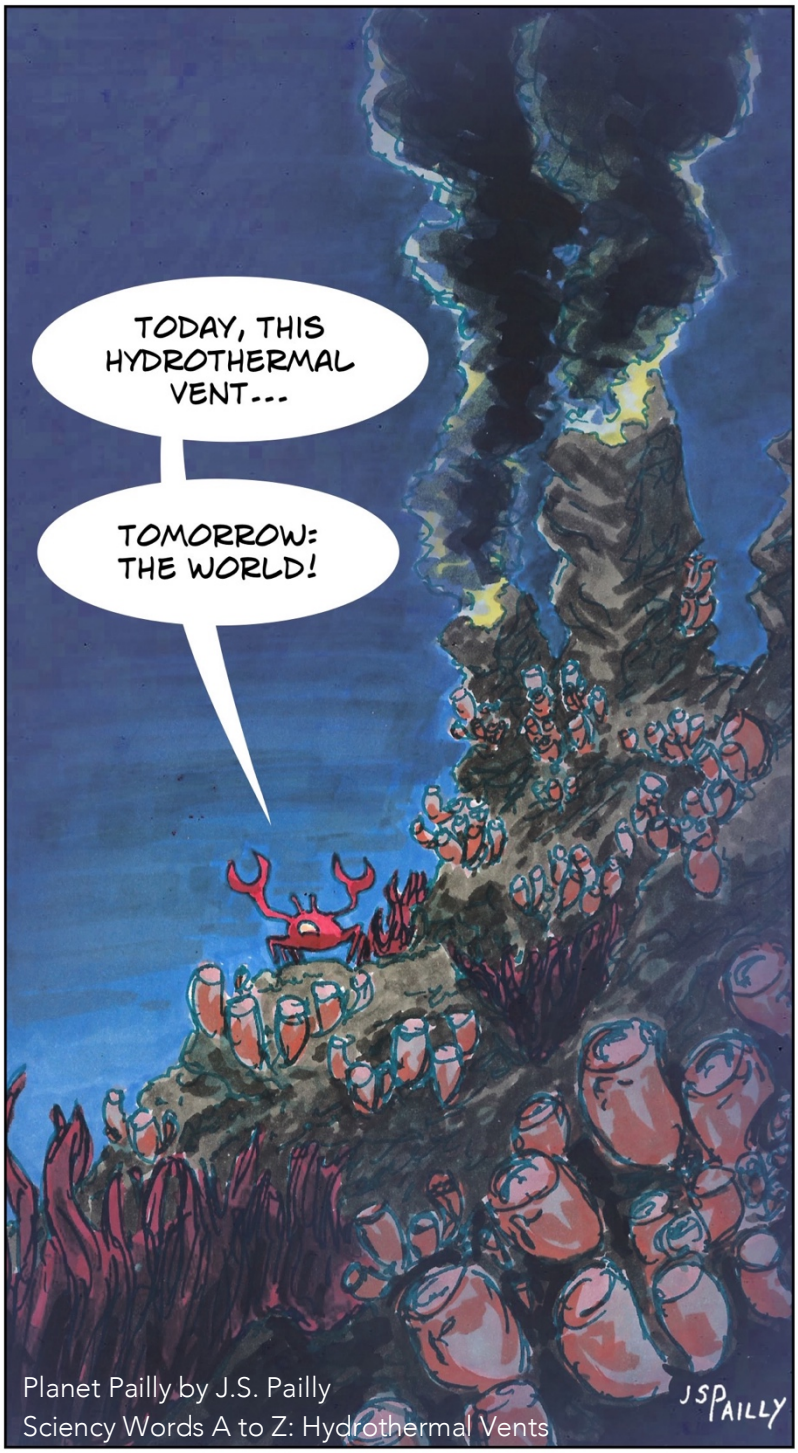

"Deep sea exploration is one of the most challenging fields that I know of. It's physically challenging and it's intellectually challenging. It is the most fun I think you can have that's legal."

Bruce Robison, Deep Ocean Explorers, History Channel & The Smithsonian Institution

AMC Axial Magma Chamber

AML Axial Melt Lens

AST Axial Summit Trough

CTD Conductivity, Temperature, Depth sonde

CM2 Coherence at the semi-diurnal M2 frequency

EMSO European Multidisciplinary Seafloor and water column Observatory

GSC Galápagos Spreading Center

LSHF Lucky Strike Hydrothermal Field

LTZ Low Temperature Zone

LVZ Low-Velocity Zone

SMS Seafloor Massive Sulfides

TAG Trans-Atlantic Geotraverse

MAR Mid-Atlantic Ridge

mbsf meter below seafloor

MEF Main Endeavour Field

msb meter sub-basement

MOR Mid-oceanic ridge

MORB Mid-Oceanic Ridge Basalts

PIV Particle Image Velocimetry

PSD Power Spectrum Density

PSDM2 PSD values at the M2 frequency during time

TE Tour Eiffel

WC White Castle

Résumé étendu

Les océans couvrent plus de 70% de la surface de la Terre ; ils cachent une grande partie des reliefs sous-marins, dont plus de 80% sont à ce jour inexplorés. Les reliefs sous-marins les plus impressionnants sont les dorsales océaniques : elles forment l'équivalent d'une chaîne de montagnes longues de ~60 000 km à la surface du globe et sont le lieu de la formation (ou accrétion) des plaques océaniques.

Cette accrétion se manifeste par une activité volcanique et tectonique extensive importante. La chaleur apportée par le magma et la perméabilité favorisée par les failles normales et les fissures favorisent l'établissement de circulations hydrothermales au sein de la croûte océanique. Ces circulations permettent des échanges thermiques (Lister, 1972 ; Lowell et al., 1995) et chimiques (Alt, 1995) importants. Les circulations hydrothermales conduisent à la formation de cellules de convection, les fluides montants de haute température formant des évents focalisés connus sous le nom de « fumeurs noirs », ainsi que des sorties de fluides de plus basses températures appelées sorties diffuses. Ces structures fournissent les éléments nécessaires pour l'émergence d'écosystèmes uniques qui survivent dans les conditions extrêmes du fond des océans (Wilcock et al., 2004).

Pour cette thèse, nous nous concentrons sur ces systèmes hydrothermaux à fumeurs noirs, mis en place via la présence d'un système magmatique sous-jacent (Van Ark et al., 2007; Kent et al., 1993; Singh et al., 2006). Ces systèmes sont les principaux champs hydrothermaux trouvés au niveau des dorsales médio-océaniques. Ils y assurent la plus grande partie des échanges de chaleur et de matière avec l'océan. Les évents focalisés à haute température créent des cheminées de sulfure, et des monts hydrothermaux (Edmond et al., 1995 ; Gamo et al., 1996 ; Tivey, 2007). Ces structures résultent directement des cellules de convection de fluide à l'échelle kilométrique, qui extraient la chaleur et les éléments chimiques des roches chaudes près des chambres magmatiques axiales (Lister, 1974 ; Wilcock & Delaney, 1996). Les fumeurs noirs ont des températures généralement supérieures à 300°C. Les émanations hydrothermales de haute température vont de pair avec des émanations diffuses, moins étudiées malgré leur découverte au même moment que les fumeurs noirs au niveau des champs hydrothermaux (Corliss et al., 1979; Edmond et al., 1979a,b).

Les fluides diffus ne sont pas aussi bien caractérisés que les fluides hydrothermaux chauds. Ils s'évacuent à partir d'un large panel de structures géologiques telles que des fissures

ou des zones poreuses dont certaines représentent une surface de plusieurs m^2. Ils sont principalement caractérisés par des températures intermédiaires à basses, avec un plus faible débit par rapport aux fumeurs noirs. Les évents diffus s'étendent sur de plus grandes surfaces de décharge, libérant ainsi des flux de chaleur et chimiques globalement plus importants que les fumeurs noirs. De plus, ils fournissent la plupart des habitats hébergeant les communautés biologiques (Baker et al., 1993 ; Barreyre et al., 2012 ; Bemis et al., 2012). Ce rôle important des fluides diffus pour la faune hydrothermale et le flux de chaleur total des champs hydrothermaux justifie l'étude de leurs mécanismes de formation.

Les évents diffus résultent de processus complexes qui se produisent près des sites hydrothermaux, et à relativement faibles profondeurs (<100-200m). Ces processus impliquent le mélange de fluides hydrothermaux avec l'eau de mer présente dans les interstices de la croûte océanique, couplé à des réactions chimiques biochimiques et abiotiques conduisant à la précipitation ou à la dissolution de minéraux (e.g. Butterfield et al., 2004; Von Damm & Lilley, 2004). Ces processus se produisent dans un environnement dynamique impacté par des paramètres externes tels que la pression et ses variations liées à la marée, les courants de fond ou encore l'activité sismique. La difficulté d'accès aux champs hydrothermaux au niveau des dorsales médio-océaniques rend difficile l'observation d'une évolution à long terme. Jusqu'à présent, les études des fluides diffus étaient parcellaires : échantillons ou mesures dispersés sur l'ensemble d'un champ hydrothermal, suivi temporel court ou absent. Ces résultats ne permettaient pas d'obtenir une résolution suffisamment fine pour observer la variation spatio-temporelle des fluides diffus à l'échelle des sites hydrothermaux, et donc l'échelle des processus et des circulations associés. De plus, la géométrie du système de plomberie sous un site hydrothermal n'est pas accessible par échantillonnage ou observations directes. La modélisation numérique aide cependant à relier les observations in-situ avec la thermodynamique et la dynamique des fluides dans le substratum (e.g. Coumou et al., 2008; Fontaine et al., 2001; Guo et al., 2020; Wilcock, 1998).

L'objectif de cette thèse est de mieux caractériser ces processus, et leur rôle de forçage sur la faune hydrothermale, en utilisant nos observations de terrain sur des évents diffus et des fumeurs d'un même site hydrothermal. Dans ce contexte, cette thèse se concentre sur l'étude de fluides hydrothermaux provenant du champ hydrothermal Lucky Strike, situé à l'axe de la dorsale Atlantique, à environ 1700m de profondeur. Le champ hydrothermal Lucky Strike se trouve à environ 400 km au sud de l'archipel des Açores, au sommet d'un des plus grands volcans axiaux observés à l'axe de la dorsale médio-Atlantique. Les sites de ce champ

hydrothermal, d'une surface d'environ 1 km^2, se répartissent autour d'une dépression située au sommet du volcan axial. Cette dépression correspond à un lac de lave fossile. L'hydrothermalisme actif dans cette zone est dû à la présence d'une chambre magmatique située à ~3.5 km de profondeur sous le fond. Cette chambre magmatique n'est pas observable tout le long de l'axe de la dorsale, mais est restreinte au volcan axial : elle fait ~ 7km le long de l'axe et est large d'environ 3km (Singh et al., 2006). La circulation hydrothermale se produit pour l'essentiel le long de l'axe, l'eau de mer pénétrant dans un domaine de quelques kilomètres de large, très fracturé et fissuré, au sommet du volcan (Crawford et al., 2013; Fontaine et al., 2014).

Le champ hydrothermal Lucky Strike présente plus de 18 sites hydrothermaux (Barreyre et al., 2012) où les fluides évacués forment des monts de sulfure allant jusqu'à 20 mètres de haut. Lucky Strike accueille la plus grande diversité d'espèces de tous les champs hydrothermaux observés sur la dorsale Atlantique. Pour pouvoir étudier cette zone, et en particulier les sorties de fluides hydrothermaux, un observatoire sous-marin multidisciplinaire du réseau européen EMSO (European Multidisciplinary Seafloor and water-column Observatory) a été mis en place, du nom d'EMSO-Azores. Installé depuis 2010, cet observatoire comporte un réseau de capteurs connectés permettant d'avoir des données en direct à l'aide de relais acoustiques et satellitaires (Best et al., 2016; Blandin et al., 2010; Colaço et al., 2011). Ce réseau est complété par des capteurs autonomes remplacés chaque année lors des missions océanographiques MoMARSAT, qui ont pour objectif d'effectuer la maintenance de l'observatoire et de compléter ces mesures annuelles par des mesures instantanées et des échantillonnages de fluides. Cette thèse porte donc sur les données des sondes autonomes et des échantillons ponctuels récoltés à l'aide de cet observatoire. Les principales questions abordées sont les suivantes :

- Quelles sont les caractéristiques des fluides diffus à l'échelle du site hydrothermal à Lucky Strike ? Comment évoluent-elles avec la distance par rapport aux fumeurs noirs et avec le temps ?
- Quelle est la géométrie et la dynamique de la circulation hydrothermale proche de la surface au niveau de ces sites hydrothermaux ?

Pour répondre à ces questions, cette thèse a utilisé une approche combinée comprenant une analyse pluridisciplinaire des données in situ et une étude par modélisation numérique.

La première partie (I) de la thèse est un état des lieux des connaissances scientifiques utiles à la compréhension des notions clés de ce travail de recherche. Cette partie est composée de trois chapitres. Le premier chapitre présente le système de dorsale médio-océanique et ses caractéristiques physiques. Le deuxième chapitre développe la formation d'une circulation hydrothermale dans la croûte océanique, incluant les fumeurs noirs et plus particulièrement les fluides diffus. Le troisième chapitre introduit des notions sur les transferts de chaleur et de masse en milieu poreux. Il inclut également l'évolution historique de la modélisation de la circulation à l'échelle du champ hydrothermal, avec un examen préalable de l'effet de la perméabilité et des précipitations minérales.

La partie II (Chapitre 4) présente nos travaux sur les caractéristiques et la formation des fluides diffus, à travers des observations et des données sur deux sites, Tour Eiffel (TE) et White Castle (WC), du champ hydrothermal de Lucky Strike. Cette partie est constituée d'un manuscrit soumis à G-Cubed.

La partie III (Chapitre 5) présente une étude numérique sur la circulation des fluides hydrothermaux dans un milieu poreux peu profond, contrainte par les observations faites sur les fluides diffus et focalisés à Lucky Strike, présentées dans la partie précédente. L'objectif de cette étude est d'évaluer l'effet des paramètres géométriques ou physiques sur la circulation des fluides et d'étudier le rôle des précipitations minérales sur la formation de fluides diffus et sur la répartition des évents à proximité des sorties de haute température.

La dernière partie est une conclusion sur les principaux résultats des études des parties II et III, qui inclut les perspectives possibles de travaux futurs sur les effluents diffus, leur impact sur le flux de chaleur total et sur l'habitabilité des champs hydrothermaux de dorsales.

Les observations et les mesures sur le terrain ont été réalisées sur 3 années (2016-2019) à l'aide de sondes de température, de pression et de courantomètres, complétées par des mesures chimiques sur des échantillons de fluides réalisés à chaque mission océanographique (i.e. une tous les ans). Ces mesures ont pu être repositionnées géographiquement et comparées aux structures géologiques correspondant aux différentes zones de sorties de fluides grâce à une cartographie de haute résolution (Ondréas et al., 2009) et des mosaïques de photographie de haute résolution (Barreyre et al., 2012) du champ hydrothermal. Ces données ont été complétées par des observations in-situ réalisées lors des plongées à l'aide des vidéos du véhicule sous-marin téléguidé ROV Victor 60000 et du submersible habité Nautile. Ces observations ont été réalisées sur les sites de TE et WC, qui présentent tous les deux une zone elliptique entre 30 à 70 m de diamètre de sortie de fluides diffus entourant un mont de sulfure où les fluides de hautes

températures sont évacués. Le site de TE peut être considéré comme plus mature étant donné la hauteur de son mont de sulfure (environ 20 m) et la présence de nombreux fumeurs noirs. Le mont de sulfure de WC ne fait que quelques mètres de haut et comporte un unique fumeur noir.

Les observations géologiques et la cartographie permettent de mettre en évidence que les deux sites hydrothermaux TE et WC comportent plusieurs types d'évents diffus avec une distribution concentrique comparable sur les deux sites. Ces types d'évents dépendent de la formation géologique dont ils émanent. Une couche de dépôts volcanoclastiques minces (<1,5 m) déposée sur les basaltes dans toute la zone du champ hydrothermal de Lucky Strike agit comme un couvercle lorsqu'elle est indurée par des précipités hydrothermaux (on l'appelle alors le slab) et comme un milieu poreux lorsqu'elle n'a pas été indurée. En ressortent trois types d'évent diffus : (i) les fissures dans le slab induré, (ii) les fissures dans les dépôts volcanoclastiques et (iii) les plaques (« patches ») de sorties d'eaux moirées au niveau des dépôts volcanoclastiques poreux.

La chimie des fluides montre que les sorties de fluides diffus des deux sites résultent du mélange d'eau de mer avec des fluides hydrothermaux. La chimie de ces fluides suggère aussi une variabilité locale et temporelle de plusieurs processus tels que le réchauffement de l'eau de mer et/ou le refroidissement du fluide hydrothermal avant mélange, ou encore la précipitation et la dissolution d'anhydrite dans le sous-sol du site hydrothermal. Ces signaux pour la précipitation et la dissolution d'anhydrite dans plusieurs échantillons de fluides peuvent être dus à des gradients chimiques et de températures élevées, dans ou sous le slab. Nous avons aussi pu montrer que ces processus n'ont pas la même intensité sur les deux sites. White Castle présente des fluides avec une plus grande proportion de fluides hydrothermaux et des indices fréquents de cristallisation d'anhydrite. Cette différence peut être interprétée dans le contexte d'une différence de maturation entre les deux sites.

Les séries temporelles de température montrent que les différents types d'évents diffus ont des dynamiques différentes même pour des évents très proches (moins de quelques mètres). Notre interprétation implique un réseau perméable à l'échelle métrique contrôlant l'écoulement des fluides via de nombreuses fractures présentes dans le basalte sous-jacent. Les fluides percolent alors à l'interface entre le basalte et les dépôts volcanoclastiques, puis sont modifiés avant d'atteindre le plancher océanique, soit lors d'une advection dans la couche volcanoclastique poreuse conduisant à un élargissement de l'écoulement ascendant avec refroidissement latéral, soit par un mélange avec de l'eau de mer entraînée dans des cavités sous le slab. Des variations de température semi-diurnes avec une amplitude allant jusqu'à 8°C ont

été enregistrées dans les séries temporelles de fluides sortant des fissures ; ces variations semblent être également liées à cet entraînement local d'eau de mer. Les fluides qui sortent au niveau des « patches » diffus dans les dépôts volcanoclastiques ne montrent pas de variations de marée d'une telle amplitude, ce qui implique soit que les fluides qui percolent hors du socle basaltique n'ont pas de variations de température importantes aux fréquences tidales, soit que ces variations sont amorties lors du passage dans la couche volcanoclastique poreuse. En tous cas notre étude montre que les modulations tidales des températures des fluides diffus aux sites TE et WC sont pour l'essentiel acquise très près du fond, dans le slab ou les volcanoclastites.

Sur la base de nos résultats sur les évents diffus, nous proposons que les fluides sortants au niveau des basaltes sous-jacents aient des températures comprises entre 58°C et 304°C avec un mélange comportant jusqu'à 21% de fluides hydrothermaux end-member. Nous constatons que des fluides chauds (>80°C) et riches en fluides hydrothermaux end-member (>9%) sortent de ce sous-sol de basalte fracturé jusqu'à 25m des fumeurs noirs à TE et WC. Nous documentons également une variabilité à l'échelle métrique entre les sorties de fluides diffus, dont certains peuvent résulter de processus dans la couche volcanoclastique ou sous le slab induré, tandis que d'autres peuvent refléter une variabilité latérale des circulations dans le socle basaltique. A partir de cette nouvelle caractérisation des fluides diffus des sites TE et WC, nous proposons une nouvelle approche pour estimer le flux de chaleur diffus à l'échelle du site, qui considère non pas les évents observés sur le fond, mais la distribution et la température des sorties de fluides correspondantes dans les basaltes, sous la couche superficielle de volcanoclastites indurées (slab) ou non-indurées. Les flux de chaleur diffuse obtenus avec cette méthode se situent dans la gamme des valeurs moyenne à supérieure des études précédentes (Barreyre et al., 2012; Mittelstaedt et al., 2012). Ces valeurs confirment que les flux de chaleur portés par les sorties diffuses des sites du champ hydrothermal de Lucky Strike sont de l'ordre de plusieurs MW à quelques dizaines de MW.

L'ensemble de ces observations nous permet d'avoir des mesures de différents paramètres physiques pour contraindre des modèles numériques ayant pour but de prédire la géométrie de la circulation des fluides sous un site hydrothermal et la dynamique de formation des fluides diffus. Ces modèles n'ont pas pour vocation de reproduire la réalité mais de comprendre dans quelles conditions il est possible de former des fumeurs à >300°C et des sorties diffuses latérales à <80°C jusqu'à plus de 25 m des fumeurs. Pour cela le rôle de paramètres sur la largeur du domaine de sortie des fluides (la taille du site) et sur leur température sont testés tels que : (i) la

perméabilité des roches sous les sites hydrothermaux, (ii) la largeur du domaine d'entrée des fluides hydrothermaux chauds sous ces sites, (iii) la vitesse de remontée initiale de ces fluides, (iv) la température à la base du modèle et (v) la hauteur du modèle ; ou encore (vi) la précipitation de minéraux comme l'anhydrite. Pour cette modélisation, nous utilisons le logiciel de modélisation multiphysique et polyvalent COMSOL©. Cette interface graphique de modélisation permet de coupler plusieurs « modules » comportant plusieurs domaines de la physique et de la chimie. Dans notre cas, nous utilisons les domaines de transfert de chaleur et d'écoulement fluides en subsurface. En couplant ces modules nous pouvons réaliser des modèles de circulations de fluides chauds au sein d'un milieu poreux, équivalent au substratum basaltique sous les sites hydrothermaux étudiés dans la partie précédente.

Ces modèles sont basés sur une boite 2D perméable d'une centaine de mètres de haut. A sa base, une frontière imperméable, à une température donnée, représente la température du milieu poreux sous-jacent, avec une entrée de fluides à 350°C en son centre, correspondant à la zone de remontée des fluides chauds sous le site hydrothermal. Le haut du modèle est une frontière ouverte à une température de 5°C qui représente l'interface avec l'eau de mer. Les paramètres physiques suivants sont alors testés pour mesurer leur impact sur la circulation hydrothermale : la perméabilité du milieu poreux, la vitesse d'entrée du fluide hydrothermal, la largeur de la zone d'entrée du fluide hydrothermal, la température de la frontière inférieure du modèle et la hauteur du modèle. L'effet sur la circulation des fluides est évalué à l'aide de prédictions du modèle qui correspondent à des observables tel que la température maximale de sortie, la température minimale des fluides dans la zone de sortie, la largeur de la zone de sortie, en général et pour des fluides ayant des températures >300°C. Ces observables correspondent aux observations faites à TE et WC. La précipitation d'anhydrite lors du réchauffement de l'eau de mer à des températures >50-150°C (Bischoff & Seyfried, 1978) est également approximée et conduit à une diminution de la porosité, entraînant une diminution de perméabilité, dans les zones où l'eau de mer entraînée dans le substratum dépasse ces températures. La précipitation d'anhydrite a déjà été modélisée (e.g. Guo et al., 2020; Larson et al., 2015; Lowell et al., 2003; Pascoe & Cann, 1995), pour tenter de reproduire la forte température des fumeurs, mais avec peu de résultats sur la dynamique des circulations diffuses.

Les modèles réalisés dans cette thèse confirment que les perméabilités importantes ($\geq 10^{-12}$ m^2) qui ont été estimées par des méthodes géophysiques (e.g. Barreyre et al., 2018; Barreyre & Sohn, 2016; Evans, 1994; Marjanović et al., 2019) permettent de former des fluides de température équivalente à celle des fumeurs noirs uniquement si les vitesses d'entrée des fluides

chauds en base de boîte sont importantes, et si la hauteur du modèle reste faible. Pour des vitesses d'entrée plus faibles, et des boîtes plus hautes, des fumeurs ne sont formés que pour des perméabilités plus faibles (10^{-14} m^2). La perméabilité est aussi un paramètre majeur pour contrôler la largeur de sortie des fluides hydrothermaux au niveau du fond (c'est à dire la taille des sites hydrothermaux). La précipitation d'anhydrite simulée dans les modèles entraîne une réduction de la gamme des températures minimum de sortie des fluides au niveau du fond, permettant d'avoir des sorties de fluides à des températures >50°C pour les différentes conditions testées précédemment.

Cette thèse a donc permis d'identifier : (i) différents types de fluides diffus ayant des dynamiques différentes en fonction des formations géologiques qui contraignent leur circulation ; (ii) le rôle de la mince couche de volcanoclastites indurées ou non au-dessus des basaltes qui modifie les caractéristiques (température, vitesse et surface de sortie, chimie) des fluides sortant des basaltes sous-jacents. Prendre en compte cet effet nous permet de proposer une estimation indépendante des flux d'énergie portés par les sorties diffuses de Lucky Strike ; (iii) une dynamique de circulation des fluides et des mécaniques qui accompagnent cette circulation, et qui dépendent de la maturité du site où s'évacuent les fluides hydrothermaux ; et (iv) différents paramètres contraignant la formation de fluides diffus proches de sorties de haute température à l'aide de modélisations numériques à l'échelle du site hydrothermal.

Les perspectives immédiates ouvertes par ce travail concernent :

(i) Une meilleure prise en compte des flux de chaleur et de matière portés par des sorties diffuses dans la formation de volcanoclastites poreuses de Lucky Strike. Le modèle conceptuel proposé en fin de partie II, prédit un passage latéral de telles sorties très lentes, à des zones de flux conductif. Cette configuration, avec des variations latérales à l'échelle métrique, et des variations temporelles documentées sur quelques mois, reste à étudier. Pour cela j'ai participé à la construction artisanale d'une sonde à deux capteurs de température (LTgrad), permettant la mesure d'un gradient de température dans les dépôts superficiels meubles et poreux. Un réseau d'une dizaine de ces sondes a été déployé pour la première fois en 2018 et sera renouvelé jusqu'en 2022. L'analyse de ces données de température permettra de mieux cerner les zones réchauffées par circulation de fluides lente ou par conduction. Cette analyse, couplée à une meilleure cartographie des zones diffuses à l'aide des mosaïques d'images couleur OTUS2, permettra de mieux évaluer les flux chimiques et de chaleur à l'échelle d'un site hydrothermal.

(ii) Les fluides diffus émis dans la colonne d'eau jouent un rôle important pour la croissance et répartition de la faune hydrothermale. L'étude de la température, et de plusieurs paramètres physico-chimiques au sein de ces communautés biologiques à Lucky Strike est menée depuis plus de dix ans par des collègues biologistes et écologues. L'analyse poussée des données temporelles de température et de chimie dans cette thèse va servir à une meilleure compréhension de la contribution des fluides hydrothermaux aux conditions de ces habitats, qui sont par ailleurs situés sur le fond, et donc également affectés par la dynamique et les variations de température et de chimie des eaux de fond. Pour faire le lien entre ces deux contributions, une chaine de sonde de température a été déployée sur le site de TE en 2016-2017 (Girard et al., 2020), puis de nouveau en 2020.

(iii) Nos modèles numériques ne prennent pas en compte le transport des espèces chimiques, ne nous permettant pas de prédire des réactions chimiques ou de contraindre des taux de précipitations/dissolutions en fonctions des espèces disponibles dans les fluides. Cette contrainte nous empêche de prédire les quantités de mélange entre les fluides hydrothermaux dits end-member et l'eau de mer dans les sorties diffuses. Une amélioration de notre modèle serait donc pertinente, dans un premier temps via le suivi de particules au sein des fluides pour suivre les mélanges, puis par la suite l'intégration d'un modèle chimique et de transport des espèces chimiques. Ces modèles numériques sont aussi limités par leur résolution (ici de 10m) qui n'est pas suffisante pour observer des variations à l'échelle du mètre comme observé in-situ. Une augmentation de la densité du maillage du modèle dans la zone de sortie des fluides et donc un temps de calcul plus important serait utile pour mieux contraindre la géométrie de circulation de ces fluides diffus proche de la surface.

(iv) Enfin, le rôle important joué par la couche de dépôts volcanoclastiques pour la dynamique des circulations de fluides diffus à l'échelle d'un site hydrothermal rend nécessaire l'étude de cette circulation à l'interface entre le substratum basaltique fracturé et les dépôts poreux. Des modèles de petite échelle (1x1 m) ont été initiés en fin de thèse pour étudier ces circulations. Contraint par les mesures de température réalisées via le nouveau réseau de sondes LTgrad, ces modèles (non inclus dans cette thèse) pourraient nous aider à mieux comprendre les processus très superficiels qui modifient les fluides diffus sortant du substratum basaltique.

Introduction

The oceans cover more than 70% of the earth's surface and hide a large part of the underwater relief with more than 80% of the ocean still unexplored. Some of the most impressive seafloor features are the ocean ridges, equivalent to the longest mountain range in the world, and resulting from processes at divergent plate boundaries, where the new oceanic tectonic plates are formed.

This accretion is accomplished through significant volcanic and tectonic activity. Fractures and faults create permeability, and the magma bodies associated with volcanic activity provide heat sources. Together, these structures support the establishment of active hydrothermal circulation in the ocean crust, resulting in important thermal and chemical exchange between the solid earth and the oceans. This circulations takes the form of hydrothermal convection cells and hot hydrothermal fluids vent out of the seafloor above the upflow zones of these cells. This results in the formation of focused high-temperature vents known as "black smokers". Focused high-temperature vents create sulfide chimneys and result directly from the km-scale fluid convection cells that mine heat and chemical elements from hot rocks next to axial magma chambers. This thesis focuses on these magmatically fueled hydrothermal systems (there is also lower temperature and less vigorous hydrothermal circulation at mid ocean ridges that mine heat from the warm geothermal gradient). High-temperature hydrothermal vents go along with diffuse vents with lower temperature fluids. Together, these vents host unique ecosystems under extreme conditions.

Diffuse vents are not yet as well characterized as hot hydrothermal vents. They are more diverse, due to their dependence on the local geology. They discharge through cracks or patches at a variable distance from the focused venting areas. They vent intermediate to low-temperature fluids, with lower flow rates relative to black smokers. Diffuse vents, however, extend over larger areas, and therefore release overall larger heat and chemical fluxes than the black smokers. They also provide the most favorable habitats for biological communities. These two significant roles justify efforts to better constrain the diversity and the mechanisms of formation of diffuse vents at mid-ocean ridge hydrothermal fields.

Diffuse vents result from complex, and still poorly understood near surface processes that involve mixing of the hydrothermal fluids with seawater entrained in the seafloor, coupled with biochemical and abiotic chemical reactions leading to mineral precipitation or dissolution. These processes occur in a dynamic environment impacted by external parameters like the

pressure head of tides, bottom currents, and seismic activity. Hydrothermal fields at mid-ocean ridges are difficult to access. For this reason, surveys of diffuse fluids are still in the exploration phase: studied vents tend to be distributed over an entire vent field so that small spatial scale variability is not constrained, time series of venting temperature, fluxes, and chemistry are short, scarce and, in most cases, not carried out on the same vents. This does not allow data acquisition at a resolution fine enough to observe the variation of diffuse fluids in time and space and therefore to understand the related processes and fluid circulations at the scale of venting sites.

The deeper circulation of hydrothermal systems that result in seafloor venting is not accessible to direct sampling or observations. Numerical modeling helps to link the in-situ observations with the thermodynamic and fluid dynamic in the substratum. Together, in situ observations, monitoring data, and modelling help to further characterize diffuse venting areas, and to better understand the structure and dynamic of near surface hydrothermal processes and their forcing role on the hydrothermal fauna.

This thesis aims to address two principal questions:

- What are the characteristics of diffuse fluids at the hydrothermal site scale at two vent sites of the basalt-hosted Lucky Strike hydrothermal field, and how do they evolve with distance to the focused vents and with time?
- What is the corresponding geometry and dynamic of near-surface hydrothermal circulation at these sites?

To answer these questions, this thesis uses two approaches: geological observations and the analysis of time series of vent fluids temperature and chemistry; and numerical modeling. For the first approach, I use high-resolution seafloor mapping, submersible videos, and time series of fluid chemistry and temperature, current and seafloor pressure at two representative hydrothermal sites, the mature Tour Eiffel site and the younger White Castle site. These data were acquired at the Lucky Strike hydrothermal field (Mid-Atlantic Ridge) during several MoMARSAT oceanographic cruises (2016 to 2020; PIs : P-M Sarradin and M. Cannat) as part of the maintenance of the EMSO-Azores submarine observatory. I first present new data on diffuse fluids and their geological context at the Tour Eiffel and White Castle sites (two hydrothermal sites with a different degree of maturation). These observations are then used to constrain numerical models of shallow (up to 300 m) hydrothermal fluid circulation in a porous media beneath a typical basalt-hosted and magma fueled hydrothermal site.

The thesis manuscript starts with an introduction of the state-of-the-art scientific knowledge to provide context to my research work. This state-of-the-art part has three chapters, starting with a general introduction on mid-oceanic ridges, the ocean crust and its permeability. The second chapter presents the basics of hydrothermal circulation in the oceanic crust and specification on hydrothermal geological structures and a more thorough description of diffuse fluids characteristics and their processes of formation. The third chapter covers notions on heat and mass transfers in porous media, with a description of numerical models of mid-ocean ridge hydrothermal circulation, including the thermodynamics of hot and diffuse fluids, the effect of permeability and mineral precipitation.

Chapter 4 is a manuscript about to be submitted to Geochemistry, Geophysics, Geosystems (American Geophysical Union and the Geochemical Society). It presents the in-situ observations at the Tour Eiffel and White Castle vent sites (Lucky Strike hydrothermal field) and proposes a conceptual model of shallow (<100 m) sub-seafloor circulation at these two sites.

Chapter 5 presents numerical simulations of vent site scale hydrothermal fluid circulation in a shallow porous media. The objective of these simulations is to evaluate the effects of parameters such as the width and flow velocity of the upflow of end-member fluids, the permeability of the substratum, and mineral precipitation from entrained seawater, on observables such as the width of the observed venting area, and the maximum temperature of focused and diffuse fluids.

Part I

State of the art

Chapter 1.
Mid-ocean ridges and their hydrothermal circulation

The Earth is composed of a rigid outer shell named the lithosphere. This rigid layer is overlying the hotter and more ductile layer of the asthenosphere. The divergent plate boundaries, also called spreading centers or mid-ocean ridges, are the place where new lithosphere is accreted to form the plates and where the hydrothermal activity studied in my thesis is located. New plates created at mid-ocean ridges are recycled in subduction zones.

1.1. General background

As lithospheric plates diverge, the asthenosphere rises beneath mid-ocean ridges (MORs) and decompression triggers partial melting. The magma separated from the solid asthenosphere rises toward the seafloor and either erupts on the seafloor forming rapidly cooled extrusive basalts (mid-oceanic ridge basalts or MORB), or slowly cools at depths forming gabbros. MORs form a volcanic chain of ~60 000 km long over the globe (Figure 1-1); the region of active accretion is 5 to 50 km wide (Macdonald, 2001). Active accretion (i.e. plate separation) results from the combination of magma emplacement and extensional faulting.

These 2 processes create the context of MORs hydrothermal activity. As seawater seeps in the oceanic crust, it is heated and starts to react with the surrounding hot rocks, resulting in hot acidic fluids rich in elements that were dissolved from the surrounding rocks. When the fluids reach a temperature such that they have become buoyant (because density and viscosity both decrease at increasing temperature), they rise up to the seafloor. At the seafloor, the hydrothermal fluids cool at the contact of seawater and precipitate dissolved chemicals, forming sulfide edifices, and chimneys. The hydrothermal fluids vent as high-temperature at focused vents called “black smokers”, and as lower temperature so called diffuse fluids, allowing thermal and chemical exchange between the crust and the oceans.

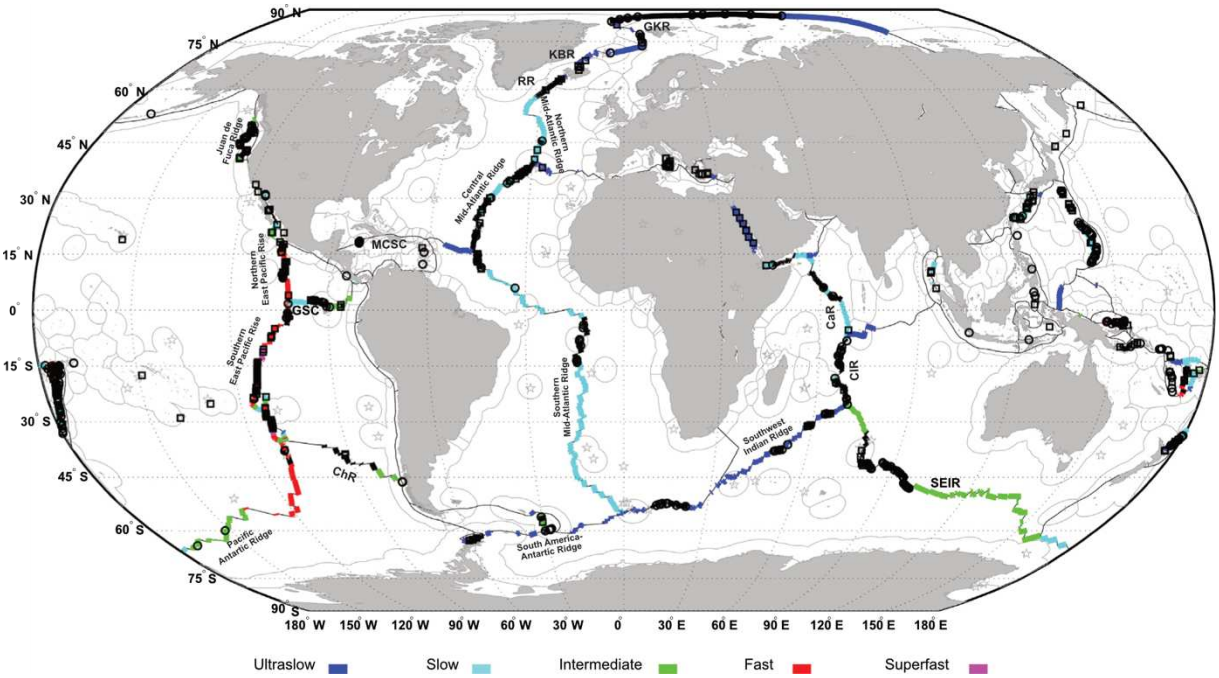

Figure 1-1 – Global map of mid-oceanic ridges from Beaulieu et al. (2015). Colors indicate spreading rate categorized as ultraslow (<20 mm/yr), slow (20–55 mm/yr), intermediate (55–80 mm/yr), fast (80–140mm/yr), or superfast (>140mm/yr). Other plots correspond to plate boundaries (black line), country exclusive economic zone (EEZ; grey lines), hotspots (gray stars) and the confirmed and inferred active vent fields for all tectonic settings (black squares). CaR: Carlsberg Ridge; ChR: Chile Ridge; CIR: Central Indian Ridge; GKR: Gakkel Ridge, GSC: Galápagos Spreading Center; KBR: Kolbeinsey Ridge MCSC: Mid-Cayman Spreading Center; RR: Reykjanes Ridge; SEIR: South East Indian Ridge.

Type of ridge	Full spreading rate (mm/yr)	Examples of ridge
Ultraslow (<20 mm/yr)	14	Southwest Indian Ridge
	18	South America-Antarctica Ridge
Slow (20-50 mm/yr)	22	Northern Mid-Atlantic Ridge
	24	Central Mid-Atlantic Ridge
	34	Southern Mid-Atlantic Ridge
Intermediate (50-80 mm/yr)	59	Galápagos Spreading Center
	60	Juan de Fuca Ridge
Fast (80-120 mm/yr)	110	Northern Eastern Pacific Rise
Superfast (>120 mm/yr)	149	Southern East Pacific Rise

Table 1-1 – Examples of spreading rates along the mid-ocean ridge system (See Figure 1-1 for locations) based on the width of magnetic anomaly stripes (Karson et al., 2015).

The proportions of magmatic, tectonic and hydrothermal processes at MORs are highly related to the accretion rate (i.e. the rate of plate divergence, or spreading rate). Spreading centers have accretion rates ranging from a few millimeters to several centimeters (ultraslow,

slow, intermediate, fast and superfast ridges; Figure 1-1 and Table 1-1). The Mid-Atlantic Ridge in the area studied for this thesis has a spreading rate of 22 mm/yr (DeMets et al., 1990).

Axial morphology is related to the spreading rate, which depends on magma supply and tectonic accommodation of the stretching of the lithosphere and will be reflected in changes in the type of volcanic and tectonic features.

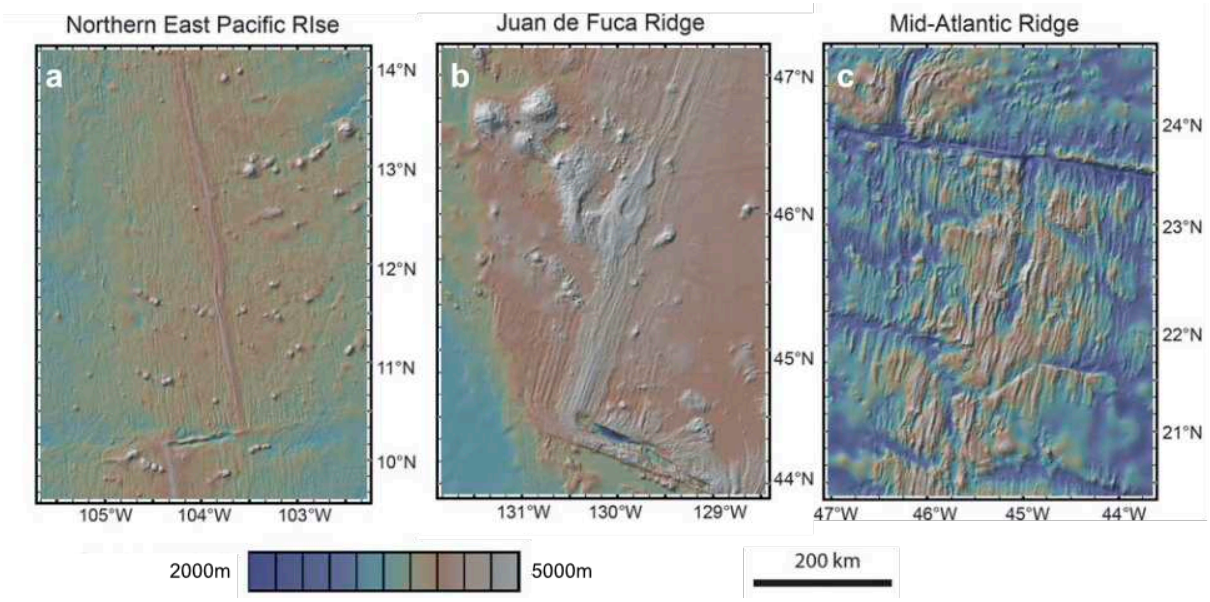

Figure 1-2 – Bathymetric maps of spreading centers as a function of spreading rate, with (a) a fast-spreading system (Northern EPR), (b) an intermediate-spreading system (Juan de Fuca Ridge) and (c) a slow-spreading system (21-24°N Mid-Atlantic Ridge) modified from Karson et al. (2015). Maps have all the same scale. Data source from GeoMapApp.

MORs are segmented by large-scale discontinuities impacting the lithospheric structure and the spreading processes. The first-order discontinuities are the transform faults and their related inactive traces, called fracture zones. Transform faults are characterized by a variable length from 30 km up to 1000 km for the longest active one, called the Romanche transform. Transform faults are composed of a transform valley (Figure 1-2), interpreted as the result of an isostatic response to thinner crust due to restricted magma supply (White et al., 1984). At the intersection with the ridge, the transform valley is deeper, creating nodal basins (Figure 1-2c), possibly as a consequence of a decrease in hydraulic head of material upwelling passively and from cooling when in contact with the fault (Sleep & Biehler, 1970).

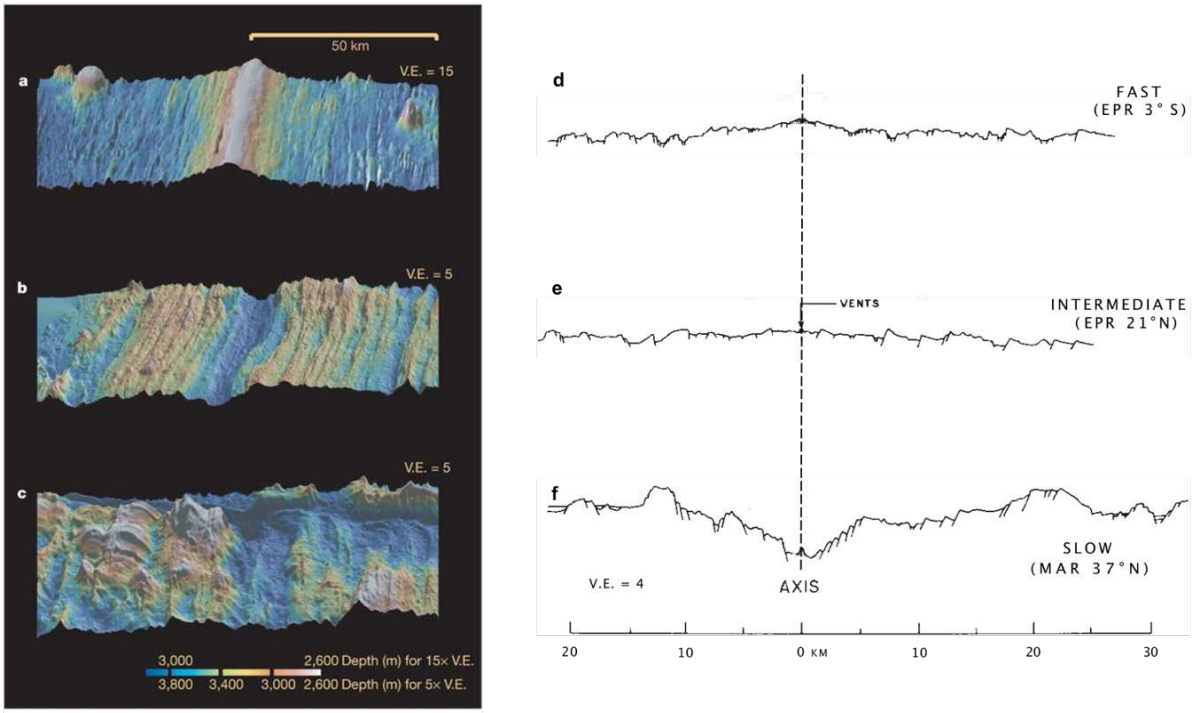

Figure 1-3 – Bathymetric maps (a, b and c) and cross-section profiles (d, e and f) of Mid-Oceanic Ridges with decreasing spreading rates (modified from Buck et al., (2005) and Macdonald (1982)). Each bathymetric map has the following dimensions: 40 km along axis and 110 km across axis (a, b and c). V.E.: Vertical Exaggeration.

Superfast- and fast-spreading MORs have a smooth axial region with young basaltic lava flows and an axial summit trough (AST) of ~100 meters-deep (Figure 1-3a and d). The axial high probably forms due to an isostatic response to the presence of melt in the shallow crust, and in the asthenospheric mantle below the ridge (Madsen et al., 1984; Wang & Cochran, 1993). As the spreading rate decreases, the morphology is progressively inverted with the formation of an axial valley delimited by normal faults with offsets of at least several hundred meters (Figure 1-3b and e). This inversion of the axial relief is linked to the ridge's thermal regime (Chen & Morgan, 1990): at fast MORs it is hot, so that the axial plate (or lithosphere) is thin. By contrast, at slow MORs the axial plate is thick and must be faulted in order for the plates to move apart (Buck et al., 2005). In addition, melt supply at slow spreading ridges is segmented and focused at segment center, while segment ends receive less melt with a thinner magmatic layer (Cannat et al., 1995; Lin et al., 1990; Tolstoy et al., 1993). As a result, half of the plate divergence at slow spreading ridges is accommodated by the activity of large offset normal faults, also called detachment faults (Cannat, 1993; Karson & Rona, 1990). In extreme cases, slip on axial valley bounding faults at slow and ultra-slow spreading ridges can create displacements of several kilometers that expose gabbros and variably serpentinized mantle-derived peridotites (Dick et al., 1981; Tucholke & Lin, 1994).

Magma, which is the main heat source for hydrothermal systems, is present at shallow depths (<3 km) below the axes of fast spreading ridges. Detrick et al. (1987) first detected by seismic reflection a reflector, called the axial magma chamber (AMC, or axial melt lens (AML)) reflector, that was interpreted as a melt lens at the roof of an underlying low-velocity zone (LVZ) made of partially crystallized gabbros. At superfast- to intermediate-spreading rates, the AMC reflectors are almost continuous below the ridge axis (Figure 1-4a). At slow-spreading ridges, by contrast, AMC or AML reflectors have only been reported so far at the Lucky Strike segment (Singh et al., 2006). The AMC at Lucky Strike is only detected for 7 km along-axis, beneath a large axial volcano that sits in the axial valley floor (Figure 1-4b). This rarity is probably related to the cooler axial regime of slow spreading ridges: the isotherms that correspond to the solidus of basaltic melts (~1000°C; Sinton & Detrick, 1992) are deeper.

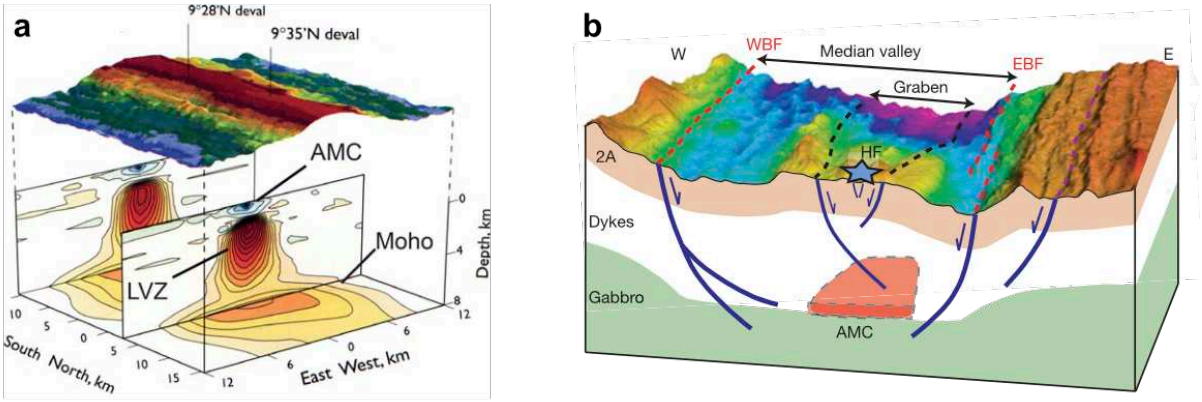

Figure 1-4 – Diagrams of Axial Magma Chambers (AMC) below their bathymetric maps (a) at the fast-spreading ridge of the Est Pacific Rise (Dunn et al., 2000) and (b) at the slow-spreading ridge of the Lucky-Strike segment (4km deep, 7km long and 4km wide AMC), Mid-Atlantic Ridge. Both diagrams show the underlying AMC with the related (a) low velocity zone (LVZ) at the EPR and (b) median valley faults going close to the AMC. HF: hydrothermal field; WBF and EBF: western and eastern boundary faults.

At intermediate-spreading MORs, a transitional morphology between fast- and slow-spreading rate systems is set. Here the variations of magma supply control the formation of structures from magma-poor rifted to magma-rich and smooth systems (Stakes et al., 2006). At these ridges, the lithosphere is relatively continuous like fast-spreading ridges but with overlying fault systems.

1.2. Structure and composition of the oceanic crust

The oceanic lithosphere comprises a low density-low seismic velocity layer corresponding to the oceanic crust, and a root of rigid, lithospheric mantle. The oceanic crust is on average 6-7 km thick from seismic refraction observations (White et al., 1992; Figure 1-5). Chen (1992) made a compilation of oceanic crust thickness from seismic data of the 70's at or near MORs, as a function of spreading rate (Figure 1-5). He did not observe any significant variation of the crustal thickness for MORs with spreading rates > 40 mm/yr. By contrast, the thickness of the oceanic crust at slow spreading ridges (SR < 40 mm/yr) varies from 3 to 9 km, due to segmentation (Figure 1-5).

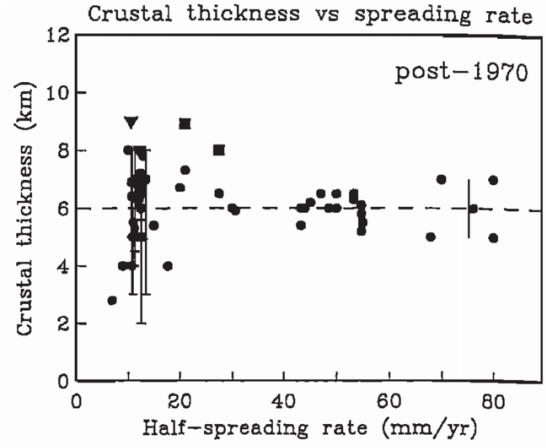

Figure 1-5 – Oceanic crust thickness as a function of spreading rate from seismic studies after 1970 with the crustal thickness variations (error bars) close to transform faults. The dashed line corresponds to the mean thickness of the crust at 20 km away from the segment end along the ridge axis. Note the constant variation above 30 mm/yr compared to the high variability for slow-spreading ridges. Figure by Chen (1992).

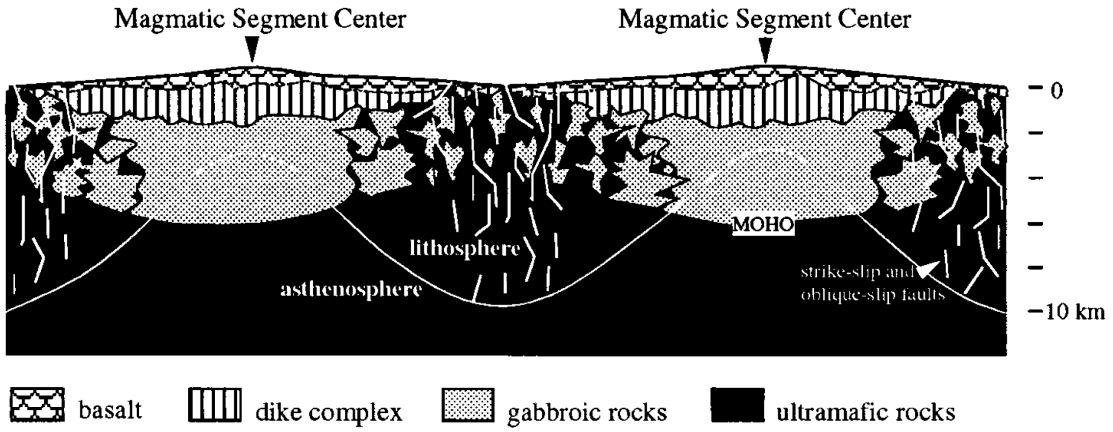

Figure 1-6 – Schematic diagram by Cannat et al. (1995) of 2 magmatic segments along a slow-spreading MOR. The lithosphere thickness varies along the ridge, being deeper at the center of MOR segments and shallower at the intersection with discontinuities at both ends of the segment.

The thickness of the oceanic crust is also variable within each segment of slow and ultraslow spreading ridges (Figure 1-6), with 7-8 km at the segment center and 2-3 km at segment ends (Cannat et al., 1995; Kuo & Forsyth, 1988; Lin et al., 1990; Tolstoy et al., 1993). For example, the oceanic crust is 7.5 km thick at the center of the Lucky Strike segment, and less than 4 km-thick at the segment ends and can thin to ~2km close to fracture zones (Seher et al., 2010a).

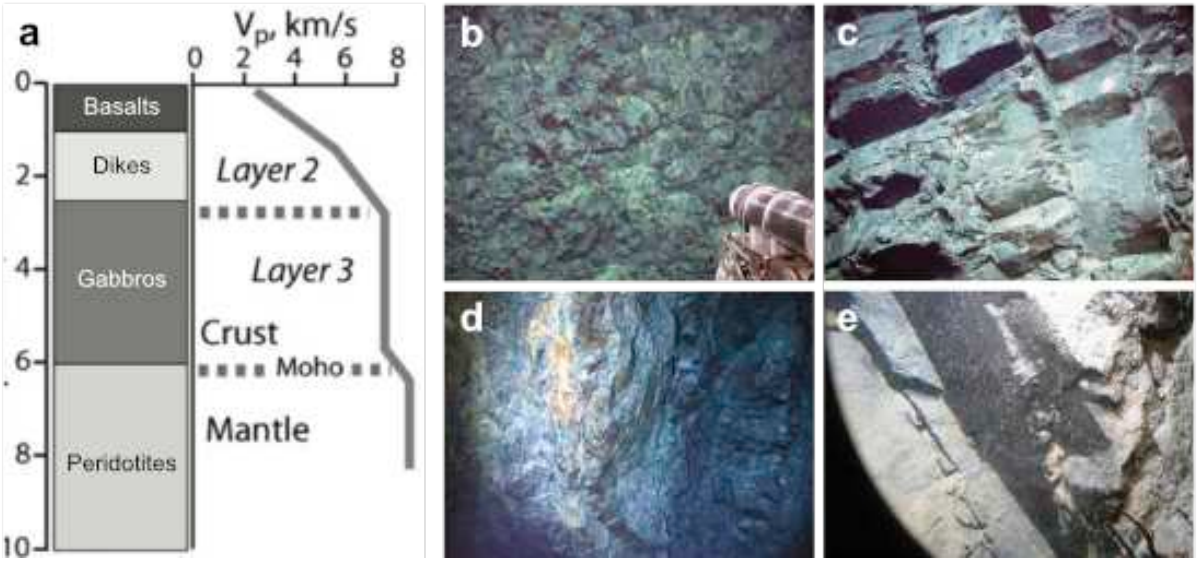

Figure 1-7 – *(a) Seismic velocity profile of P waves (km/s) in the oceanic lithosphere and the related seismic layers compared to the associated lithologies (Mével, 2003). (b-e) Examples of geological features exposed by tectonic windows and forming the crust at intermediate- to fast-spreading ridges: (b) pillow lavas, (c) sheeted dikes (d), faulted lavas and dikes (lower left), and (e) gabbroic rocks (lower right) occur in a regular layered sequence. Field of view is ~2 m for all images. Images from Pito Deep Cruise, 2003, WHOI, NSF.*

A good part of our knowledge on the oceanic crust composition comes from seismic refraction data. Since the early 60s, seismic refraction has shown that the oceanic crust formed at fast and intermediate spreading rates, and at and near segment centers of slow and ultraslow ridges, consists of 3 main layers (Raitt, 1963). By analogy with observations made in ophiolites, the Penrose model (1972) proposes a geological interpretation of these 3 layers (Figure 1-7):

- Layer 1 is composed of sediments consolidated with their accumulation on the seafloor; this layer thickness increases with the crustal age, and is almost absent at the ridge axis.
- Layer 2 is characterized by a large seismic velocity gradient, extrusive basalts then sheeted dykes. (Becker, 1989). Within layer 2, a reflector called the 2A/2B boundary is commonly observed, which may be due to a rapid decrease in fracture porosity and therefore in the proportion of fluids with depth (McClain et al., 1985; Wilcock et al., 1992). An alternative hypothesis is that layer 2A corresponds to a

larger proportion of highly porous extrusive lava, with more massive lava flows and dykes below. Layer 2A has a mean axial thickness of ~150-250m. Layer 2B is interpreted as mostly composed of sheeted dikes (Christeson et al., 2007).

- Layer 3 is characterized by a small seismic velocity gradient, and is interpreted as a layer of gabbro.

The oceanic lithosphere is composed of the 3 layers of the oceanic crust, overlying a fourth layer composed of a portion of the upper mantle (i.e. lithospheric mantle). The transition between crust and mantle is marked by the Mohorovičic discontinuity (Moho), which corresponds to a jump of seismic velocities to 8.0-8.2 km/s.

At slow and ultraslow spreading ridges, segment ends do not display this layered seismic structure. Instead, seismic velocity increases more regularly from seafloor to the base of the crust. The geophysically-defined oceanic crust does not only contain magmatic rocks but rather a mixture of lava, gabbros and serpentinized mantle rocks that have been exhumed along detachment faults (Cannat, 1993; Cannat 1995). The decrease of seismic velocities can be explained by the presence of gabbroic material and serpentinized peridotites, that have both lower density than the fresh mantle.

1.3. Permeability of the young oceanic upper crust

Permeability is the major hydraulic property controlling fluid circulation in the seafloor, from seawater infiltration to upflowing hydrothermal fluids (Lowell & Burnell, 1991). The crustal layers defined by seismic studies are inferred to have distinct permeability ranges, impacting the shape, intensity and path of hydrothermal fluids. Permeability is expected to decrease with distance from the active ridge because fracture porosity would not be maintained by extensional deformation. Instead, it would rather become clogged by mineral precipitates from the circulating fluids (Becker & Davis, 2003). Permeability also decreases with depth, due to higher lithostatic pressure and to lithology changes that impact the pores size and the cracks density (e.g. from pillow flows to massive flows and dikes).

Measuring permeability is a complex task: in the laboratory the samples are small and the measurements only pertain to small scales; in situ measurements are more relevant in terms of the scales of hydrothermal circulation. Table 1-2 summarizes measurements made in young oceanic crust (off-axis) of mid-ocean ridges with bore holes, using electric resistivity and drill

string packers. String packers are deployed in an already drilled hole, and are used to isolate a portion of the hole for hydraulic experiments. The permeability is measured by pumping fluids into the isolated portion of the hole and by monitoring the diffusion of these fluids into the host rock. The permeability values are estimated for an equivalent porous media, and called "bulk permeability". A second method is called "cross-hole", that uses two bore holes, one open where cold fluids are pumped and one monitored to measure pressure variations. This method provides bulk permeabilities for larger scales (Figure 1-8).

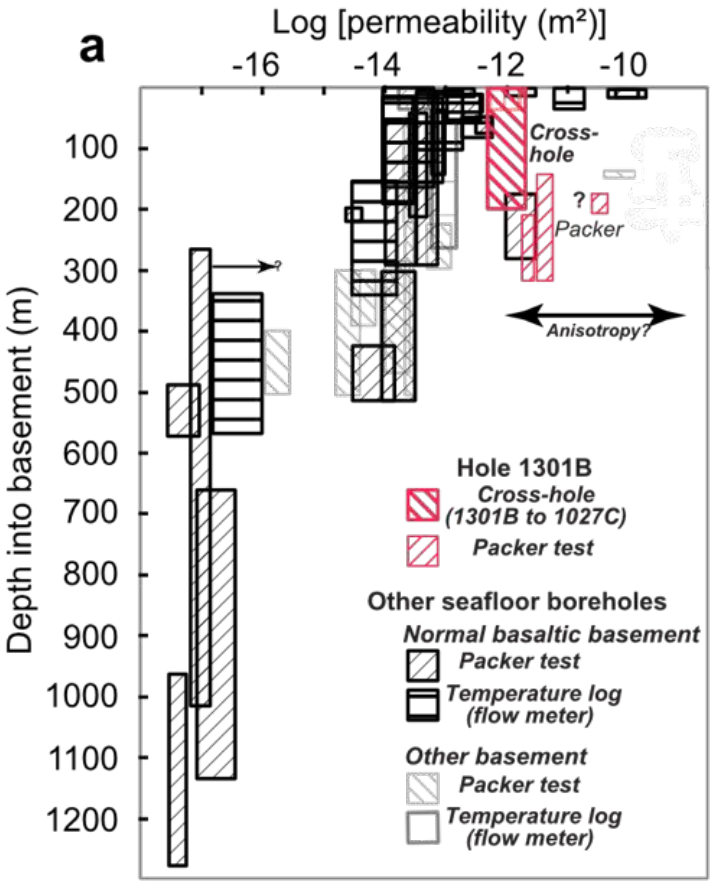

Figure 1-8 – Diagram of permeability global data as a function of depth from packer and single-hole flow experiments by thermal logs in core hole from (Fisher et al., 2008). Note the higher permeability below the 300m.

Packers and cross-hole experiments give a large range of permeability values from 10^{-11} m^2 in the shallow extrusive layer up to 10^{-16} m^2 at the deepest drilled basalts (Figure 1-8 & Table 1-2). The range of permeability is higher closer to the surface. Fisher et al. (2008) have measured the highest permeability values observed with the packer method. They interpreted these high values as due to an azimuthal anisotropy of the studied area (eastern flank, Juan de Fuca ridge) consistent with fluids flowing along the preferred orientation of faults. Faults orientation is therefore a major parameter for the permeability.

Indirect permeability estimates for zero-age oceanic crust are also possible through geophysical measurements. Seismic data can be used, with velocity-porosity and porosity-permeability relationships (Carlson, 2014; Evans, 1994; Marjanović et al., 2019). Electrical resistivity (Becker, 1990; Evans, 1994). The permeability of the upper oceanic crust at mid-ocean ridges has also been estimated from the poroelastic response of hydrothermal systems to tidal loading (Barreyre et al., 2014b,2018; Barreyre & Sohn, 2016; Crone et al., 2011). These indirect methods yield estimates of the effective permeability over larger scales than the packer experiments, and are also adapted to estimate the permeability of zero age crust, which is not accessible to drilling (too fragile and too hot).

Indeed, the different methods used for the estimation of permeability provide results that are relevant at different scales. Packer tests in borehole are measuring the permeability at the scale of the sealed column of a maximum of few hundred meters (Table 1-2). In comparison, estimates based on other geophysical parameters are applied to larger and deeper volumes, which may contain localized zones of higher permeability (for example large faults). Indirect estimations from geophysical studies give permeabilities between 10^{-13} and 10^{-9} m^2 for layer 2A and lower permeabilities between 10^{-17} and 10^{-12} m^2 in layer 2B (some studies that are not indicating the delimitation between layers 2A and 2B give permeabilities between 10^{-16} and 10^{-9} m^2 (Table 1-2)).

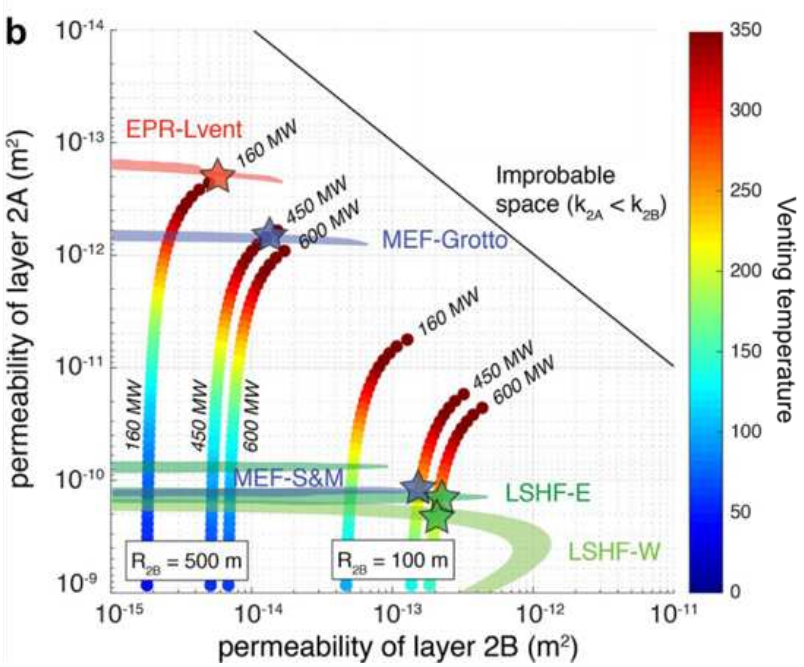

Figure 1-9 – Constraints on layer 2A and 2B permeability as a function of the observable phase-lag between tidal loading and vent temperature (colored areas) for 5 venting hydrothermal areas. Gradient colored lines correspond to permeabilities of 2A and 2B compatible with different heat flow (MW) for 2 different radii possible of upflow zone R_{2B}. Domain with an extrusive layer of lower permeability compared to the layer 2A is treated as improbable

If we take the example of permeability estimation via poroelasticity (Barreyre et al., 2018), this estimate represents the effective permeability of the whole zone of hydrothermal upflow, but does not account for the probable decrease in permeability with depth or for the heterogeneities in the subsurface. This study is based on the poroelasticity of the crust impacting the subseafloor fluid flow with water column pressure variations created by tides, leading to a phase lag between the observed fluid temperature at hydrothermal vents and the pressure head measured in the surrounding water column (detailed in section 2.4.4.2).

Figure 1-9 (Barreyre et al., 2018) illustrates these possible phase lags at each studied hydrothermal venting area (EPR-L vent, MEF-Grotto and -S&M, LSHF-E and LSHF -W) for the different permeabilities of layers 2A and 2B, represented as light-colored surfaces. These phase lags are compared with 2 sets of 3 estimated heat outputs (160-450-600 MW), for 2 possible radii of a cylindric upflow zone in layer 2B (R_{2B}=100m and R_{2B}=500m) as a function of the permeability of layer 2A and 2B. The intersection between the estimated venting temperature from the heat flow and the possible phase lag can constrain the permeability of both layers 2A and 2B for each site. Note that the estimated permeabilities for both layers are all above the estimation by borehole measurement (Table 1-2). High temperature systems (>300°C) are difficult to obtain at high permeability for layer 2A. By comparing both sets of upflow zone radius, it seems that a narrow one facilitates the formation of hot vents and will be consistent with higher permeability for the layer 2B (at least for LSHF and MEF-S&M), highlighting the important role of the deeper layer. By comparing values obtained from joint vent fields, we see that nearby sites (MEF-Grotto and MEF-S&M here) can have different effective permeabilities (Figure 1-9), pointing out the horizontal variability of the system.

If parameters like permeability can impact hydrothermal advection in such important ways and given that the composition and structure of the oceanic crust is also variable, hydrothermal venting at the seafloor can be key in the characterization of the subseafloor. The exploration of hydrothermal fields and the monitoring of hydrothermal fluids are therefore of major interest in advancing our knowledge of the oceanic crust and also in understanding the different processes that influence fluid circulation in a young crust, and constraining their role in hosting submarine fauna.

Reference	Permeability (m^2)	Depth into sub-basement (msb)	Method	Location	Crustal age
(Becker et al., 1983)	>6.0 x 10^{-14}	0-100	Packer test	Costa Rica Rift Hole 504B	6.2 Ma
(Morin et al., 1992)	3.0 x 10^{-14}	19-158	Packer test	Mid-Atlantic Ridge, west flank Hole 395A	7,3 Ma
	7.0 x 10^{-15}	158-347			
	<< 10^{-16}	347-571			
(Fisher et al., 1997)	5-9 x 10^{-12}	10	Packer test	Juan de Fuca Ridge, east flank Hole 1026B,	3,5 Ma
(Fisher, 1998)	1.6 x 10^{-14}	11-174	Packer test	Middle Valley, Juan de Fuca Ridge, Hole 858G	<200ka
	8.0 x 10^{-14}	61-91			
(Becker & Fisher, 2008)	1.7 x 10^{-12}	207-318	Packer test	Juan de Fuca Ridge, Hole 1301B	3.5 Ma
	3.2 x 10^{-12}	152-318			
	2.0 x 10^{-11}	177-207			
(Davis et al., 2010)	3-5 x 10^{-13}	0-318	Packer test	Juan de Fuca Ridge, eastern flank Hole 1301B	3.5 Ma
(Winslow et al., 2013)	4.7 x 10^{-12}	215	Packer test	Costa Rica Rift, southern flank Hole 504B	5.9 Ma
	3.7 x 10^{-12}	48		Juan de Fuca Ridge, eastern flank Hole 1026B	3.5 Ma
	6.6 x 10^{-12}	318		Juan de Fuca Ridge, eastern flank Holes U1301A and U1301B	3.5 Ma
	1.5 x 10^{-11}	108			
(Becker & Fisher, 2000)	3 x 10^{-11}	10	Packer test	1024C, Juan de Fuca Ridge 1026B, Juan de Fuca Ridge 1027C, Juan de Fuca Ridge	0.9 Ma 3.5 Ma 3.6 Ma
	2 x 10^{-13}	47			
	2 x 10^{-14}	54			
(Fisher et al., 2008)	0.7-2.0 x 10^{-12}	0-318	Cross-hole	Juan de Fuca Ridge, eastern flank Holes 1301B-1027C	3.5 Ma
(Becker, 1985)	<<10^{-16}	2-101	Electrical resistivity	Costa Rica Rift, south flank Hole 504B	5.9 Ma
(Becker, 1990)	1-2 x 10^{-14}	19-257	Electrical resistivity	Mid-Atlantic Ridge, west flank Hole 395A	7.3 Ma
(Evans, 1994)	5.8 x 10^{-12}	Near seafloor	Seismic Velocity/Electrical esistivity	East Pacific Rise, ridge crest	0-100 ka
	7.8 x 10^{-17}	1000			
(Davis et al., 1996)	2.0 x 10^{-12}	600	Seismic velocity	Juan de Fuca Ridge, east flank	1 Ma
(Marjanović et al., 2017)	10^{-13}-10^{-16}	1800 (no delimitation)	Seismic velocity	Est Pacific Rise 9°16'N-9°56'N	On-axis
(Barreyre et al., 2014)	10^{-10}	2A (~600 msb)	Poro-elastic response	Mid-Atlantic Ridge, Lucky Strike hydrothermal field	On-axis
(Barreyre & Sohn, 2016)	10^{-10}	2A (300-600msb)	Poro-elastic response	Mid-Atlantic Ridge, Lucky Strike hydrothermal field	On-axis
	10^{-14}-10^{-13}	2B			
	10^{-10}-10^{-13}	2A (~450 msb)		Juan de Fuca Ridge Main Endeavour	
	10^{-14}-10^{-13}	2B			
	10^{-13}	2A (~155 msb)		Est Pacific Rise 9°50'N	
	10^{-14}-10^{-13}	2B			
(Barreyre et al., 2018)	10^{-10}	2A	Poro-elastic response	Lucky Strike hydrothermal field	On-axis
	8 x10^{-12}	2B			
	3 x10^{-12}	2A		Main Endeavour Field Grotto	
	9 x10^{-13}	2B			
	9 x10^{-9}	2A		Main Endeavour Field S&M	
	9 x10^{-12}	2B			
	9 x10^{-13}	2A		East Pacific Rise Lvent	
	4 x10^{-14}	2B			
(Crone et al., 2011)	10^{-9}-10^{-14}	1500 (no delimitation)	Poro-elastic response	East Pacific Rise 9°50'N	On axis?
(Marjanović et al., 2019)	$10^{-12.7}$-$10^{-10.3}$	2A	Seismic velocity	East Pacific Rise 9°50'N	On-axis
	10^{-17}-10^{-10}	2B			

Table 1-2 – Tab modified from Fisher (1998) of indirect estimates of bulk permeability in the upper igneous oceanic crust with different techniques.

Chapter 2.
Hydrothermal activity at Mid-Ocean Ridges

2.1. Discovery of hydrothermal systems at Mid-Ocean Ridges

The first evidence of hydrothermal activity at a mid-ocean ridge was published by Murray & Renard (1891) after the HMS Challenger expedition at the Eastern Flank of the East Pacific Rise (EPR). They described samples of metal-rich sediments as "coherent, dark red-brown sediment, […] plastic when wet". New observations came during the 1960s: hot acidic brines (Charnock, 1964) rich in metals and silica linked to minerals deposits of sulfides, anhydrite and silica were recovered in the Red Sea at 2000m deep, allowing new hypotheses relating hydrothermal discharge from subseafloor fluid circulation driven by a possible magmatic heat source (Backer & Schoell, 1972; Miller et al., 1966). During the same period, sediments enriched in metals were confirmed near the crest of the EPR (Bostrom & Peterson, 1966).

Heat flux measurements were also a major clue for the presence of fluid circulation in the oceanic crust at mid-oceanic ridges: during the exploration of the new theory of plate tectonics, numerous measurements of conductive heat flow were made to estimate the thermal evolution of the oceanic lithosphere. These measurements were lower than the predicted by models for ocean basins younger than ~60 Ma. Lister et al., (1972) suggested that hydrothermal circulation could be the dominant heat transfer process at ridge crests, highlighting their potential importance for lithosphere evolution (see section 2.2 for thermal models and heat flux).

The first direct observation of hydrothermal vents at mid-oceanic ridges happened at the Galapagos Spreading Center (GSC) in 1977, with the discovery of low temperature hydrothermal fluids and a unique chemo-synthetic fauna (Corliss et al., 1979; Edmond et al., 1979a,b) . The first observation of hot focused vents, or "black smokers", was reported at the EPR 2 years after in 1979, with the first exploration of seafloor massive sulfides (SMS) deposits (Spiess et al., 1980). In the following decades and until today, more than 700 hydrothermal fields have been identified at MORs, either by direct observations of venting areas on the seafloor or inferred from oceanographic surveys (Figure 2-1). The exploration of submarine hydrothermal systems at mid-oceanic ridges has now extended to various geological settings such as slow-spreading ridges with the Trans-Atlantic Geotraverse segment (TAG) hydrothermal field at the Mid-Atlantic Ridge (MAR, Rona, 1980; Rona et al., 1975; M. Scott et al., 1974; R. Scott et al., 1974), back-arc basins starting with the Okinawa Trough (Kimura

et al., 1988), and ultramafic-hosted alkaline hydrothermal vents (Lost City at the Atlantis Massif of the MAR; Kelley et al., 2001; Rona et al., 1987). Hydrothermal fields have also been explored at submarine volcanic arcs (e.g. the Aeolian arc; Gamberi et al., 1997). Current exploration methods mainly identify active hydrothermal fields from oceanographic investigations of the water column through deployment of conductivity, temperature, transmissometer packages making measurements at different depths (Baker et al., 1995) or with autonomous systems (German et al., 2008). Hydrothermal plumes resulting from seafloor hydrothermal discharge impact the water column composition and its physical characteristics (temperature, conductivity, concentration of suspended particles). However, inactive/dead/extinct and low temperature hydrothermal sites are undetectable with these methods (Beaulieu et al., 2015). These methods are also not appropriate to detect low-temperature and particle-poor diffuse hydrothermal sources or to identify closely spaced hydrothermal vents. Therefore, it has been proposed that the occurrence of hydrothermal activity at fast- to intermediate-spreading ridges could be 3 to 6 times higher than the actual observed systems (Baker et al., 2016)

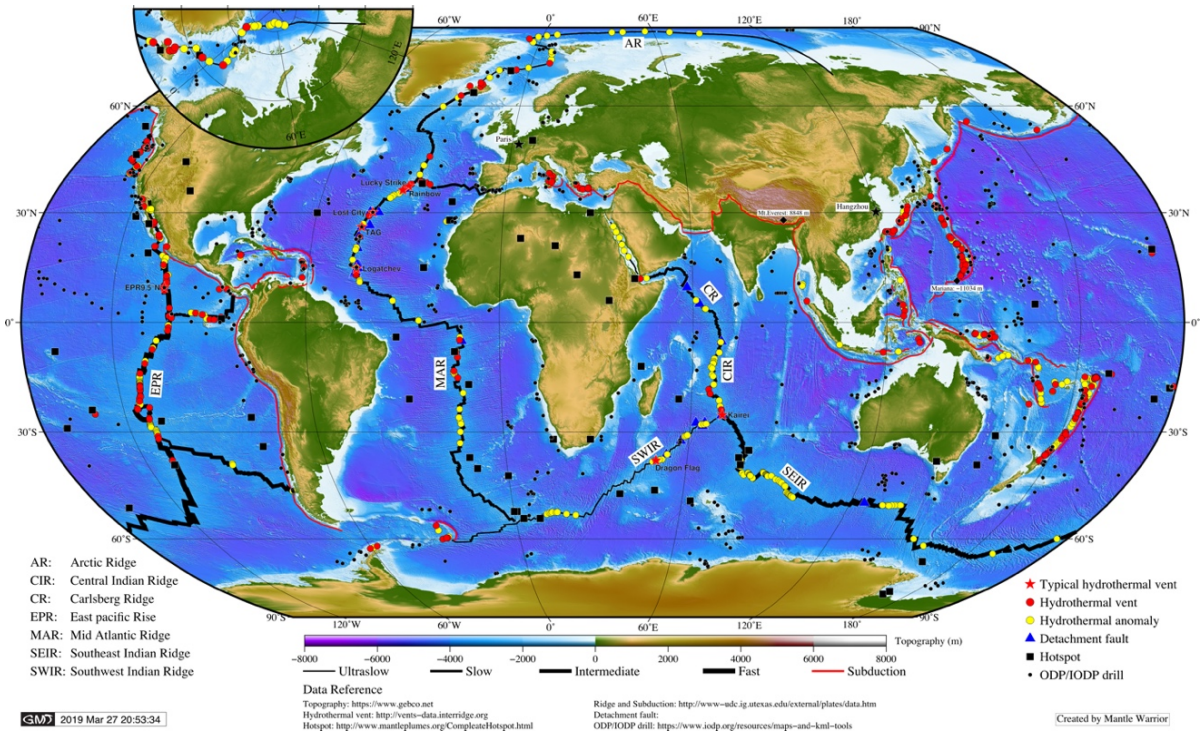

Figure 2-1 – Distribution of submarine hydrothermal fields around the world from the InterRidge Vents Database (Beaulieu & Szafrański, 2020). This map shows the active (red circle) and main studied (red stars) hydrothermal fields. Unconfirmed hydrothermal activity is shown in yellow circles. Ultraslow to fast mid-oceanic ridges and subduction zones are indicated respectively by black and red lines. Map Courtesy of Jie Chen, PhD candidate of Institut de physique du Globe de Paris (Jie Chen (2021)). Bathymetry map of global Mid-Ocean Ridge, hydrothermal vent fields, and detachment faults.doi:10.6084/m9.figshare.14680419.v1. https://ndownloader.figshare.com/files/28754505.)

2.2. Hydrothermal activity at MORs

Heat flow is one of the main factors that constrains the thermal structure of the oceanic lithosphere. Thermal gradients of heat flow associated with conductive cooling of the oceanic lithosphere are directly measured within the overlying sediments. At the MORs axis, newly accreted oceanic lithosphere in contact with seawater cools with time and thickens as plates spread. Off-axis topography is then correlated to both the increase of seafloor depth and the age of oceanic plates, as evidenced by heat flow measurements.

Half-space cooling thermal models of the oceanic lithosphere adequately predict this relationship (Davis & Lister, 1974; Parsons & Sclater, 1977; Figure 2-2a) for lithosphere with ages up to 50-70 Myrs (Figure 2-2b). At the axis, these models predict an infinite heat flow and are therefore not able to predict heat flux at the ridge (Parsons & Sclater, 1977; Stein & Stein, 1994). As mentioned above, heat flow measurements for young oceanic crusts (< 10-20 Myrs) are lower than the values predicted by these semi-conductive, half-space cooling models (Figure 2-2b). This difference between predicted and in-situ measured values is attributed to cooling of the upper lithosphere by axial hydrothermal circulation, both on-axis (the topic of this chapter), and off-axis (not addressed here).

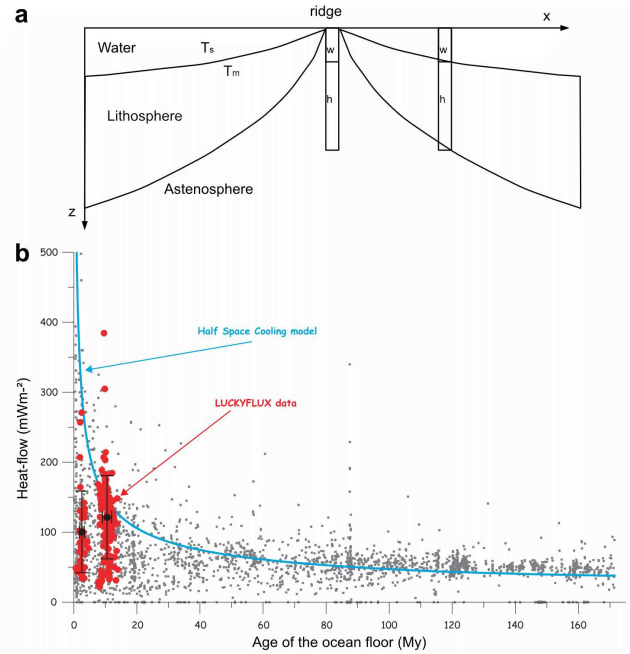

Figure 2-2 – (a) Schematic diagram of the half-space cooling model with 2 examples of formed columns, one at the ridge and one at the ridge flank. Both columns have the same mass for the same area since the water column increases away from the ridge to compensate the higher density of the lithosphere. (b) Heat flow as a function of age of the ocean floor (Lucazeau et al., 2006) for complied heat flow data (grey) and for LUCKYFLUX data from the Lucky Strike segment (red). Averages of these two fluxes are shown in dark points. The blue line is the half space cooling model predictions for the heat flow as a function of the age of the oceanic crust.

However, it is possible to make a simple estimation of the amount of heat that needs to be released (Cannat et al., 2004), by hydrothermal convection and conduction, to account for the cooling of the upper lithosphere on-axis. The extent of this cooling is estimated based on geological and geophysical observations. In Figure 2-3, we reproduce this calculation for a simplified system with a Penrose-type crust. The heat loss comprises the intrinsic heat of melt (released over the interval ΔT_1), the latent heat of crystallization H_f, and the intrinsic heat of the magmatic rocks (released over ΔT_2 for extrusive lava, and ΔT_3 for gabbros and dikes). Other variables are the thickness of the magmatic layers (h_e for the extrusive basalts and h_{dg} for the dikes and gabbros), and the spreading rate s_r. Parameters for the calculation are: the crust density ρ; the latent heat of crystallization H_f; and the thermal capacity of melt and magmatic rocks ($C_{p,1}$ and $C_{p,2}$ respectively).

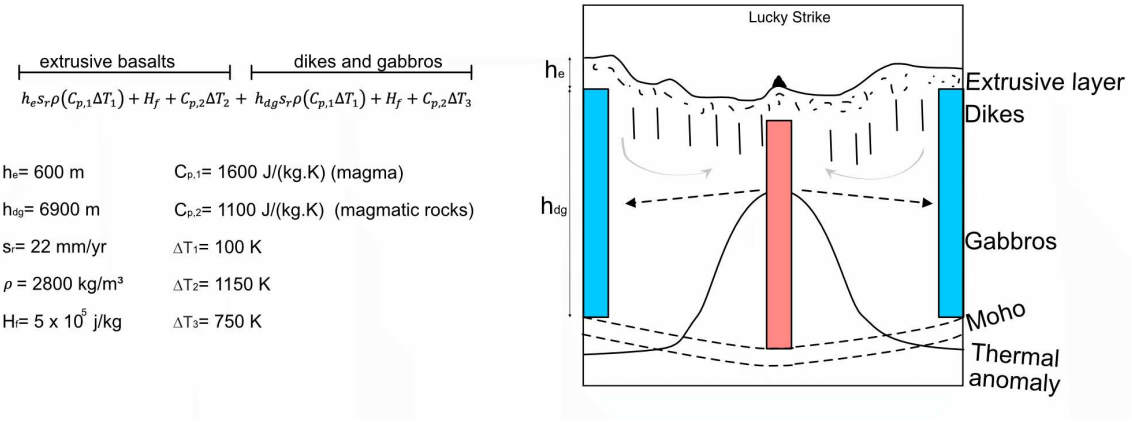

Figure 2-3 – Estimation of the heat supply per km of ridge advected by magma. The right diagram shows the cooling of a magmatic layer at the ridge center (red) to build a magmatic layer of h_e+h_{dg} height(blue).

Using values discussed in Cannat et al. (2004) for temperature intervals and thermal parameters (see Figure 2-3), we apply this approach to the center of the Lucky Strike segment with the following parameters: a spreading rate of 22 mm/yr (Cannat et al., 1999; DeMets et al., 1990), a depth for the basaltic extrusive layer at the median valley of h_e= 600 m (Seher et al., 2010b); a layer of dikes and gabbros of h_{dg}= 6900m with a total crustal thickness of 7500m (Crawford et al., 2010). We calculate a heat flux of 2.6 MW/km for the basaltic extrusive layer and of 22.7 MW/km for the dikes and gabbroic layer. The oceanic crust is thicker at the center of Lucky Strike segment and decreases down to less than 4 km at its segment ends. The values estimated here are therefore high end-member values of the time integrated heat flux associated with cooling of the crust at Lucky Strike. Comparing these values to estimates of the heat flux of the Lucky Strike hydrothermal field (118-389 MW (Wilson et al., 1996) and 187-1086 MW

(Barreyre et al., 2012)), it becomes clear that either the vent field extracts heat from several km of the ridge axis with the more effective process of convection, or that the heat extraction is intermittent, as documented by Humphris & Cann (2000) at the TAG field.

2.3. Formation of hydrothermal fluids

The hydrothermal circulation found at MORs is the result of seawater penetration into the permeable new upper oceanic crust. In this substratum, the fluid physical and chemical characteristics evolve. As the fluid descends, it will become hotter and less dense, and will then rise to the seafloor. In this section, we describe the processes involved at each step of this pathway (Figure 2-4) for a basalt-hosted hydrothermal system, as presented by Alt (1995).

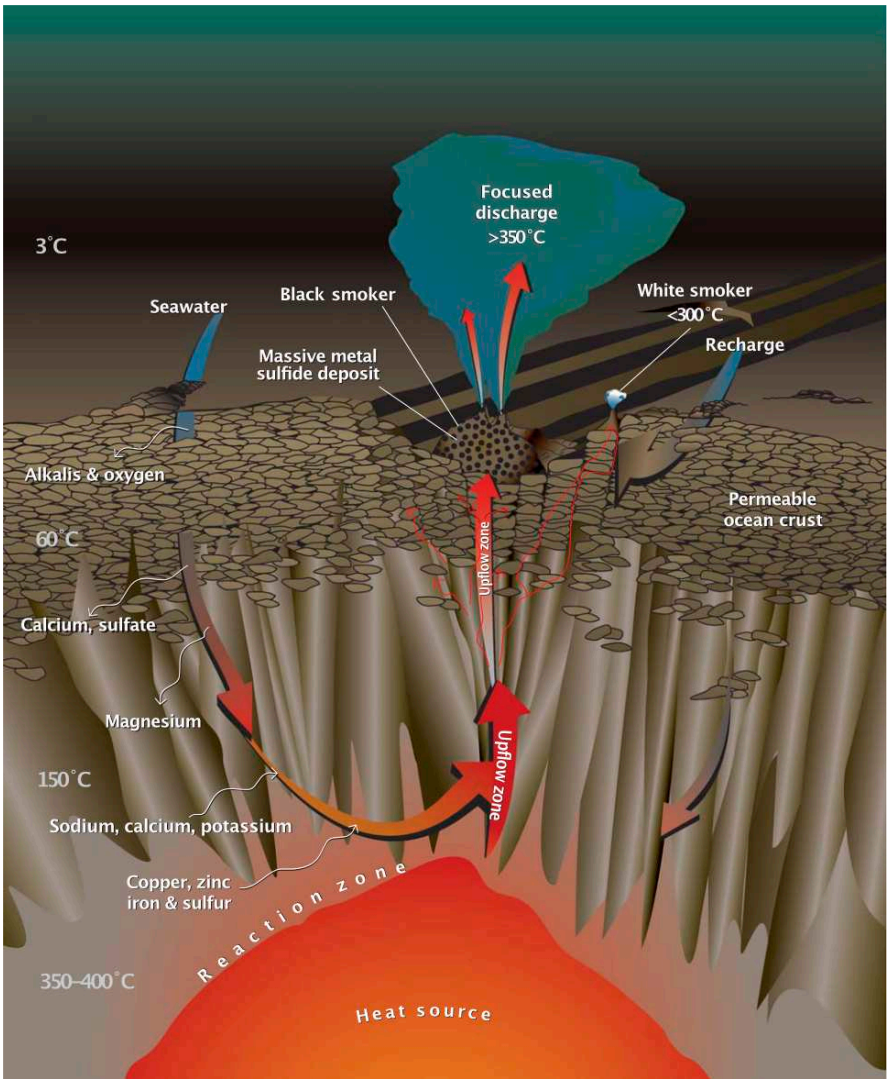

Figure 2-4 – Schematic cross section of the oceanic lithosphere and the associated hydrothermal cell, with the different reactions between the circulating fluids and the surrounding rocks. The convection cell is separated in 4 zones: the recharge zone, the reaction zone at the roof of the axial magma chamber, the up-flow zone and the discharge zone at the seafloor surface. Figure from Humphris and McCollum, Oceanus, 41 (2), 1998.

2.3.1. Recharge zone

The first step for hydrothermal circulation is the infiltration of seawater in the oceanic crust. This process takes place in the "Recharge zone", which is defined as a zone where the 2-5°C oxidizing seawater is penetrating and starts to flow down in the volcanic layers (Figure 2-4). This infiltration is possible through fracture networks and the high intrinsic porosity of the extrusive layers (Johnson et al., 2010). The extent and spatial distribution of seawater infiltration are not easy to evaluate with direct observations. However, it can be evidenced by anomalously low heat flow at the seabed (e.g. Johnson et al., 2010).

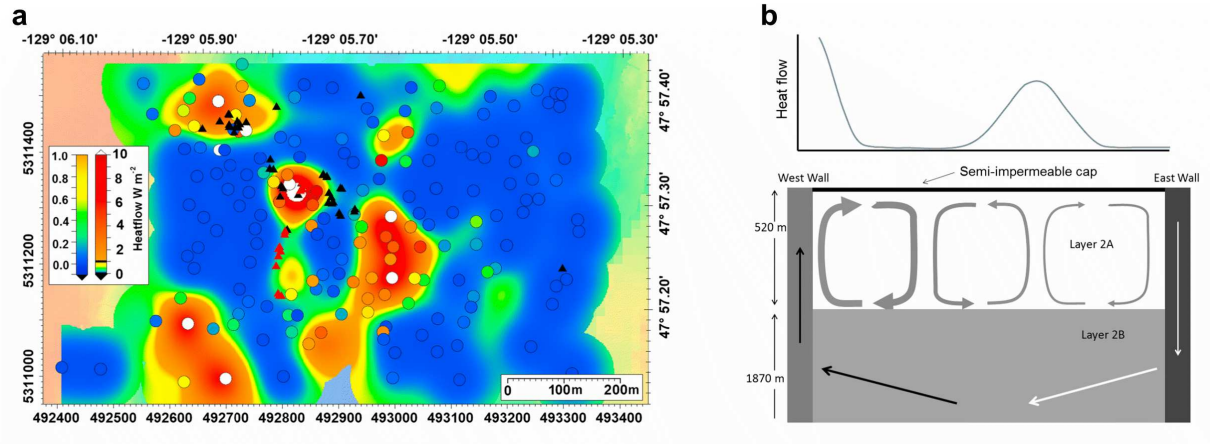

Figure 2-5 – (a) Interpolated heat flow and corresponding measurements (colored circles) at the seafloor of the Raven field at the Juan de Fuca Ridge, with active hydrothermal vents (red triangles) and dead sulfides stacks (black triangles). (b)Proposed model of fluid circulation and recharge zones for the layer 2A and 2B. The model is constrained by heat flow measurements moving away from hydrothermal venting sites and the permeability of geological structures. Note the clockwise convective cell close to the upflow zone below a semi-impermeable cap. The adjacent convective cell is counterclockwise, forcing an upflow zone of lower velocity leading to a heat flow anomaly at the surface. Figures from Salmi et al., 2014.

Heat flow measurements carried out at the seafloor on the Juan de Fuca Ridge with thermal blankets recorded heat flow time-series in large areas with a good resolution between each measurement (Johnson et al., 2010; Salmi et al., 2014). Estimates of heat flow at the hydrothermal field scale carried out so far have focused in near vent areas and may represent not only the recharge domain of the main hydrothermal circulation, but also secondary entrainment of seawater near vents. Heat flow measurements made at the Raven hydrothermal field at the JFR with these thermal blankets show the presence of large areas (>50% of the measurements) of low heat flux between 0-0.11 $W.m^{-2}$ (Figure 2-5a) suggesting a possible recharge zone with entrainment of seawater within 20m of active hydrothermal vents (Salmi et al., 2014). The authors interpret these patterns of low heat flow at the seafloor as shallow hydrothermal circulation in the upper hundred meters of the extrusive layer 2A. This circulation

is constrained by a semi-impermeable sediment layer acting like a cap at the top of the system (Figure 2-5b). Heat flow measurements expended to include both flanks of the axial ridge highlight additional and deeper hydrothermal circulation across the segment axis circulating into the hot rock of the layer 2B (Figure 2-5b). Heat flow can also be measured in thin sediments using a short heat flow and resistivity probe. For example, Becker et al. (1996) conducted heat flow measurements at the TAG hydrothermal mound and observed low heat flow domains forming a belt around the focused venting sites suggesting local recharge.

Descending fluids go through deeper and hotter parts of the crust. The base of the recharge zone can be indirectly constrained by microseismicity (Crawford et al., 2013; Tolstoy et al., 2008; Wilcock et al., 2002). At the Lucky Strike hydrothermal field, seismic events relocated at depths of ~2500-3000 m, a few hundred meters above the AMC reflector that underlies the Lucky Strike volcano (Combier et al., 2007; Singh et al., 2006), and ~500m to the north and south of the active sites, have been interpreted as due to a rapid cooling of hot rocks by hydrothermal downflow (Crawford et al., 2013). In this study, two possible sources of fluids were therefore proposed to exist along the axis (Figure 2-6a): one ~500m north and the other south of the active hydrothermal field flowing through adjacent faults or narrow weak and permeable axial regions (Crawford et al., 2013). Similar observations were made at the fast-spreading East Pacific Rise with a narrow zone of seismicity extending down to ~2km deep at the AST axis (Figure 2-6b; Tolstoy et al. (2008)). There, microseismicity extends to very shallow depths in zones interpreted as downflow, or recharge zones (Tolstoy et al., 2008).

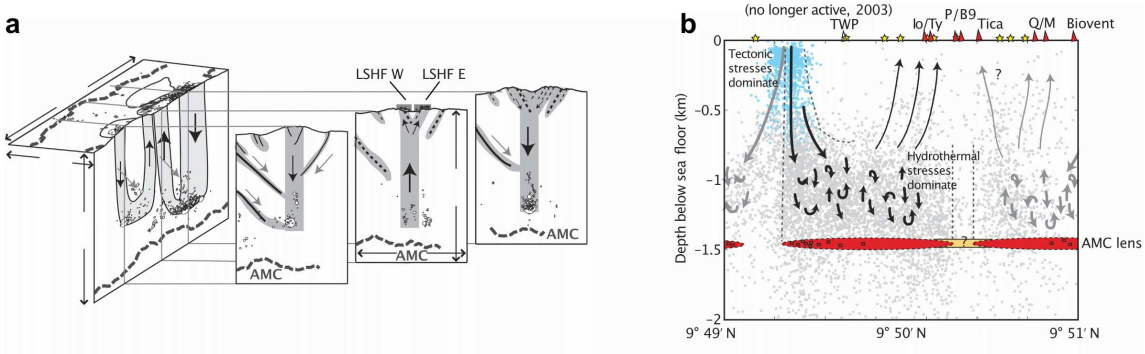

Figure 2-6 – Proposed model of hydrothermal circulation beneath (a) the Lucky Strike segment from Crawford et al. (2013) and (b) the 9°49-51'N EPR segment from Tolstoy et al. (2008), from microseismicity. (a) Cross section of the Lucky Strike segment, with the estimated down- and upwelling hydrothermal zones (in grey) along imaged faults (black lines) by seismic reflection (Combier et al., 2007) and extrapolated faults from seafloor observations (black dashed-lines). AMC reflectors are indicated by large grey dotted-lines. (b) Cross section of the 9°49-51'N EPR segment, with the earthquakes generated by tectonic stresses in blue and those generated by hydrothermal stresses in grey. Black lines correspond to the estimated hydrothermal flow from the best-defined hydrothermal cell.

Chemically, the fluid evolves all the way through the recharge zone. Seawater reacts with rocks at low temperature (<60°C) to produce Fe-oxyhydroxides minerals. Alkalis (Na, K, Rb and Cs) from seawater are trapped into celadonite and nontronite clay minerals filling pores and veins (Figure 2-4). Deeper in the crust, Mg is fixed in saponite clay minerals for temperatures <170°C, smectite (<200°C) or chlorites (>200°C), along with a release of Ca into the fluid (Figure 2-4). Anhydrite ($CaSO_4$) is precipitated when seawater is heated for temperature between 150°C and 300°C, over 300°C anhydrite start to be unstable as fluids start to be more acidic and the remain SO_4^{2-} give form to sulfides (Bischoff & Seyfried, 1978; Guo et al., 2020). Anhydrite is a unique mineral in hydrothermal systems due to its retrograde stability resulting in dissolution of precipitated anhydrite below 150°C (see section 2.3.3).

2.3.2. Reaction zone

The descending fluids cannot penetrate into hot and ductile magmatic products, and thus, a cracking front is formed at the base of the hydrothermal system (Lister, 1974). This front corresponds to the boundary between the colder, brittle and permeable crust and the underlying hotter, ductile and impermeable layers. The region of the cracking front is conductively heated from below, and a conductive boundary layer forms, with a strong temperature gradient. Temperature and pressure conditions reach their maximum in this region, as do the exchange of heat and chemicals between the hydrothermal fluids and the surrounding rocks. Above 350°C and under the acidic, reducing conditions, the rocks release sulfur and metals like Fe, Mn, Cu or Zn into the fluid. This region is also where exchange of volatiles like CO_2 or ^3He may take place between the magma chamber and the fluid.

Fluid-rock interaction in the cracking front region also lead to phase separation (Von Damm, 1995). The critical point of seawater is reached at 407°C and 29.85 MPa (Bischoff & Rosenbauer, 1988). These conditions are commonly reached or overcome in the reaction zone. may take place between the magma chamber and the fluid. Below the critical point, seawater "boils" to produce a low salinity vapor phase containing dissolved gases and metals, and a liquid phase- this is subcritical phase separation. Above the critical point, seawater "condenses" a small amount of brine with poor volatiles concentration - this is super-critical phase separation (Figure 2-7a).

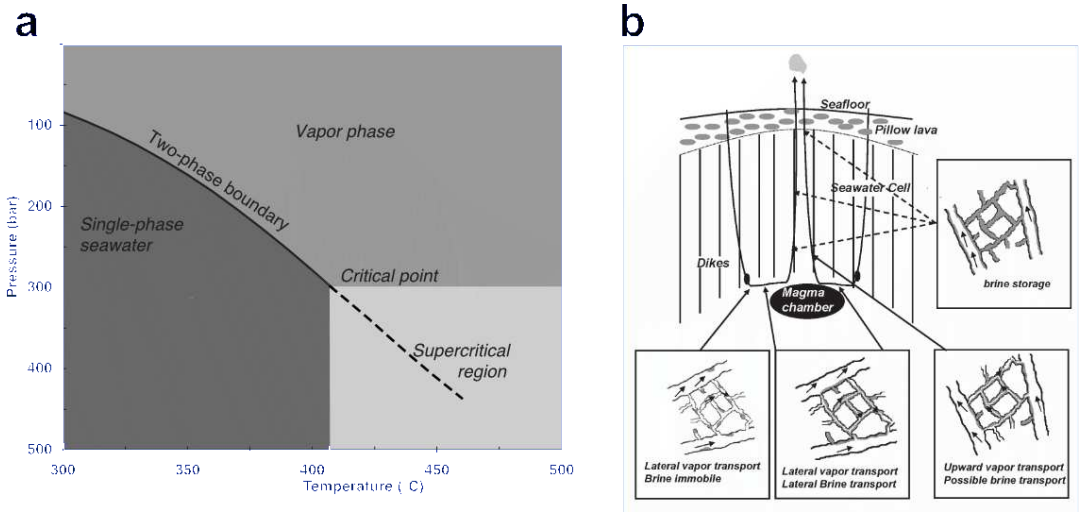

Figure 2-7 – (a) Diagram of the two-phase boundary and the critical point of seawater for temperature between 300 and 500°C and pressure between 0 and 500 bar. Modified from Koschinsky et al. (2008) (b) Schematic diagram of hydrothermal circulation model and brine dynamic storage (Fontaine & Wilcock, 2006). The grey area corresponds to brine, the black circles correspond to the reaction zone where phase separation happen and black arrows correspond to vapor and brines flows.

The brine is dense and remains at depth, while the vapor phase flows to the surface in the larger cracks (Fontaine & Wilcock, 2006) (Figure 2-7b). The higher density of the brine is expected to limit its entrainment in the upflow zone (Figure 2-7b). The position of phase separation in the deep reaction zone or in the upflow zone is a first-order control on hydrothermal vent fluid salinity (Von Damm, 1995). Numerical models have predicted that a permeability interface within the crust (as for example the layer 2A - 2B transition) is needed to produce hydrothermal venting fluids with the observed range of temperature and salinity (Fontaine et al., 2007b).

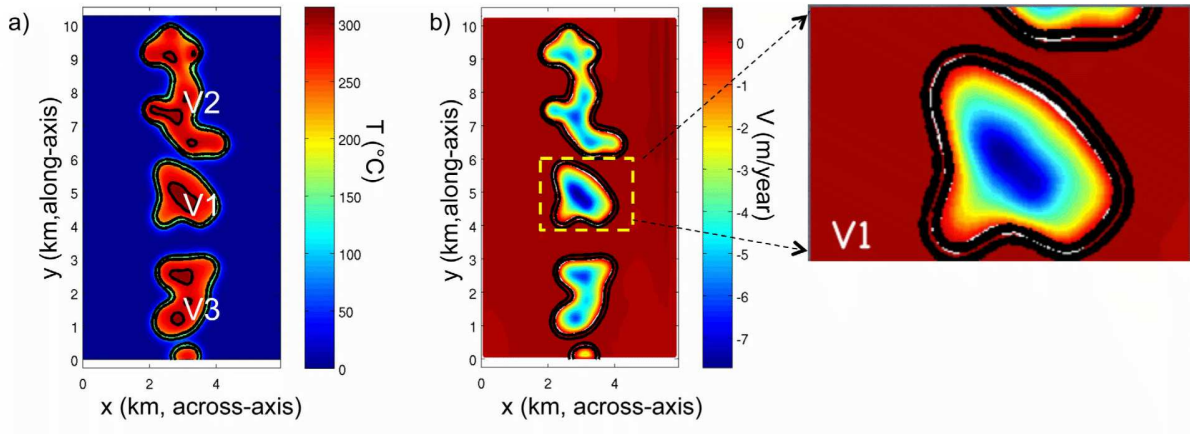

Figure 2-8 – Results from Fontaine et al. (2014) models with (a) the model surface temperature (Black lines for 100° and 200°C isotherms) and (b) the model surface Darcian velocity with upflow (negative values) and downflow (positive values)along the axis (White lines for the transition between upflow and downflow). Here, the model is based on bottom temperature corresponding to wide cross-axis gradient with the highest temperature at the center, and a homogeneous permeability of 3×10^{-14} m^2. Not the transition between upflow and downflow at 200°C on the V1 zoom.

Water heated up to 200°C has a viscosity decrease by one order of magnitude making it more mobile, while density varies by only 10%, maintaining a downward movement (Coumou et al., 2008, Figure 2-8a). At near phase change conditions (i.e. ≥400°C at most MORs hydrothermal systems) both the density and the viscosity of the fluid decrease substantially and the fluid flow start to rise (Figure 2-8b). The upflow region is also called the discharge zone.

The hot temperature and the metal-rich composition of black smoker fluids are indications that the flow in the upflow zone is rapid and focused: the hot hydrothermal fluid does not cool enough in the upflow zone, and its chemical signature is largely preserved due to limited interactions with the surrounding rocks (Edmond et al., 1979).

2.3.3. The stockwork formation

Close to the seafloor below the hydrothermal mound, however, the upflowing hot hydrothermal fluid locally interacts with entrained cold seawater, resulting in mineral precipitation and formation of a stockwork. This shallow region of the upflow zone was first described from evidence at ophiolites and then described by submersible in-situ observations in a fault scarp at the Galapagos sulfide mound (Embley et al., 1988). Key information was then provided by drilling at the TAG hydrothermal mound. During Leg 158 of the Ocean Drilling Program (ODP), 7 cored holes with a maximum penetration of 125.7 mbsf (meter below sea floor) provided constraints on the hydrothermal mineralogy composition and stratigraphy in three dimensions (Figure 2-9a; Humphris et al., 1995a, 1995b, 2015). The observed sequence was found to be comparable to massive sulfide deposits observed at the Cyprus ophiolite (Hannington & Scott, 1988). Massive sulfides are present only in the first meters of the sequence at TAG. The underlying layers are composed of clastic breccias whose composition changes with depth. Up to 45 mbsf, the breccias are composed of pyrite clasts surrounded by a matrix rich in anhydrite. Below that, the matrix also contains silica. Underlying this breccia, basaltic breccia and fresh basalt are surrounding highly altered basalt. The stockwork formation grows in time with the different processes creating these mineral assemblages (Fouquet et al., 1998). Massive sulfides on the top of the stockwork growth at the surface when buried and recrystallized in the sulfide mound surface. Anhydrite formation in veins help the internal growth of the formation while underlying basalt are weathered by fluid circulation, silicified into pyrite/quartz assemblage to increase the depth of the stockwork (Fouquet et al., 1998).

These observations provide a general concept for the formation of hydrothermal vent sites, through seawater entrainment and upflow of end-member hot fluids in the sulfide mound and below (Figure 2-9a). The intense discharge of hot hydrothermal fluids creates shallow recharges of cold seawater entrained in the shallow sub-seafloor (Humphris et al., 1995a). When heated, the seawater precipitates anhydrite in the pore and cracks, changing the permeability and sealing the fluid upflow zone. Silica can act in the same way to seal the system (Fouquet et al., 1998). Based on the TAG ODP drilling, seawater entrainment extends down to at least 58 mbsf, while the presence of fresh basalt at the bottom of the cores shows that the upflowing fluids is contained in a narrow zone (Humphris et al., 1998).

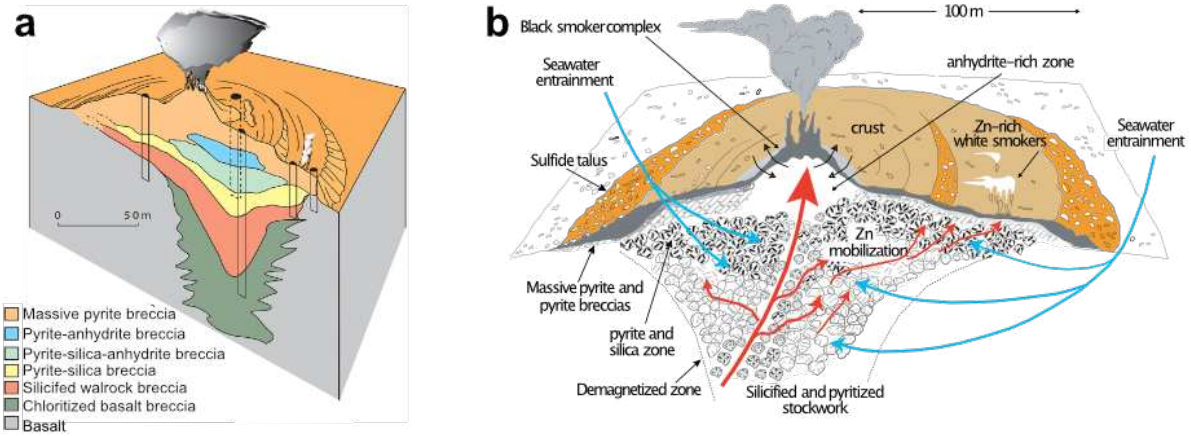

Figure 2-9 – Cross-section of the hydrothermal mound of TAG with (a) subsurface stratigraphy determined with the indicated drill hole sites of the ODP LEG 158 and (b) dynamic of fluid circulation in the sulfide mound with the associated mineral precipitations. (a) From bottom to top, fresh basalts are altered by the circulation of hydrothermal fluids and seawater highlighted by basalt chloritization. Above, the substratum is dominated by breccia of pyrite clasts surrounded by silica and then by anhydrite in the shallower parts. The top of the sulfide mound is covered by pyrite formed by massive sulfide precipitation. Figure from Humphris et al. (2015). (b) Vigorous venting from deep-seated convection cells (red arrows) are percolating at the seafloor forming black smokers and mixing in the mound with cold seawater (blue arrows) entrained in the edifice. Figure by Humphris & Tivey, 2000 and Tivey, 2007.

2.4. Scales and characteristics of basalt-hosted hydrothermal venting at MORs

In this part, I first describe the spatial scales of hydrothermal discharge at several well documented MOR magma-fueled hydrothermal field. I then describe the relations between focused and diffuse vents, from published in situ and monitoring studies.

2.4.1. Hydrothermal fields, sites and vents

High temperature black smokers and associated diffuse hydrothermal vents have been observed in all ranges of mid-ocean ridge environments: (i) at slow-spreading ridges, with the example of Lucky Strike hydrothermal field ;Figure 2-10a; e.g. Barreyre et al., 2012) or TAG (Figure 2-10c; e.g. Edmond et al.,1995;James and Elderfield, 1996); (ii) at intermediate spreading ridges, such as the Axial Seamount at the Endeavour segment of the Juan de Fuca ridge (Figure 2-10b; e.g. Schultz et al., 1992; Rona and Trivett, 1992); and (iii) at the fast spreading East Pacific Rise: 9-10°N hydrothermal field (Figure 2-10d; Ramondenc et al., 2006, Von Damm and Lilley, 2003).

These hydrothermal fields have different spatial distributions. In this thesis I use the term hydrothermal field for the entire domain of hydrothermal activity at a given ridge location. In some instances, this term can be ambiguous: for example, at the EPR 9°N or in the Endeavour region of the Juan de Fuca, authors have named as “vent fields” some hydrothermal zones of less than a km apart. A hydrothermal site is a set of hydrothermal vents, black smokers and/or diffuse, that are grouped over a few decameters. At black smoker fields, the sites typically comprise a sulfide mound surrounded by diffuse vents (e.g. Barreyre et al., 2012). Again, this can be ambiguous, as the TAG mound for example does present this configuration but with a diameter of 200 m, which is bigger than typical vent sites. The TAG field includes 3 regions of active venting (Figure 2-10c): the main chimney complex on the upper terrace of the TAG mound, the lower temperature white smokers in the Kremlin area and the diffuse flow low temperature zone (LTZ). The TAG field is associated with an active detachment, and there is no documented AMC just under it at depths as is the case for the other well studied hydrothermal fields taken as examples here.

The EPR 9°N and Endeavour vent fields consist of several sites (also called fields by some authors), that are distributed along-axis over distances of several km. This is likely because the AMC in these fast and intermediate spreading examples is present under most of

the ridge length. At the EPR between 9°N and 10°N, 18 vent sites or fields are located in the AST, separated by a few kilometers and typically <10m tall, suggesting that they are recent (Figure 2-10d; Von Damm & Lilley, 2004; Fornari et al., 2004).

At the Juan de Fuca Ridge, several longer-lived hydrothermal fields (or sites) are found along the bounding faults of the small axial valley. The sulfide mounds at these sites are up to 45 m-high (Kelley et al., 2012). At the ASHES hydrothermal area at the Axial Caldera of the JFR, there are two distinct fields (Figure 2-10b), with vents whose activity appears to depend on the eruptive and volcanic activity (Butterfield et al., 2004). In comparison, the Lucky Strike hydrothermal field is made of several vent sites, spread out in a square-shaped 1 km^2 area at the top of the Lucky Strike axial (and segment center) volcano. The sites tend to be distributed along the small offset normal faults that rift the top of the volcano (Figure 2-10a; Barreyre et al., 2012; Humphris et al., 2002; Ondréas et al., 2009). One site (or very small field) is 1.5 km away to the east (Capelinhos; Escartin et al., 2015).

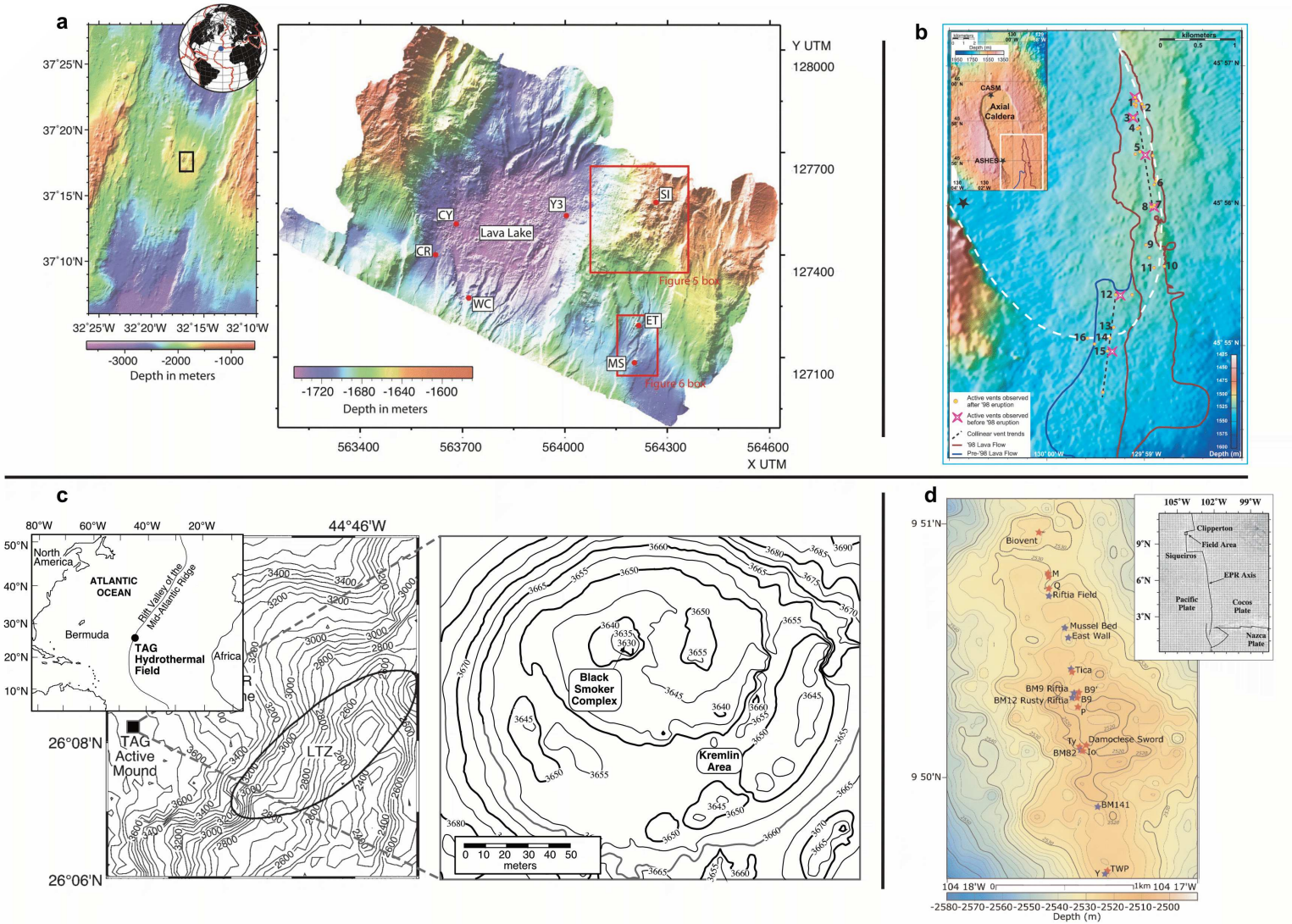

Figure 2-10 – Bathymetric maps and hydrothermal activity position at mid-ocean ridges with different spreading rates: (a) Lucky Strike hydrothermal field (right) at the axial seamount of the Lucky Strike segment (left) at the Mid-Atlantic Ridge (Barreyre et al., 2012). (b) Summit of the "Axial Volcano" caldera at the Juan de Fuca ridge (top left) and the hydrothermal vent along the south-west boundary faults (Butterfield et al., 2004). (c) Trans-Atlantic Geotraverse hydrothermal field on the hanging wall of a detachment fault at the Mid-Atlantic Ridge (left; Humphris and Tivey, 2000) with details of the top of the hydrothermal mound (right; Humphris et al., 1995). (d) Hydrothermal focused (red) and diffuse (blue)vents along the Est Pacific Rise axis between 9° 46-51'N (right mini-map)(Fornari et al., 2004).

2.4.2. Discrete vents and related structures

The most studied discrete vents at hydrothermal fields are the hot focused hydrothermal vents also known as black smokers or hydrothermal chimneys. They are the direct result of hot hydrothermal fluids venting at velocities between 39-5000 mm/s (Table 2-1), mixing with the ocean-bottom seawater at the exit of the hydrothermal edifice, with an orifice of diameter between 0.5-20 cm (e.g. Mittelstaedt et al., 2012; Rona & Trivett, 1992; Schultz et al., 1992; Spiess et al., 1980). If the concentration in metal and sulfur are high enough at the encounter with seawater, precipitation of a anhydrite framework followed by sulfide creates new geological formation around the exit of the hot hydrothermal fluids. To be able to carry substantial amounts of these metals in solution, the hydrothermal fluids are hotter than 300°C (Hannington et al., 1995), temperature being the main parameter over pH for mineral precipitation at the exit's orifice (Tivey, 1995). Hydrothermal fluid temperatures observed at focused vents can go up to 400°C but have a large range of temperature, down to 108°C (Table 2-1). These temperatures are in general very stable (e.g. Barreyre et al., 2014; Sohn et al., 1998; Tivey et al., 2002) and are not directly representative of the fluid temperature at depth, as variable temperatures are measured at focused vents of the same hydrothermal mound (Tivey et al., 2002). Complexities in the turbulent fluid flow in chimneys are proposed to cause the wide range of observed morphologies (Tivey & McDuff, 1990).

Chimneys can grow at rates of 5-10cm per day (Johnson & Tunnicliffe, 1985). The first mineral to precipitate is anhydrite ($CaSO_4$), and in the case of the Lucky Strike vents, barite ($BaSO_4$; Figure 2-11a). Anhydrite does not precipitate in large quantities below 150°C, as Ca and SO_4 concentrations both decrease mainly in seawater when the range of temperature is 150-200°C, with 1g of anhydrite precipitated per kg of seawater (Bischoff & Seyfried, 1978). Bischoff & Seyfried (1978) also observe that anhydrite is the only precipitate from heated seawater for temperatures of 150-250°C; this process is therefore critical to form the skeletal structure of chimneys. Heating of seawater penetrating the oceanic crust will also create precipitation of anhydrite at 150-200°C but additional Ca from basalts oxidation can reduce the temperature of precipitation to 80°C (Alt et al., 1989; Bischoff & Seyfried, 1978). Anhydrite formation in the subseafloor can also be forced by upwelling hot hydrothermal fluids (Sleep, 1991) or by conductive heating of the circulating fluid by the hot surrounding rocks (Mills & Elderfield, 1995). The wall can be built rapidly through precipitation of sulfates in the order of days until reaching a steady state system (Tivey & McDuff, 1990). As the chimney grows, the structure and mineralogy of the wall evolve radially. When the chimney starts to be mature and

that the outside wall is in an environment with temperatures <150°C, the wall made of anhydrite dissolves in seawater due to its retrograde solubility (Bischoff & Seyfried, 1978). At the contrary, barite that is part of the first precipitated mineral when present in the hydrothermal fluids does not dissolve due to its low solubility at low temperatures (Blount, 1977) and formed at temperatures of ~100-300°C (Hannington et al., 1995). Chimney formation by precipitation of sulfates like anhydrite and barite isolate the hot fluids from the surrounding cold seawater and therefore allows for precipitation of Fe-Cu-sulfides (Figure 2-11a). Tivey (1995) observed that Cu-Fe-sulfides formed at high temperature when the chimney is mature can be accompanied by Fe-sulfides (pyrite) and Fe-Zn-sulfide (sphalerite) formed at lower temperatures (Figure 2-11a).

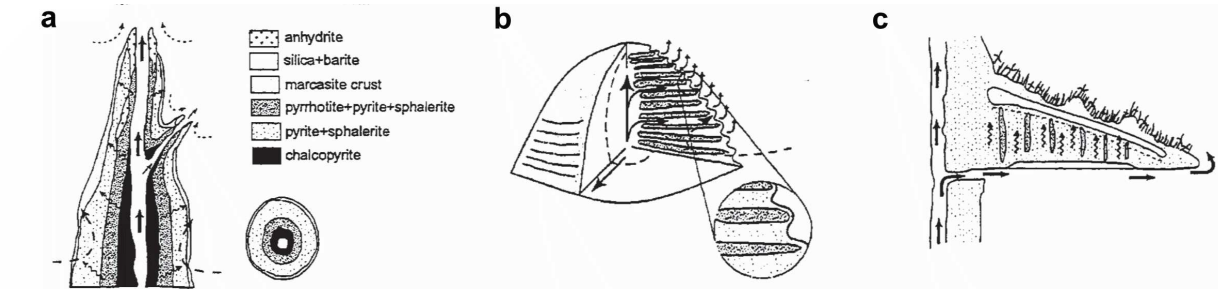

Figure 2-11 – Schematic diagrams of (a) a cross-section for a typical black smoker chimney with the related mineral zonation, (b) beehive structure with repetitive horizontal layers of Fe-Cu-sulfides and (c) a flange structure with vertical inside structure composed of Fe-Cu-sulfides and underlying supply of hydrothermal fluids. Figure from Hannington et al. (1995).

Black smokers are in general located at hydrothermal mounds (not the case at the EPR), where massive sulfides provide a thermic insulation for upflowing fluids from the surrounding seawater. Large hydrothermal mounds are formed by the incorporation of smaller mounds and chimneys (Hannington et al., 1995). The early stages of growth of small hydrothermal mounds are accompanied by the accumulation of sulfide debris (broken fragments of the chimneys; Figure 2-12a). Inside the hydrothermal mound, trapped fluids precipitate sulfides and rework older deposits in fractures and open pores (Figure 2-12b). These processes are similar to those associated with the stockwork formation (Fouquet et al., 1998; see section 2.3.3). More mature hydrothermal mounds have a more stable sulfide talus, where focused vents can form, further enlarging the sulfide mounds (Figure 2-12c).

Black smokers coexist with more complex venting structures like lateral flanges or "beehive-like" chimneys. Beehive structures are composed of a bulbous outside shell of low-temperature pyrite, marcasite and sphalerite and with an inside porous interior of pyrrhotite

(Fouquet et al., 1993) or of anhydrite (Koski et al., 1994) (Figure 2-11b). Venting temperatures are in general lower in beehives structures than at focused vents, reflecting a larger degree of mixing of hydrothermal fluids with entrained seawater (Hannington et al., 1995). Lateral flanges observed at sulfide mound are formed by mineral precipitation (sulfide and sulfate) on the side wall of sulfide edifices via fluids leaking through factures (Delaney et al., 1992; Lonsdale & Becker, 1985). Fluids sampled on the flange are more mixed and lower temperature (30-50°C; Hannington et al., 1995) and flanges commonly host large biomass (for example large populations of mussels at the Tour Eiffel site; Sarradin et al., 1999).

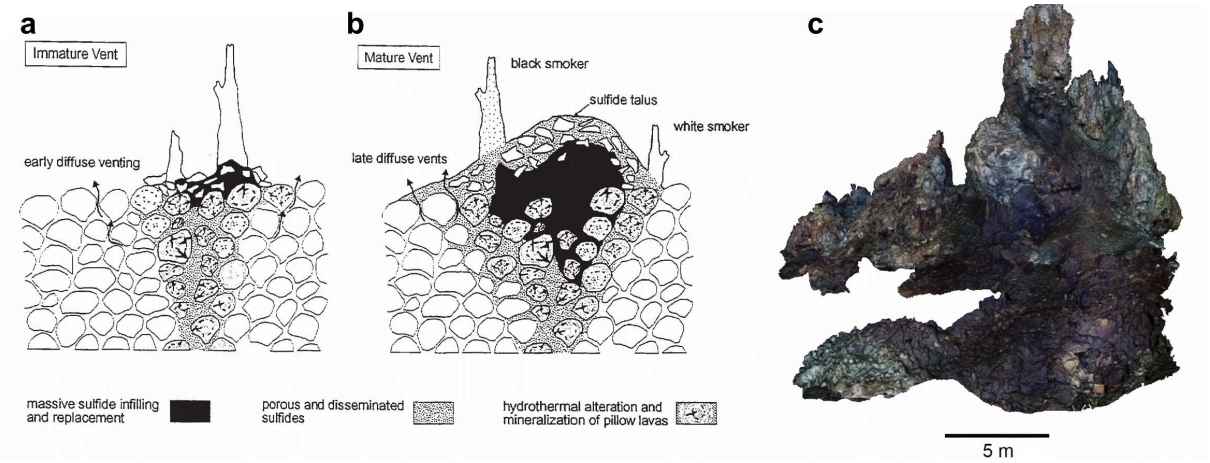

Figure 2-12 – Schematic diagrams from Hannington et al. (1995) of hydrothermal vents. (a) Immature vent at the early stage of sulfide mound formation. (b) Mature vent with a developed mound with large massive sulfide deposits. (c) 3D model of the Tour Eiffel vent site of the LSHF from the base of the sulfide mound to the top. Figure from Girard et al. (2020) Note focused vents via spiers structures at the top of the site.

Focused hydrothermal vents may be black or white smokers, depending on their metal content. White smokers have lower fluid temperatures (100 to 300°C) and form smaller chimneys rich in Zn (Converse et al., 1984; Fouquet et al., 1993; Hannington et al., 1995; Koski et al., 1994). White smokers result from cooling of the end-member fluid and precipitation of metals in the sub-surface (Hannington et al., 1995; Tivey, 1995) The white to almost translucid color of the fluid venting from these structures may also come from particles of silica, anhydrite or barite due to mixing with seawater (Hannington et al., 1995; Tivey, 1995). Black and white smokers commonly coexist in the same field, or even in a same site. It is the case at the TAG hydrothermal field, where the now inactive Kremlin area appears to have consist of only white smokers (Edmond et al., 1995; Thompson et al., 1988).

2.4.3. Types of diffuse fluids

Diffuse hydrothermal vents were discovered at the « Galapagos Spreading Center » (GSC) in 1977 (Corliss et al., 1979; Edmond et al., 1979a,b; Lonsdale, 1977). They were the first type of hydrothermal vent described at MORs, with temperatures <17°C. Diffuse vents are defined based on one or several of the 3 following characteristics: venting temperatures are lower than at most focused vents, venting velocities are smaller, and the venting orifices or cracks have a larger surface (Von Damm, 2000). Diffuse fluids are difficult to study in-situ due to their low venting velocity (a few cm per second or less), and to the variety and spatial extent of venting structures. Another difficulty comes from the fact that diffuse vents provide good habitats for the hydrothermal fauna, that commonly covers the venting structures. Sampling close to hydrothermal fauna can be also a cause of chemical composition modification for the sampled hydrothermal fluids (Johnson & Tunnicliffe, 1985; Johnson et al., 1988; Sarrazin & Juniper, 1999). Finally, due to the low venting velocities, the fluids are extensively mixed with ambient seawater.

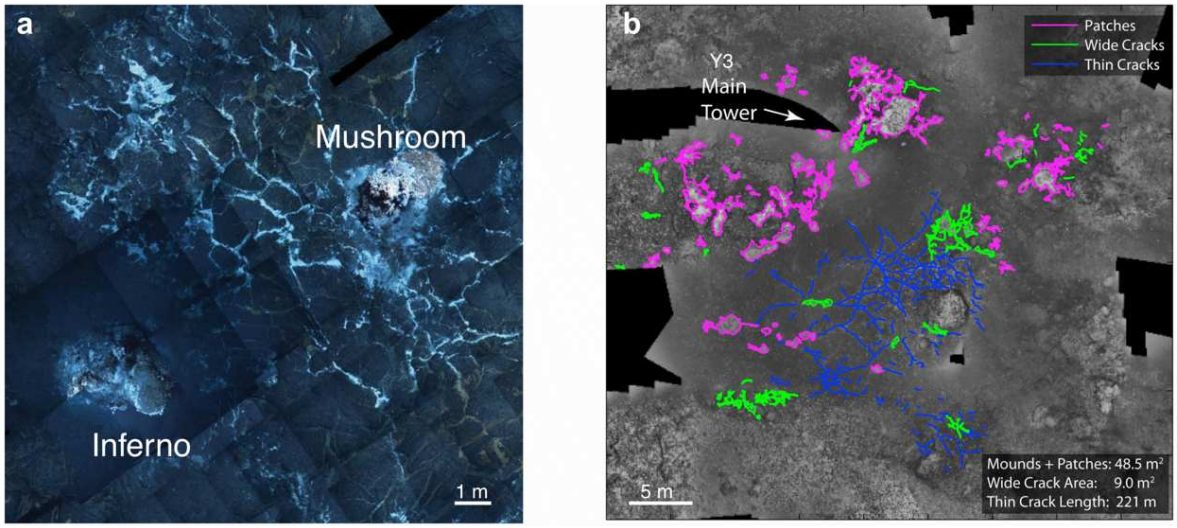

Figure 2-13 – Mosaics of (a) Mushroom and Inferno sites at the ASHES hydrothermal field at the JFR and of (b) Y3 site at the LSHF, Mid-Atlantic Ridge. Main chimneys are surrounded by diffuse fluids venting into cracks and patches radiating around the sulfide mound in the seafloor. (a) Images from the ROV Jason in 2010 at ~5m above the seafloor (Karson et al., 2015). (b) Images from the ROV Victor 6000 in 2008 at ~10mabove the seafloor (Mittelstaedt et al., 2012).

The most detailed descriptions of diffuse vents have been provided for the ASHES vent field in the Axial Seamount Caldera (Figure 2-14a-c; e.g. Butterfield et al., 2004; Pruis & Johnson, 2004; Rona & Trivett, 1992), for hydrothermal sites-fields at the Endeavour segment

(Figure 2-14 d-e; e.g. Foustoukos et al., 2009; Lee et al., 2015; Schultz et al., 1992; Tivey, 2004), both at the Juan de Fuca ridge; at the TAG hydrothermal field (Figure 2-14f; Schultz et al., 1996; Sohn, 2007) and at the Lucky Strike hydrothermal field (Figure 2-14g-h; e.g. Barreyre et al., 2012, 2014b; Cooper et al., 2000; Mittelstaedt et al., 2012) on the MAR; and at the 9°N hydrothermal sites-fields at the EPR (e.g. Converse et al., 1984; Von Damm & Lilley, 2004; Ramondenc et al., 2006).

Structure related to focused vents describe in section 2.4.2 can also bring vent of diffuse fluids. Flanges, that probably result from cracks venting high temperature end-member fluids at sulfide mounds, are commonly described as diffuse vents because of their spatial extent. Similarly, localized diffuse venting structures such as beehive vents in place on chimney-like structure, are commonly described as “diffuser” (Tivey, 2007). By contrast, white smokers which also take the form of chimneys are described as diffuse vents due to the venting of relatively low temperature fluids (Hannington et al., 1995). Sulfide mounds are also venting low-temperature fluids through the porous massive sulfides or at the basalt-sulfide contact (Tivey et al., 2002), like at the JFR with bacterial mats on top of the sulfide mound (Figure 2-14e) or with fauna patches highlighting diffuse venting (Figure 2-14d). At the TAG hydrothermal field, shimmering waters vent from cracks into blocks of sulfides (Figure 2-14f; Sohn, 2007; Tivey, 2007) or out of “diffuser” chimneys with porous walls where low temperature fluids emanate at low velocity (Tivey, 2007). At several vent fields, diffuse venting is described beyond the sulfide mounds (Figure 2-13) in the substratum (Barreyre et al., 2012; Von Damm & Lilley, 2004; Mittelstaedt et al., 2012). At the Lucky Strike field, diffuse fluids vent from cracks or flanges on the sulfide mounds, and in cracks (Figure 2-14g) or patches in the surrounding volcaniclastic formations (Figure 2-14 g-h; Barreyre et al., 2012, 2014; Humphris et al., 2002; Ondréas et al., 2009).

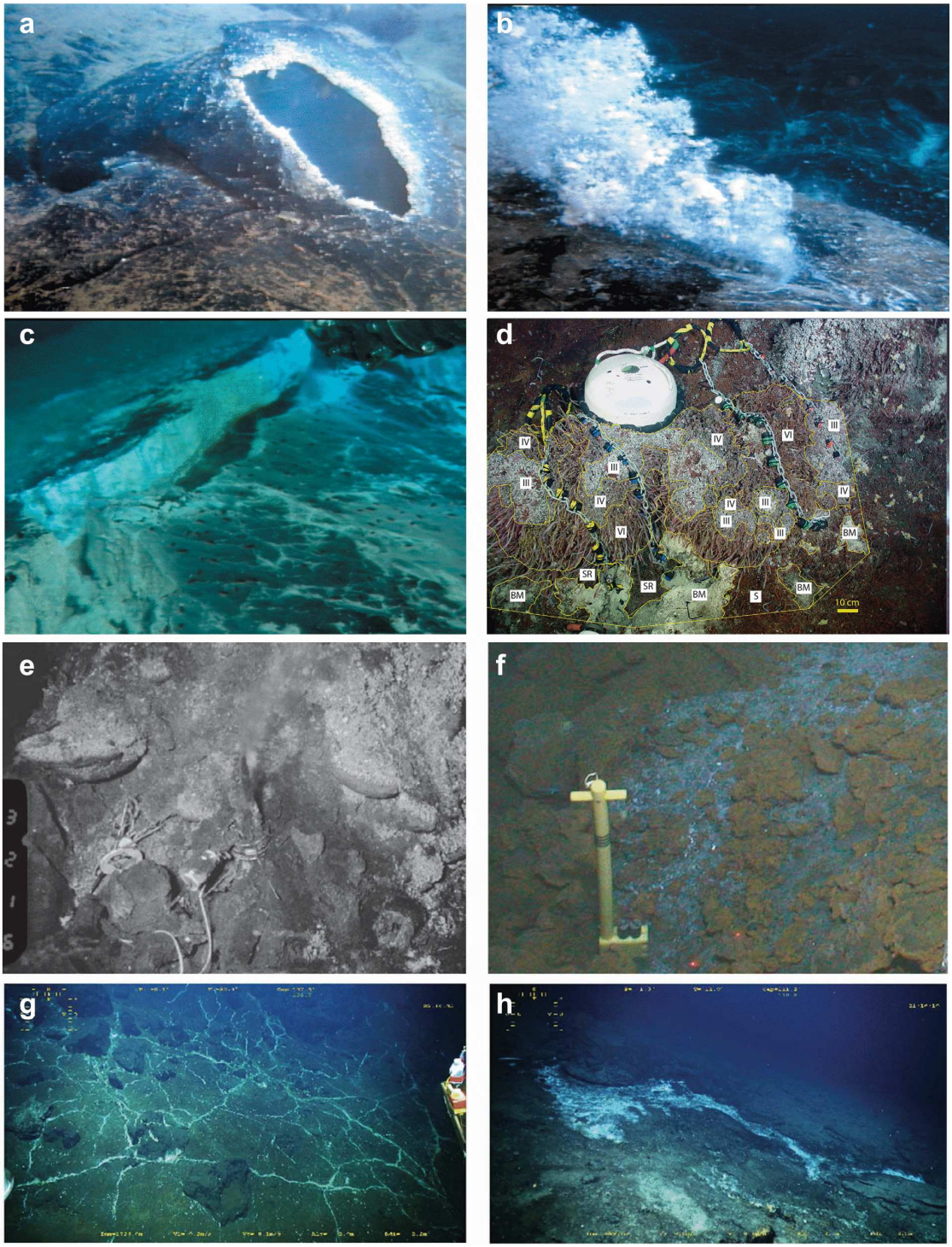

Figure 2-14 – Images of active diffuse venting areas observed at different hydrothermal field sites. (a) "Milky" fluid venting from an opening in lava flow. (b) Large emanation of floc (agglomeration of suspended particles) and from a lobate flow and (c) White bacterial mat and dark worms along a crack of several meters long, with temperatures up to 78°C. These 3 first pictures are from the Axial Caldera close to the ASHES hydrothermal field, JFR (Butterfield et al., 2004) (d) Fauna assemblage in a diffuse venting area at the Grotto site, Main Endeavour hydrothermal field, JFR (Lee et al., 2015). (e) Diffuse venting at flanges on the sulfide mound close to a focused vent of the Monolith site at the northern cleft segment, JFR(Tivey et al., 2002). (f) Temperature probe deployed in a diffuse area of shimmering water on the upper terrace of the TAG hydrothermal field (Sohn, 2007). (g) Diffuse fluids highlighted by white bacterial mats and mineral deposits in cracks at the Y3 vent at the LSHF corresponding to Figure 2-13a. (h) Patch of diffuse fluids with associated bacterial mats at the LSHF, MAR (Barreyre et al., 2012).

The typology of diffuse vents can be related to the geology of the substratum. At the Axial Seamount Caldera, diffuse fluids vent preferentially at eruptive fissures (Butterfield et al., 2004; Mittelstaedt et al., 2016), out of cavities in old lava flows, out of crevices in pillow lavas or of parallel centimetric cracks in thin lava flows, or in former lava lake surfaces following an eruptive phase (Figure 2-14 a-b) (Butterfield et al., 2004; Mittelstaedt et al., 2016; Pruis & Johnson, 2004). Diffuse fluids are also found discharging along faults (Curewitz & Karson, 1997) of the caldera edge (Figure 2-14c; Butterfield et al., 2004; Mittelstaedt et al., 2016). Finally, at hydrothermal fields located on sedimented areas, such as in the Guaymas basin, diffuse fluids vent through pelagic sediments (Little et al., 1988).

Diffuse vents are diverse, and diffuse venting areas can be localized (around high-temperature chimneys (Tivey et al., 2002), patchy (Ramondenc et al., 2006), or disseminated (Corliss et al., 1979; Ondréas et al., 2009), mostly depending on local geology. Most studies of diffuse venting so far have aimed at diffuse vents adjacent to hot focused vents (e.g. Barreyre et al., 2012, 2014b; Mittelstaedt et al., 2012).

Published data on diffuse fluids temperature range between close to that of ambient seawater 2.7-5°C (Table 2-1), up to 130°C (Table 2-1). Some authors describe diffuse fluids with temperatures between 10-100°C as intermediate fluids (Barreyre et al., 2014). Fluid velocity measured out diffuse venting structures range from 1 mm/s to 150 mm/s, which is at least an order of magnitude lower than velocities at most focused vents (Table 2-1).

The chemistry of most diffuse fluids is consistent with dilution of end-member zero-Mg sulfide- and metal-rich fluids with seawater (Von Damm & Lilley, 2004; Edmond et al., 1979a,b). Cooper et al. (2000) analyzed several diffuse fluid samples from the Lucky Strike field and show, based specifically on Li concentration (an element that is extracted from basalt at temperature above 150°C and is therefore a tracer for the end-member fluid component), that several samples are close to conductively heated seawater. They proposed a conceptual model in which seawater is entrained in a sulfide and silica indurated formation specific to Lucky Strike vent sites and called the slab (Costa, 2014; Fouquet et al., 1994; Langmuir et al., 1997). In their model, the slab forms an impermeable cap above the upflowing end-member fluids, that cool conductively and transfer heat to the entrained seawater (Figure 2-15).

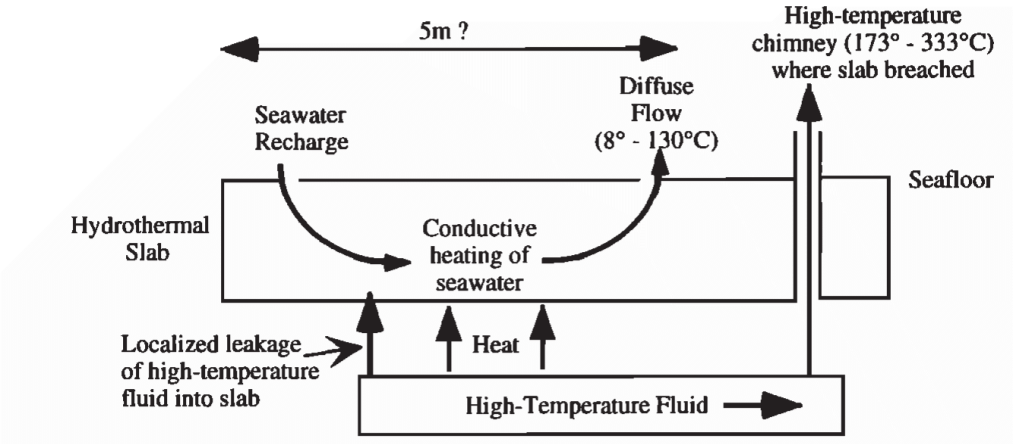

Figure 2-15 – Conceptual model from Cooper et al. (2000) for the formation of diffuse fluids at the Lucky Strike hydrothermal field based on the chemical composition of diffuse fluids.

Conductive cooling of hydrothermal fluids can also complicate the system by heat and mass transfer through mineral precipitation. In a comprehensive review of EPR diffuse fluids by Von Damm & Lilley (2004), differences between the diffuse fluids and adjacent high temperature endmember fluids were best explained by nearly conservative mixing with a minor component of conductive heating of the seawater. A simulation of conductive cooling of end-member fluids by Foustoukos et al. (2009) predicts a decrease in pH resulting from the precipitation of metal mineral phases. Reactions with the basalts in the substratum of hydrothermal sites, during the cooling of hydrothermal end member fluids could result in the crystallization of magnetite and pyrite in the stockwork (Fouquet et al., 1998; Humphris et al., 1995a). Von Damm & Lilley (2004) also proposed a geochemical model that shows that the composition of diffuse fluids, particularly their Mg content, cannot be produced from conductive cooling of the end-member fluids (By definition, end-member fluids are Mg=0.) alone and requires a certain degree of mixing with seawater. These processes and reactive transport with the surrounding subsurface rock (usually basalt) influence the chemistry of diffuse fluids (Crowell et al., 2008; Foustouskos et al., 2009).

Mineral precipitation from end-member fluids is also not just caused by decreasing temperature: it can be enhanced by mixing with seawater. Metals, sulfide, anhydrite and silica are precipitated in large quantity as oxygen fugacity increases (Butterfield et al., 2004; James & Elderfield, 1996). Sr isotopic analysis of fluids at the Biovent site at the EPR 9°46-54'N and compared to fluids sampled at ODP Hole 504B borehole show that an inferred fluid <150°C can also be modified by interaction with the surrounding basalts (seawater interacting with basaltic rock at the base of the drill hole) (Ravizza et al., 2001).

Mixing between the hot, reducing venting fluids and colder, oxidizing seawater creates temperature and chemical gradients that can thus enhance rates of chemical transformations. These gradients also support rich microbial life adapted to catalyzing thermodynamically favorable reduction– oxidation reactions (Butterfield et al., 2004; Von Damm & Lilley, 2004; Foustoukos et al., 2009; Wankel et al., 2011). Removal of H_2 and important concentration of CH_4 highlight the process of methanogenesis with reduction of CO_2 by $4H_2$ happening through microbial activity below the seafloor (Von Damm & Lilley, 2004).

Vent Field name	ref.	T°C Diffuse fluids	T°C Focused fluids	Type of diffuse venting	Diffuse venting Velocity (mm/s)	Focused venting velocity (mm/s)	Estimated focused heat flow (MW)	Estimated Diffuse heat flow (MW)
Guaymas Basin	(Little et al., 1988)	<20	×	Pelagic sediments	30-50 (math. model)	×	×	-
EPR 21°N	(Macdonald et al., 1980)	-	350-400	-	-	1000-5000	-	-
EPR 21°N	(Converse et al., 1984)	-	126-313	-	-	700-2360	220#	-
EPR 9°50'N, Biotransect	(Fornari et al., 1998)	-	240-388	-	-	-	-	-
EPR 9°50'N, Biotransect	(Scheirer et al., 2006)	<40	<385	Faunal assemblage	-	-	-	-
EPR 9°50'N, Bio9	(Ramondenc et al., 2006)	10	368-388	Faunal assemblage	30-50	100-430	42	285
ASHES, JFR	(Pruis & Johnson, 2004)	<45	-	Fractured sheet flows	13-16	-	-	-
North ASHES, JFR	(Peter A. Rona & Trivett, 1992)	5-27	108-326	Patches	55-140	200-900	4,4+/-2,2	45+/-30
ASHES, JFR	(Mittelstaedt et al., 2016)	<10°C	-	Cracks	1-58	-	-	2.05+/-1.9
Endeavour segment, JFR	(Schultz et al., 1992)	4-18	348-352	Faunal assemblage	70-150	400-500	2.9#	58.2+/-4.6#
MEF, Endeavour segment, JFR	(Larson et al., 2007)	-	358-370	-	-	-	-	-
MEF, Endeavour segment, JFR	(Larson et al., 2009)	-	375-379	-	-	-	-	-
MEF, Endeavour, JFR	(Cuvelier et al., 2014)	<15	-	Faunal assemblage	-	-	-	-
Endeavour, JFR	(Lee et al., 2015)	<45	-	Faunal assemblage	-	-	-	-
MEF & Mothra, Endeavour segment, JFR	(Wankel et al., 2011)	9-81	108-319	-	1-100	39-355	-	-
Clef Segment, JFR	(Tivey & Johnson, 2002)	2.1-20.8 (mean)	303-305	Beehive chimney, patches	-	-	-	-
Lucky Strike field, MAR	(Langmuir et al., 1997)	8-14	200-333	Cracks	-	-	-	-
Lucky Strike field, MAR	(Cooper et al., 2000)	7.9-130.6	280-333	Cracks and patches	6-58	-	-	-
Lucky Strike field, TE site, MAR	(Sarrazin et al., 2009)	4.6-16.4	-	Cracks	1.1-4.9 substratum level (41.9-183.6 sensor level)	-	-	-
TAG field, MAR	(Kinoshita et al., 1996)	2.7-30°C	~345-368	Sulfide sediments	-	-	-	-
TAG field, MAR	(Schultz et al., 1996)	14-25°C	-	Sulfide terrace	5.1	-	-	-
TAG field, MAR	(Kinoshita et al., 1998)	~2.7-3.5	-	Water column	-	-	-	30-100
TAG field, MAR	(Sohn, 2007)	<52	150-350	cracks	-	-	-	-
Lucky Strike, MAR	(Mittelstaedt et al., 2012)	10-38	200-301	Cracks and patches	4-111	220-1190	0.12+/-0.6	18.6+/-2.2#
Lucky Strike field, MAR	(Barreyre et al., 2012)	-	-	Cracks and patches	-	-	8-50	187-1036
Lucky Strike field, MAR	(Barreyre, Escartín, et al., 2014)	<100	195-332	Cracks and patches	-	-	-	-

Table 2-1 – Characteristics of focused and diffuse vents and fluids at MOR black smoker vent fields (with the exception of Guayamas): temperature, velocity and estimated heat flux. Studies where diffuse or focused vents are not present are indicated by crosses (×), studies where parameters are not described even if focused or diffuses vents are present at the hydrothermal site/field are indicated by (-). Heat fluxes are estimated at the scale of the hydrothermal field excepted for values indicated by # that are estimates at vent sites scale.

2.4.4. Monitoring of hydrothermal fluids

Time and space variations of focused and diffuse fluid temperature and velocity can provide constraints on the evolution of the hydrothermal system, at field (kilometer) and site (hectometer to decameter) scales. Discrete measurements made with remotely operated and manned submersibles have proved inadequate to study this very dynamic environment. Variations modulated over periods of several hours, days or months (e.g. tides, inertial currents) require longer monitoring times (Table 2-2).

The temperature of venting fluids is monitored with autonomous temperature probes deployed for long periods. Temperature is a key physical parameter: as a limiting and determining parameter for the fauna, and as a tracer for mixing with seawater and for conductive cooling or heating in the subsurface. At a diffuse vent of the Rose Garden hydrothermal field at the Galapagos Spreading Center, Johnson et al. (1988) showed for example a good correlation between fluid temperature and sulfide and oxygen concentrations. Acquisition of relatively long (12.5 days) temperature time series of diffuse fluids was initiated by Little et al. (1988) at a 5x5m diffuse patch covered by bacterial mats of the Guaymas Basin field (Table 2-2). These authors emphasized the difficulty encountered in separating the effect of hydrothermal fluid temperature variations, from the effect of ambient seawater temperature variations due to currents.

The position of the temperature probes is an important parameter that impacts the temperatures measured at diffuse vents. This is due to two distinct factors. One is intrinsic to diffuse vents: venting velocities and temperatures are variable along a given crack with localized venting (Mittelstaedt et al., 2012) and over a given diffuse patch (e.g. Tivey et al., 2002). The other factor is related to how the temperature probes are positioned. In studies of hydrothermal habitats, the probes are typically placed on the seabed, next to the studied fauna and therefore measure temperatures in the mixing zone between the oozing fluids and the near bottom seawater. In studies that aim to characterize the hydrothermal fluid, probes have measuring rods that are positioned in the cracks, or in the porous basement at venting patches. In a few studies (Scheirer et al., 2006; this study), thermistors are deployed at several depths in and above the substratum (Figure 2-16). For probes positioned in cracks, a source of uncertainty is illustrated in Figure 2-16a where it is difficult to know if the tip of the probe is in the crack or in a cavity beneath the slabby substratum (Figure 2-16a). The position of probes deployed in high-density fauna can also be uncertain, in the substratum, or in the fauna (Figure 2-16b; Scheirer et al., 2006). The Diffuse Effluent Measurements System (DEMS; Mittelstaedt et al., 2012) measures temperature and estimates venting velocities at the seafloor above cracks

(Figure 2-16c). Instruments such as the Medusa (Cooper et al., 2000; Schultz & Elderfield, 1997), the Flow Visualizer (Sarrazin et al., 2009), or the Hydrologically sealed sampler (Figure 2-16d; Pruis & Johnson, 2004) isolate the venting fluids from ambient seawater and allow for temperature measurements and sampling of the hydrothermal effluents at the seafloor. The Thermal Blanket (Johnson et al., 2010; Salmi et al., 2014) isolate the venting fluids from ambient seawater and allow for temperature measurements and sampling of the hydrothermal effluents at the seafloor.

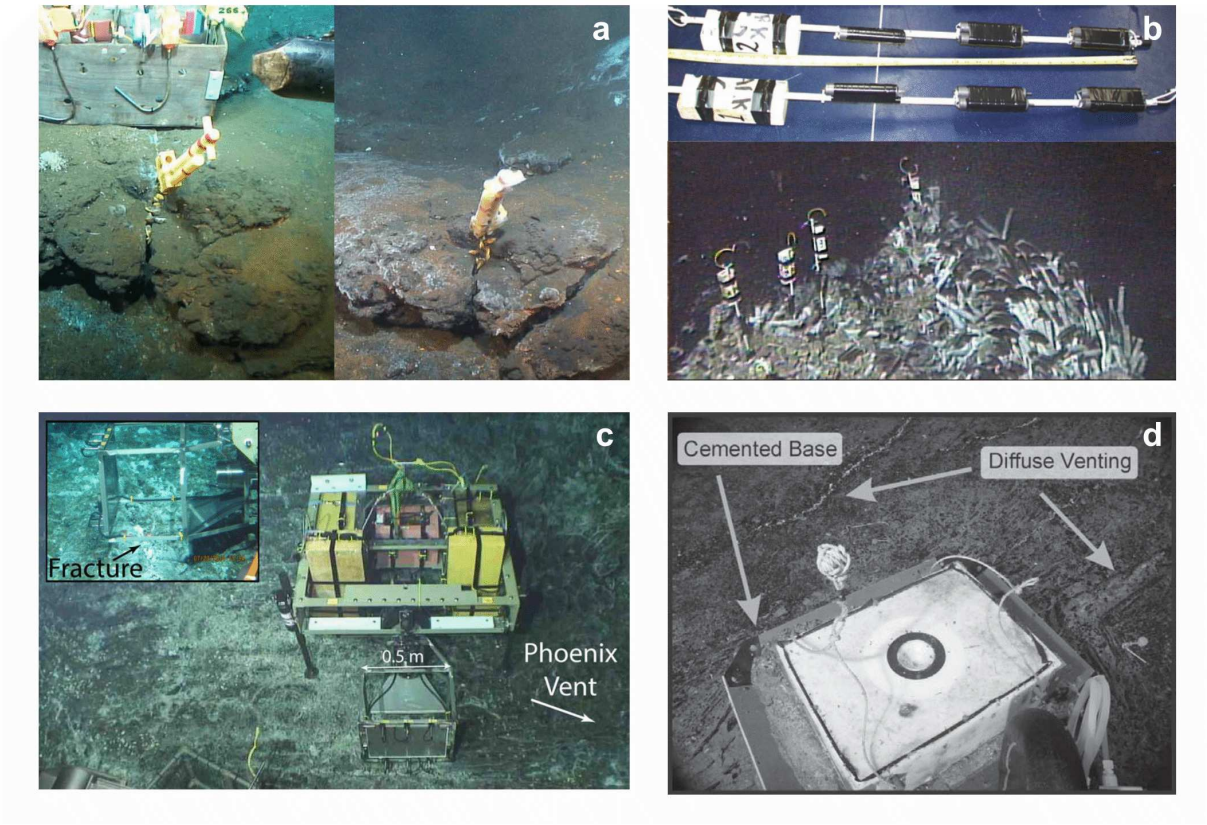

Figure 2-16 – Video frame of different probes deployed to measure temperature of diffuse fluids at (a) the Lucky Strike hydrothermal field in cracks (Barreyre et al., 2014), at (b) the EPR segment with stick arrays deployed at the Bio141 site into tubeworms (Scheirer et al., 2006), at (c) the ASHES hydrothermal field on the JFR above cracks with the DEMS system composed of a deep-sea camera and 6 thermistors (Mittelstaedt et al., 2016)and (d) with the cemented base sampler deployed above a crack also at the ASHES hydrothermal field (Pruis & Johnson, 2004).

Time series measurements of fluid temperature at focused and diffuse hydrothermal vents have revealed both episodic and periodic variations, the latter being dominated by semi-diurnal variations at tidal frequencies.

Reference	Location	Duration (days)	Number probes	Probe type	Probe position	Pressure probes	Current meter	Proposed cause of tidal modulation
(Little et al., 1988)	Guaymas Basin	12	1	Temperature probe	On seabed	No	No	Tidal currents
(Chevaldonné et al., 1991)	13°N EPR	4	4	THYDRO	On sulfide mound	No	No	Tidal currents
(Schultz et al., 1992)	Endeavour segment, JFR	44	1	Flow meter	On sulfide mound	No	No	Tidal "pumping"
(Kinoshita et al., 1996)	TAG field, MAR	200	8	Temperature probes	In vent	No	Yes	Tidal currents
(Schultz et al., 1996)	TAG field, MAR	7	3	MEDUSA	On seabed	No	No	"Deep" processes
(Kinoshita et al., 1998)	TAG field, MAR	8	3 vertical arrays	Temperature thermistors	In plume	No	Yes	Tidal currents
(Tivey et al., 2002)	Clef Segment, JFR	*~300*	40	Temperature thermistors	On sulfide mound	No	Yes	Tidal currents
(Pruis & Johnson, 2004)	ASHES, Cracks vents, JFR	206	1	Fluid sampler	On seabed	No	No	None
(Scheirer et al., 2006)	EPR 9°50'N, Biotransect	0.5-2 yars	~10	Temperature probe	In fauna	No	Yes	Tidal currents
(Sohn, 2007)	TAG field, MAR	1 year	21	Temperature probe	In vent	No	No	Tidal pressure
(Barreyre et al., 2014)	Lucky Strike, MAR	3 years	54	Temperature probe	In vent	Yes	Yes	Tidal pressure and currents
(Lee et al., 2015)	Endeavour , JFR	~360	~40	iButton probes	In fauna	Yes	No	Tidal pressure and currents
(Cuvelier et al., 2014)	Endeavour , JFR	23	10	Temperature probes	In fauna	Yes	No	Tidal currents
(Mittelstaedt et al., 2016)	ASHES, JFR	12	1	DEMS	On seabed	No (estimated)	No	Tidal pressure and currents

Table 2-2 – Temperature monitoring of diffuse fluids with the associated measurement period, number of probes used and their type. We also indicate if the study had a pressure probe or currentmeter deployed at the hydrothermal site at the same time as temperature records and what was process was invoked in these studies to explain the tidal modulation of fluid temperature.

2.4.4.1. Episodic variations

The first observation of a link between a submarine eruption and hydrothermal activity at a MOR was reported by Baker et al. (1999) for the January 25, 1998 eruption at the Axial Volcano Caldera (JFR). Temperatures measured in the plume thanks to a mooring show a ~0.5°C temperature rise following the eruption with a return to temperatures 0.1°C above the temperatures observed previously (Figure 2-17a). This two stages event was interpreted as primarily due to hydrothermal heat extraction from the erupted lava. A sudden temperature increase in focused vent fluids was reported by Sohn et al. (1998) at the EPR 9°50'N field, after an intense seismic swarm in March, 1995. The short-termed effect was a temperature increase of 7°C for one week, 4 days after the swarm. A long-term component followed, with a slow temperature increase over more than two year. The swarm of microearthquakes was interpreted as caused by the opening of a vertical fracture network triggered by the subsidence of the AMC, allowing fluid circulation into a deeper and hotter part of the oceanic crust (Sohn et al., 1998).

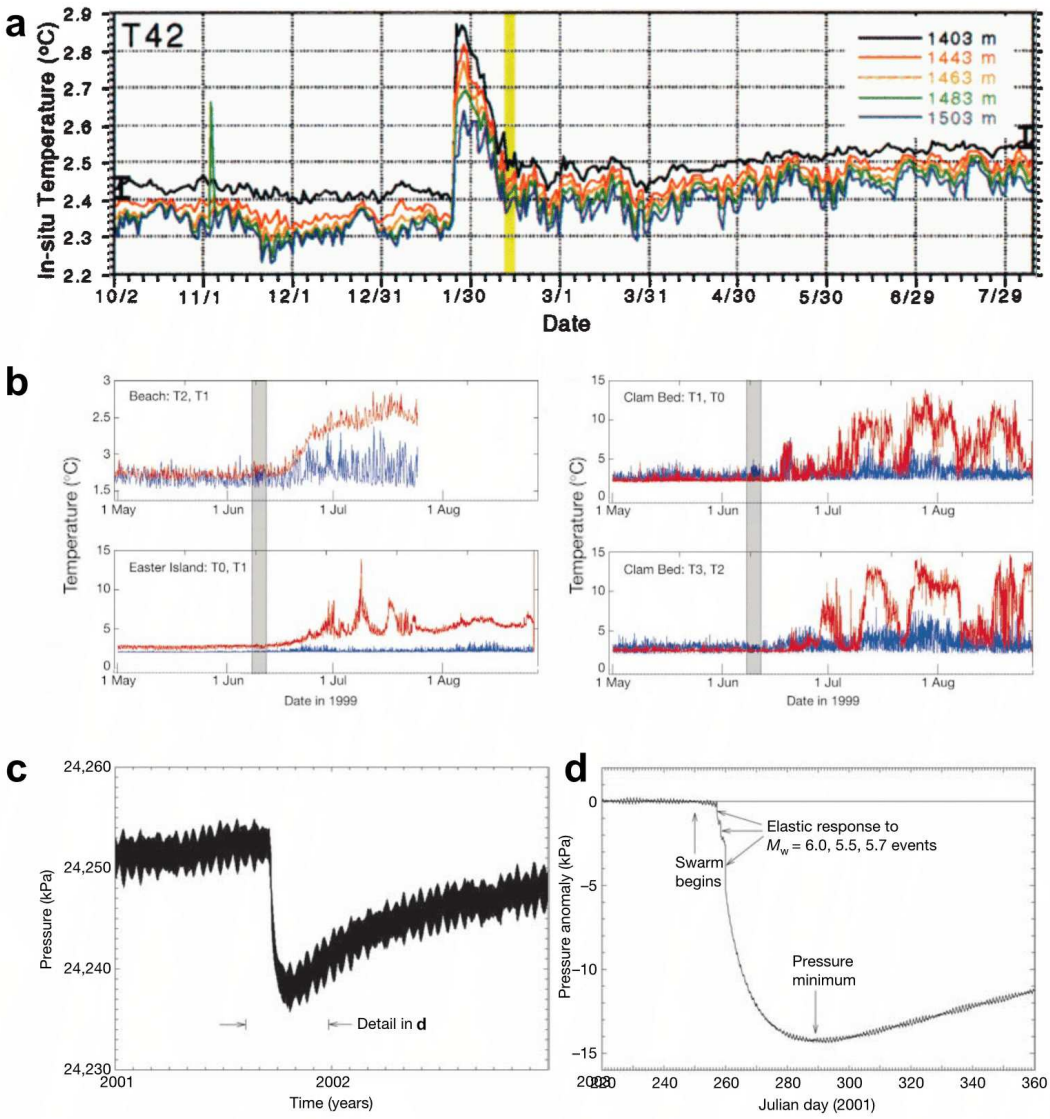

Figure 2-17 – Examples of episodic variations into temperature series for probes deployed at hydrothermal vents (a) at the ASHES hydrothermal field of the JFR after the 1998 submarine eruption (Baker et al., 1999); (b) at the Endeavour axial valley on the JFR after the 1999 seismic swarm (Johnson et al., 2000). (c)Example of episodic variation in pressure time series in ODP Hole 857D after the 2001 seismic swarm, 30km north top the measurement site at the JFR (Davis, 2004). (d) corresponding to a zoom on (c) at the level of the episodic perturbation.

Johnson et al. (2000) reported changes in venting temperature at two diffuse venting sites of the Endeavour segment (JFR), following a seismic swarm on June 8, 1999. This swarm was interpreted as tectonic and there was no evidence for an eruption at the seafloor. Temperature time-series from 2 different venting sites, distant by 2 km, show an increase in temperature, up to 10°C, 4 to 11 days after the main shock. The vent temperatures then oscillated for about a month and settled to higher values (Figure 2-17b). These changes in temperature were associated with a tenfold increase in hydrothermal fluid fluxes at the two sites and therefore resulted from a profound change in the hydrothermal system, following the June 8 earthquake (Johnson et al., 2000). Borehole experiments have also documented the hydrological impact of

a 2001 seismic swarm, further north and off-axis the JFR (Figure 2-17c). Davis et al. (2004) measured a long period pressure drop in the borehole following the earthquakes, and interpreted it as due to lateral diffusion of fluids from the region of the earthquake source to the borehole through the oceanic crust sealed on the top by sediments. Episodic variations resulting from tectonic or volcanic activity were also detected in the chemistry (Lilley et al., 2003), the flow rate (Crone et al., 2010) of high-temperature focus vents, and the coherence of semi-diurnal temperature variations with seafloor pressure, also at focused vents (Barreyre & Sohn, 2016). This last effect is proposed to reflect changes in the poroelastic behavior of the upper crust (see next section).

Most episodic perturbations of vent fluids temperatures show no correlation with seismicity and are not correlated between nearby vents (Barreyre et al., 2014b). At focused vents from the Lucky Strike field, these episodic changes are commonly in the form of a drop of several degrees (°C), then a temperature rise over a few days (Barreyre et al., 2014b). These variations were interpreted as local hydrologic perturbations involving influx of seawater in the sulfide edifice (Barreyre et al., 2014b). This is illustrated in a rare case of an intra-site anti-correlation of venting temperatures between two nearby focused vents (Figure 2-18; Barreyre et al., 2014b). At diffuse vents, episodic perturbations can be rises or decreases in temperature, and there is usually no return to a reference temperature. This reflects the time and space variability of diffuse vents in terms of the relative proportion of entrained seawater.

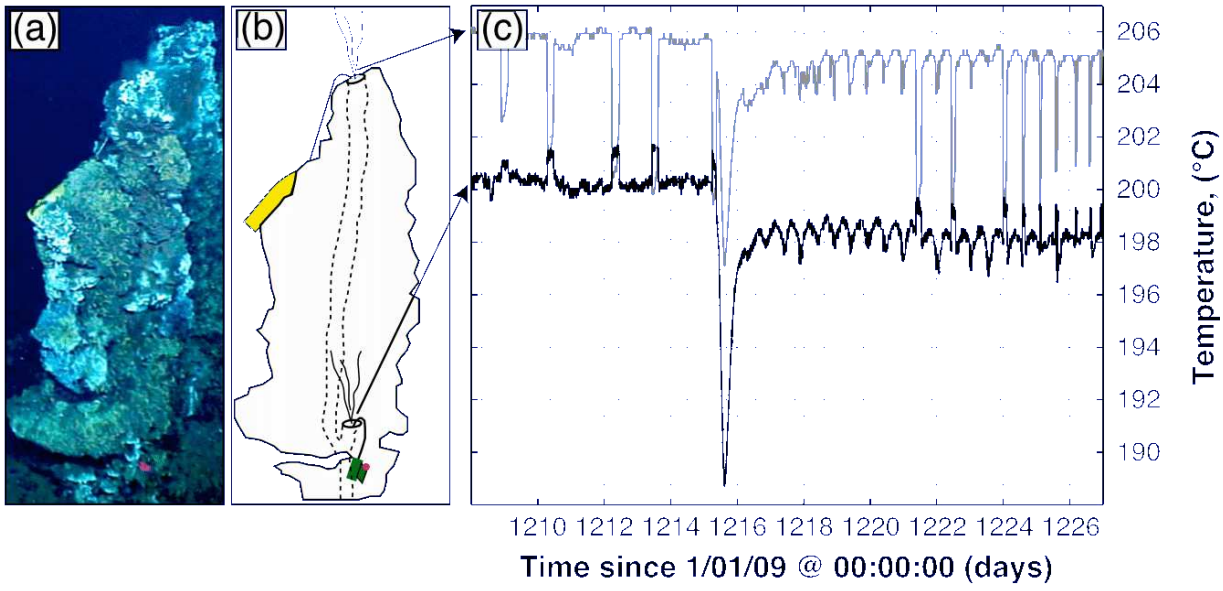

Figure 2-18 – Temperature anomalies for hydrothermal fluid of the LSHF site. Temperature probes are deployed at (a) the Sintra site of the LSHF at (b) different orifices *(Barreyre et al., 2014). (c) Temperature record of both probes. Note the common anomaly at the 1215 day of recording while other perturbations are anti-correlated.*

Episodic variations reported at diffuse vents from the TAG hydrothermal field take the form of an alternation of “flow” periods with higher temperature, and “no flow” periods with seawater temperature (Sohn, 2007). These perturbations were interpreted as the result of reorganizations of the fluid flow in the subsurface following changes of the permeability structure of the substratum via crystallization/dissolution of minerals, seismic activity, hydrofracturing, etc.

2.4.4.2. Tidal modulation of venting temperature

* **Tides and tidal frequencies**

This introduction on tides is primarily based on Hicks (2006) and Hendershott (2005). Tides are formed through the gravitational effect of the Earth, the Moon and the Sun. The effect of the Moon is "roughly" twice as large as that of the Sun. Caused by the revolution of the moon, the maximum coefficient of tides is observed at the new moon also called “syzygy” (Sun-Moon-Earth alignment, Figure 2-19). This period of spring tides is when the coefficients are the strongest. The neap tides are minimum tide amplitude at the first and last quarters when the sun and the moon are at a 45° angle to the Earth (Figure 2-19). During the full moon (Sun-Earth-Moon alignment) we also have a period of spring tides but weaker than in the new moon. The strongest spring and neap tides (respectively maximal and minimal tidal coefficients) happen twice a year, in March and September. The lowest spring and neap tides happen in June and December. These variations are the result of the elliptical orbit of the Earth around the Sun and of the Earth’s inclination at the equinox when the gravitational attraction of the Sun is at its maximum and when it is on the plane of the celestial equator. The lowest spring and neap tides correspond to the solstice when the Sun reaches its most northerly or southerly excursion relative to the celestial equator.

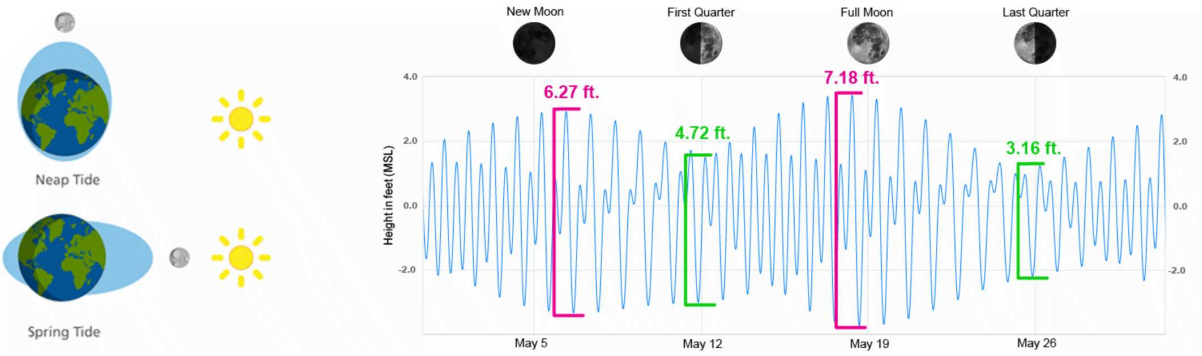

Figure 2-19 – Left: diagram of Earth-Moon-Sun alignment correlated to spring and neap tides. Right: diagram of the observed tide amplitude with the difference between spring (purple) and neap (green) tides at Santa Barbara, CA from May 2019.

The generating potential of the tide can be expressed as the sum of single frequency terms grouped together according to wavelength periods: diurnal, semi-diurnal, third diurnal, quarter diurnal, etc. The frequencies are named with a letter to represent the orbital object involved: M for the moon, S for the Sun and K for combination of the moon and sun interaction. This letter is followed by a letter or number indicating the periodicity: a for annual, m for monthly, f for semi-monthly, 1 for diurnal, and 2 for semi-diurnal. Each component can be associated with the contribution of the potential of the different orbital characteristics of the Earth, the Moon and the Sun. The M2 frequency (0,517 days period) "would be on its own if the lunar orbit coincided with the equator and if there were no eccentricity" (Poincaré, 1910). K2 (0,4986 days period) describes the effect of Moon's orbit tilting. More than 400 frequencies are calculated, but most of the tidal energy resides in semi-diurnal (M2, L2, S2 and K2), diurnal (K1, O1, Q1 and P1) and long period (fortnightly Msf and monthly Mm) frequencies. Waves composed through the interactions of different single frequency waves are marginal but locally important if resonance or reflection phenomena take place. If two interacting constituents are both semidiurnal (e.g. M2 and N2), the result will be a quarter diurnal constituent (e.g. MN4) and a low frequency constituent. For another example, the interaction of M2 (semi-dirunal) with K1 (diurnal) produces a terdiurnal constituent MK3 and a diurnal constituent MK.

Tides are impacted by irregular ocean depth, reflection and interaction of tidal waves with topography, turbulences, bottom friction, meteorological factors like storms (impacting directly the water level through bathymetric pressure). To give an order of magnitude, the pressure increase per meter of immersion is 100 hectopascals. An atmospheric depression of 50 hectopascals is therefore significant. Meteorological events have indeed been shown to impact temperatures at littoral hydrothermal vents. Chen et al. (2020) documented the effect of a typhoon on a hydrothermal system at the Lutao volcanic island. Deep-sea hydrothermal systems are less exposed to changes of fluid flow variations due to catastrophic meteorological events. However, several studies have documented the impact of winter storms, generating inertial waves and low-frequency currents (Cannon & Thomson, 1996) on hydrothermal systems and on the temperature of diffuse fluids (Lelièvre et al., 2017) at MORs.

Tides affect hydrothermal vents through two categories of mechanisms: (i) the velocity and heading of bottom currents are themselves modulated by tides, and currents entrain near bottom water masses that can differ in temperature. This effect is most expected for temperature recorded at diffuse vents by probes that are emplaced at the bottom of the edifice in the gradient zone between the oozing hydrothermal fluids and the bottom seawater; (ii) cyclical tidal loading affects the internal stress distribution in the poroelastic hydrothermal circulation domain and

results in predictable changes in flow velocities and in the temperature of upflowing fluids (Wang and Davis, 1996; Wilcock and McNabb, 1996; Jupp and Schultz, 2004). This poroelastic effect has been documented at focused vents from EPR (e.g. Scheirer et al., 2006), JDF (e.g. Mittelstaedt et al., 2016; Schultz et al., 1992; Tivey et al., 2002) and MAR (e.g. Barreyre et al., 2014b; Kinoshita et al., 1996; Schultz et al., 1996; Sohn, 2007) vent fields.

* **Tidal modulations of diffuse venting temperatures and bottom currents**

Little et al. (1988) attributed the semi-diurnal temperature variations recorded in diffuse fluid temperature at the Guaymas field, to tidally-controlled bottom currents: current velocity would thin the boundary layer at the interface between the ground and the water column (Figure 2-20). The temperature probe installed during this study was located 3 cm above the ground and vent's shimmering waters, and was therefore well exposed to currents.

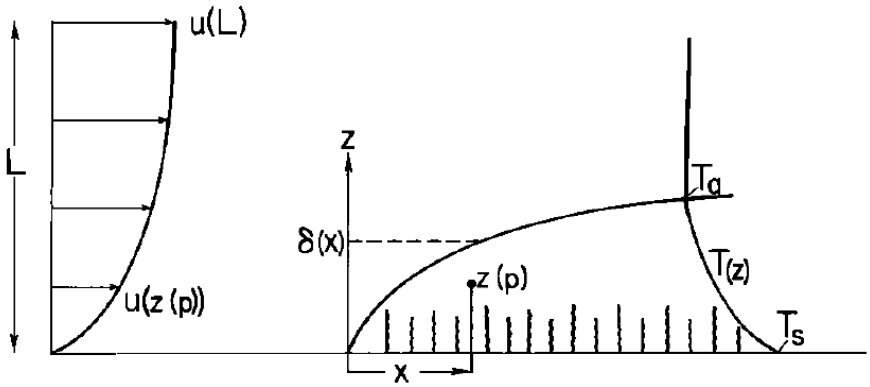

Figure 2-20 – Schematic of the boundary layer model (Little et al., 1988) defined by various parameters: U(L) is the maximum velocity recorded at 10 m above the bottom, U (z(p)) is the velocity at sensor depth, x is the distance between the sensor and the leading edge of the heated surface, δ is the boundary layer thickness, T_a is the ambient temperature, T_s is the heated surface temperature, z is the vertical distance from the seafloor surface, T (z) is the temperature profile within the boundary layer.

In this interpretation, temperatures are expected to be maximum when currents are slow. The change of temperature can be calculated from the thickness δ of the boundary layer as a function of current velocity U (Figure 2-20). The boundary layer thickness is $\delta = CU^{-1/2}$ for a uniform current and a constant thermal diffusivity C.

Tivey et al. (2002) measured semi-diurnal, diurnal and inertial temperature variations in diffuse fluids at the JDF ridge and interpreted them also as primarily controlled by currents. Their assertion is supported by the recording, by the temperature probes and by nearby current meters, of an additional signal with a period of 4 days that was attributed to storms. In this study, the temperature probes formed is deployed on the seabed and not inside the substratum. Periods when the tidal current was blocked by local relief correspond to periods that lack the semi-diurnal signal of diffuse fluids temperature (Figure 2-21). Tivey et al. (2002) interpreted these semi-diurnal variations as due to the lateral entrainment by currents of hot hydrothermal

fluids coming from vents outside the measurement zones. They explained a phase lag between tidal signals of fluids temperature and current time-series by either a temporal drift of the current meter or local complexities of the currents due to the topography.

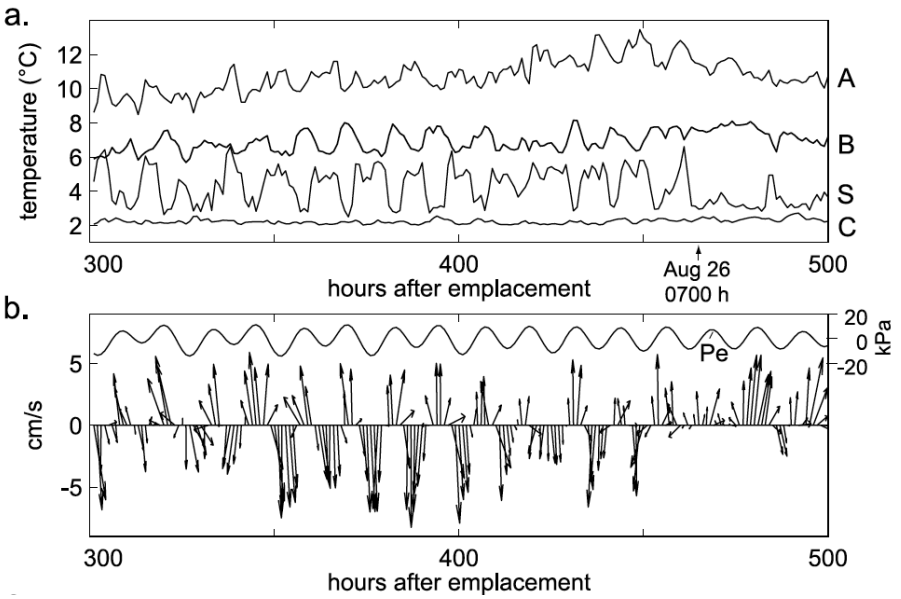

Figure 2-21 – (a) Time series recorded by thermistors deployed at the Monolith hydrothermal site at the JFR. (b) Current velocity timeseries and tidal estimates of pressure variations for the same period as temperature time series. Figure by Tivey et al. (2002).

In the case documented by Tivey et al. (2002) , the semi-diurnal temperature increases of 1.5-2°C correspond to higher current velocity: higher current velocity brings more hot fluids from nearby vents. The effect is therefore distinct from that proposed by Little et al. (1988).

Scheirer et al. (2006) described a similar effect at the EPR 9°50'N, with probes deployed in faunal assemblages (mussels and giant tube worms). Barreyre et al. (2014) reported 3 years of monitoring at focused and diffuse vents of the Lucky Strike field. They showed a high coherence between fluid temperature and current velocity at the M2 tidal frequency for low temperature (<10°C) diffuse venting cracks, commonly associated with higher temperatures at lower current velocities (Figure 2-22a and c), suggesting an effect similar to that described by Little et al. (1988).

* **Tidal modulation by tidal pressure and the poroelasticity theory**

By contrast, high temperature focused fluids and medium temperature diffuse fluids at Lucky Strike have a higher M2 coherence with seafloor pressure, indicating a predominant role of the poroelastic behavior of the substratum (Barreyre et al., 2014b). To establish this higher coherence, it is necessary to have near bottom current and head pressure recordings at locations near the monitored vents (Figure 2-22a). Tidal modulation of fluid temperature (up to 0.5°C) and/or velocity were observed at focused vents of the JFR hydrothermal fields (Larson et al.,

2007, 2009), at other diffuse vents of Lucky Strike (Mittelstaedt et al., 2016; Schultz et al., 1992, 1996), and at diffuse vents of the TAG field (Sohn, 2007) and have been interpreted as partially due to the poroelastic response of the substratum. Tidal pressure variations in interstitial fluids were also measured in boreholes off-axis the JDF ridge (Davis & Becker, 1999; Davis et al., 2000).

In the oceanic crust, changes in the tidal load induce a time dependent effect that results from the poroelastic behavior of the system made of the porous matrix and the interstitial fluid (Wang and Davis, 1996; Wilcock and McNabb, 1996; Jupp and Schultz, 2004; Crone and Wilcock, 2005; Crone et al., 2011). The theory of poroelasticity was introduced by Biot (1941) with the term “consolidation” to explain the process of squeezing water out of an elastic porous media under load. The tidal load is borne partly for one part by the solid matrix, that deforms elastically, and partly for the other part by the fluid that causes a pore pressure perturbation. The deformation of the matrix, controlled by its elastic properties, contributes to this pore pressure perturbation. The latter is therefore composed of an instantaneous component, due to the variation of the hydrostatic pressure in the system, and a time-dependent component, due to matrix deformation.

Jupp & Schultz (2004) demonstrated with a simple one-dimensional model of a poroelastic seafloor with a homogeneous permeability that tidal pressure loading can create variations in the venting temperature and velocity of MOR hydrothermal fluids, in the phase lag between variations of these parameters, and in the tidal forcing. They show that the tidally induced response is dependent on the depth down to which tidally induced pore pressure signals can diffuse over a tidal cycle, also called the "skin depth"; this response also depends on the distance over which the background fluid flow can advect a thermal signal over a tidal cycle, also called the “advection length scale”. Jupp & Schultz (2004) developed a simplified expression that relates the phase lags between tidal forcing, the fluids exit temperature and velocity variations, to the effective permeability of the hydrothermal upflow zone. This one-dimensional poroelastic model was used by Barreyre et al. (2014b) and Barreyre & Sohn (2016) to propose estimates of upflow zone effective permeability at several vent fields (see section 1.3). Barreyre et al. (2018) present an improved analytical model that allows estimates of effective upflow zone permeability from phase lags in a two-layered medium that is a better approximation of the layered permeability structure of the oceanic upper crust. The role of poroelasticity on the entrainment of seawater and on the fluid flow in the shallow subseafloor near black smoker sites was investigated by Crone & Wilcock (2005). They showed that tidal forcing may enhance mixing and therefore influence microbial life in the subseafloor. They also

showed that tidal loading of a medium with a continuous permeability structure cannot produce temperature variations over a few tens of Celsius degrees (°C).

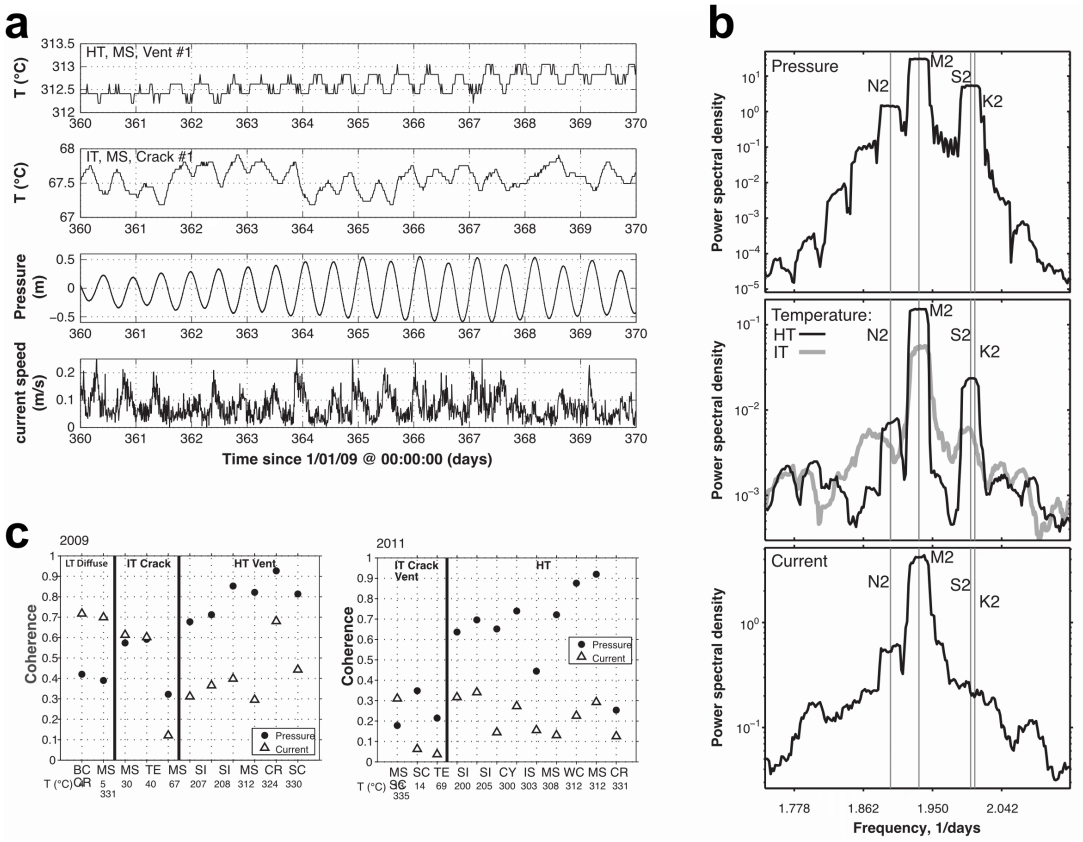

Figure 2-22 – Figures from Barreyre et al. (2014) with: (a) tidal variations for high- and intermediate-temperature records from the Montségur hydrothermal site of the LSHF and the corresponding bottom pressure and current velocity timeseries; (b) Power spectral density diagrams at the semidiurnal harmonics (N2, M2, S2, K2) for the water column pressure, fluid temperature and bottom current velocity; (c) Coherence plot for years 2009-2010 and 2011-2012 between fluid temperature and either the pressure (black dots) or either the current velocity (white triangles) with the 3 types of fluids described in this study: high-, intermediate- and low- temperature fluids for the hydrothermal sites of the LSHF.

2.4.5. Diffuse and focused hydrothermal energy fluxes

As seen in section 2.2, hydrothermalism plays a major role in the cooling of the new accreted oceanic lithosphere. Stein and Stein (1992) attribute 32 TW to the global oceanic heat flux with 1± 4 TW occurring through hydrothermal flow within the oceanic crust at the axis of MORs. Little et al. (1987) introduce a notion of scale for estimates of MOR hydrothermal heat fluxes: macroscale for the flux over a ridge segment, mesoscale for a hydrothermal field, and microscale for a specific vent. The proportion of hydrothermal heat flux at diffuse vents is generally estimated to be greater than that of focused vents (Rona and Trivett, 1992; Schultz et al., 1992; Baker et al., 1993; Ginster et al., 1994; Elderfield & Schultz, 1996; Nielsen et al., 2006; Stein & Fisher, 2001; Ramondenc et al., 2006; Veirs et al., 2006; German et al., 2010; Mittelstaedt et al., 2016). This higher estimate is because the surface of diffuse venting is much

larger than that of focused vents. Venting heat flux depend on the temperature of the fluid, the fluid velocity and the surface of venting.

Effort to estimate heat flow at the microscale have first concerned primarily the focused vents. Fluid velocity can be estimated with the help of video records using Particle Image Velocimetry (PIV; e.g. Macdonald et al., 1980; Mittelstaedt et al., 2012; Rona & Trivett, 1992). Flow meters have also been used (Converse et al., 1984). The heat flux is then estimated with the following equation:

$$H = \pi r^2 v \rho C_p \Delta T$$

With r the radius of the venting chimney orifice, v the flow rate, ρ the density of the venting fluid, C_p the heat capacity of the fluid and ΔT the difference in temperature between the hydrothermal fluid and the surrounding cold seawater. Estimation of heat flux for diffuse fluids is more complex, because their temperature and venting velocities are known to be spatially and temporally variable, and because they must be mapped using ROV observations and seafloor imagery (e.g. Barreyre et al., 2012). The total heat output of a hydrothermal site can also be determined from its buoyant plume (Goto et al., 2003; Little et al., 1987). The review of heat flux estimates made by Ramondenc et al. (2006) shows that water column measurements tend to give higher estimates of the total heat flux than the sum of direct measurement at several vents.

The heat flux partition between focused and diffuse vents at the scale of a hydrothermal field is highly variable: estimates of diffuse emanations are below the detection limit for the Rainbow hydrothermal field (MAR; German et al., 2010) to up to 95% of the total heat flux in most other investigated black smoker vent fields. Veirs et al. (2006) estimated an equal partitioning between diffuse and focused fluxes for the Endeavour segment (JFR), with a total heat flux of 8-42 MW. The total hydrothermal heat flux between 9°50.1-9°50.7'N at the EPR is estimated as 325 MW with 10 to 1000-time higher diffuse than focused fluxes (Ramondenc et al., 2006). Rona & Trivett (1992) estimated a heat flux of 4.4±2 MW for the high-temperature plumes over the ASHES hydrothermal field (JFR), and a heat flux of 15-75 MW for the plume from lower temperature diffuse sources at the same field. Measurements of hydrothermal tracers in the buoyant plume in the water column over the north Cleft field (JFR; Baker et al., 1993) suggest that diffuse discharge dominates the heat flux by a factor of 2 (600 MW of the total estimated heat flux of 800 MW).

Zooming to the scale of a 5x5m hydrothermal site in the Endeavour segment, Schultz et al. (1992) estimate a heat flux of 2.9 MW for the focused vents, and of 58.2±5 MW for the

percolating diffuse fluids. At Lucky Strike, the diffuse heat output at the field scale is estimated as 612±424 MW, corresponding to 75-90% of the total heat flux (Barreyre et al., 2012). At the scale of the 30x50m Tour Eiffel site, diffuse fluids may be responsible for 18.75±2.2 MW, representing 95% of the total estimated heat flux for this site (19.82±2.88 MW; Mittelstaedt et al., 2012).

Hydrothermal heat fluxes also affect the substratum, triggering secondary seawater circulation, and result in complex conductive heat fluxes in the seabed at and near vent sites (Becker et al., 1996; Johnson et al., 2010; Salmi et al., 2014). Low (<50 mW/m2) conductive heat flow is measured within meters of vents at the Endeavour segment and interpreted as downflow zones (Johnson et al., 2010; Salmi et al., 2014). At the TAG field, conductive heat flow range between 0.1 and 100 W/m^2 over less than 50m (Becker et al., 1996).

2.4.6. Diffuse hydrothermal fluids and the hydrothermal fauna

Hydrothermal vent at MORS are widely known for the discovery of rich, dense and complex faunal ecosystems (Figure -2-23) in extreme conditions with no light, hot temperature, toxic conditions and high pressure (Corliss et al., 1979). These ecosystems are based on chemosynthesis realized by chemoautotrophic or chemoheterotrophic microbes as primary producers (Lutz & Kennish, 1993). Chemosynthesis is the conversion of carbon compounds and other molecules into organic compounds. In this biochemical reaction, methane (CH_4) or an inorganic compound such as hydrogen sulfide (H_2S) or hydrogen gas, is oxidized to act as the energy source for microbes. These ecosystems independent of photosynthesis were a clue to involve hydrothermal vents of the past as possible sites for the origin of life (Baross & Hoffman, 1985; Martin et al., 2008).

Endemic and extremophiles microbes are part of archaea and bacteria, belonging to two of the three fundamental domains of life, according to the classification of Woese et al. (1990). They live around the vents, in symbiose with multicellular organisms or live inside the body of these organisms. These microbes are the base for any hydrothermal ecosystem be being at the base of the food chain. Suspended bioparticles formed by flocculation and released in the hydrothermal plumes are consumed by suspension feeders and bacterial mats growing at the level of diffuse fluids (Figure -2-23a and c) are eaten by “grazers” organism. Another possibility is the nutritive role as a symbiont in macro-organisms (Figure -2-23d;Tunnicliffe, 1991. At the edge of hot focused vents, animals in symbiosis with these microbes are mussels, shrimps or tube worms. The repartition of the hydrothermal fauna on hydrothermal edifice is dependent

from their distance to fluids exits but also to the exposition to deep-sea current capable to bring plume material (Girard et al., 2020).

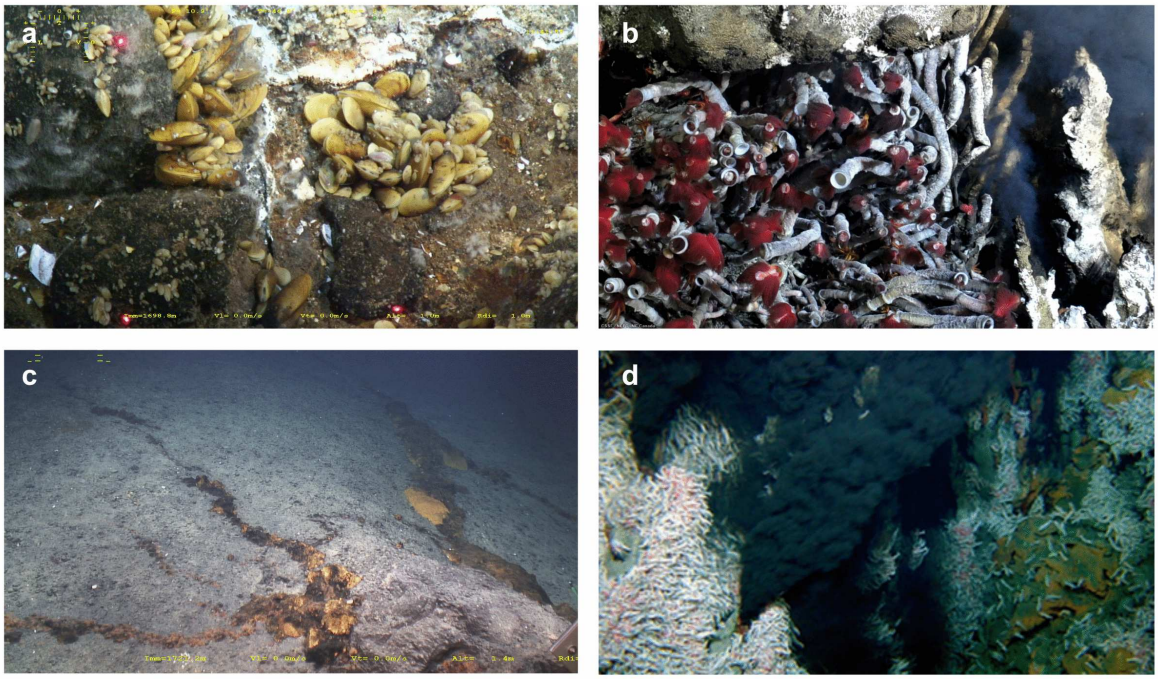

Figure -2-23 – (a) Bathymodiolus azoricus mussel assemblage at the Tour Eiffel site of the LSHF (b) Ridgeia piscesae tubeworms in various states, some alive and healthy, others dead at the Endeavour main site, Juan de Fuca ridge (c)bacterial mats at the LSHF (d) Rimicaris exoculate swarm on smoker walls (Rainbow, Ifremer, ATOS cruise), these shrimps live in symbiosis with bacteria hosted on specialized appendages and inside the inner surface of their gill chamber.

Since the discovery of hydrothermal vents at MORs, the fact that the highest temperature that some bacteria can tolerate is around 113-121°C (Blöchl et al., 1997; Kashefi & Lovley, 2003), points to diffuse venting areas as a welcoming environment for chemosynthetic microbes. Observation of large amounts of biomass expelled from the seafloor during magmatic events at MORs highlights their presence in the substratum (Haymon et al., 1993). Hydrothermal geochemical fluxes also show an impact of the subsurface microbial communities with for example excess of methane or depletion of hydrogen (Butterfield et al., 2004; Wankel et al., 2011).

The tidal cycle that impacts fluids temperature and venting velocity also impacts the bacterial community and the macro fauna. Flow perturbations due to tides have a stimulating effect for microbiological activity by increasing the mixing with oxidizing seawater (McCollom & Shock, 1997). Lelièvre et al., 2017 show that ocean tides and winter storms can impact hydrothermal vent species. Two hypotheses are introduced: bottom currents generate abiotic condition at tidal rhythm causing the fauna behavior to adapt in search of optimal conditions, or these biological rhythms are encoded by clock genes corresponding to the anticipated answer

of organisms to environmental condition variations. In support of the second interpretation, Mat et al. (2020) show that the physiology of mussels at the Lucky Strike hydrothermal field is tuned to tidal cycles, while mussels acclimated to laboratory conditions have a daily cycle. They also show that these tidal behavioral rhythms have a molecular expression and therefore involve gene expression.

Chapter 3.
Numerical and mathematical modeling of hydrothermal circulation at the hydrothermal field scale at mid-ocean ridges

The difficulty of access to the subseafloor for direct measurements or sampling of the oceanic crust necessitates modeling of the physical and chemical processes occurring in a porous medium to increase the understanding of hydrothermal fluid circulation in the oceanic crust. This section aims to compile some numerical and mathematical approaches that describe the formation and evolution of hydrothermal cells in oceanic crust. Instead of a comprehensive review of all models of hydrothermal circulation over the last 40-50 years, I choose to focus on key relevant studies addressing the physics of smoker-like and diffuse-like activities, and which provide the foundation of my modeling approach (see Chapter 5).

Hydrothermal circulation is dependent on a heat source and a medium (i.e., host rock) that fluids can penetrate and interact with. These characteristics, and the depth of the convection cell, are constrained using either characteristic measurements of venting fluids released at the seafloor or derived from numerical modeling. Such models facilitate testing of the effects of each parameter against observations, as well as predictions of the geometry of hydrothermal circulation and its evolution with time.

In this section, we first develop the basics of modeling fluid circulation in porous media. Then, we summarize published numerical studies in two- or three-dimensions that describe kilometer-scale hydrothermal cells, the thermodynamics of hot and diffuse fluids in a cold porous media, and the effect of the different physical parameters. Finally, we introduce models that explore the role of mineral precipitation as a parameter impacting the permeability and therefore the circulation of hydrothermal fluids in the upper crust.

3.1. Modeling of fluid circulation in a porous media

Several historical models of hydrothermal circulation consider the oceanic crust as uniform medium with zones of higher permeability in the form of cracks, described physically as pipes containing laminar flow. As laminar flows does not have lateral mixing or lateral variations in size, these single-pass models prevent any interactions with the surrounding media

containing cold fluids. Describing the oceanic crust as a porous medium with localized variations of physical parameters (e.g., porosity, permeability) is another approach used in most of the recent numerical and mathematical models. The volumetric flow of fluids in a homogeneous porous medium is described by the Darcy law:

$$v = \frac{-k}{\mu} \nabla p$$

With v being the Darcy velocity of the fluid depending on the permeability k of the porous media, μ the dynamic viscosity of the fluid and ∇p the total pressure drop. Permeability is the measure of the ability of the porous media to allow fluid to pass through it. The viscosity and density of the fluid depend on the temperature and pressure conditions. The Darcy flow equation is completed by the continuity equation of mass conservation that describes the mass balance for a single-phase fluid:

$$\varepsilon \frac{\partial \rho_f}{\partial t} + \nabla . (\rho v) = 0$$

where ε is the porosity, or the fraction of the void volume over the total volume of solid material. The last equation is the conservation of energy in the fluid-rock mixture:

$$\rho C_p \frac{\partial T}{\partial t} + \rho_f C_{p,f} (v . \nabla T) = \lambda \nabla^2 T$$

with the specific heat capacity of the solid medium C_p and of the fluid $C_{p,f}$.

3.2. Fluid circulation models at the hydrothermal field scale

Modeling of MOR hydrothermal convection began in the early 70's before the discovery of underwater hot springs on the seafloor. The existence of these hot springs was expected because of the probable existence of a discrete zones of high permeability like faults or dykes at the oceanic ridge crest, and was highlighted by heat flow measurements suggesting hydrothermal discharge at the Mid-Atlantic Ridge crest (Scott et al., 1974). From this assumption, Bodvarsson & Lowell (1972) and Lowell (1975) apply a theory for convective flow in a uniformly and isotropic fluid-saturated medium to develop steady state and time-dependent thermal models of submarine hot springs. The model consists of two vertical fractures and a horizontal contact zone (Figure 3-1a) with a laminar flow into it, and the heat driving the circulation being at the horizontal section (BC, Figure 3-1a). Lowell (1975) shows the important role of crack width on the flow rate and its direct impact on the temperature of venting fluids due to thermal conduction in the upflow zone (Figure 3-1b). The principal driving

mechanism is the heat loss to the surrounding rock, with venting fluid temperatures decreasing with time with the geothermal gradient. This approach does not consider the presence of a heat source below the horizontal contact zone or the heterogeneity of the oceanic crust that can impact the fractured system.

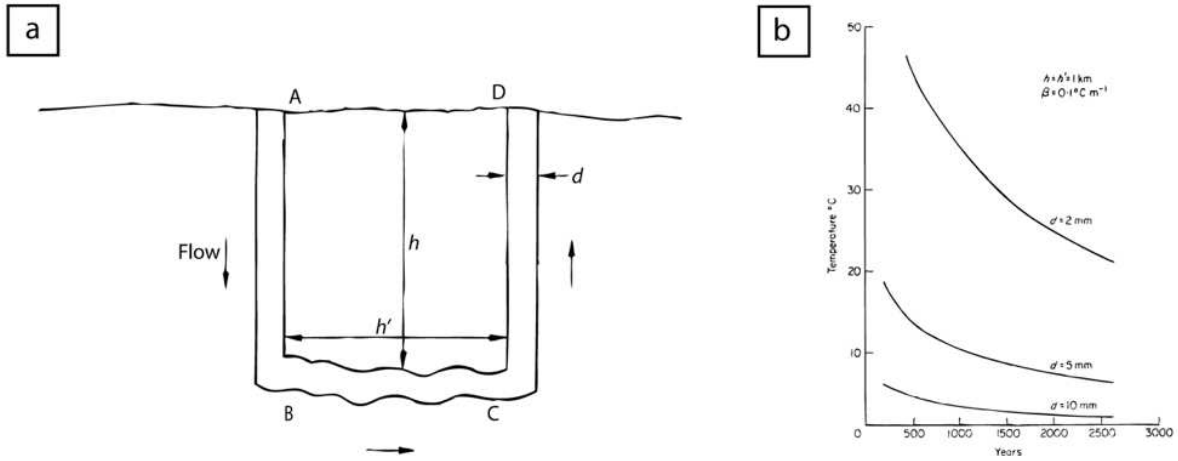

Figure 3-1 – (a) U-tube aka single-pass model geometry of Lowell (1975) made of 2 vertical fracture (AB & CD) of width d and depth h connected to a contact zone (BC) of length h'. The fluid enters at A with a temperature of T=0, and return to the surface at D. (b) Spring temperature plot at D as function of time for various fracture width β

After the discovery of discrete venting structures at the seafloor, the main goal of subsequent models was to obtain venting temperatures above 350°C, as observed at hydrothermal sites. Similar single-pass models with a fault adjacent to hot rocks give the same result: short-lived hot venting systems with fluid temperatures largely below 350°C even for deeper circulation and higher flow velocities (Strens & Cann, 1986) or differing flow velocities between the recharge and discharge zones (Strens & Cann, 1982). To be able to move from short-lived to long-lived stable hydrothermal systems with venting temperatures up to 350°C, 3 alternatives are given: (i) a larger volume of hot rocks which imply deeper recharge zones, (ii) no high permeability structures like faults in the upflow zone that allow fluids to extract more heat in an extensive area through a porous media, and (iii) an additional heat source such as an axial magma chamber (Cann et al., 1985). Magma-driven models lead to heat exchange by conduction through a bottom conductive boundary layer between the magma-chamber and the overlying region of heat uptake in the hydrothermal cell (Lowell & Burnell, 1991). The thickness and permeability of this region are critical parameters that ensure temperature and flow rate are similar to focused vents for the first ~100 years. After this period, they observed significant decrease of heat flow suggesting that this parameter is not the only or main factor needed to stabilize a hot-temperature hydrothermal circulation (Lowell & Burnell, 1991).

The use of an equivalent homogeneous porous medium also began in the 70's with the advent of single-pass flow analyses (Fehn & Cathles, 1979; Ribando et al., 1976). These models introduce Darcy's law and the isotropic/anisotropic property of the porous media. Models with vertical permeability anisotropy or with local zones of higher permeability are tested to focalize a vigorous flow to the surface. Rosenberg & Spera (1990) introduce a model with a medium composed of 2 layers of equal height but with different isotropic permeabilities as an analog for the permeability field of the oceanic crust (see section 1.3) and show that the intensity of convection is highly dependent on the permeability ratio between the 2 layers. At the interface between the 2 layers, the flow becomes more focused in the upper, higher permeability layer, but no estimation of venting fluid temperature at the surface is specified (Rosenberg & Spera, 1990; Yang et al., 1996a).

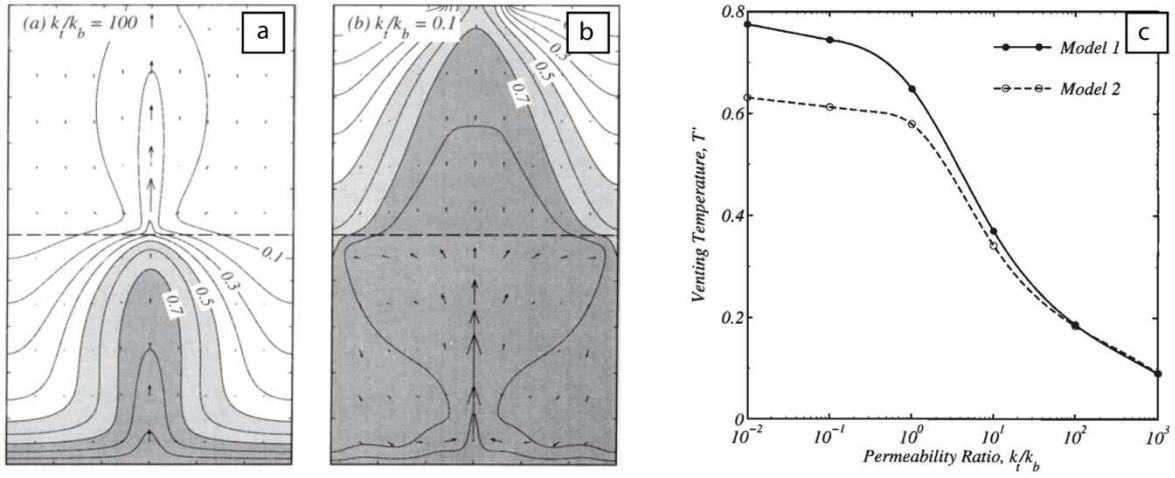

Figure 3-2 – Solutions of Wilcock (1998) for a steady state convection model with a bottom temperature of 500°C, a top boundary layers and with fluid proprieties approximating seawater, consisting of 2 layers of equal thickness. The difference for both solutions is the permeability ratio between the top and bottom layers kt/kb at (a) 100 and at (b) 0.1. Contours and grey shading corresponding to the nondimensional temperature field and arrows to the relative magnitude and direction of flow. (c) Maximum non-dimensional temperature as a function of the permeability ratio. Here we are interest in the model 2 with an open boundary layer like on (a) and (b), the model 1 corresponding to an isothermal top boundary layer with a constant temperature. For a bottom temperature of 400°C, the maximum venting temperature obtained at low permeability ratio is 260°C.

Wilcock (1998) uses a two-layer model in which the permeability ratio between the top (k_t) and bottom (k_b) layer ranges between 0.1 and 100 (Figure 3-2a). Like Rosenberg & Spera (1990), the pattern of convection is highly different from models assuming a uniform permeability with much more recirculation in the upper layer. The large Darcy velocities in the upper high permeability layer are the reason for this pattern and cause low temperature venting with a top high permeability layer and the opposite for a bottom high-permeability layer (Figure

3-2a and b). Venting temperatures are therefore very sensitive to the vertical permeability variations, with a decrease from 70% to 10% between the initial bottom temperature and the resulting venting temperature at the top boundary of the model (e.g. model with bottom temperature of 700°C will have venting temperature between 490 and 70°C), respectively for the lowest to biggest permeability ratio (k_t/ k_b) between the 2 layers (Figure 3-2c).

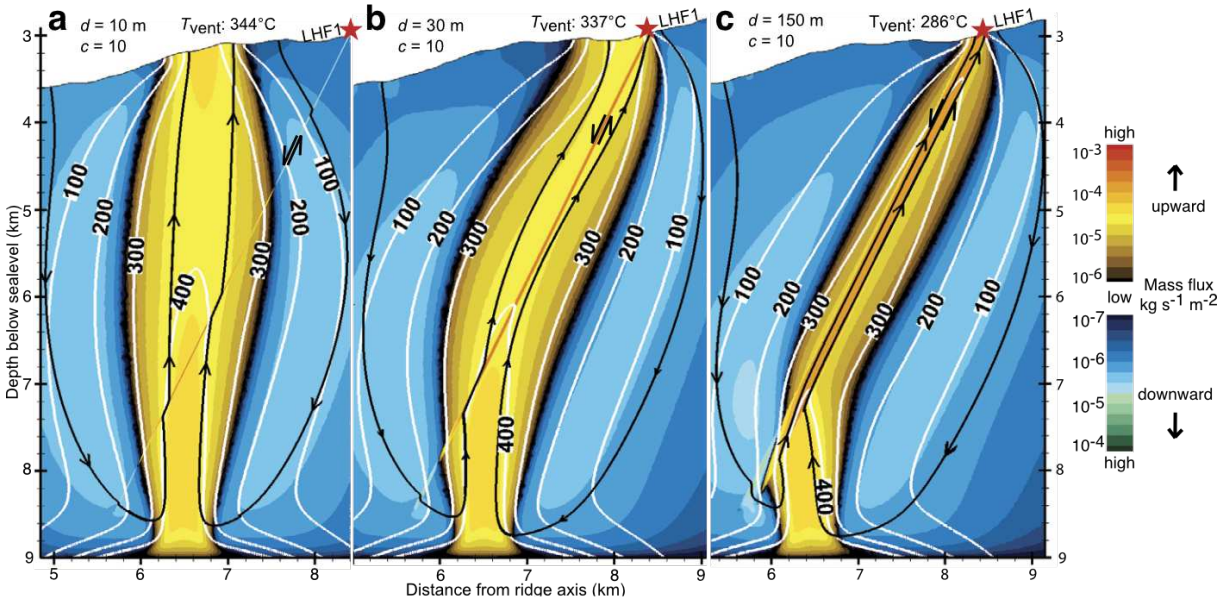

Figure 3-3 – Results of the model by Andersen et al. (2015) for a diagonal fault with a permeability 5 × 10^{-15} m^2 into a porous media with a permeability of 5 × 10^{-16} m^2. The width of the fault is varied between the 3 models, from (a) 10m, to (b) 30m and (c) 150m. Black flow lines show the convective pattern of the hydrothermal cell and white lines are the isotherm. The color gradient is the upward (yellow) and downward (blue) mass flux.

Discrete vertical and horizontal permeability variations along the path of fluid circulation is another possible control on the channeling of circulating hydrothermal fluids. For example, the single-pass models mentioned above call for the presence of higher permeability zones equivalent to cracks or dykes, that can also be introduced into 2D and 3D homogeneous porous models. Yang et al. (1996b) developed a 3D model with a central vertical column with a permeability (10^{-12} m^2) one order of magnitude higher than the surrounding (10^{-13} m^2) to describe the flow in a conduit within a hydrothermal mound (TAG in this study). The higher specific conductivity (compared to the oceanic crust) of the sulfides is shown to help maintain venting temperatures above 350°C. The large amount of anhydrite observed by drill core in the TAG hydrothermal mound highlights a significant entrainment of seawater and a possible significant cooling, not observed by the model of Yang et al. (1996b). Since fractured zones control hydrothermal discharge in submarine systems, (Yang et al., 1998) incorporate a planar fracture where fluid follows laminar conditions instead of a vertical low permeability column.

This fracture induces and maintains convections cells, with increasing aperture being the main parameter that increases the maximum fluid velocity. To model hydrothermal flow in a medium comprising a seismically imaged oblique fault whose permeability amplitude and width need to be constrained, Andersen et al. (2015) developed 2D models with contrasting horizontal permeabilities. It appears that specific conditions need to be met to vent high-T fluids: if the fault zone is too wide or permeable, cooling through mixing decreases the temperature whereas thin less permeable faults are not able to channel the fluid flow (Figure 3-3).

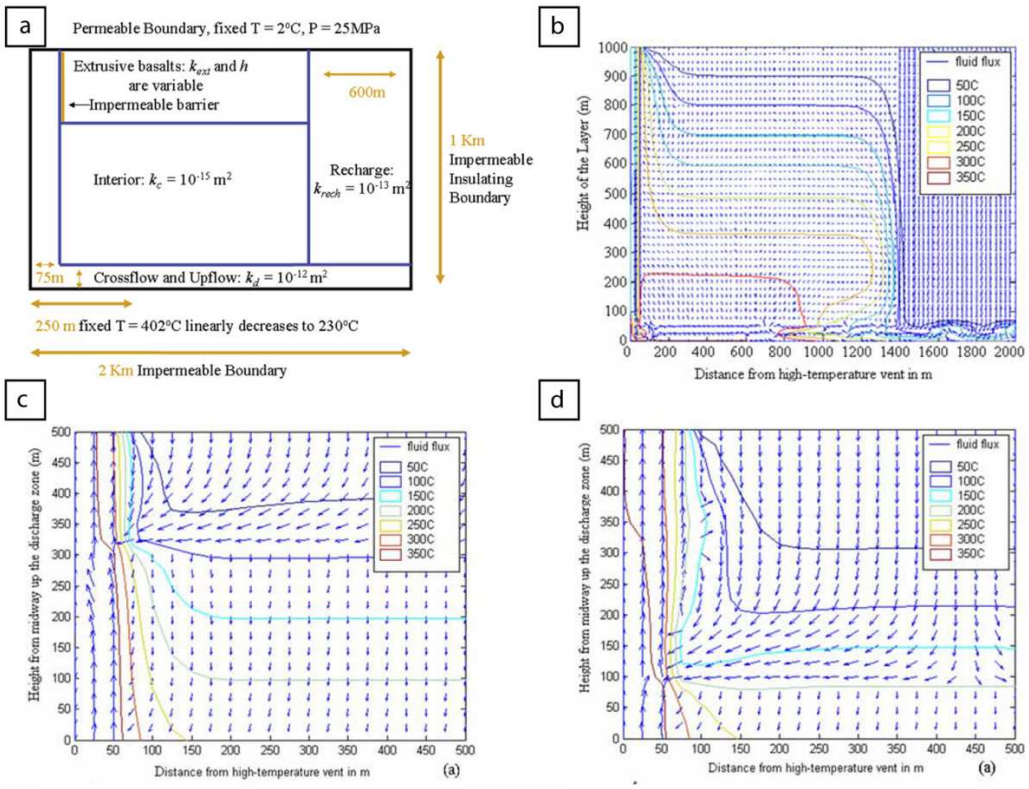

Figure 3-4 – Diagram and solutions of numerical models by Lowell et al. (2007). (a) Geometry of the model with a top extrusive layer include only in (c) and (d). (b) Fluids flow vectors and isotherm for model results without a top extrusive layer. (c) Solutions for the 500x500m upper left of the previous model (b) for a model with an extrusive layer with a height of 200m and a permeability of 10^{-13} m^2. (d) Solutions with the same parameters of models (c) but with an extrusive layer with a larger height of 400m.

To simulate a high temperature discharge in faults/fractures zones, Lowell et al. (2007) developed models varying the size and permeability of the different zones, from 10^{-13} m^2 in a wide recharge zone (Lowell & Yao, 2002) to 10^{-12} m^2 in a narrow upflow zone (Figure 3-4a). The resulting pattern of circulation for this model is a highly channelized upflow zone with a recharge flux compressing the isotherm at the bottom of the model (Figure 3-4b). The resulting discharge zone has temperatures equivalent to high-temperature discrete vents. Then Lowell et

al. (2007) study the effect of an extrusive layer on the circulation dynamic with a top higher permeability layer (Figure 3-4c) and the possible effect of a deeper extrusive layer (Figure 3-4d). These models help to highlight the role of cold downflowing fluids from the lateral recharge zone with the hot upwelling fluids. The presence of the extrusive layer enhances the mixing of hot and cold fluids, reducing the temperature of the hydrothermal vent. By doubling the thickness of the extrusive layer (Figure 3-4d), Lowell et al. (2007) show that a deeper intrusive layer does not have a great impact other than slightly reducing the discrete vent temperature.

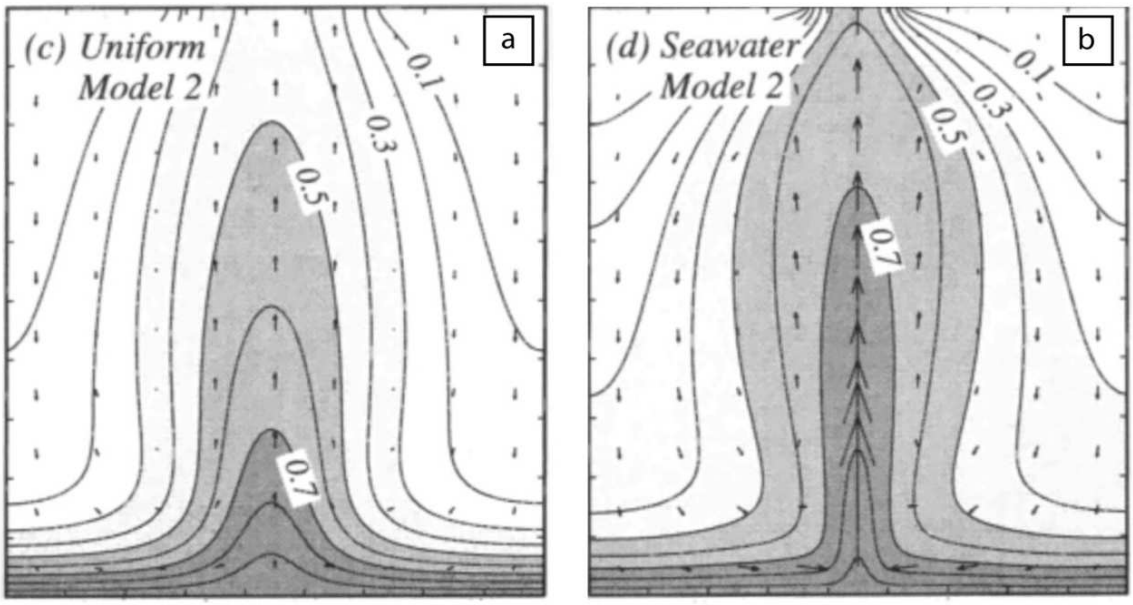

Figure 3-5 – Solutions of Wilcock (1998) for a steady state convection model with a bottom temperature of 500°C and an open top boundary layers. (a) Uniform fluid properties and (b) fluid proprieties approximating seawater are used. Contours and grey shading corresponding to the nondimensional temperature field and arrows to the relative magnitude and direction of flow.

These parameters (porosity and permeability) are linked to the solid medium where the fluid is circulating, though the fluid properties and thermodynamics may also impact the final venting temperature at the top of the model. Initial models of hydrothermal circulation used simplifications such as constant viscosity and/or heat capacity and the Boussinesq fluid approximation which states that for a fluid flow dependent of the temperature, variations in fluid properties other than density are ignored except when dependent of the gravitational acceleration, expressed as $\frac{\partial \rho}{\partial t} + \nabla.(\rho u)$. Wilcock (1998) greatly improved the model by introducing non-linear temperature- and pressure-dependent fluid properties (viscosity, density, and heat capacity) for a single-phase fluid approximating seawater. The properties of seawater

cause a higher buoyancy with a lower viscosity close to the hot bottom boundary layer, thereby increasing the plume temperature by bringing in more hot fluids in the upflowing plume (Figure 3-5a and b) (Jupp & Schultz, 2000; Wilcock, 1998). This variable viscosity also leads to a wider upwelling plume (Figure 3-5b). These seawater properties control the ability of the convective system to transport energy through buoyancy in parallel with the strong dependence on permeability (Driesner, 2010; Driesner & Heinrich, 2007). Fluids heated up to 200°C move rapidly downwards because their temperature-dependent density decreases only by 10% while their viscosity decreases by one order of magnitude making them more mobile (Coumou et al., 2008, Figure 3-6a). Above 300°C the density and the viscosity decrease substantially and the fluids start to rise (Figure 3-6a).

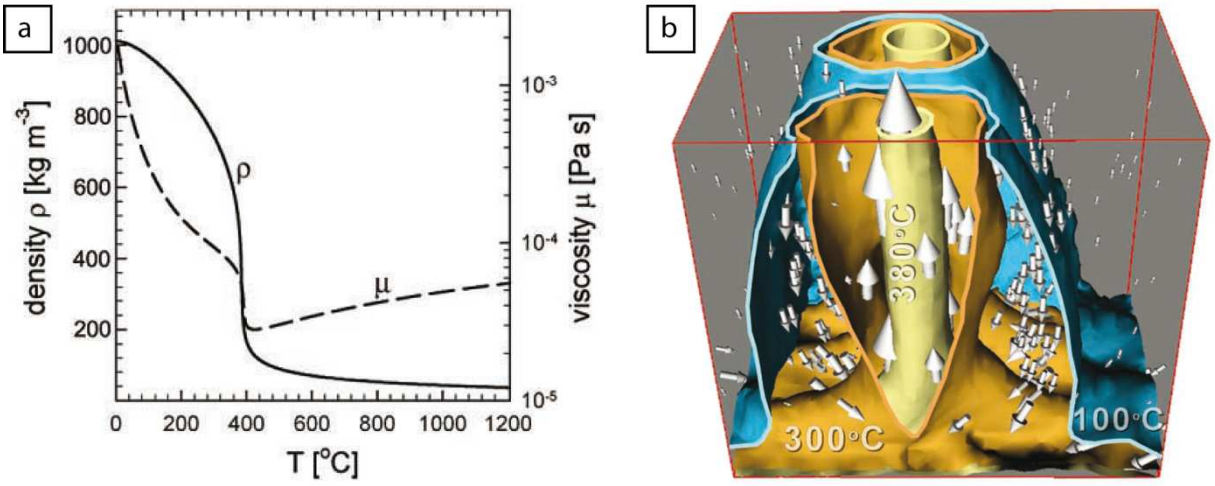

Figure 3-6 – (a) Diagram of density and viscosity of the fluid as a function of the temperature and the pressure. (b) Cross-section of a thermal plume with isotherm of 100°C (blue), 300°C (brown) and 380°C (yellow)and the corresponding mass fluxes (arrows). Note the important downflow zone between the 100 and 300°C isotherms. Figures by Coumou et al., 2008

New more sophisticated 2D and 3D models have been created to better describe the complex thermodynamics and patterns of these hot fluids in a cold porous medium while incorporating constraints from in-situ measurements or observations. If fluids upflow from the brittle roof of the magma chamber through a crustal section with a constant permeability, then smoker formation is possible. The core of the venting zone can reach temperature up to 380-450°C, while conductive cooling across the upflow zones leads to minimum venting temperature of 200-250°C on the sides of the hot upflow area, and any fluids of lower temperature move down (Coumou et al., 2008; Fontaine & Wilcock, 2007a). The venting of warm (i.e., a few tens of °C) fluids characterized by diffuse emanations is not possible with these constant permeability models. However, if one considers that a permeability contrast

naturally exists between the dyke and lava sections, then the venting temperatures decrease. This is because the hot rising fluids in the low-permeability dykes mix with cold fluids that circulate only in the high-permeability lava section (Lowell et al., 2007; Rosenberg & Spera, 1990; Wilcock, 1998). To obtain widespread low-temperature diffuse fluids, Pascoe & Cann (1995) confirm the need to have a more permeable top layer than the underling zone, allowing cold seawater to be entrained and dilute the hydrothermal fluid. In this case the venting of warm fluids more typical of diffuse emanations is possible; however, such mixing prevents the formation of smoker-like fluids. These "layered" models can eventually explain the formation of large areas of diffuse venting (e.g., Galapagos), but not the concomitant venting of hot smoker-like fluids and warm diffuse-like ones.

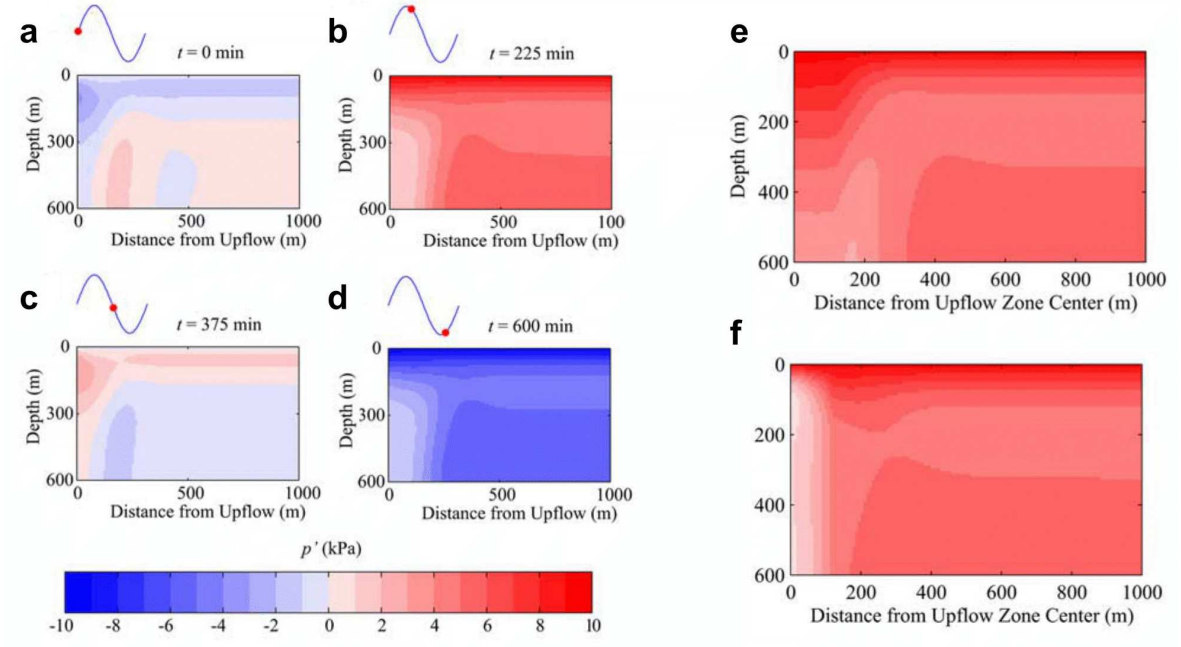

Figure 3-7 – The left panel (a-d) is time-series of pressure perturbation p' over a semidiurnal tidal cycle. (shown at the top left corner, red dot corresponding to the phase of the tidal loading). The right panel (e-f) is the pressure perturbation p' just after high tide (like panel b) for a higher (e) or lower (f) permeability in the upflow zone. Note that the diffusive component of p' dominate the upper part and the instantaneous component of p' dominate the right lower part of the model domain. Figures from Crone & Wilcock (2005).

A recent advancement in numerical models is the integration of poroelasticity (mechanism detailed in section 2.4.4.1) to model the possible magnitude of tidal variations of fluid temperature, and velocity measured at the seafloor, as a response to tidal loading of the porous subseafloor. Crone & Wilcock (2005) developed a 2D numerical model of poroelastic convection to study the effect on the modulation of temperature, pressure, fluid velocity, and the mixing of hydrothermal fluids with seawater.

The predicated variations of pressure perturbation p' of the pressure field during a semidiurnal tidal cycle (12.5h) are shown in Figure 3-7a-d. The upper part of the model (~100 mbsf) is dominated by a diffusive component of p' staying nearly in phase with the tide (e.g. positive pressure perturbation for high tide, Figure 3-7b). The lower part on the other hand corresponds to the instantaneous component of p' that is in phase with the tidal loading due to the compressive stress in the poroelastic media. These perturbations are impacted by the upflow zone (on the left of the model, Figure 3-7), where horizontal flow leads to high pressure gradients. It modulates the adjacent region (~300 mbsf) by creating a low-pressure region near the upflow zone (for high tide, fluid is forced to move from the high loading zone to the low pressure upflow zone, increasing the pressure in the bottom of the model and lowering it just above). Therefore, the tidal loading on the porous media can change the pressure field and the fluid circulation. A change in the upflow zone permeability causes the diffuse component of p' present close to the surface to go deeper (for higher permeability, Figure 3-7e) or to be limited closer to the surface (for lower permeability, Figure 3-7f). The direct effect is a widening or narrowing of the high-pressure deep zone, impacting the horizontal circulation of fluids.

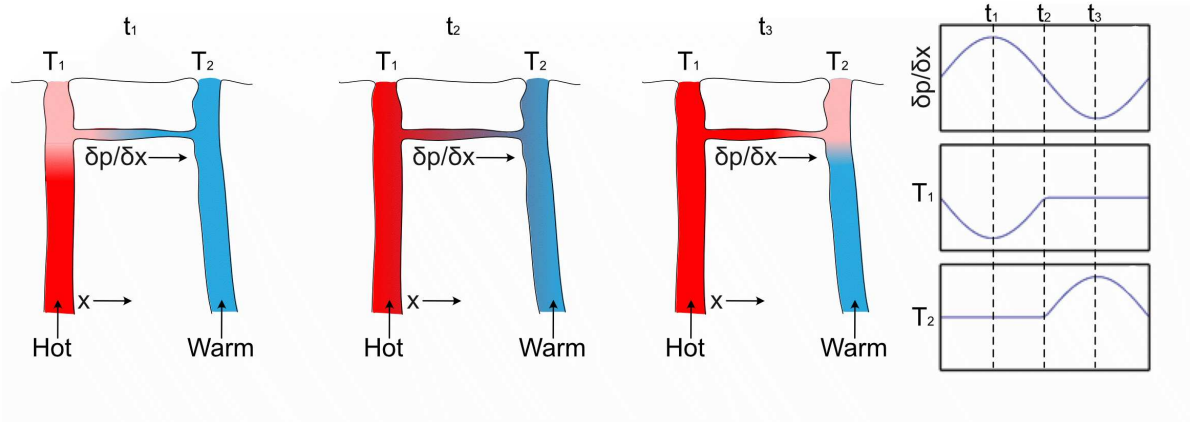

Figure 3-8 – Schematic diagram of the hypothesis off Crone & Wilcock (2005) to explain high amplitude temperature variation during tidal cycle that implies a fractured medium impacted by horizontal pressure gradients. When the pressure gradient is positive in the x direction, fluid from the warm crack flow through the hot cracks, cooling the system (t1) and vice versa when the pressure gradient is negative (t3).

The effect of these pressure perturbations on the different variables of the model are variable. The Darcy velocity shows some flow reversal between the region of outflow and inflow (x~130-145m, Figure 3-7) at each tidal cycle. The amplitude of these perturbations is highly sensitive to the permeability, as Darcy velocity is dependent on the porosity and therefore the permeability as described by Darcy's law. The major zones of possible reversal

of the velocity are in region of lower temperature at the edge of the upflow zone. For temperature, the pressure perturbation advect the isotherms horizontally with the highest perturbation occurring at the border of the upflow zone. The maximum temperature perturbation obtained with this system is only of 10^{-4}°C which is significantly less than semi-diurnal temperature variations reported for MOR diffuse vents (amplitudes up to several degrees (°C); see Chapter 4). Crone & Wilcock (2005) assumes that all walls of the rocks are in thermal equilibrium with the fluid. But even if only a small fraction of the rock is in thermal equilibrium (<1%) and that the remaining rocks create temperature perturbations, the maximum amplitude of temperature variation would be of the order of 0.1°C. One way to explain temperature variations higher than 10^{-4}°C is to move from a continuous medium to a cracked medium where horizontal pressure gradient would change the temperature in a specific crack during tidal cycles (Figure 3-8). This highlights the importance of recognizing the non-continuous component of the medium for the upper crust to interpret fluid flow circulation Crone & Wilcock (2005).

3.3. Mineral precipitation and channeling of upflowing hydrothermal fluids

Pascoe & Cann (1995) argue that when the hot rising fluids mix with seawater in a crust with layered-permeability, precipitation of hydrothermal minerals should occur in zones of large temperature gradients at the interface between the top, more permeable layer and the lower, less permeable one. This precipitation will progressively clog the porosity and decrease the permeability of the initially more permeable upper part of the upflow zone, eventually leading to the formation of smoker-like vents as the permeability contrast diminishes. This conceptual precipitation-assisted, two-fold model for the formation of "mature" hydrothermal vent fields with smokers and diffuse flow rests on observations made in the stockwork of ophiolites, e.g., Troodos in Cyprus, where Cann & Strens (1989) infer the formation of impermeable, insulating "mineral shells", around upflow zones. Observations of magnetic anomalies centered around hydrothermal sites at the Juan de Fuca Ridge highlight upflow zones with alteration of basalts by hydrothermal fluids. Despite the presence of fault zones linking vent sites, they maintain a distinct delineation between each low magnetic anomaly, suggesting the formation of an "armored" up-flow stockwork zone with a shape of a pipe due to mineral precipitation that limits the upflowing of hydrothermal fluids to a small area (Tivey & Johnson, 2002).

A handful of studies have since attempted to test the effect of mineral precipitation on MOR hydrothermal flow dynamics. Fontaine et al. (2001) develop a model of hydrothermal convection including precipitation of anhydrite and sulfides. They show the formation of precipitation fronts at the top of the hydrothermal upflow in the substratum. As proposed by Pascoe & Cann (1995), this creates an impermeable front that prevents hot fluids from reaching the seafloor, allowing for the formation of hot vents. These results highlight the need to have events like seismic activity to reset or increase the permeability to aid in the formation of hot vents. Lowell & Yao (2002) show that clogging fluid pathways by anhydrite can impact the dynamics of the recharge zone close to the venting site. By reducing the permeability, the 150°C-isotherm rises in the recharge zones with time, creating a tendency to spread the area of anhydrite precipitation. They also show that if anhydrite precipitation happens, thus lowering the porosity of the recharge zone, then the recharge zone needs to be 10-100 times larger than the venting zone to be able to have stable high-temperature vents for time periods of several decades. More recently, sophisticated thermo-hydro-chemical models allow for reactive transport giving a more precise simulation of the evolution of permeability and saturation of mineral species during time. Guo et al. (2020) succeed at producing such a reactive transport model, to create low-permeability, sub-vertical wall structures that facilitate the focusing of high-temperature fluid fluxes to produce hot vents stable for 5000 years. The walls are composed of anhydrite in the deeper part (50-300 mbsf) and of sulfide minerals in the shallow subsurface.

An attempt to model the impact of mineral/anhydrite precipitation on diffuse flow formation is presented by Lowell et al. (2003). They use a 2-loop single-pass analytical/mathematical model containing a mixing area between focused and diffuse upflow. Lowell et al. (2003) derive conditions in favor of each 3 styles of venting, i.e., diffuse flow only, focused flow only, or focused and diffuse flow together. In particular they show that the third regime is possible only if the permeability of the mixing and focused upflow zones are commensurate, in the range of 10^{-12}-10^{-11}m^2. Their mathematical formulation also provides constraints on the thickness of impermeable anhydrite walls that could form in the mixing zone.

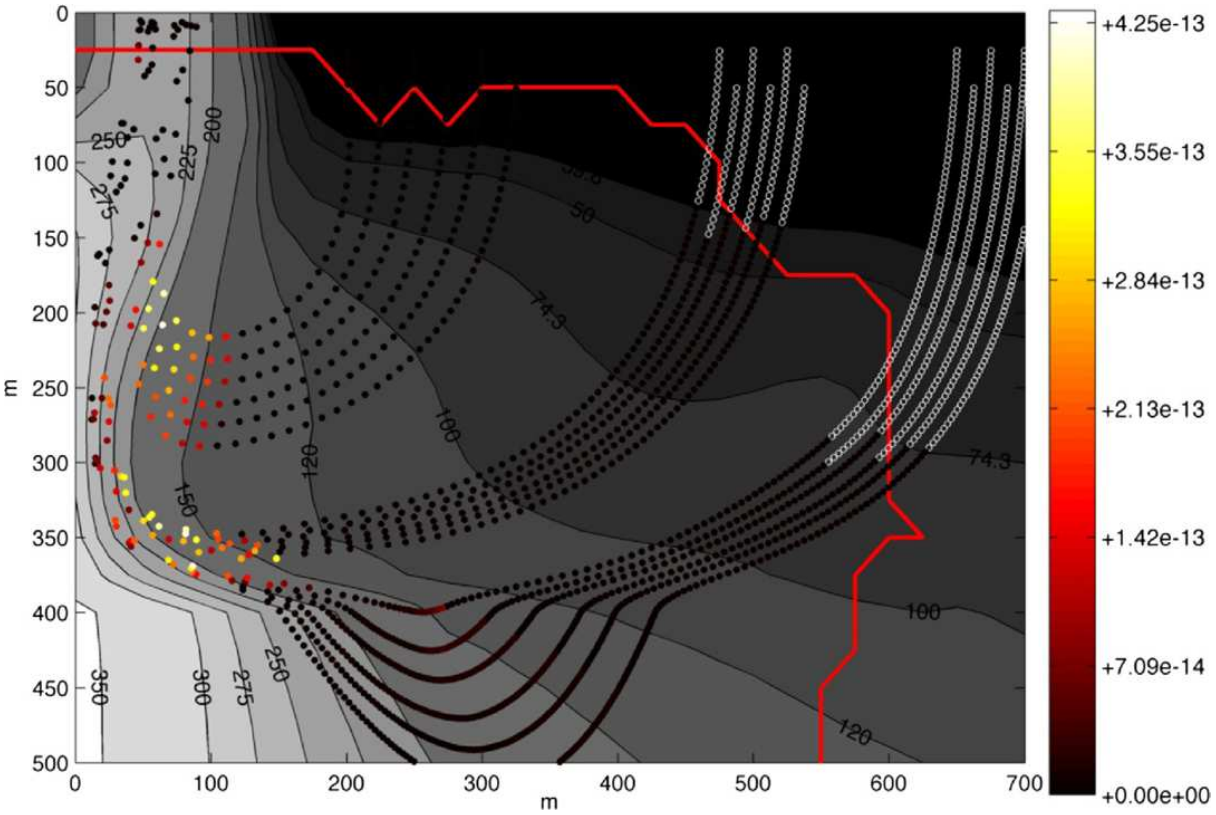

Figure 3-9 – Temperature field for a porous model composed of a bottom layer with a temperature from 400°C to 300°C from left to right and with a 400m thick extrusive layer with a permeability of 10^{-12} m^2 overlying a layer of 10^{-13} m^2. Red line is the delimitation for mixing as the dominant mechanism for temperature control. Particle tracking highlighted by circle shows the deposition rate of anhydrite in mol/cm3/s for 3 downflow zones entering at 3 different depths in the upflow system of hotter temperature. Figure from Larson et al. (2015).

2D numerical models by Lowell et al. (2007) use a 25m wide low permeability region (10^{-15} m^2) between the discharge zone and the top extrusive layers (Figure 3-4), to imitate the precipitation of anhydrite. The inhibition of the mixing with seawater due to the low permeability region keeps the upflow zone hotter than in the previous models (Figure 3-4) and manifests itself with a second region of high heat exiting at the surface on the cold side of the low permeability region. A simulation of anhydrite precipitation is developed by Larson et al. (2015) with a combination of thermal and chemical models. They observe a pattern of anhydrite formation 100m away from the upflow zone center with a maximum rate of deposition of 4.25×10^{-7} $mol/m^3/s$ (Figure 3-9). They also obtain sealing times for the porous medium between 320-600 years, but the spatial resolution of their model (25x25m) is too low to quantify steeper temperature gradients, likely leading to underestimated sealing times.

These models show it is possible to obtain high-temperature hydrothermal venting fluids by focusing upflow fluids by setting up low permeability layers on the side of the upflow zone created through mineral precipitations. They can estimate the width and depth of the low permeability zone and the rate of deposition of minerals like anhydrite due to interactions between hot hydrothermal fluids and cold seawater. Their 10m-scale resolution is too low to be able to observe high lateral temperature gradients between focused and diffuse venting areas and the geometry of fluid circulation in the last hundred meters below hydrothermal sites are poorly constrained. Those aspects of the modeling of hydrothermal fluid circulation, which do not correspond to in-situ observations of diffuse fluids distribution and temperature, will be developed in this thesis to improve our understanding of diffuse fluid formation and the corresponding fluid circulation in the shallow sub-seafloor.

Part II

Near seafloor hydrothermal circulation at the Lucky Strike vent field from geological mapping and time series of fluid temperature and chemistry, Mid-Atlantic Ridge, Mid-Atlantic Ridge.

Foreword

This chapter presents our work on the characteristics and formation of diffuse fluids through monitoring of 2 hydrothermal venting sites of the Lucky Strike hydrothermal field: Tour Eiffel and White Castle. The chapter is composed of a manuscript that will be submitted to the *Geochemistry, Geophysics, Geosystems* journal of the American Geophysical Union and the Geochemical Society. We use geological observations, seafloor mapping, and time series of fluid chemistry and temperature, current and seafloor pressure at two representative hydrothermal sites, the mature Tour Eiffel site and the younger White Castle site. The goal is to use these observations to picture the hydrothermal shallow sub-seafloor circulation and the related formation of diffuse by mixing of seawater with hydrothermal fluids in the upper hundred meters of the oceanic crust at the Lucky Strike hydrothermal vents.

This work was carried out as part of the LuckyScales ANR project whose goal was to acquire, analyze and model time-series to understand the dynamic of the Lucky Strike hydrothermal ecosystem through multidisciplinary studies based on monitoring as part of the EMSO-Azores submarine observatory. I processed the data, prepared the figures and wrote the paper, under the guidance of Mathilde Cannat. Valérie Chavagnac conducted the in-situ sampling of hydrothermal fluids and their chemical analysis on-shore. Fabrice Fontaine was involved in the shipboard acquisition of the monitoring data.

For this project, I participated to 4 observatory maintenance cruises (Momarsat 2017 to 2020). My role was to help maintain the array of temperature probes deployed at hydrothermal vents, as well as the near bottom current meters and seafloor pressure probes. As part of this work, I also helped build the in house LTGrad probes that we used to measure gradients of temperature in the seabed deposits, and I participated in the design of a new low-cost low-temperature probe which we deployed for the first time in 2020. Finally, still as part of this observatory maintenance activity, I helped publish the EMSO-Azores observatory temperature time-series data and metadata for the 2012-2020 period in the SEANOE open data platform.

Chapter 4.
Near seafloor hydrothermal circulation at the Lucky Strike vent field from geological mapping and time series of fluid temperature and chemistry, Mid-Atlantic Ridge.

Benjamin Wheeler[1], Mathilde Cannat[1], Valérie Chavagnac[2], Fabrice Fontaine[1 and 3]

[1] Université de Paris, Institut de Physique du Globe de Paris (IPGP), UMR 7154 CNRS, 1 rue Jussieu, 75238 Paris cedex 05, France (cannat@ipgp.fr)

[2] Géosciences Environnement Toulouse (GET) UMR 5563 CNRS, Observatoire Midi-Pyrénées Université de Toulouse, 14 Avenue Edouard Belin, 31400 Toulouse

[3] Observatoire Volcanologique du Piton de la Fournaise (OVPF), 14RN3 - km 27, 97418 La Plaine des Cafres, La Réunion

Abstract

We report on a 3 year monitoring experiment at the basalt-hosted Lucky Strike hydrothermal vent field, Mid-Atlantic Ridge. The experiment focused on low to medium temperature, so called diffuse vents, known to account for most of the total energy flux at mid-ocean ridge hydrothermal systems, and to provide key habitats for the hydrothermal fauna. Our results document the time and space variability of diffuse venting temperature and chemistry, the effect of tidal loading and currents, of mixing, cooling or heating of end-member hydrothermal fluids and seawater, and of anhydrite precipitation or dissolution in the substratum of two vent sites, one (Tour Eiffel) being larger and more mature than the other (White Castle). Based on these results, we develop a conceptual geological model for the dynamics of vent site scale hydrothermal circulation at the Lucky Strike field, that confirms the role of the thin (< 2 m) volcaniclastic formation deposited on the brecciated basalt substratum of both sites. This formation is either porous, or impermeable if indurated by hydrothermal precipitates, and forms an intermediate layer between the vents at the seabed and the fluids as they flow out of the brecciated basalt substratum. Mixing with seawater, heat exchange, slow porous upflow, mineral precipitation and dissolution in this intermediate layer affect venting temperatures, their variations at semi-diurnal tidal frequencies, fluid chemistry and venting velocity. Our interpretation of what fluids actually flow out of the basalts underneath points to relatively hot (> 80°C) and end member rich (> 9%) fluids coming out of a network of meter-spaced permeable cracks up to 25 m from the black smokers at both vent sites, yielding diffuse heat flow estimates of at least 7.5 MW at White Castle, and 28.9 MW at Tour Eiffel. These values are in the median to upper range of previously published estimates of diffuse energy fluxes at the Lucky Strike vent sites, which were based on seabed venting temperatures and velocities.

Key-words

Key-words: Mid-oceanic hydrothermal system, diffuse venting, geology, fluid temperature time-series, fluid chemistry, tidal forcing, currents, near seafloor hydrothermal circulation, spatial and temporal variability of hydrothermal habitats

4.1. Introduction

Hydrothermal circulation at mid-ocean ridges transfers most of the magmatic heat associated with the accretion of new oceanic crust (Lister, 1972; Lowell et al., 1995) and is one of the main mechanisms for chemical transfers between the solid Earth and the ocean (Alt, 1995; Elderfield and Schultz, 1996). Mid-ocean ridge black smoker type hydrothermal systems result from km-scale hydrothermal cells in which seawater is modified through reactions with the host rocks (Alt, 1995; Lister, 1974; Wilcock & Delaney, 1996). This km-scale circulation is manifest at the seafloor as discharging fluids carrying reduced chemical compounds that are a source of energy for unique ecosystems (Wilcock et al., 2018). There are two types of hydrothermal vents: focused vents in the form of black or white smokers (Edmond et al., 1995; Gamo et al., 1996), and diffuse vents that expel lower temperature fluids, but extend over larger and more scattered surfaces (Baker et al., 1993; Barreyre et al., 2012; Bemis et al., 2012). Focused vents (smokers), at temperatures commonly >300°C, form chimneys, sulfide mounds, and lateral flange structures (Tivey, 2007). Diffuse venting fluids show a wider range of temperatures, from a few hundred degrees, to near seawater temperatures (Barreyre et al., 2014b; Kinoshita et al., 1996; Little et al., 1988; Mittelstaedt et al., 2016; Pruis & Johnson, 2004; Scheirer et al., 2006; Schultz et al., 1992, 1996; Sohn, 2007; Tivey et al., 2002), and a larger panel of venting systems, depending of the substratum and on the distance to the sulfide mounds and smokers (Bemis et al., 2012).

On sulfide mounds, diffuse vents occur at flanges, bulbous chimneys called diffusers (Tivey, 1995) and in cracks of the sulfide structure (Barreyre et al., 2012; Embley et al., 1990; Glickson et al., 2007). Further from the smokers, diffuse fluids vent from cracks in lava flows (Butterfield et al., 2004; Mittelstaedt et al., 2016), in sulfide-rich detritic material (Sohn, 2007; Tivey, 2007), or, in the case of the Lucky Strike vents, in volcaniclastic deposits (Humphris et al., 2002; Langmuir et al., 1997). Diffuse fluids have also been described as venting from patches of seafloor, revealed by the presence of bacterial mats (Barreyre et al., 2012; Mittelstaedt et al., 2016), or through pelagic sediments (Little et al., 1988) Diffuse fluids vent at significantly lower rates than focused fluids. Estimated diffuse venting flow velocity ranges between 1 to 5 mm/s for diffuse vents hosting bacterial mats at the Lucky Strike vent field (Sarrazin et al., 2009), average 2 cm/s for fluids venting out of cracks, also at Lucky Strike (Cooper et al., 2000; Mittelstaedt et al., 2012), and up to 20 cm/s estimated for diffuse fluids at the ASHES vent field, Juan de Fuca Ridge (Rona & Trivett, 1992), against 20 to 330 $cm.s^{-1}$ for focused vents (Converse et al., 1984; Ginster et al., 1994; Mittelstaedt et al., 2012; Ramondenc

et al., 2006; Rona & Trivett, 1992). Diffuse venting fluids are important for their contribution to total hydrothermal heat fluxes with an estimated ratio of diffuse/total heat flux of up to 95% (Baker et al., 1993; Barreyre et al., 2012; Mittelstaedt et al., 2012; Ramondenc et al., 2006; Schultz et al., 1992), and for their role in hosting chemosynthetic life at temperatures that allow the growth of microbial and macrofaunal communities (Corliss et al., 1979; Cuvelier et al., 2009; Holden & Daniel, 2004; Jannasch & Mottl, 1985; Juniper et al., 1995).

Several mechanisms have been proposed for the formation of diffuse fluids at mid-ocean ridge black smoker type hydrothermal systems: mixing of primary hydrothermal fluids with seawater in the subsurface (Edmond et al., 1979, Butterfield et al., 2004; Kelley et al., 2002); conductive cooling (Cooper et al., 2000) of the primary fluids accompanied by mineral precipitation removing metals (Butterfield et al., 2004); or conductive heating of seawater in a substratum heated by high-temperature hydrothermal fluids circulating under a formation of low permeability (Cooper et al., 2000). The chemistry of diffuse fluids is variable, with evidence for the precipitation of sulfide, due to mixing with seawater (James & Elderfield, 1996), or to biological oxidation of H_2S (Butterfield et al., 2004; Koschinsky et al., 2002). Anhydrite and silica precipitation have also been documented (James & Elderfield, 1996; Tivey et al 1995; Fouquet et al 1994; Cooper et al., 2000). The chemistry of diffuse effluents has also been shown to be affected by microbial activity producing methane (Butterfield et al., 2004; Von Damm & Lilley, 2004) and organic species (Foustoukos et al., 2009).

Analytic and numerical models of black smoker type mid-ocean ridge hydrothermal systems, have helped understand these observations. Diffuse venting models have been scaled to the dimensions of individual hydrothermal sites (several tens to a few hundred meters), with a central domain of focused venting. The heat source is the conduit of high temperature and high flow rate end-member fluids, and the surrounding rocks are modelled as a continuous porous medium. These models reproduce the entrainment and mixing of seawater in the subseafloor (Larson et al., 2015; Lowell et al., 2003, 2012, 2015; Lowell & Yao, 2002), the conductive cooling or heating of end-member fluids or of seawater (Lowell et al., 2003), and the precipitation of minerals such as anhydrite (Guo et al., 2020; Lowell et al., 2003). Permeability, and the geometry of the heat source, are the main parameters in these models. Lowell et al. (2007) show that the formation of low temperature diffuse fluids (<150°C) requires that the permeability of the discharge zone be at least one order of magnitude larger than that of the surrounding rocks. High permeabilities, however, lead to the entrainment of large volumes of cold seawater, resulting in efficient cooling of the upwelling fluids, which is in conflict with in situ observations of high temperature focused vents (Andersen et al., 2015;

Coumou et al., 2008; Lowell et al., 2007). The precipitation of minerals such as anhydrite is proposed as a key mechanism to clog the permeability in domains of heated seawater, creating a low permeability shell around the conduit of high temperature end-member fluids and allowing for the simultaneous formation of black smokers and of lower temperature diffuse fluids (Guo et al., 2020; Lowell et al., 2003).

In this paper, we present the results of a 4 years monitoring study of diffuse and focused vent fluids temperature and chemistry at two representative vent sites of the basalt-hosted Lucky Strike hydrothermal field, Mid-Atlantic Ridge (Langmuir et al., 1993): The Tour Eiffel (TE) and White Castle (WC) sites (Figure 4-1). The Lucky Strike hydrothermal field hosts the long term EMSO-Azores observatory node (European Multidisciplinary Seafloor and water-column Observatory; (Best et al., 2016; Blandin et al., 2010; Colaço et al., 2011)). It includes 18 documented vent sites (Barreyre et al., 2012), each associated with the upflow of end-member hydrothermal fluids. Each vent site consists of a sulfide mound with several black smokers, set in a wider, semi-elliptical domain of diffuse venting. Tour Eiffel is one of the largest Lucky Strike vent sites, with a ~15m-high sulfide edifice; White Castle has a smaller, 3 m-high sulfide edifices.

The monitoring experiment we report on was carried out as part of the EMSO-Azores observatory and combines time series measurements of fluid temperature in venting fractures, diffuse patches, and black smokers at these two vent sites, fluid chemistry from repeated sampling of a selection of these venting locations, and time series of seafloor pressure, and near seafloor current direction and velocity. We place these results in their geological context based on high resolution mapping (Ondréas et al., 2009), photographic mosaics of the seafloor (Barreyre et al., 2012), and dive-observations using the remotely operated underwater vehicle (ROV) VICTOR 6000 (Simeoni et al., 2007), or the Nautile manned submersible. Our work documents the time and space variability of diffuse venting temperature and chemistry, the effect of tidal loading and currents, of subseafloor mixing, cooling or heating of end-member hydrothermal fluids and seawater, and of anhydrite precipitation or dissolution. Based on these results, we discuss the subseafloor processes that lead to the formation of diffuse effluents at the large and more mature Tour Eiffel site, and at the smaller and less mature White Castle site, and propose a conceptual geological model for the dynamics of vent site-scale, near surface, hydrothermal circulations at the basalt-hosted mid-ocean ridge Lucky Strike vent field, and how these characteristics affect estimates of hydrothermal heat fluxes, and the diversity of hydrothermal habitats.

4.2. Geological context

The Lucky Strike hydrothermal field (Langmuir et al., 1993) is located at the summit of a domal axial volcano, ~10km in diameter, at the center of the Lucky Strike segment of the mid-Atlantic ridge (Escartín et al., 2014; Humphris et al., 2002; Ondréas et al., 2009). With two exceptions not shown in Figure 4-1(the Ewan and Capelinhos sites described in Escartin et al., 2015), vents are distributed in and around a summit depression that is floored by a fossil lava lake (Fouquet et al., 1994; Ondréas et al., 2009). This depression is bound to the north and to the south by two cone-shaped volcanoes that formed on top of the larger domal axial volcano, prior to the activity of the lava lake (Humphris et al., 2002; Ondréas et al., 2009). The northern cone-shaped volcano is rifted in two; the southern cone-shaped volcano is more recent and, although faulted and fissured in its center, is not yet rifted (Figure 4-1). The extensively faulted and fissured domain that extends NNE-SSW in the center of both cone-shaped volcanos, is thought to have accommodated most of the recent plate divergence at this latitude (Escartín et al., 2014; Humphris et al., 2002; Miranda et al., 2005). Sheet lavas that filled the lava lake are mostly unfaulted, and therefore most recent (Ondréas et al., 2009). These sheet lavas also overlay a variably developed layered volcaniclastic formation, up to a few meters-thick, that rests on the pillows, lava tubes, and brecciated basalts that form the lower slopes of the two cone-shaped volcanos (Eissen et al., 2003; Ondréas et al., 2009).

One vent site (Sintra; Figure 4-1) is located on a hummocky bench (the hummocks correspond to extinct sulfide edifices; Ondréas et al., 2009) to the east of the fossil lava lake. Most other vent sites are located to the northwest, southwest and southeast of the fossil lava lake (Figure 4-1). The southwestern sites (White Castle included; Figure 4-1) all have small (<3 m-high) sulfide edifices. Tour Eiffel, one of the southeastern sites, has a massive, ~15 m-high sulfide edifice.

The heat source for hydrothermal activity at Lucky Strike, with an estimated energy flux of 200 to 1000 MW (Barreyre et al., 2012), is most likely an axial melt lens that has been detected with multichannel seismic data ~3-4 km beneath the seafloor (Singh et al., 2006). This reflector is ~2 km-wide in the across-axis direction and extends along axis ~7km, below the domal volcano (Combier et al., 2015; Crawford et al., 2010). Microseismicity recorded in 2007-2009 by the EMSO-Azores OBS (Ocean Bottom Seismometer) network (Crawford et al., 2013) suggests that thermal cracking associated with hydrothermal heat extraction, and to the base of hydrothermal downflow, occurs for the most part at depths of 2.5-3.5 km, and within 1-2 km to the north of the vent field, in a 1 km-wide ridge-parallel corridor that corresponds with the extensively fractured NNE-SSW domain in Figure 4-1 and extends beneath the fossil lava lake.

Numerical models that incorporate a higher permeability and higher magmatic heat flux in this narrow corridor (Fontaine et al., 2014) reproduce this configuration, further supporting the interpretation of a mostly along-axis, main hydrothermal circulation mining heat from near the AML depth. Source P, T conditions were characterized using the Si-Cl geothermobarometer (Fontaine et al., 2009) on black smoker fluids, showing supercritical conditions for all venting sites at ~440°C and 2600 mbsf (Chavagnac et al., 2018), consistent with the depth of microseismic events (Crawford et al., 2013).

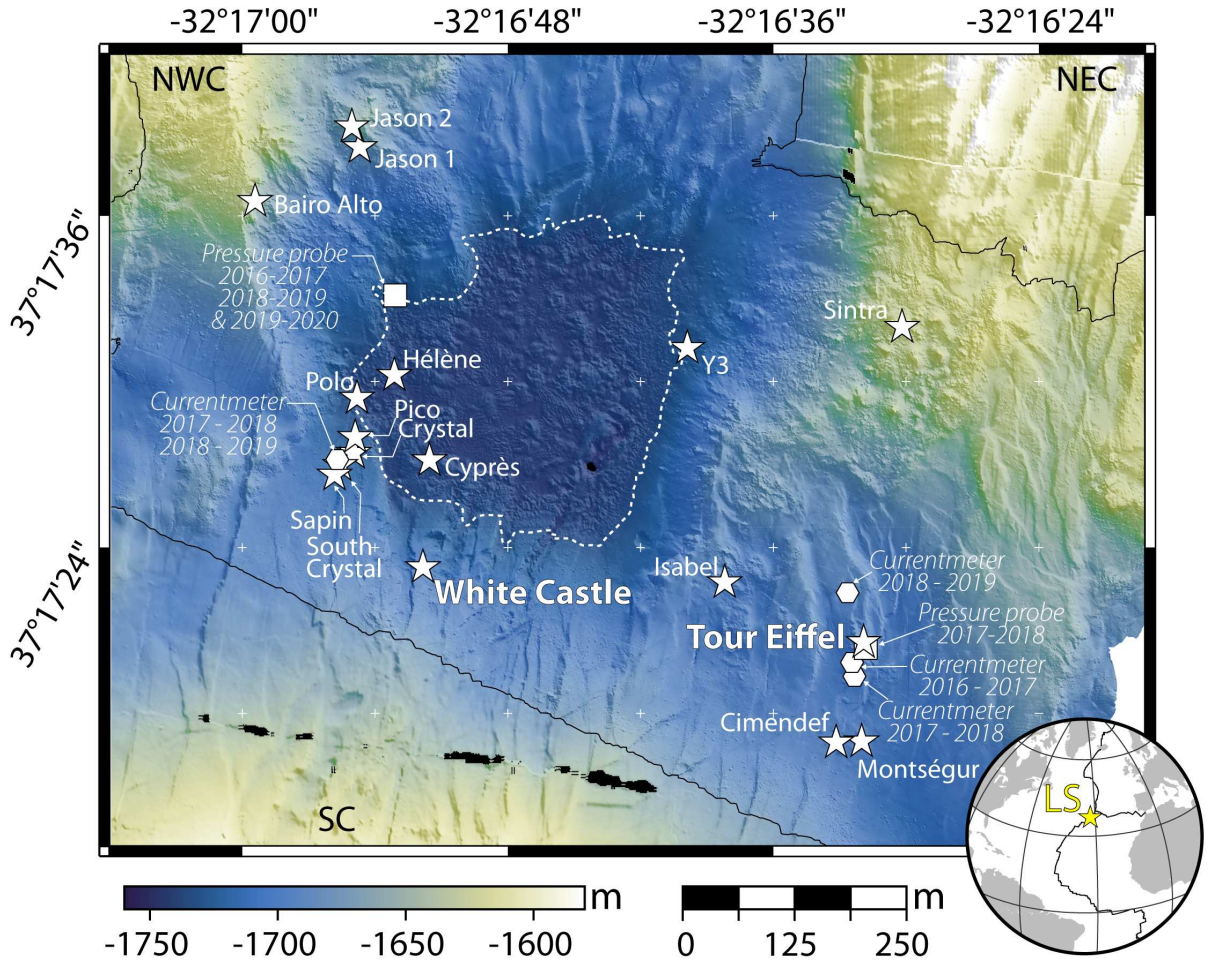

Figure 4-1 – Map of the Lucky Strike hydrothermal field (LSHF). High resolution bathymetry from Ondréas et al., 2009 and Escartin et al., 2015. Hydrothermal sites (white stars), including the 2 sites studied here (Tour Eiffel and White Castle) are distributed around a fossil lava lake (white dotted line). Also shown are the location of currentmeters (diamonds), and pressure probes (squares) used in the 2016-2020 monitoring experiment. NWC: Northwest Volcanic Cone; NEC: Northeast Volcanic Cone; SC: South Volcanic Cone.

The distribution of vent sites at the Lucky Strike hydrothermal field suggests that shallow faults act as permeable pathways for hydrothermal fluids in the near seafloor substratum (Barreyre et al., 2012; Humphris et al., 2002). A two-layer circulation domain, with a more permeable extensively faulted upper few hundred meters, is supported by seismic modelling (Arnulf et al., 2014), and has been used to propose a poroelastic model using the observed phase

lag between focused venting fluid temperature and tidal pressure in the time-series record of Lucky Strike smokers to estimate the effective permeability of the extrusive/intrusive layers (Barreyre et al., 2014a; Barreyre & Sohn, 2016; Barreyre et al., 2018).

Black and white smokers at the Lucky Strike vent fluids at temperatures ranging from 175°C at the Sintra site in the near extinct northeastern venting area, to 364°C at the Crystal site (Barreyre et al., 2014b; Charlou et al., 2000; Chavagnac et al., 2018; von Damm et al., 1998; Langmuir et al., 1993; Pester et al., 2012). These hydrothermal fluids have high concentrations in barium compared with other black smoker vent fields in the Atlantic, a characteristic that is interpreted as due to a hot spot influence on the composition of the basaltic crust at Lucky Strike (Charlou et al., 2000; Langmuir et al., 1993). Lucky Strike end-member fluids also have lower concentrations in alkaline and metallic elements relative to other Mid Atlantic Ridge vent fields. This was initially interpreted as a result of having a highly altered basaltic reaction zone derived from a long history of hydrothermal activity (Charlou et al., 2000; von Damm et al., 1998; Langmuir et al., 1997). Following the sampling of more metal rich focused fluids at the recently discovered Capelinhos site, Chavagnac et al. (2018) proposed an alternative interpretation, calling for higher rates of metal deposition in the substratum of the other Lucky Strike sites. Substantial sulfide precipitation in the sub seafloor is also suggested by the wide range of Se contents measured in copper-sulfide deposits at Lucky Strike focused vents (Rouxel et al., 2004a).

Lucky Strike diffuse fluids have been less extensively studied than the focused fluids. Barreyre et al. (2012, 2014b) provided a detailed field-scale map of diffuse venting areas, and distinguished, from diffuse temperature time series, between low (<10°C) and intermediate temperature (>10°C) diffuse vents. Cooper et al. (2000) sampled diffuse fluids from several Lucky Strike vent sites with the Medusa flow velocity and temperature tool (Schultz & Elderfield, 1994). They proposed an origin of these fluids by mixing of less than 7% endmember fluid, with conductively heated seawater, thus calling for a site-scale shallow secondary hydrothermal circulation (Cooper et al., 2000). Site-scale circulation involving seawater is also supported by the large range of $\delta^{34}S$ values measured in sulfide deposits, with the higher $\delta^{34}S$ values reflecting a contribution of reduced seawater sulfate, part of which may be associated to bacterial activity (Rouxel et al., 2004a, 2004b).

4.3. Data and methods

4.3.1. Dive observations

We use video images from 27 ROV VICTOR 6000 dives and 5 HOV Nautile dives, carried out during the 2016 to 2020 EMSO-Azores maintenance cruises. These videos allow us to identify changes in the geology or in the distribution of the fauna from one year to the next, and to document instrument deployment and recovery, and fluid sampling operations. In addition to high-resolution bathymetry (Ondréas et al., 2009), and video images, we use two sets of high resolution georeferenced photomosaics to relocate the sampling and monitoring sites. Both sets were acquired with the OTUS (Simeoni et al., 2007) camera of the ROV Victor 6000, in black and white for complete coverage of the field acquired in 2008-2009 (Barreyre et al., 2012), and in color for a partial coverage of the TE and WC sites acquired in 2018.

4.3.2. Fluid sampling and fluid chemistry

Fluid temperature is measured with the ROV or Nautile probe prior to sampling. A 200 mL titanium gas-tight sampler with a syringe was used to sample focused fluids. A bell-shaped, partly transparent sampler (Figure 4-2) was used for most diffuse fluids (a syringe was used for a few samples; Table 4-2): sampling is triggered when shimmering fluids have filled the bell and pushed ambient seawater out. This ensures minimum mixing with ambient seawater. Two samples are taken consecutively whenever possible to assess the short-term variability of the fluid chemical composition. Fluid samples are filtered (0.45 μm Millipore filters), and transferred into aliquots to be stored at 4°C on board the ship. Salinity, conductivity, pH, and reduction potential Eh are also measured on board. Shore-based analyses are performed at the Geosciences Environment Toulouse (GET) laboratory. Ca, Na, K, Mg, Si, Fe, Mn and Li concentrations were determined with an inductively coupled plasma atomic emission spectrometer (ICP-AES) Horiba Ultima2 instrument. Cl, Br, and SO4 are measured using a technique called High Precision Ion Chromatography (HP-IC). The instrument is calibrated using mono elemental solutions, multi elemental solutions, and IAPSO standard solution (Besson et al., 2014). Analytical precision is better than 2%. The composition of end-member hydrothermal fluids is recalculated by linear extrapolation to zero-Mg from the 4 samples made at each site each year using the least-squares regression method (Von Damm, 1988).

Near bottom seawater concentrations of Mg, Na, Cl, Ca, SO4, K and Br were obtained from near seafloor CTD casts within 100m of the Tour Eiffel and White Castle vent sites. For other elements, we used (Millero et al., 2008) as a seawater chemical composition reference.

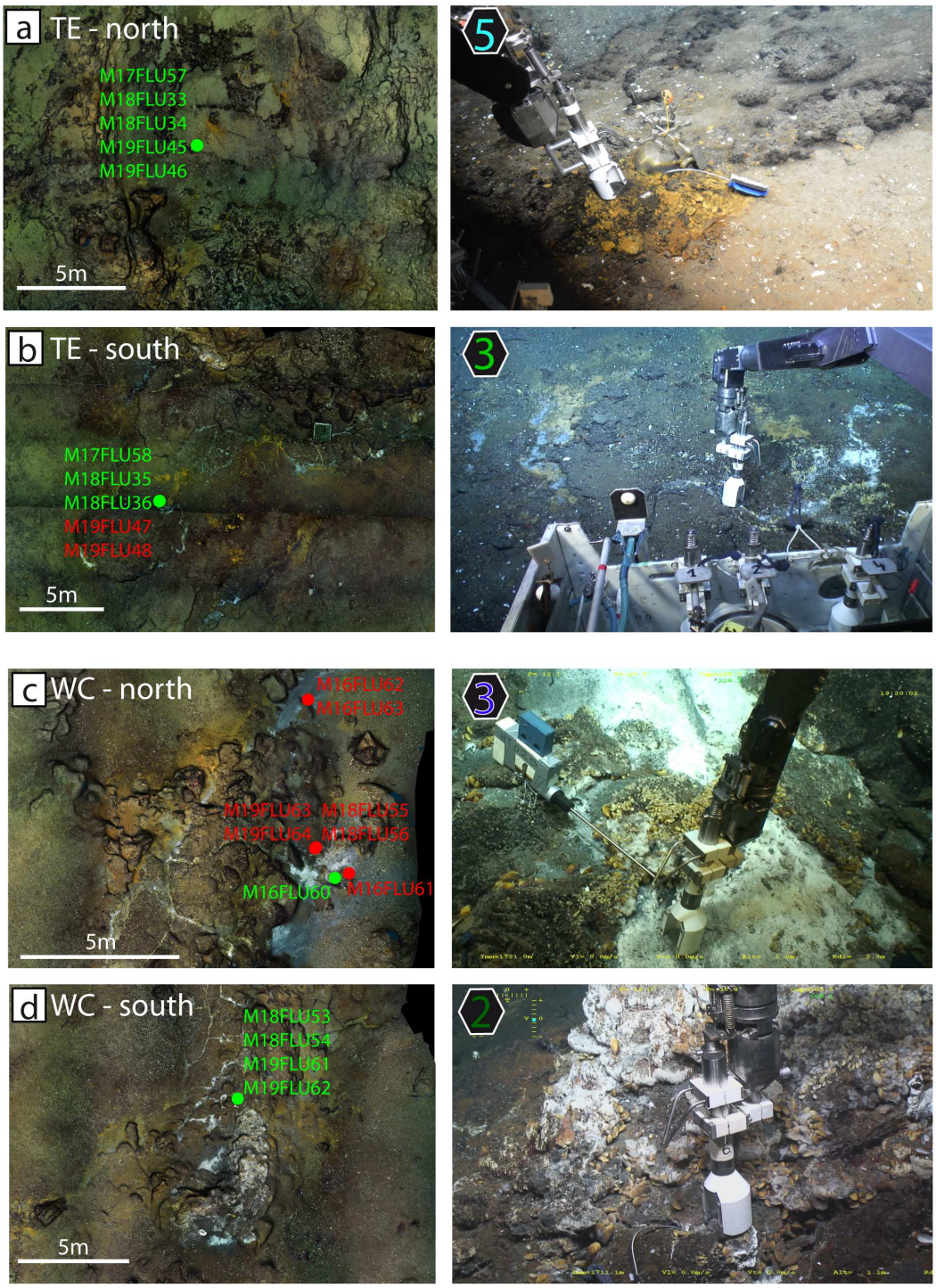

Figure 4-2 – Diffuse fluids sampling at 4 temperature monitoring locations shown in the Tour Eiffel (TE) and White Castle (WC) maps of Figure 4-4. Details of mosaic of OTUS seafloor photographs (left panels) and ROV video snapshots (right panels). Sample numbers (Table 4-2) are shown in green when sampling was performed within 1 m of a functional autonomous temperature probe, and in red if performed >1m away. (a) TE-5 monitoring location (north of Tour Eiffel), bell-shaped fluid sampler collects fluids at vent nested in yellow Fe-oxidizing bacterial mats. (b) TE-3 monitoring location (south of Tour Eiffel), bell-shaped fluid sampler collects fluids at crack hosting mussels and white bacterial mats. (c) WC-3 monitoring location (north of White Castle), bell-shaped fluid sampler collects fluids over white diffuse venting area, near the edge of sulfide-indurated, mussel-hosting, slab formation. d) WC-2 monitoring location (south of White Castle) bell-shaped fluid sampler collects fluids at crack near base of sulfide mound.

4.3.3. Times series data acquisition

4.3.3.1. Fluid temperature

Fluids temperature time series were obtained with autonomous temperature probes, placed into venting orifices, cracks, or diffuse patches. We used five types of temperature probes (Figure 4-3, a to h), high-temperature WHOI-MISO probes (HTW), and their newer version (HTWN, MISO 1010 Hi-Temperature vent fluid and attitude data logger), high-temperature NKE probe (HTNKE), low temperature WHOI-MISO probes (LTW) and in-house low temperature probes (LTGrad) made of two iButton® (DS1922L) temperature sensors from Maxim Integrated in small titanium housings distant by 7 cm, designed to evaluate the temperature gradient in sandy diffuse patches. HTW, HTNKE and LTW have been described in Barreyre et al. (2014). HTW and HTWN record temperatures up to 450°C. HTW contain 2 J-type thermocouples and their data loggers, one with an accuracy of $\pm 2.5°C$ and a resolution of 0.21°C, and one with a resolution of 0.024°C, and an accuracy of $\pm 0.21°C$. HTWN have a logger resolution of 0.03°C and a logger accuracy of $\pm 0.6°C$. HTNKE probes can record temperature up to 450°C with a resolution of 0.1°C and an accuracy of $\pm 0.5°C$. LTW probes loggers can record temperature of up to 125°C with a resolution of 0.14°C at 25°C and with an accuracy of $\pm 0.53°C$ at 50°C. iButton probes can record temperate of up to 125°C with a resolution of 0.5°C and an accuracy of $\pm 0.5°C$ at 65°C. We use data from 28 successful 1-year temperature probe deployments. 16 deployments covering a total of 4 years (2016-2020) at vents TE-1 to TE-5 for the Tour Eiffel vent site, and 9 deployments covering a total of 3 years (2016-2019) at vents WC-1 to WC-3 at the White Castle site (Table 4-1). The logger clock and the recorded temperature were checked on board before each deployment. Data and metadata for each deployment (sampling intervals, time of deployment and recovery, clock drift) are available on the EMSO-Azores data portal (Cannat et al., 2018a, 2020a, 2021a, 2021b).

4.3.3.2. Seafloor pressure

Seafloor pressure time-series for 2016-2017 and 2018-2020 were recorded with a SBE 53 Bottom Pressure Recorder (Seabird Scientific) deployed on a benchmark called JPPW near the northwest shore of the fossil lava lake (Figure 4-1; instrument shown in Figure 4-3i). In 2017-2018 this probe was not deployed and we use data from the SBE 54 Tsunami Pressure Sensor (SBE54; Seabird Scientific), a component of the EGIM (EMSO Generic Instrument Module) deployed near the TE site (Figure 4-1). The SBE53 has an accuracy of 0.6 psia and a resolution of 0.0004 psia and was deployed with a sampling interval of 2 minutes. The SBE54 has an accuracy 0.6 psia and a resolution of 0.0011 psia and was deployed with a sampling interval of

15 minutes. The autonomous clock of each probe was checked before deployment, and clock drift was calculated on board after recovery. Data and metadata (sampling frequency, time of deployment and recovery, clock drift, etc.) are available for 2019-2020 on the EMSO-Azores data portal (Ballu et al., 2021; Sarradin et al., 2018). (note to editor: seafloor pressure data for other years are being put online now, we will provide a DOI in the revised version of this manuscript).

4.3.3.3. Current direction and velocity

Two TCM-3 bottom currentmeters by Lowell Instruments LLC were used to record bottom current direction and velocity within 200 m of the TE and WC sites (Figure 4-1). TCM-3 instruments are made of a buoyant housing hosting the logger, a magnetometer, and an accelerometer. The buoyant housing is tied to a ballast (Figure 4-3j) and its orientation and tilt are used to calculate current direction and velocity, based on factory calibration. Measurements are made in bursts of 15s spaced by 1 mn, with a sampling rate of 8 Hz during the burst. The magnetometer has an accuracy of +/- 1° and a resolution < 0.001 Gauss, the accelerometer has an accuracy < 0.01g and a resolution < 0.001g. For current velocities < 5 cm/s, uncertainties for the direction of the current are larger than the nominal accuracy of the magnetometer. The autonomous clock of the probe is checked before deployment, and clock drift is calculated on board after recovery. Data and metadata (sampling frequency, time of deployment and recovery, clock drift, etc.) are available on the EMSO-Azores data portal (Cannat et al., 2017, 2018b, 2020b).

	Tour Eiffel			White Castle			
	Temperature	Monitoring site	Current	Temperature	Monitoring site	Current	Pressure
2016-2017	HTWN012	TE-1	TCM3-3	HTWN013	WC-1	x	SBE53 106234
	LTW020	TE-2		HTNKE29016	WC-2		
	LTW003	TE-3					
	LTW018	TE-5		HTWN020	WC-3		
2017-2018	LTW013	TE-2	TCM3-1	HTW008	WC-1	TCM3-3	SBE54 54-049
	HTNKE29012	TE-3		HTNKE30001	WC-2		
	LTW040	TE-4					
	LTW018	TE-5		HTWN011	WC-3		
2018-2019	HTW019	TE-1	TCM3-3	HTW014	WC-1	TCM3-1	SBE53 106234
	HTNKE30001	TE-2					
	HTNKE29008	TE-3		HTNKE29016	WC-2		
	HTNKE29009	TE-4					
	HTNKE29012	TE-5		HTWN019	WC-3		
2019-2020	HTNKE30014	TE-4					SBE53 106220
	HTNKE38003	TE-5					
	LTGrad4	TE-5					

Table 4-1 – EMSO-Azores observatory data used in this study: names of the instruments (temperature probes, currentmeters and pressure probes) for each deployment year and monitoring site.

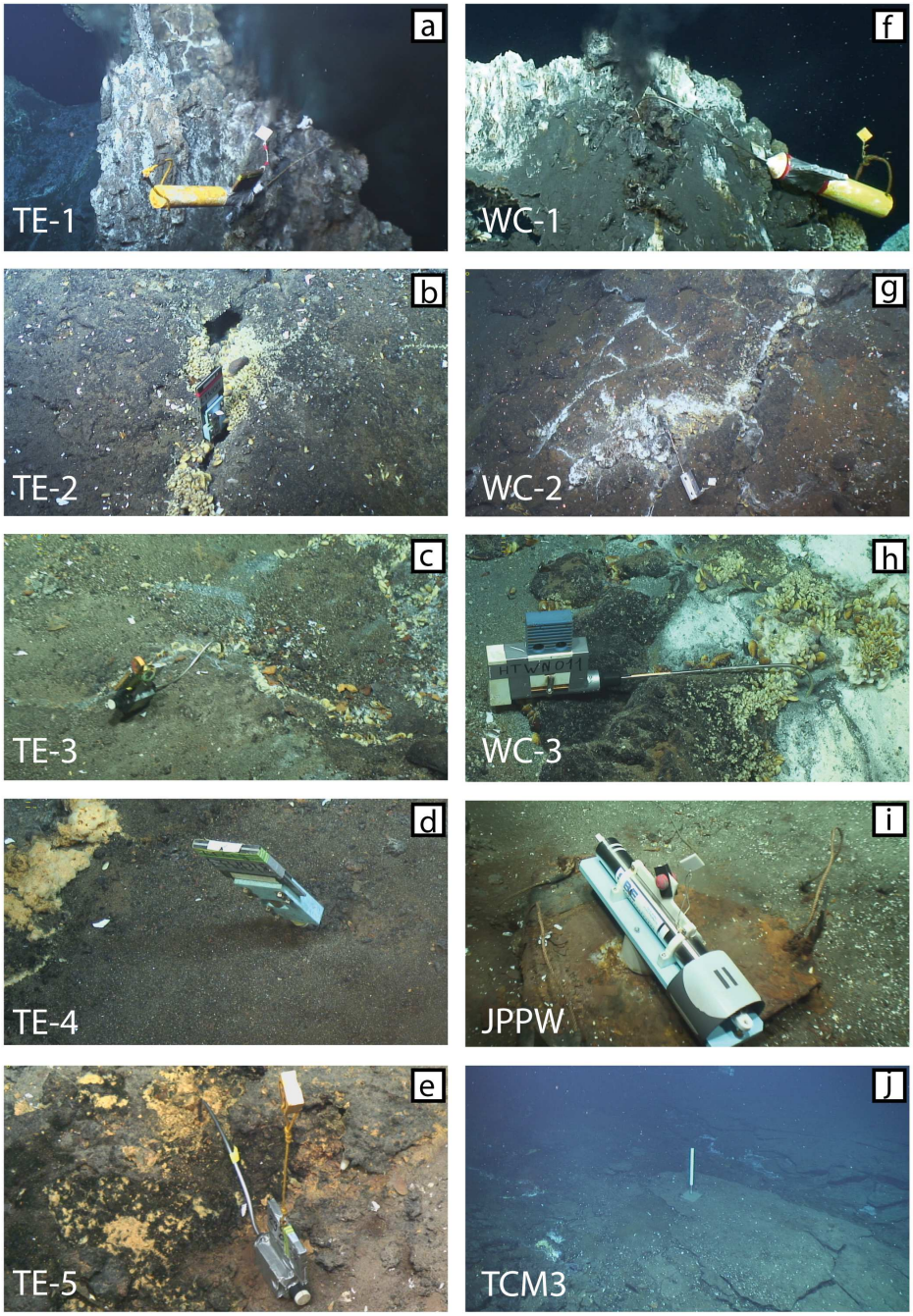

Figure 4-3 – ROV video snapshots showing examples of the temperature probes (a to h; see location in the Tour Eiffel and White Castle maps of Figure 4-4), pressure probes (i), and currentmeters (j) deployed at the LSHF as part of our monitoring experiment. (a) high-temperature WHOI (HTW) probe deployed in 2017 at focused vent (monitoring location TE-1). (b) low-temperature WHOI (LTW) probe deployed in 2017 in crack of sulfide-indurated slab (monitoring location TE-2); note bacterial mats and mussel assemblage. (c) high-temperature NKE (HTNKE) probe deployed in 2018 in mussel-lined crack of non-indurated slab (monitoring location TE-3). (d) LTW probe deployed in 2017 in brownish sandy area next to yellow iron-oxidizing bacterial mats (monitoring location TE-4). (e) LTW probe deployed in 2018 in vent nested in yellow iron-oxidizing bacterial mats (monitoring location TE-5). (f) HTW probe deployed in 2017 at focused vent (monitoring location WC-1). (g) HTNKE probe deployed in 2016 in crack in sulfide-indurated slab (monitoring location WC-2). (h) new high-temperature WHOI (HTWN) probe deployed in 2017 in sandy area next to sulfide-indurated slab (monitoring location WC-3); note mussels on slab material and white barite precipitates and bacterial mats in sandy diffuse venting area. (i) SBE53 pressure probe deployed in 2018 at the JPPW benchmark (Figure 4-1). (j) TCM3 currentmeter deployed in 2016 on non-indurated layered volcaniclastics (slab) to the south of Tour Eiffel (Figure 4-1).

4.3.3.4. Processing of time-series data

After recovery of the instruments, all time-series are plotted and checked visually for data gaps, and outliers. The clock drift correction is applied, assuming a linear drift. Spectral analysis of the recorded time-series is performed using the multi-taper method described by Thomson (1982) with adaptive weighting (Percival & Walden, 1993). This method has been used, and is described, in previous studies of the Lucky Strike vent temperature time series (Barreyre et al., 2014b; Barreyre & Sohn, 2016). We focused our study on the time variability of the power spectral density (PSD), coherence and phase lag at the semi-diurnal M2 frequency between fluid temperature, seawater pressure head and bottom current velocity. We used a sliding time window of 30 days, with a 1 days sliding time and a time bandwidth product of NW=4 (Thomson, 1982). Phase lag estimates are considered statistically robust for time periods with coherence > 0.75.

4.4. Geology and the distribution of diffuse vents at the Tour Eiffel and White Castle hydrothermal sites

Figure 4-4 shows 3D (a and c) and plan (b and d) views of the TE and WC sites. For TE, mapping of the outer limits of the site, and of the main venting areas, is adapted from Barreyre et al. (2012) and (Mittelstaedt et al., 2012). Both sites consist of a sulfide mound with several focused vents (smokers; Figure 4-3a and f), a wider domain of sulfide deposits and sulfide indurated volcaniclastic deposits (Figure 4-5a), and an outer domain of non-indurated to slightly indurated volcaniclastic deposits (Figure 4-5b). These deposits are commonly degraded into a sandy material (Figure 4-5b) and are made of layered hyaloclastites (Figure 4-5c), with scoriaceous horizons (Dias et al., 2008; Yves Fouquet et al., 1994). They are up to 1.5 m-thick and rest on brecciated basalts (Figure 4-5c and e). The sulfide, silica and barite indurated volcaniclastic deposits have been referred to as the "slab formation" (Yves Fouquet et al., 1994). They are made of clasts of basalt, basalt glass, plagioclase crystals, barite and sulfur grains, cemented by amorphous silica and barite (Costa, 2014; Yves Fouquet et al., 1994; Langmuir et al., 1997). The slab acts as a cap through which fluids can only vent via cracks (Figure 4-5a). Cracks in the slab formation, and in the non-indurated volcaniclastic formation (Figure 4-4b) are commonly associated with tilting and with local, meter-scale swelling or collapse of the ground, probably due to anhydrite precipitation or dissolution in the shallow substratum, as proposed for the TAG hydrothermal field (Humphris et al., 1995b). The faulted terrane to the northwest of TE shows an extinct site (Figure 4-4a), with broken sulfide chimneys and

depressions up to 15 m across and 2 m-deep, that we interpret as due to dissolution of the anhydrite that had formed in the shallow substratum when the site was active.

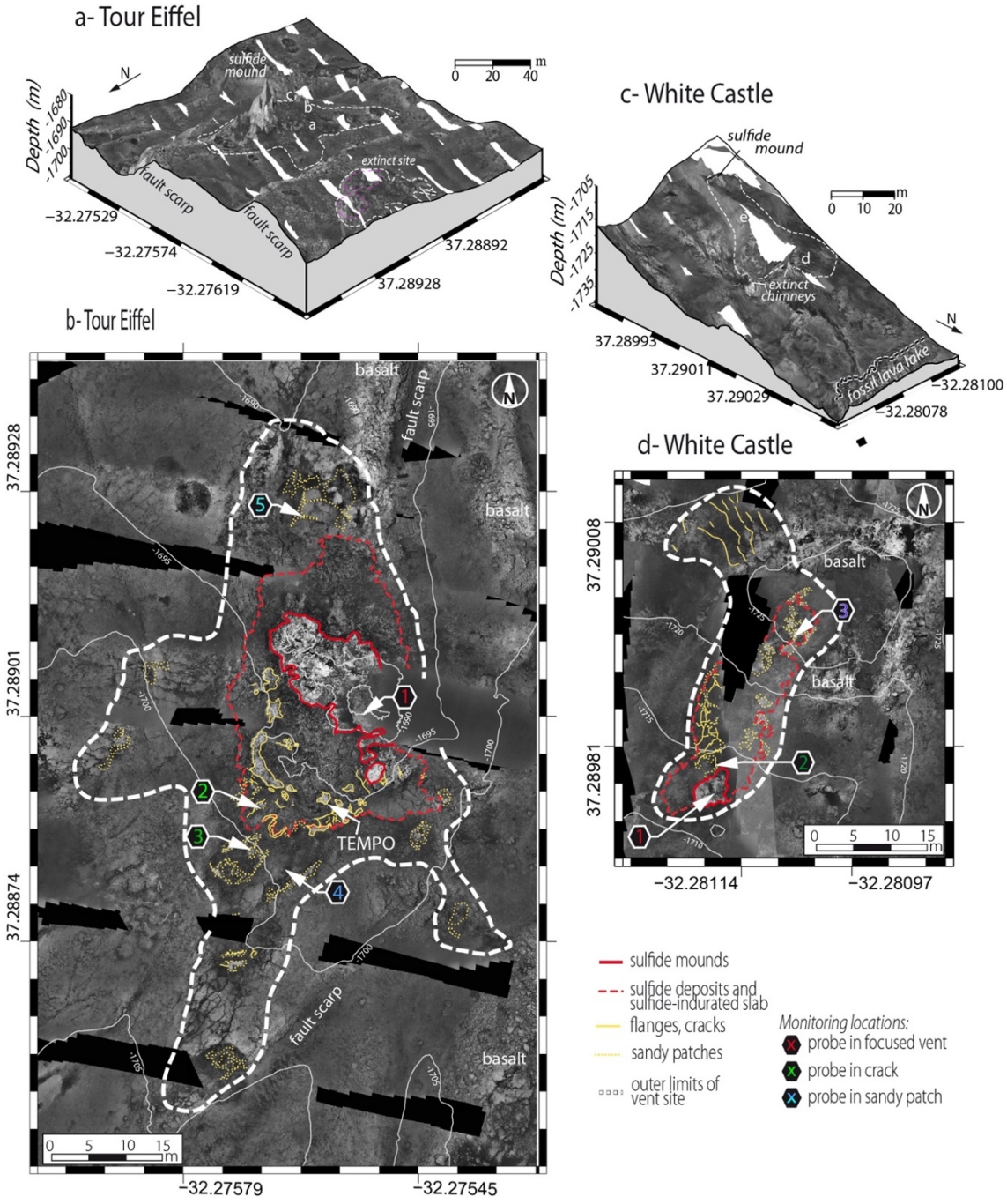

Figure 4-4 – Geological setting of the Tour Eiffel (TE), and White Castle (WC) hydrothermal sites. (a) and (c) 3D views of photomosaic draped over HR bathymetry; (b) and (d) map views with temperature monitoring locations shown by numbers in hexagons: red for focused vents, green for diffuse venting cracks, and blue for diffuse venting sandy patches; TEMPO is an ecological monitoring module. In these maps, TE and WC are shown at the same scale. White dashed line is outer contour of sites; other contours, see legend; (a) 3D view of photomosaic at the TE site; a, b, and c letters refer to location of ROV video snapshots in Figure 4-5; dashed white line is outer contour of the active TE site, and of an extinct site to the west, with two elliptical depressions (dashed pink lines) interpreted as collapsed areas after anhydrite dissolution. (b) map view of photomosaic at TE site, modified from Barreyre et al. (2012); (c) 3D view of photomosaic at the WC site; d letter refers to location of ROV video snapshot in Figure 4-5; dashed white line is outer contour of site; double dashed white line is outer limit of fossil lava lake; (d) map view of photomosaic at WC site.

TE (Figure 4-4, a and b) is a mature venting site with a ~15m-high sulfide mound. It is located on top of a N to NNW-trending, 2 to 24 m-high east-facing fault scarp (Figure 4-4a). The TE sulfide mound is set in a 35x25m elliptical domain of indurated slab with small sulfide chimneys and flanges (Figure 4-4b; Girard et al., 2020). The outer limits of the TE site, defined so as to enclose all nearby active diffuse venting areas (Figure 4-4b), extend up to 90 m along the fault scarp. The substratum of the TE site is, as for the WC site, made of a thin (0 to 1.5 m-thick) formation of layered volcaniclastic deposits, over variably brecciated basalts pillows (Figure 4-5c and e). Diffuse fluids vent from flanges and cracks, feeding mussels, arthropods, echinoderms, crustaceans (Cuvelier et al., 2009; Dover et al., 1996) and bacterial mats (Crépeau et al., 2011; Sarradin et al., 1999). Domains of thick (> 30 cm) sulfide indurated slab have meter-spaced cracks, a few cm-wide, that host small size mussels and bacterial mats (monitoring location TE-2; Figure 4-3b, 5a and 6a). Diffuse vents in domains of thinner indurated slab, and in non-indurated volcaniclastic deposits include narrower mussel lined cracks (monitoring location TE-3; Figure 4-3c and 6a), and diffuse patches hosting white bacterial mats and small mussels. Most diffuse vents are located in the southern regions of the site. In the non-indurated volcaniclastic deposits north of the TE site, a network of sinuous cracks vents shimmering waters (monitoring location TE-5; Figure 4-3e and 4b) and is lined with yellowish Fe(II)-oxidizing bulbous bacterial mats and ferruginous crust. Similar sinuous cracks lined with yellowish bacterial mats and ferruginous crust occur in the brownish sandy volcaniclastic deposits in the west and south of the TE site. In the south, these are found within meters of white bacterial mats and mussels hosting cracks and patches (Figure 4-6a). Monitoring location TE-4 (Figure 4-3d and 6a) is set in such a brownish sandy domain, where there is no visual evidence of venting. Over the 3 years of the experiment, we did not observe major changes in venting and faunal assemblages at and near monitoring locations TE-3, TE-4 and TE-5. At TE-2, a decrease in white mineral deposits and bacterial mats around the cracks was observed since 2016.

The WC site (Figure 4-4c and d) is set in in a ~30m long elliptical volcanic depression, in the extensively fissured northern slopes of the southern cone-shaped volcano (Figure 4-1), and only 50 m to the south of the fossil lava lake shores (Figure 4-4c). The 3 m-high WC sulfide mound is located on the southern rim of the elliptical depression (Figure 4-4c and 6b). The indurated slab domain at WC extends downslope to the north of the sulfide mound, and to the bottom of the depression (Figure 4-4d and 5e). The slab is fractured, and also forms isolated panels, 1-3 m across, particularly in the lower slopes (Figure 4-5e). These slab panels are surrounded by a grey sandy substrate (Figure 4-5e) made of disaggregated volcaniclastic

deposits with variable proportions of sulfide and anhydrite. Similar yet less extensive domains of grey sandy substrate are also seen along the outer limit of the slab at TE (Figure 4-5b). At both WC and TE, these grey domains vent slowly oozing fluids and host hydrothermal fauna (polychaetes, gastropods and/or isolated small mussels). They are locally capped by a thin (1-3 mm) white barite precipitate (Figure 4-3h and 5e). These grey domains pass laterally to the brownish sandy domains (no visual evidence for fluid venting; Figure 4-5b and e). The outer limits of the WC site, enclosing all active diffuse venting areas, also include a set of radial cracks lined by orange iron oxidizing bacterial mats and ferruginous crust (Figure 4-5d). These resemble the cracks observed at TE (Figure 4-3d and e), but there is no visual evidence for fluid venting at the WC cracks.

.

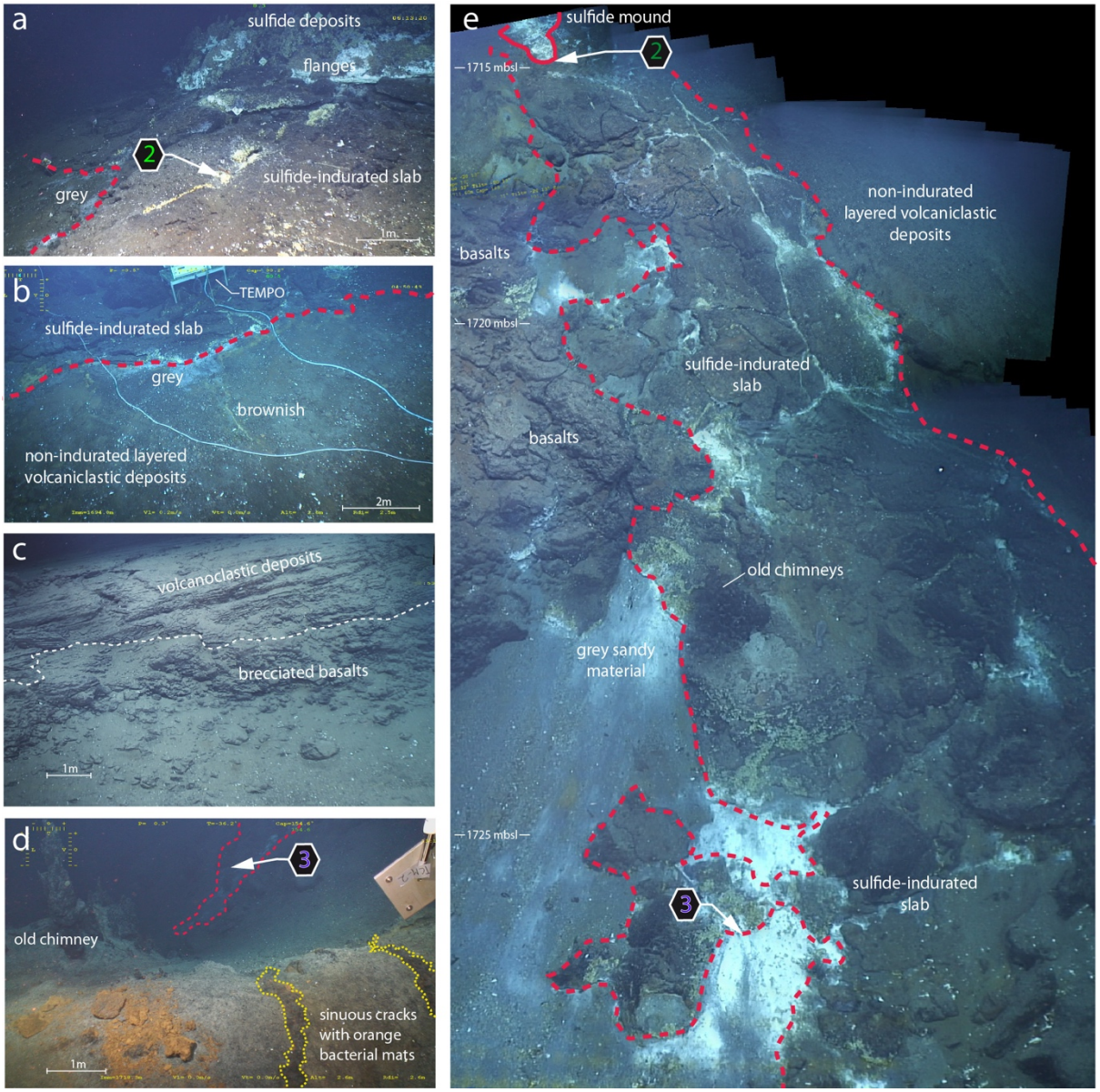

Figure 4-5 – ROV video snapshots at and near the Tour Eiffel (TE), and White Castle (WC) sites. Location of snapshots in Figure 4-4a and c. Scales are indicative. (a) view to NNE over monitoring location TE-2 (mussel-lined venting crack in sulfide-indurated slab), note small sulfide mound in background with white barite deposits and bacterial mats; red dashed line is limit to non-indurated slab, as in Figure 4-4b; (b) view to the north showing the ecological module TEMPO (and connecting cables) at the edge of the sulfide-indurated slab (red dashed line), with non-indurated slab (layered volcanoclastic deposits) in foreground (c) view to the west over minor fault scarp exposing the brecciated basalt basement of the TE site, with layered volcanoclastic deposits (non-indurated slab) on top; (d) view to the south over the edge of the WC depression, fissures lined with brown-yellow bacterial mats in sandy volcaniclastic formation; (e) view to the south over monitoring locations WC-2 and WC-3, photomosaic of ROV video snapshots covering depths of 1713 to 1727 mbsl. Red line is limit of WC sulfide mound, and red dashed line is limit of sulfide-indurated slab, with small extinct sulfide chimneys, as in Figure 4-4. Note brecciated basalt basement to the left, non-indurated layered volcanoclastic deposits to the right, network of venting fissures lined by mussels and white bacterial mats in indurated slab, and grey to brown sandy material with patches of white barite precipitates in the lower slopes.

Similar to what we observed at TE, diffuse fluids at WC vent in mussel-lined cracks and flanges in the sulfide mound, and in centimeter to decimeter-wide cracks in the indurated slab (Figure 4-5e). Decimeter-wide cracks open onto a grey substrate with slowly oozing fluids, similar to that observed in the lower slopes (Figure 4-5e). Several cracks connect to the sulfide mound (Figure 4-6b) and locally host white smokers with decimeter-sized sulfide chimneys (Figure 4-3g and 6b). Over the monitoring period, we observed a horizontal growth of the sulfide mound by close to 2 m toward the north, over the fissured slab. Monitoring location WC-2, in a venting crack in the slab, was moved further north along the same crack in 2017 because its 2016 location had become part of the sulfide mound (Figure 4-6b). Downslope to the north, diffuse vents occur in the grey sandy material beneath (monitoring location WC-3; Figure 4-3h) and within a few meters, of the slab fragments. Between 2016 and 2018, a mm-thick white barite precipitates had formed an impermeable cap to fluids oozing through the grey sandy material next to monitoring location WC-3 (Figure 4-3h). This cap was broken to insert the temperature probe.

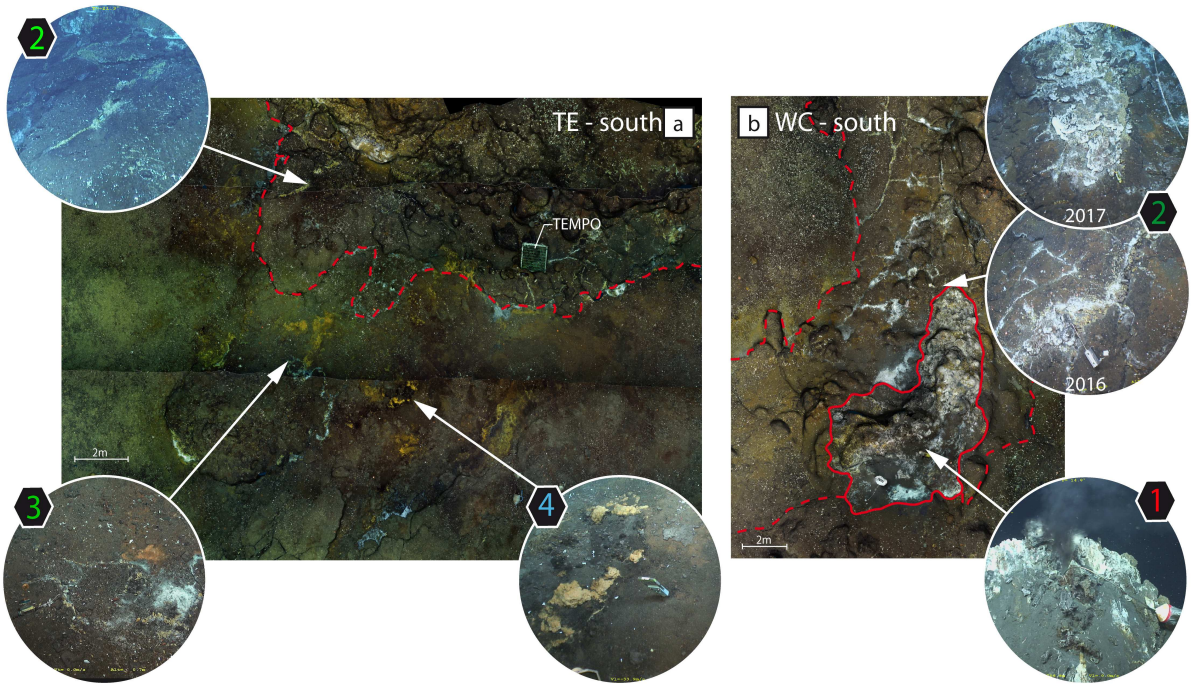

Figure 4-6 – High-resolution OTUS photomosaics (acquired in 2018) for the southern part of Tour Eiffel (TE) and White Castle (WC) sites, with ROV video snapshots of monitoring sites TE-2, TE-3, TE-4, WC-1 and WC-2. Red lines (dashed and plain) as in Figure 4-4b and d. (a) south TE. Note white barite and bacterial mats on sulfide deposits north of TE-2 mussel-lined crack, square frame that hosts the TEMPO ecological module, array of fine mussel-lined cracks at TE-3, yellow bacterial mats just west of TE-4, and corresponding orange patches in the OTUS photomosaic. (b) south WC. Note black smoker at WC-1, location of WC-2 in crack near base of WC sulfide mound, with northward growth of this mound between the 2016 and 2017 probe deployments (WC2 snapshots look south over the same area).

TE	°C			mmol/L	mmol/L	mmol/L	mmol/L	µmol/L	µmol/L	µmol/L	µmol/L	mmol/L	mmol/L	µmol/L	mmol/L	µmol/L	µmol/L		mV	mmol/L	
Year	**Temp (ROV)**	**Sample name**	**Position**	**Mg**	**Si**	**Na**	**Cl**	**Mn**	**Fe**	**Cu**	**Zn**	**Ca**	**SO_4**	**Ba**	**K**	**Sr**	**Br**	**pH**	**E_h**	**H_2S**	**P(%).[Mg/Si]**
2019	60	**M19FLU47#**	TE-3	55.219	0.188	483.220	550.204	2.950	*bdl*	*bdl*	0.396	12.313	28.320	0.390	11.314	77.162	906.635	6.820	133.000	0.656	-0.0590
	60	**M19FLU48#**	TE-3	53.701	0.168	494.601	549.393	2.094	*bdl*	*bdl*	0.291	12.380	28.290	0.308	11.424	75.224	902.777	6.830	132.000	0.513	9.6814
	55	**M19FLU45**	TE-5	52.108	1.700	480.622	549.533	15.233	*bdl*	*bdl*	0.331	15.472	30.801	0.553	11.116	84.800	898.733	7.110	125.000	1.568	0.0428
	326	**M19FLU25-28**	**TE-1**	**0.000**	**13.951**	**345.200**	**432.932**	**158.844**	**391.250**	***bdl***	**0.127**	**42.660**	**0.014**	**11.983**	**22.327**	**71.231**	**724.637**	**3.798**	**-28.250**	**10.061**	
2018	51.6	**M18FLU35**	TE-3	44.730	0.084	446.658	542.965	1.287	0.035	0.008	0.018	11.153	28.248	0.249	9.784	116.522	483.857	7.180	48.000	9.976	-0.5190
	51.6	**M18FLU36**	TE-3	45.985	0.523	444.164	504.633	8.385	0.138	*bdl*	0.101	12.087	25.654	0.375	10.002	117.750	449.178	6.260	-99.000	0.180	2.8676
	54	**M18FLU33**	TE-5	45.262	0.653	441.577	538.701	25.309	*bdl*	0.267	*bdl*	15.519	30.759	0.975	10.016	139.753	481.159	6.970	102.000	5.700	3.9078
	54	**M18FLU34**	TE-5	44.749	0.675	452.389	528.930	27.758	0.066	0.157	0.338	15.680	30.505	0.981	9.822	140.294	472.969	6.950	5.000	1.012	4.1343
	323	**M18FLU1-4**	**TE-1**	**0.000**	**14.553**	**336.500**	**398.235**	**233.562**	**478.351**	***bdl***	**0.297**	**39.083**	**1.471**	**10.740**	**18.671**	**66.081**	**634.861**	**3.898**	**-60.250**	**0.669**	
2017	55	**M17FLU58**	TE-3	48.396	0.738	491.445	526.616	10.202	*bdl*	*bdl*	*bdl*	11.963	26.352	*nd*	10.982	62.746	473.536	6.230	-82.000	*nd*	4.1885
	46	**M17FLU57**	TE-5	49.482	0.598	493.218	545.353	19.237	*bdl*	*bdl*	*bdl*	13.732	30.015	*nd*	10.491	68.701	491.845	7.220	-5.000	*nd*	3.1161
	320	**M17FLU49-52**	**TE-1**	**0.000**	**15.366**	**368.978**	***nd***	**268.741**	**599.061**	***bdl***	***bdl***	**37.505**	***bdl***	**18.927**	**19.252**	**77.272**	***bdl***	**3.720**	**-81.500**	***nd***	
	4.9 (CTD)	**Seawater.TE 1657m**		**53.559**	***nd***	**475.635**	**550.713**	***nd***	***nd***	***nd***	***nd***	**10.270**	**28.909**	***nd***	**9.531**	***nd***	**824.359**	***nd***	***nd***	***nd***	

WC	°C			mmol/L	mmol/L	mmol/L	mmol/L	µmol/L	µmol/L	µmol/L	µmol/L	mmol/L	mmol/L	µmol/L	mmol/L	µmol/L	µmol/L		mV	mmol/L	
Year	**Temp (ROV)**	**Sample name**	**Position**	**Mg**	**Si**	**Na**	**Cl**	**Mn**	**Fe**	**Cu**	**Zn**	**Ca**	**SO_4**	**Ba**	**K**	**Sr**	**Br**	**pH**	**E_h**	**H_2S**	
2019	68	**M19FLU61#**	WC-2	49.082	0.915	480.295	545.656	16.300	*bdl*	*bdl*	*bdl*	14.692	26.714	1.405	11.879	80.628	903.870	*nd*	*nd*	*nd*	4.991
	68	**M19FLU62#**	WC-2	48.703	0.430	445.869	561.039	7.863	*bdl*	*bdl*	*bdl*	11.976	28.296	0.719	10.664	81.210	927.645	*nd*	*nd*	*nd*	1.863
	40	**M19FLU63*#**	WC-3	46.421	0.072	450.614	546.925	0.831	0.020	0.212	0.187	11.451	28.259	0.206	10.539	77.652	902.755	*nd*	*nd*	*nd*	-0.599
	40	**M19FLU64***	WC-3	49.276	0.148	449.366	545.893	2.072	0.138	0.204	0.392	11.211	28.160	0.593	10.581	77.328	892.518	*nd*	*nd*	*nd*	-0.100
	306	**M19FLU09-12**	**WC-1**	**0.000**	**16.468**	**376.569**	**501.091**	**217.205**	**243.886**	***bdl***	***bdl***	**42.785**	**2.383**	**9.391**	**24.114**	**95.340**	**796.214**	***nd***	***nd***	***nd***	
2018	40	**M18FLU53**	WC-2	36.714	2.853	434.935	516.495	89.234	78.680	*bdl*	0.170	15.846	22.599	2.520	11.750	195.524	475.000	5.430	-105.000	nd	20.297
	40	**M18FLU54**	WC-2	36.258	3.089	435.612	518.749	91.910	80.721	*bdl*	0.054	16.396	22.394	2.136	11.949	184.730	474.531	5.420	-104.000	0.017	21.892
	35	**M18FLU55**	WC-3	42.802	0.930	456.617	519.010	27.076	0.329	*bdl*	*bdl*	12.736	25.613	2.444	10.619	179.373	471.458	6.150	-80.000	0.071	5.932
	35	**M18FLU56**	WC-3	40.986	1.716	444.642	512.556	50.612	8.871	*bdl*	*bdl*	14.439	23.899	2.598	11.359	154.093	461.791	5.860	-110.000	0.208	11.663
	319	**M18FLU17-21**	**WC-1**	**0.000**	**15.342**	**384.756**	**483.061**	**333.466**	**428.489**	***bdl***	***bdl***	**39.758**	**0.087**	**44.293**	**21.828**	**151.767**	**763.358**	**3.773**	**-70.250**	**9.626**	
2016	131	**M16FLU60**	WC-3	38.938	2.338	384.376	372.113	98.535	3.122	0.283	0.254	16.428	14.982	1.782	12.036	110.778	524.109	5.620	-175.000	2.908	16.265
	40	**M16FLU61***	WC-3	52.451	1.010	402.981	295.396	19.287	*bdl*	0.060	*bdl*	12.121	15.940	0.638	9.940	102.041	386.710	6.320	-124.000	3.209	5.182
	78	**M16FLU62***	WC-3	55.219	0.403	418.055	276.156	6.498	*bdl*	0.115	*bdl*	11.318	13.669	0.274	11.602	112.595	371.735	6.580	-67.000	2.566	1.355
	67	**M16FLU63***	WC-3	54.072	0.363	409.882	383.210	5.940	*bdl*	0.756	*bdl*	11.213	18.728	0.266	9.087	90.015	526.175	6.840	-63.000	3.446	1.156
	316	**M16FLU13-16**	**WC-1**	**0.000**	**16.176**	**382.113**	**496.278**	**283.057**	**272.432**	***bdl***	***bdl***	**42.188**	**5.244**	**4.006**	**19.377**	**120.917**	**795.180**	**4.570**	**-106.250**	**26.533**	
	4.7 (CTD)	**Seawater.WC 1680m**		**58.632**	***nd***	**508.289**	**555.583**	***nd***	***nd***	***nd***	***nd***	**11.048**	**29.377**	***nd***	**9.951**	***nd***	**831.443**	***nd***	***nd***	***nd***	0
		Seawater. Millero et al. (2008)		**54.100**	**0.178**	**468.000**	**545.000**	**0.000**	**0.000**	**0.001**	**0.028**	**10.280**	**28.300**	**0.140**	**10.210**	**87.000**	**838.000**				

* Samples collected not right at the temperature probe location, but less than 2m away

No bell during this sampling

bdl : below detection limit

nd : no data

Table 4-2 – Temperature and chemical characteristics of focused and diffuse fluids sampled at the Tour Eiffel (TE) and White Castle (WC) monitoring locations in 2016, 2017, 2018 and 2019 (Figure 4-2 and 4b and d). Temperature was measured with the ROV or Nautile probe prior to sampling. Eh is the redox potential. P[%].[Mg/SI] is the percentage of endmember fluids in diffuse fluids, calculated from Mg/Si ratios (X.-G. Chen et al., 2020). Also shown are the composition of near seafloor seawater in two CTD casts, and the Millero et al. (2008) standard seawater composition.

4.5. Time series of focused and diffuse fluid chemistry at the Tour Eiffel and White Castle vent sites

The chemistry and sampling temperature of focused and diffuse effluents sampled in 2016, 2017, 2018 and 2019 at the Tour Eiffel and White Castle monitoring sites, and of seawater sampled near these sites, are presented in Table 4-2. Focused endmember fluids (temperatures > 306°C) have low pH (≤ 4.5) and redox potential ($E_h < 0$), are depleted in Na and Cl and enriched in H_2S, Si, Ca, Ba, Fe, Cu and Zn compared to seawater. SO_4 concentrations are variable, with high values (>1 mmol/L) measured in 2018 at TE, and in 2016 and 2019 at WC. Chlorinity is consistently lower at TE (Cl < 433 mmol/L; Na < 369 mmol/L) than at WC (Cl up to 501 mmol/L in 2019), consistent with previous observation of lower Cl concentration at the southeastern Lucky Strike sites (Von Damm et al., 1998; Langmuir et al., 1997). Other major cations like Ca and K do not show distinct difference of concentration between the two sites, while in any given year, Mn is more abundant in WC endmember fluids, and Fe more abundant at TE. Strontium is consistently more abundant at WC (up to 151 µmol/L). Overall, the endmember fluid compositions in Table 4-2 are similar to concentrations measured in fluids sampled in 2013 at the same two sites (Chavagnac et al., 2018) consistent with a hydrothermal system that was stable during this time range. We use these endmember fluids as a reference to study the composition and time evolution of diffuse fluids chemistry.

Diffuse fluids were sampled in 2017, 2018 and 2019 at temperature monitoring locations TE-3 and TE-5 at TE, in 2018 and 2019 at or near monitoring locations WC-2 and WC-3 and in 2016 (WC-3 only) at WC (Table 4-2). Temperatures measured with the ROV (2016, 2017, 2018) or with the manned submersible Nautile (2019) probe just before sampling ranged between 35°C and 131°C (Table 4-2). Diffuse fluids pH range between 5.42 and 7.22, intermediate between seawater and high-temperature focused fluid values. It varies at a given sampling location between the three years of sampling. The most acidic values (5.42-5.62; Table 4-2) correspond to fluids sampled in 2016 at monitoring location WC-3 (diffuse patch in grey sandy material; Figure 4-2), and in 2018 at monitoring location WC-2 (crack in the slab within one meter of the edge of the sulfide mound; Figure 4-2), while fluids sampled at monitoring location TE-5 in sandy volcaniclastic deposits with Fe-oxidizing bacterial mats and ferruginous crust (Figure 4-2) have consistently higher pH over the years (6.95 to 7.22; Table 4-2).

Mg concentrations in diffuse fluids vary between 36.2 mmol/L (WC-2 crack in 2018; Table 4-2) and 55.2 mmol/L (diffuse venting patch near WC-3 in 2016; Table 4-2), close to

seawater concentration. Variations in Mg concentrations plotted against Cl concentrations can be compared to conservative mixing trends between seawater and endmember fluids (Figure 4-7a). Higher Mg concentrations were measured at all sampling sites in 2019, compared to previous years (Figure 4-7a). This may indicate a lesser input of end-member fluids in the formation of diffuse fluids at both the WC and TE sites this year. Alternatively, and this is the hypothesis we rank higher, it may be that sampling performed in 2019 with the manned submersible Nautile incorporated a greater proportion of entrained seawater. Na concentrations increase with chlorinity, and are also higher than endmember fluid values (Table 4-2). Ca (11.1 to 16.4 mmol/L) and K (9.0 to 12.0 mmol/L) concentration ranges are similar or higher than seawater values. Ba concentrations (0.20 to 2.52 μmol/L; Table 4-2) are higher than Millero et al. (2008) seawater values, with the highest concentrations measured at the WC-2 crack (Table 4-2 and Figure 4-2d and 6b).

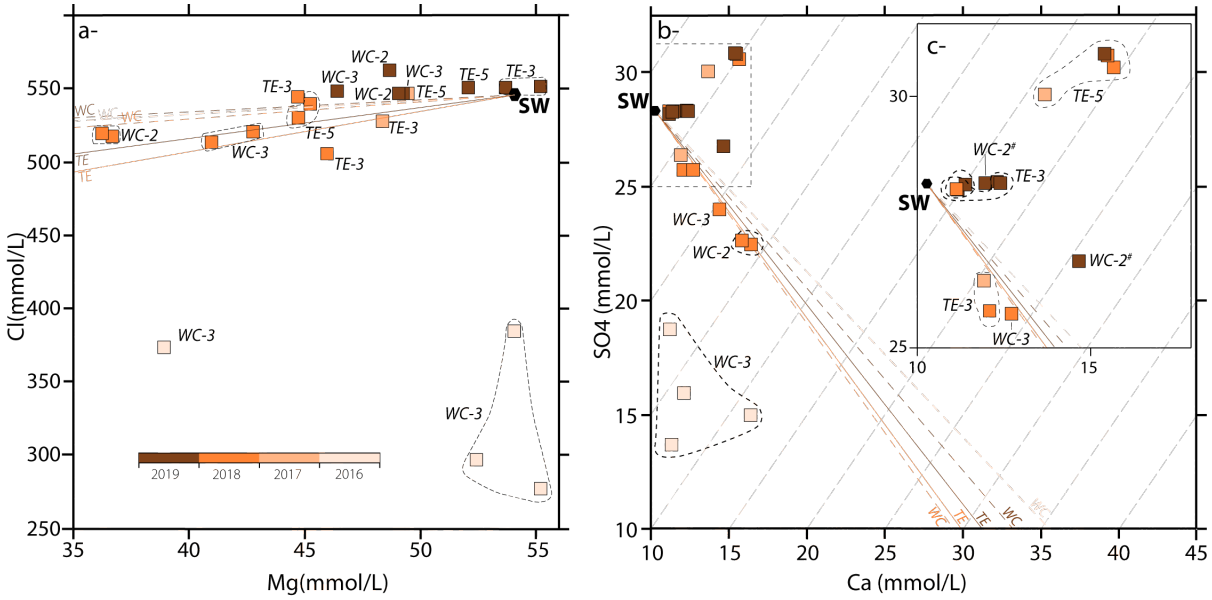

Figure 4-7– Magnesium, chloride, calcium and sulfate ion contents measured in diffuse fluids from Tour Eiffel (TE) and White Castle (WC) monitoring locations (Figure 4-4a and c; and Figure 4-2) in 2016, 2017, 2018 and 2019 (color scale and Table 4-2). Solid and dotted lines labelled WC or TE join the measured end-member fluid compositions (sampled at monitoring locations TE-1 and WC-1; see Supplementary Figure S1), to seawater composition (SW) from Millero et al. (2008). (a) Magnesium and chloride contents. Except for fluids sampled at and near the WC-3 monitoring location in 2016, data plot near the end-member fluid to SW lines. (b) and (c) Calcium and sulfate ion contents. Fluids sampled at and near the WC-3 monitoring location in 2016 are again outliers. Other samples plot near, or above the end-member fluid to SW lines. Grey dashed lines show the trends expected for anhydrite dissolution or precipitation. Compositions at monitoring location TE-5 would for example suggest on-going anhydrite dissolution in the substratum.

The chlorine-poor 2016 WC-3 samples depart from the Mg-Cl mixing line shown in Figure 4-7a. These samples also have very low SO_4 concentrations (Figure 4-7b). In contrast to the procedure adopted in later years, the four 2016 WC-3 samples were collected at 4 distinct

locations, only one of which (M16FLU60) comes from the autonomous temperature probe's location, the other 3 come from diffuse venting patches in the grey sandy material within 4 meters of the probe (Figure 4-2c). Sample M16FLU60 has the lowest Mg concentration (38.93 mmol/L), and the highest temperature (131°C), but low Cl, Ca and SO_4 concentrations similar to those of the other 3 2016 WC-3 samples (Figure 4-7a and b). Figure 4-7b shows total SO_4 relative to Ca concentration and lines joining seawater to TE and WC endmember fluids concentrations (Supplementary Figure S1). With the exception of the 2016 WC-3 samples, the diffuse fluids plot either on or above these lines, in a domain that would correspond to anhydrite dissolution. Fluids sampled at the TE-5 monitoring location (Figure 4-2a) consistently plot in the dissolution domain in 2017, 2018 and 2019. Other diffuse vents show variable behavior over the years of sampling. Fluids sampled at the TE-3 crack (Figure 4-2b) plot close to the mixing line in 2017 and 2018, then into the anhydrite dissolution domain in 2019 (Figure 4-7b and c). Fluids sampled at the WC-2 crack (Figure 4-2d and 6b) plot close to the mixing line in 2018, then also into anhydrite dissolution in 2019. Fluids sampled near the WC-3 diffuse patch (Figure 4-2c) plot in the anhydrite precipitation domain in 2016, on the mixing line in 2018, and into the dissolution domain in 2019 (Figure 4-7b and c).

Si concentrations range between 0.07 and 3.08 mmol/L (Table 4-2). The highest values are measured for the WC-2 crack (Table 4-2). Si concentrations tend to decrease at increasing Mg, as expected for increasing dilution of the endmember fluid with seawater (Seyfried & Bischoff, 1977), with significant scatter (Supplementary Figure S2). Dilution calculated from Mg concentrations in diffuse fluids and from Si concentrations in seawater and in endmember fluids (X.-G. Chen et al., 2020) range between 0.04% (highest degree of dilution for the TE-5 diffuse venting patch in 2019) and 21.98% (most concentrated value measured at the WC-2 crack in 2018; Table 4-2). Dissolved Mn (dMn) has been shown to trace the dilution of near vents plumes of hydrothermal endmember fluids in seawater (Field & Sherrell, 2000; Hawkes et al., 2013; Waeles et al., 2017), because its kinetics of oxidation are slow compared to the flow velocity of the fluid (Cowen et al., 1990). Mn concentrations in diffuse fluid samples (Table 4-2) range between 0.8 μmol/L (WC-3 in 2019) and 91.9 μmol/L (WC-2 in 2018). Diffuse fluids sampled at TE have Mn concentrations ≤ 27.75 μmol/L. Mn concentrations tend to decrease at increasing Mg and decreasing Si (Supplementary Figure S2), as expected for increasing dilution of the endmember fluids with seawater.

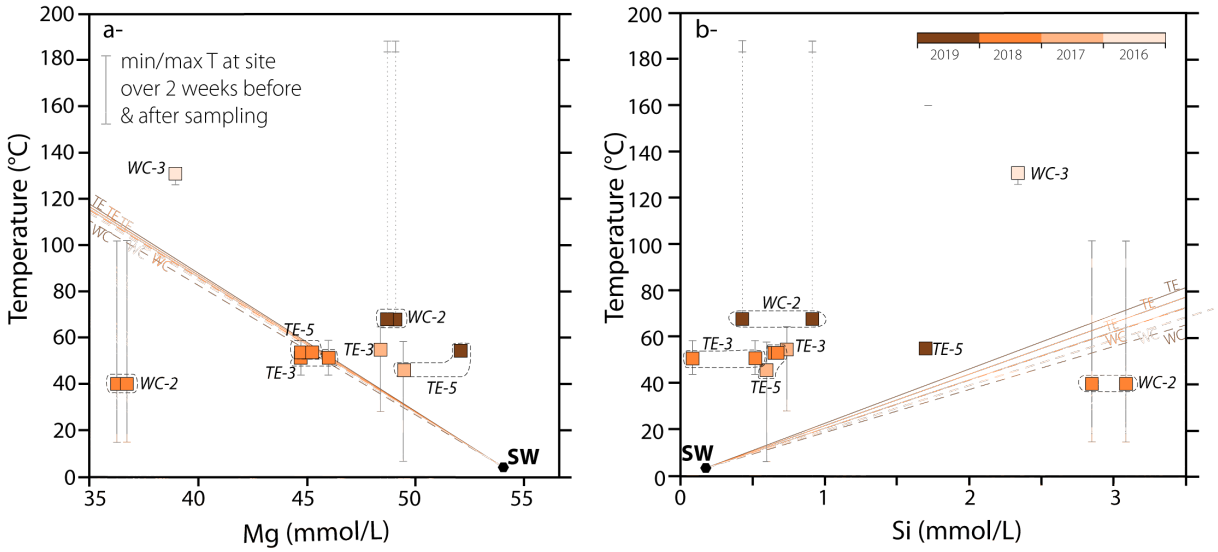

Figure 4-8 – Magnesium and silica contents, and temperature of diffuse fluids sampled at the Tour Eiffel (TE) and White Castle (WC) monitoring locations (Figure 4-4a and c; and Figure 4-2) in 2016, 2017, 2018 and 2019 (color scale and Table 4-2). Samples collected more than 2 m away from autonomous temperature probe locations (Table 4-2) are not shown. Solid and dotted lines labelled WC or TE (see Supplementary Figure S1) join the measured focused end-member fluid compositions and/or temperature, to seawater composition (SW) from Millero et al. (2008). (a) Fluid temperature and magnesium content. (b) Fluid temperature and silica content. Temperature values (Table 4-2) were measured by the ROV or Nautile prior to fluid sampling. Grey error bars show the min and max temperature measured by autonomous temperature probes deployed at corresponding monitoring location for a period of a week before and after fluid sampling.

In Figure 4-8, we plot Mg and Si concentrations against sampling temperature (the temperature measured with the ROV or the manned submersible probe prior to sampling), for samples collected at monitoring locations TE-2, TE-3 and TE-5, and WC-2 and WC-3. Samples collected within 6 m from these locations (Figure 4-2 and Table 4-2) are not shown but fit similar trends. With the exception of the 2016 WC-3 sample (131°C), sampling temperatures range between 35° and 78°C and show no correlation with either Mg or Si concentrations (Figure 4-8), the two proxies for degree of dilution (the same is true for Mn concentrations; Supplementary Figure S2). Indicative dilution lines, joining seawater concentrations and near seafloor temperature, to endmember focused fluids concentrations and temperatures (Supplementary Figure S1), help identify samples for which sampling temperature is either lower, or higher than expected from their degree of dilution. Diffuse fluids sampled at TE plot either on or above the dilution lines, suggesting that their temperature is either consistent with simple dilution (2018 samples from TE-3 and TE-5 based on the Mg proxy; Figure 4-8a), or that they are too hot (2017 and 2019 samples from TE-3 and TE-5 based on the Mg proxy, or all the TE samples based on the Si proxy; Figure 4-8b). Diffuse fluids sampled at WC show more contrasted characteristics, and more variable behavior over the 4 years of sampling. WC-2 fluids plot below the dilution lines in 2018 (fluid temperature too low to be consistent with simple dilution), then above the lines in 2019 for both Mg and Si concentrations. WC-3 fluids

plot above the dilution lines in 2016 (fluid temperature too high to be consistent with simple dilution). Figure 4-8 also shows the range of temperatures measured by autonomous probes at each venting location over 2 weeks, one week before and one week after sampling. Sampling temperatures for the TE monitoring locations and for the 2018 WC-2, and 2016 WC-3 samples, fall within these ranges, indicating that these samples likely do adequately represent the fluids that vent out of each monitored location. Temperatures recorded by the autonomous temperature probes in 2019 at WC-2 are > 120°C (Figure 4-8a and b), significantly higher than sampling temperatures at these sites for the same year. In both cases, these discrepancies arise because the hotter fluid at the exact location of the temperature probe came out in a very restricted portion of the venting crack that was not accessible with the sampler because of the rugged local topography. These WC-2 samples are therefore representative of fluids venting less vigorously within a few decimeters from the probes.

4.6. Time variation of focused and diffuse fluids temperature at the Tour Eiffel and White Castle vent sites

4.6.1. High-temeprature focused fluids

Temperatures recorded over the 3 years of survey at focused vents TE-1 (Figure 4-3a) and WC-1 (Figure 4-3f) are mostly between 295°C and 329°C, with occasional drops of temperature (down to a minimum of 182 °C; Figure 4-9a), interpreted as due to local hydraulic perturbations in the sulfide edifices (Barreyre et al., 2014b). A steady and slow temperature decrease, down to 260°C, in June to August 2019 at TE-1 is also probably due to a local event, possibly sulfide precipitation in the near vent conduit. Aside from these occasional events, endmember fluid temperature displays periodic or semi-periodic variations (Figure 4-9b and c), with amplitudes between 0.1 and 15°C. At the TE-1 vent, these variations have a low overall energy at the semi-diurnal tidal frequencies (N2, M2, S2, K2; Figure 4-10a). Temperature variations at semi-diurnal tidal frequencies carry higher Power Spectrum Density (PSD) energies at the WC-1 vent, particularly in 2016-2017 (Figure 4-10b).

In Figure 4-9d, we plot the coherence at the semi-diurnal M2 frequency (CM2) between focused, end-member fluid temperature at TE-1 and WC-1, and seawater pressure. CM2 varies between 0 and 0.75 at the TE-1 vent, and between 0 and 0.95 at the WC-1 vent. With the exception of a full year of high coherences in 2018-2019 at WC-1, CM2 is variable over timescales of a fortnight to a few months (Figure 4-9d). In 2016-2017 there is a weak coincidence between periods of higher CM2 at TE-1 and WC-1 (for example in April to June 2017; Figure 4-9d). This is not the case, however, in 2018-2019 (and there is no TE-1 record

for 2017-2018). Coherences near or above 0.75 are recorded repeatedly at WC-1 in 2017-2018, typically at the apex of periods of increasing, then decreasing coherence that, together, last ~2 weeks (for example in August 2017), to 5 months (December 2017 to March 2018). CM2 is low at both TE-1 and WC-1 in 2016-2017, with only a few days with values > 0.75 in June 2017 at WC.

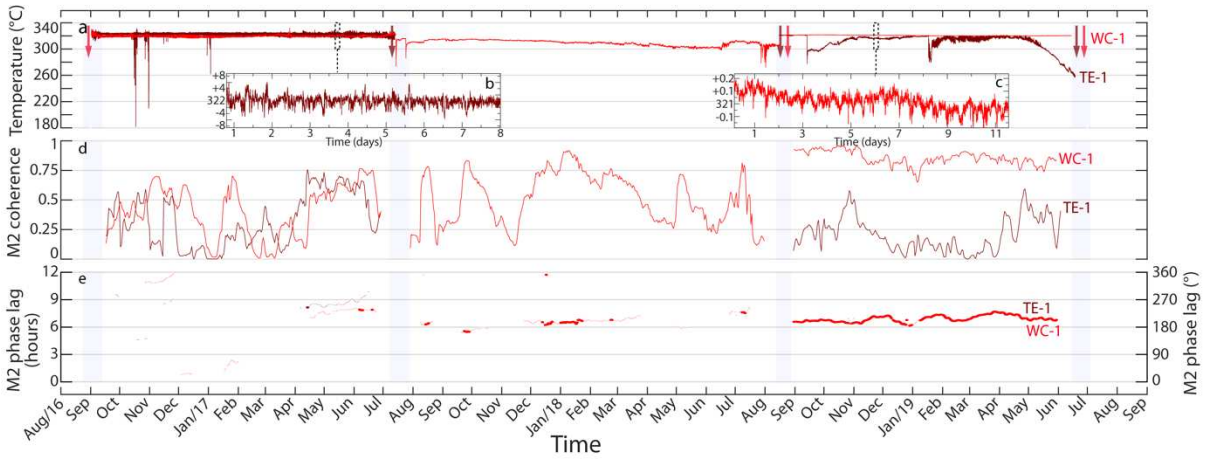

Figure 4-9 – Temperatures recorded over the 3 years of survey at focused vents TE-1 (dark red) and WC-1 (light red; location in Figure 4-4b and d) and time variations of the coherence and phase lag with seafloor pressure at the M2 tidal frequency (30 days sliding window, 1 day sliding time). Light grey intervals correspond to maintenance cruises. (a) Temperature time-series. Colored arrows show timing of fluid sampling at these vents (Table 4-2). (b) Zoom on temperature time-series at TE-1 between 05/11/2017 and 05/18/2017. (c) Zoom on temperature time-series at WC-1 between 11/18/2018 and 11/28/2018. (d) Time variation of the coherence calculated between temperature and seafloor pressure at the M2 tidal frequency. (e) Time variation of the phase lag calculated between temperature and seafloor pressure at the M2 tidal frequency for M2 coherence > 0.75 (thicker lines), or > 0.5 (thin lines).

In 2017-2018 and 2018-2019, periods with CM2 > 0.75 at WC-1 correspond to phase lags of 195° to 231°, comparable or above phase lag values reported for previous years at these and other Lucky Strike focused vents (Barreyre et al., 2014; Barreyre & Sohn, 2016). Phase lags calculated at WC-1 for periods of lower coherence (0.5-0.75) are consistent with these values (Figure 4-9e), as are the values calculated for the short intervals of high CM2 (> 0.75) at TE-1 in 2018-2019 (Figure 4-9e). Higher phase lag values (210 to 282°) are calculated for coherences > 0.5 in April to June of 2017 at both WC-1 and TE-1 (Figure 4-9e). The 2018-2019 WC-1 phase lag record also shows smooth variations (177 to 210°) occurring over 1.5 to 2.5 months, as also reported by Barreyre and Sohn (2016) for older Lucky Strike temperature time series, and smaller amplitude variations (<15°) occurring over periods of ~2 weeks (Figure 4-9d).

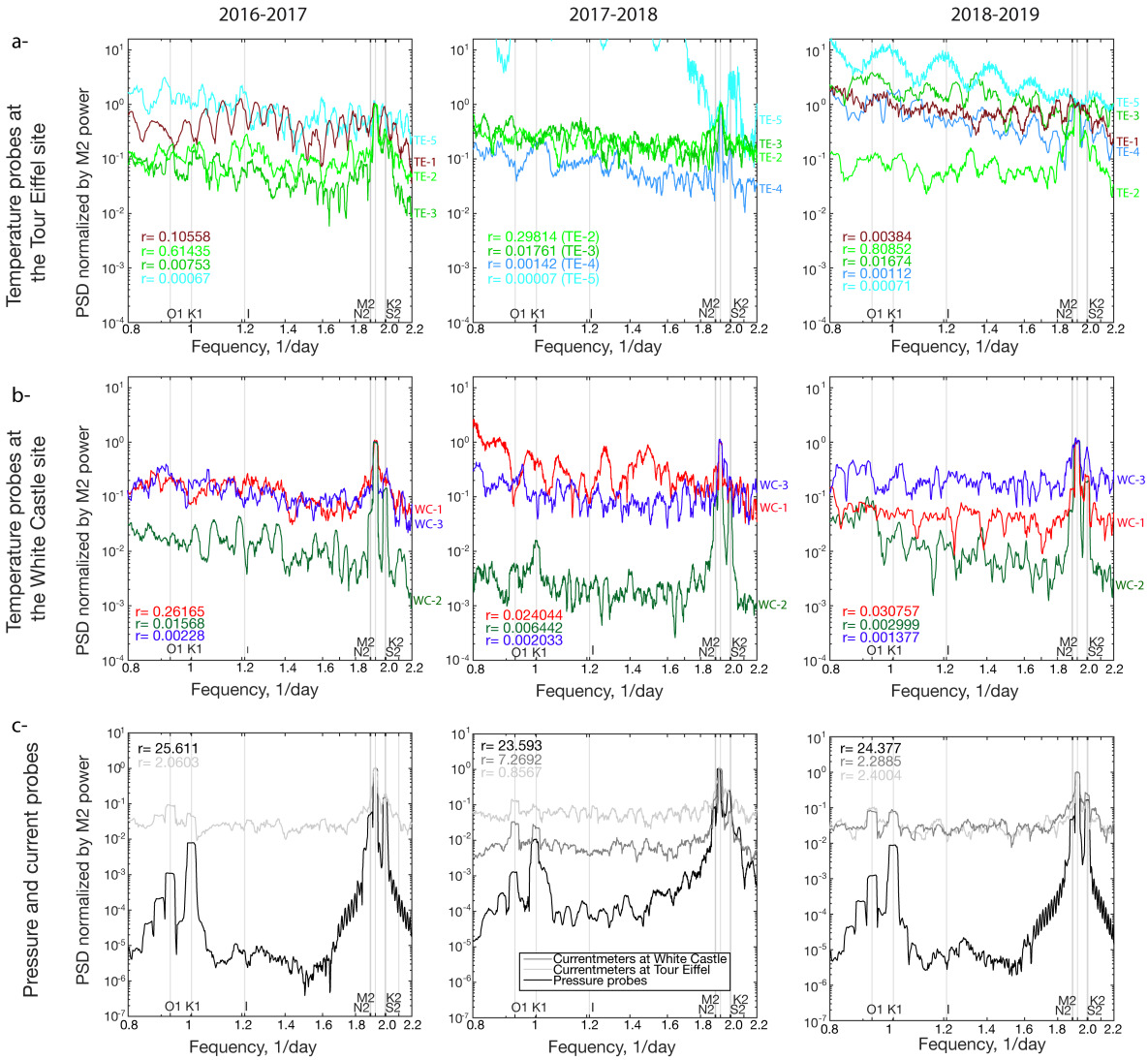

Figure 4-10 – Power spectrum density (PSD) plots around the diurnal (O1, K1) and semi-diurnal (N2, M2, S2, K2) harmonics peaks for venting temperatures at the TE and WC monitoring locations, for seafloor pressure, and for current velocity, over the 3 years of the experiment (2016-2017, 2017-2018 and 2018-2019). PSD values for venting temperatures shown in red for focused vents, green for diffuse vents in cracks, and blue for diffuse vents in sandy areas. PSD values for each time-series are normalized to the PSD value at the M2 semi-diurnal frequency; corresponding normalizing coefficients (r) are shown in the plots. (a) PSD plots for venting temperatures at TE monitoring locations. PSD values for near seafloor seawater temperatures (recorded after the probes fell off the vents in February to August 2018 at TE-5 in march to July 2019 at TE-4) are shown in grey. (b) PSD plots for venting temperatures at WC monitoring locations; (c) PSD plots for seafloor pressure and current velocity.

PSD values for vent fluid temperatures at the M2 frequency (PSDM2) carry information on both the coherence and the amplitude of the corresponding semi-diurnal temperature variations. Abrupt changes in PSDM2 values over time correspond to events in the temperature records (for example in January 2019 at TE-1; Figure 4-9a and 11a), while smoother changes that occur over periods of about 2 weeks (for example the local maxima at WC-1 in mid-May, early June and mid-June 2017; Figure 4-11a) tend to correspond to fortnightly (spring) high amplitude tides (Supplementary Figure S3). PSDM2 are consistently higher at WC-1 than at TE-1, except in mid-January to early February 2019 (Figure 4-11a; corresponding amplitude of

semi-diurnal temperature variations up to 6°C), as TE-1 fluid temperatures recover from a sharp 41°C drop (Figure 4-9a). PSDM2 at WC-1 are highest in mid-November to mid-December 2016 (corresponding amplitudes of semi-diurnal temperature variations up to ~3°C), and in May to late-June 2017 (corresponding amplitudes of semi-diurnal temperature variations up to ~2.5°C). These two periods show moderate to low CM2 (Figure 4-9d), pronounced fortnightly PSDM2 variations (Figure 4-11a), and scattered phase lag values that differ from the ~164° to ~229° values recorded in 2017-2018 and in 2018-2019 (Figure 4-9e). By contrast, focused fluid temperature records that show the highest CM2 and the most stable phase lag values (for example September to early November 2018 at WC-1; Figure 4-9d and 9e), have lower PSDM2 values (corresponding amplitudes of semi-diurnal temperature variations up to ~1°C), and less pronounced fortnightly PSDM2 variations (Figure 4-11a).

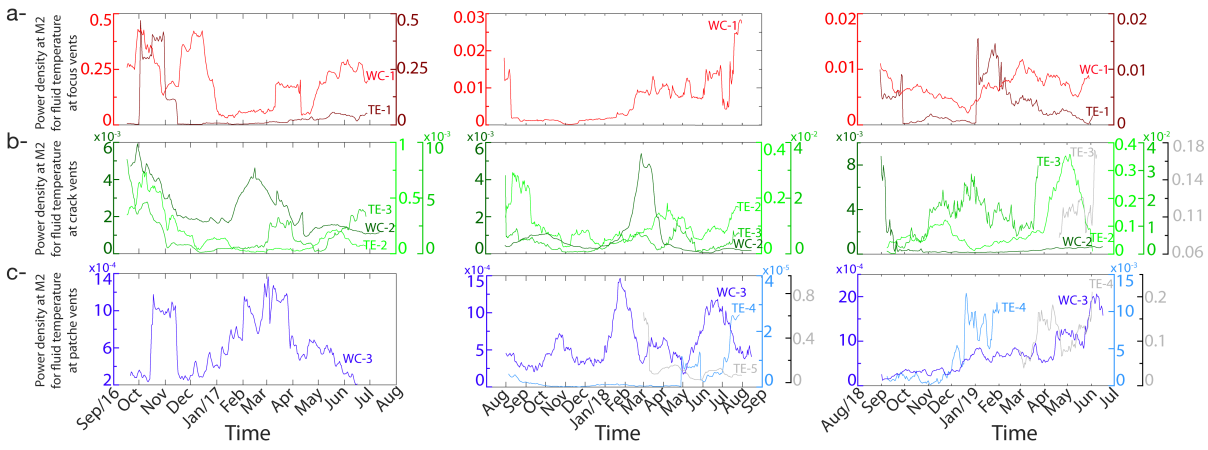

Figure 4-11 – Time variation of the power spectrum density (PSD) of venting temperatures at the M2 frequency over the 3 years of the experiment; 30 days sliding window, 1 day sliding time. (a) focused vents; darker red for WC-1; (b) diffuse venting cracks; darker green for WC-2. (c) diffuse venting sandy patches; darker blue for WC-3. PSD time variations for probes that had fallen off vent and recorded near seafloor seawater temperatures are shown in grey.

4.6.2. Diffuse fluids in cracks

Temperatures recorded over the 3 years of survey at venting cracks (Figure 4-12a) range between 7°C and 80°C at TE-2 and TE-3 (Figure 4-3b and 3c), and between 18°C and 307°C at WC-2 (Figure 4-3g). Lower temperatures were recorded at TE-3 from early April 2019 onward as the probe appears to have moved, then fell off the crack and recorded near seafloor seawater temperatures (Figure 4-12a). The high temperatures recorded at WC-2 in 2016-2017 (Figure 4-12a) are only 10 to 40°C lower than those recorded at the WC-1 focused vent 4 meters away (Figure 4-9a). From august 2017 on, temperatures at WC-2 decreased from around 210°C to 170°C in January 2018, <50°C in March, and ~20°C in August 2018; WC-2 fluid temperatures increased again to ≥200°C following the August 2018 redeployment (Figure

4-12). Temperatures at TE-2 remained low (7 to 18°C) over the 3 years of the experiment, while temperatures at TE-3 varied between 25 and 80°C, over periods of a few days to several months (Figure 4-12a). In addition to the occasional events and longer-term temperature variations described above, diffuse fluids at the 3 monitored cracks display smaller amplitude (0.1 to 8°C) periodic variations, with significant PSD signatures for the semi-diurnal tidal frequencies (N2, M2, S2, K2; Figure 4-10a and b) particularly at TE-2. The lowest semi-diurnal PSD signature was recorded for TE-3 in 2018-2019 (Figure 4-10a).

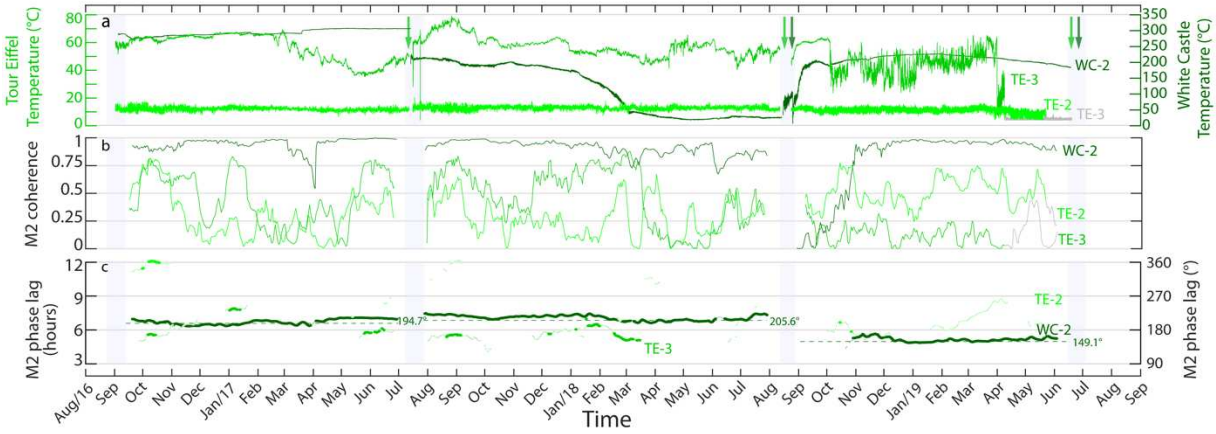

Figure 4-12 – Temperatures recorded over the 3 years of survey at diffuse vents in cracks TE-2 (pale green), TE-3 (bright green), and WC-2 (dark green); see location of monitoring sites in Figure 4) and time variations of the coherence and phase lag with seafloor pressure at the M2 tidal frequency (30 days sliding window, 1 day sliding time). Light grey intervals correspond to maintenance cruises. (a) Temperature time-series. Colored arrows show timing of fluid sampling at these vents (Table 4-2). (b) Time variation of the coherence calculated between temperature and seafloor pressure at the M2 tidal frequency. (c) Time variation of the phase lag calculated between temperature and seafloor pressure at the M2 tidal frequency for M2 coherence > 0.75 (thicker lines), or > 0.5 (thin lines). Light grey intervals correspond to maintenance cruises.

The coherence between venting fluid temperatures and seawater pressure at the semi-diurnal M2 frequency (CM2) is variable between cracks, and through time at a given crack. CM2 is consistently high (> 0.75) at WC-2, except in March 2017 and in September to the end of October 2018 (Figure 4-12b). CM2 is by contrast most commonly low (< 0.75) at TE-2 and TE-3, with higher overall values at TE-3 in 2016-2017 and 2017-2018, and the reverse in 2018-2019 (Figure 4-12b). CM2 variations at these two cracks, that are distant by about 8 m (Figure 4-6a), vary over timescales of a fortnight to a few months, and there is a weak coincidence between several periods of higher CM2 at the two cracks. For example, CM2 are higher at both TE-2 and TE-3 in October 2016, January 2017, may-June 2017, August-September 2017, and late June 2018 (Figure 4-12b). There are, however, exceptions, such as in early to mid-march 2018 (higher CM2 at TE-3, lower at TE-2), and late march to early April 2018 (lower CM2 at TE-3, higher at TE-2; Figure 4-12b).

Phase lags at the M2 frequency (Figure 4-12c) are 187 to 215° at WC-2 in 2016-2017 and 2017-2018, consistent with phase lags calculated for the focused fluid at WC-1 in 2017-2018 and 2018-2019 (Figure 4-9e), and greater than phase lag values reported for earlier years at these and other Lucky Strike focused vents (Barreyre et al., 2014b; Barreyre & Sohn, 2016). Yet in 2018-2019, phase lag values at WC-2 are only 141 to 164°, nearly 2 hours less than in the previous two years, and then at the nearby WC-1 vent over the same period (Figure 4-9e). Fortnightly phase lag variations, with amplitudes up to ~7°, are well developed in the WC-2 record (Figure 4-12c). Phase lags calculated for TE-2 and TE-3 venting temperatures during the rare periods of CM2 > 0.75 are variable (Figure 4-12c), distinct from one another, and distinct from those calculated for the focused fluid at TE-1 (Figure 4-9e). A brief period of high CM2 at TE-2 in October 2018 corresponds to phase lags of 175° to 201°. Periods of CM2 > 0.75 are more common at TE-3 (Figure 12b), yielding phase lag values of 231° to 238° in late December 2016-early January 2017, then of 152° to 194° in several periods between late May 2017 and late March 2018 (Figure 4-12c). As observed at focused vents (Figure 4-9e), there is a good consistency in every case with phase lag values calculated for lower CM2 values (>0.5). This helps delineate the time evolution of phase lags over periods of a few weeks to months: for example, the progressive increase of phase lag value at TE-3 in October and November 2016, or the progressive decrease in February 2018 (Figure 4-12c).

PSD values at the M2 frequency (PSDM2) for vent fluid temperatures vary over time (Figure 4-11b) between 0.02 and 0.75°C^2/Hz for the TE-2 crack (the amplitude of corresponding semi-diurnal variations is up to 6°C), and 1.10^{-4} to 8.10^{-3}°C^2/Hz for WC-2 (amplitudes of semi-diurnal temperature variations up to 15°C). PSDM2 for the TE-3 crack are between 1.10^{-4} and 3.10^{-2}°C^2/Hz (amplitudes of semi-diurnal temperature variations up to 7°C). PSDM2 for near-bottom seawater temperature, measured after the TE-3 probe fell out of the crack in April 2019, are 1 order of magnitude higher (amplitudes of semi-diurnal temperature variations up to 2°C). PSDM2 values at the three monitored venting cracks vary over timescales of several days to 6 months (Figure 4-11b). Fortnightly spring tides (Supplementary Figure S3) correspond with local PSDM2 maxima at WC-2, TE-2 and TE-3 in early October 2016, at WC-2 and TE-2 in mid-March 2017, and in early March 2018 at WC-2 and TE-3 (Figure 4-11b). By contrast, the PSDM2 peak at the end of February 2018 at WC-2 corresponds to a PSDM2 low at TE-3 (Figure 4-11b), and to lower amplitude neap tides (Supplementary Figure S3). PSDM2 values also varies over timescales of months at the WC-2, TE-2 and TE-3 cracks. At WC-2 three maxima (late September to October 2016, February to late march 2017, and February to late march 2018; Figure 4-11b) peak near the fall or spring equinox, when tidal

amplitudes are highest. Another, in early September 2018 occurs as temperatures in the crack were rising from <50°C to ~200°C (Figure 4-12a). These four PSDM2 maxima also correspond to periods of slightly to significantly lower CM2 (Figure 4-12b). By contrast, several periods of higher PSDM2 at both the TE-2 and TE-3 cracks (Figure 4-11b) also have higher CM2: for example, in October 2016, may-June 2017, August 2017, and late June 2018 (Figure 4-12b).

4.6.3. Diffuse fluids in sandy patches

Temperatures recorded over the 3 years of survey at diffuse venting sandy areas (Figure 4-13a) range between 55° and 58°C at TE-5 (Figure 4-3e), and between 125° and 160°C at WC-3 (Figure 4-3h). Temperatures at TE-5 have been stable over the 3 years of recording. Temperatures at WC-3 increased throughout the year in 2016-2017 and 2017-2018, and decreased in 2018-2019 (Figure 4-13a). Temperatures measured in brownish sandy material at TE-4 (Figure 4-3d), with no visible evidence for fluid venting, varied between 35°C and 39°C over (from low to low) ~136 days (late September to end of December 2018) to 140 days (late October 2017 to mid-March 2018; Figure 4-13a). The probes fell out of TE-5 in late February 2018, and out of TE-4 in mid-February 2019, subsequently recording near seafloor seawater temperatures (Figure 4-13a).

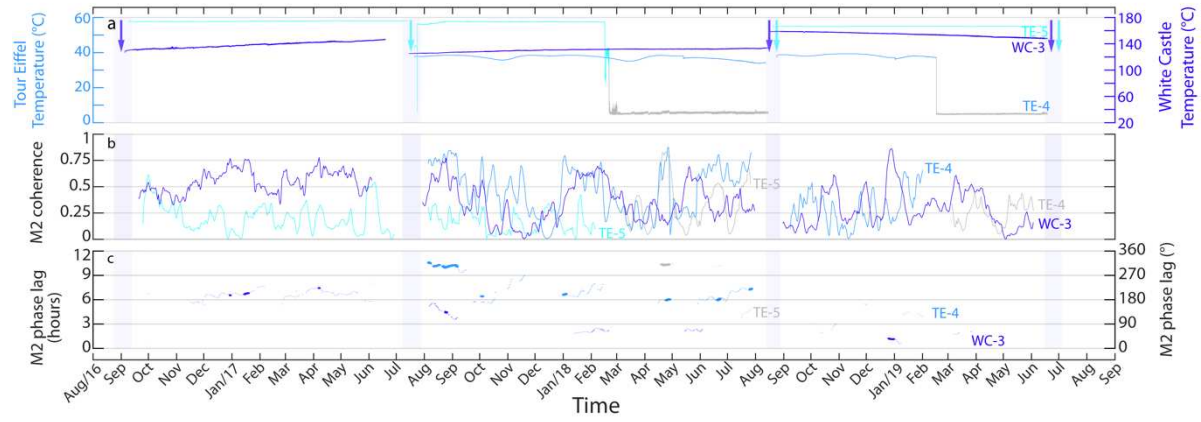

Figure 4-13 – Temperatures recorded over the 3 years of survey at diffuse vents in sandy areas TE-4 (pale blue), TE-5 (electric blue), and WC-3 (dark blue; see location of monitoring sites in Figure 4-4) and time variations of the coherence and phase lag with seafloor pressure at the M2 tidal frequency (30 days sliding window, 1 day sliding time). Light grey intervals correspond to maintenance cruises. Temperature recorded in the vent at monitoring site TE-5 do not show periodic variations at tidal frequencies (Figure 4-10a); they are shown in panels b and c (in grey) only for periods when the probe had fell off the vent and recorded near seafloor seawater temperatures. (a) Temperature time-series. Colored arrows show timing of fluid sampling at these vents (Table 4-2). (b) Time variation of the coherence calculated between temperature and seafloor pressure at the M2 tidal frequency. (c) Time variation of the phase lag calculated between temperature and seafloor pressure at the M2 tidal frequency for M2 coherence > 0.75 (thicker lines), or > 0.5 (thin lines). Light grey intervals correspond to maintenance cruises.

Temperatures measured at WC-3 and TE-4 also display small amplitude (0.1 to 0.6°C) periodic variations, with weak yet significant PSD signatures at the semi-diurnal tidal frequencies (N2, M2, S2, K2; Figure 4-10a and b). By contrast, diffuse fluids at TE-5 show no significant semi-diurnal temperature variations (Figure 4-10a) and are therefore not included in the study of coherence, phase lag and PSD at the M2 frequency. The coherence with seawater pressure at the M2 frequency (CM2) is mostly low (<0.75) at both WC-3 and TE-4 (Figure 4-13b), with variations over timescales of a fortnight to a few months, as observed for the focused vents and diffuse venting cracks (Figure 4-9d and 13b, and supplementary Figure S4).

Phase lag values calculated between temperature and pressure at the M2 frequency for those rare periods with CM2 > 0.75 (Figure 4-13b) are scattered at both WC-3 and TE-4 (Figure 4-13c): 200° to 204° in 2016-2017 and 34,5° to 36° in end-December 2018 at WC-3; 303° to 317° at TE-4 in August to early September 2017, then 192° to 220° in early October 2017, early January 2018, late April, late June, and late July 2018 and August 2018. Fortnightly CM2 maxima that coincide at WC-3 and TE-4 (for example in early October 2016, late September to early November 2017, and in late June 2018) correspond to spring tides (Supplementary Figure S3). CM2 variations over longer timescales (up to several months) are distinct between the two vents, and also between these vents and the nearby venting cracks or focused vents (Supplementary Figure S4). CM2 at WC-3 is higher in January, April and August 2017, then again in January to mid-February 2018, in late May and late December 2018, and in March 2019 (Figure 4-13b). With the exception of the January to mid-February 2018 period, these CM2 highs correspond to low PSDM2 values (Figure 4-11c). CM2 values at TE-4 are very low in 2016-2017, higher in august 2017, in January to mid-February, mid to late April, and June 2018. Corresponding PSDM2 values are low to very low (Figure 4-11c). In mid to late April 2018, the CM2 maxima in the TE-4 record coincides with a CM2 maximum for the near bottom seawater temperature record from the fallen probe at TE-5 (Figure 4-13b).

4.6.4. Bottom current velocity and venting temperatures

Current velocities near the TE and WC sites vary between 0.11 and 30 cm/s (Figure 4-14a). Diurnal (O1, K1) and semi-diurnal (N2, M2, S2, K2) tidal related signals carry relatively high energy (Figure 4-10c). Both the coherence at M2 between current velocity and seafloor pressure (Figure 4-14b), and the PSD at M2 (Figure 4-14d) are variable over timescales of weeks to months, and the broad trends of these variations share similarities between the sites on a given year of deployment. There are, however significant differences between sites, and between deployments at a given site. The strongest semi-diurnal signals, with the highest coherence to seafloor pressure (CM2), are recorded for the currentmeters deployed near WC in

2017-2018, and near TE in mid-April to late June 2017 (Figure 4-10c and 14b and d). High coherence values are also recorded at both TE and WC during the 2018-2019 deployment, and corresponding PSDM2 values for that year are lower at WC than on previous deployment years. Phase lags between current velocity and seafloor pressure for periods of higher coherence (> 0.75) vary between 32 and 84° at WC, and ~0 to 70° at TE (Figure 4-14c). Inter-sites and inter-deployments differences in the spectral content of the current velocity records probably result for the most part from the location of the currentmeters relative to local relief: contrary to the temperature probes, the TE and WC currentmeters were not set at the same exact locations from one year to the next (Figure 4-1), and local topography deflects and modifies near bottom currents (Tivey et al., 2002).

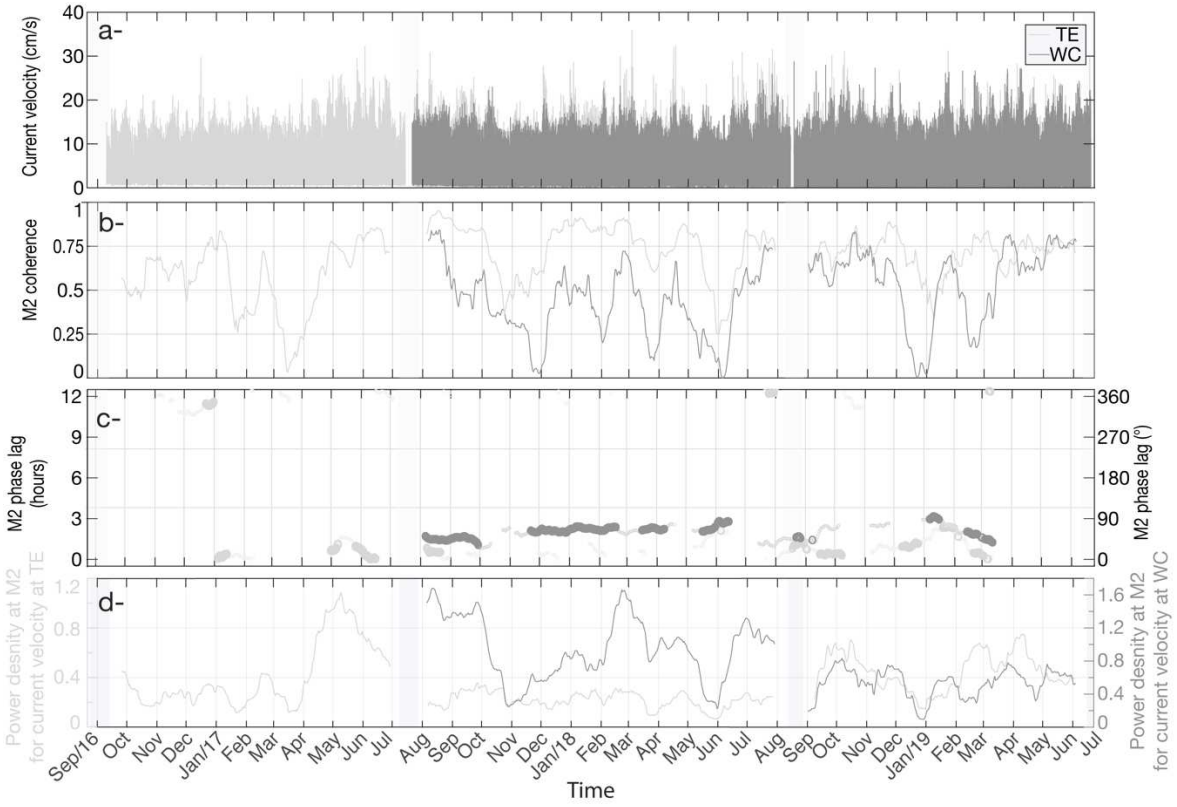

Figure 4-14 – Current velocity variations recorded over the 3 years of survey at near seafloor depths (1m) near the TE and WC sites (see location of currentmeters in Figure 4-1) and time variations (30 days sliding window, 1 day sliding time) of the coherence and phase lag with seafloor pressure at the M2 tidal frequency. Light grey intervals correspond to maintenance cruises. (a) Current velocity time-series. (b) Time variation of the coherence calculated between current velocity and seafloor pressure at the M2 tidal frequency. (c) Time variation of the phase lag calculated between current velocity and seafloor pressure at the M2 tidal frequency for M2 coherence > 0.75 (thicker lines), or > 0.5 (thin lines).

Given these local variations, it is likely that if we could deploy currentmeters at individual temperature monitoring locations, their data could also differ, even over distances of meters, because of the rugged topography of the TE and WC sites. Current data available at this point nonetheless allow us to identify 3 patterns for the relations between coherence values at the M2 frequency for venting temperatures and pressure (CM2; Figure 4-9, 12 and 13), and for venting

temperatures and current velocity (CM2c; Supplementary Figure S5). In the first pattern, CM2 is consistently greater than CM2c, suggesting a weak impact of currents on fluid exit temperature; this is the case at WC-1 in 2018-2019 (Figure 4-15a), and also at WC-2 for the 3 years of monitoring (Supplementary Figure S6). In the second pattern, CM2c is significantly greater than CM2, suggesting that tidally-modulated variations in current velocity do affect venting temperatures; this is the case at TE-2 for most of the 2018-2019 deployment (Figure 4-15b). In the third pattern, that is shared by all the other temperature records (Supplementary Figure S6), CM2 and CM2c are overall lower, values > 0.75 are uncommon and correspond to either CM2 > CM2c (for example at WC-1 in December 2017 and January 2018; Figure 4-15c), or CM2c > CM2 (for example at WC-1 in March 2018 or at TE-2 in October 2017 and February 2018; Figure 4-15c and d).

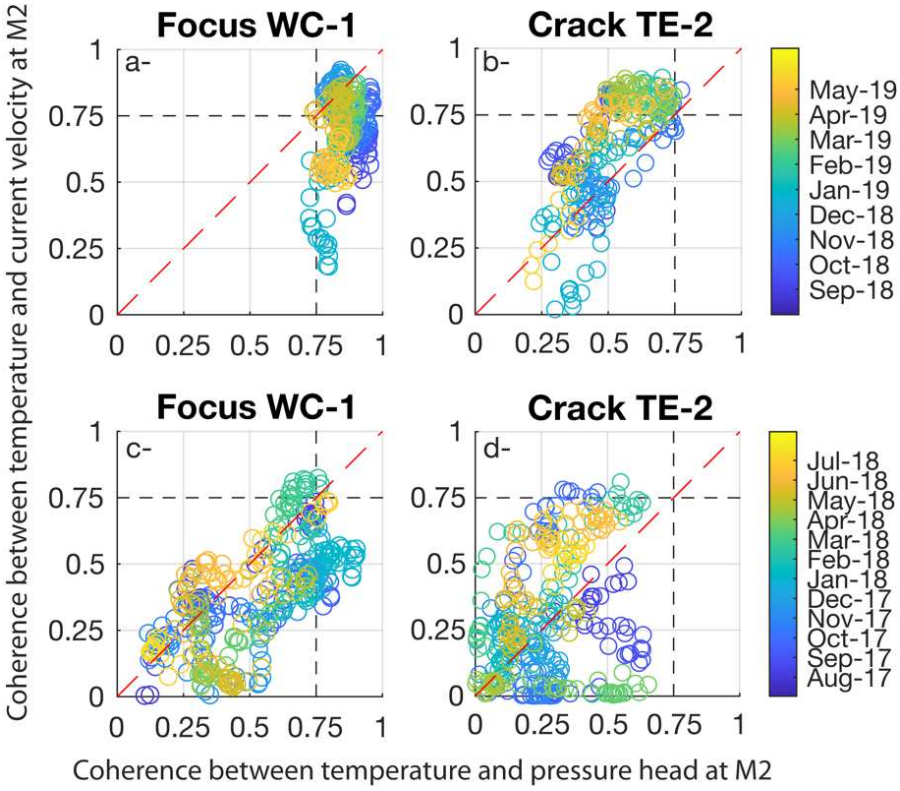

Figure 4-15 – Plots showing coherence values at the M2 frequency between venting temperatures at monitoring locations WC-1 and TE-2 and current velocity, as a function of their coherence with seafloor pressure also at the M2 frequency. Coherence values calculated for a 30 days sliding window, with a 1 day sliding time. Each dot represents 1 day (dates indicated by color scale). (a) temperature at focused vent WC-1 in 2018-2019; (b) temperature at diffuse vent in crack TE-2 in 2018-2019; (c) temperature at focused vent WC-1 in 2017-2018; (d) temperature at diffuse vent in crack TE-2 in 2017-2018.

4.7. Discussion

Previous studies of diffuse vents characteristics and variability at Lucky Strike and other mid-ocean ridge hydrothermal sites (Little et al., 1988; Mittelstaedt et al., 2012; Pruis & Johnson, 2004; Butterfield et al., 2004; Rouxel et al., 2004b; Barreyre et al., 2014b; Cooper et al., 2000) have used shorter time series, focused, for most of them, on a smaller number of vents and did not integrate, to the extent that we do here, fine scale geological mapping. Our study is also to date the most documented work on the time variability of both fluid temperature and fluid chemistry at diffuse vents of a mid-ocean ridge black smokers vent field.

Reporting on our results in the previous sections emphasizes the complexity of these diffuse venting systems: (i) three types of vents depending on local geology (cracks in sulfide-indurated deposits, cracks in non-indurated deposits, and diffuse venting patches in sandy material); (ii) variations between vents in the degree of mixing between end-member black smoker fluids and seawater; (iii) variations between vents, and with time at a given vent, in chemical indicators for the precipitation or dissolution of sulfates in the substratum; (iv) vent temperature variations that are uncorrelated between vents only a few decimeters apart, and reveal tidal forcing effects that vary in amplitude and phase lag, again between nearby vents, and also at a given vent through time. We also document common characteristics of diffuse venting systems at the Tour Eiffel and White Castle vent sites: the same three types of diffuse vents, a comparable concentric distribution of these vent types with respect to the black smokers at each site; and significant differences between the two sites: a greater proportion of mixed end-member fluids, and more temperature and chemical variability with time at WC diffuse vents, with evidence for both sulfate precipitation and dissolution in the subseafloor; more stable fluid temperatures and compositions at TE diffuse vents, with evidence at some vents for lower proportions of mixed end-member fluids, for some degree of conductive heating of the seawater component, and for periods of sulfate dissolution in the subseafloor.

In this discussion, we address the spatial distribution of the different types of diffuse vents at TE and WC, the range of temperature and chemistry of their effluents, and their time variability, and how these characteristics inform us about fluid circulations at the hydrothermal site scale, and to what extend the differences identified between diffuse vents at TE and WC could result from the former being a more mature hydrothermal vent site. We then discuss whether this calls for revisiting previously published estimates of diffuse hydrothermal heat fluxes at the Lucky Strike field. Finally, we discuss the implications of our results in terms of the time and space variability of hydrothermal habitats at Lucky Strike vents.

4.7.1. Characteristics of diffuse vents at TE and WC

A key outcome of our study is the difference, not made in previous description and maps of the Lucky Strike vent field, between diffuse vents located in the sulfide-indurated volcaniclastics, or slab formation, that surrounds the black smoker-bearing sulfide mounds at the TE and WC sites (Figure 4-4), and diffuse vents that are located in the variably degraded and sandy volcaniclastics further away from these mounds. Our temperature monitoring and fluid sampling locations document this distinction. Figure 4-4b and 4d show the limits of the sulfide-indurated slab at TE and WC, with a horizontal imprint of 540 m^2 and 141 m^2, respectively (Table 4-3). Monitoring location TE-2 is our reference for fluids venting out of a crack in the outer region of the slab at TE (Figure 4-3b and 6a), while WC-2 monitors fluids venting next to the sulfide mound at WC (Figure 4-3g and 6b). Fluid temperatures, and tidal variations measured at WC-2 are close to those at the nearby WC-1 smoker, and the sulfide mound (horizontal imprint of only 8 m^2, against 168 m^2 at TE; Table 4-3) has grown during the experiment to include the original WC-2 location (Figure 4-6b). By contrast, TE-2 has the lowest maximum temperature (18°C) of all monitored diffuse locations, and its complex tidal temperature variations can be in part related to stronger currents flushing the crack with colder seawater. This is consistent with local geology, showing that TE-2 may receive seawater not only from above, but also laterally, through voids that exist between successive layers of slab (Figure 4-5a). TE-2 is less than 3 m away from an actively venting flange (Figure 4-5a and 6a) with barite precipitates that suggest fluid temperatures in excess of 130°C. This flange is in a comparable position, relative to the TE slab and sulfide mound domains (Figure 4-4b), to the venting patch monitored by the TEMPO ecological module (Sarrazin et al., 2007) that measured a maximum fluid temperature of 148°C in 2018-2019 (Laes-Huon et al., 2019). TE-2 is also 4.5 m from the TE-3 crack, in non-indurated volcaniclastics with a thin sulfide and sulfate indurated upper crust (Figure 4-3c). Temperatures recorded at TE-3 are up to 80°C, and the estimated end-member fluid contribution is up to 9.6% (Table 4-2). Similar to TE-2, TE-3 temperatures show complex tidal variations, with amplitudes up to 8°C, but there is no indication for a role of current velocity variations. TE-3 is located 25 m (horizontal distance) away from the TE-1 smoker. WC-3 is at a comparable distance from the WC-1 smoker (20 m), in grey sandy material with a thin crust of barite (Figure 4-3h), against the outer edge of the slab (Figure 5e). Temperatures recorded at WC-3 are up to 160°C, with fluids that contain up to 16% end-member hydrothermal component (Table 4-2), and much smaller amplitudes (< 0.6°C) for variations at tidal frequencies than recorded at the TE-2 or TE-3 cracks. Fluids sampled in nearby grey sandy areas in 2016 (Figure 4-2c, left hand panel) had up to 5% end-member fluid,

and temperatures of 40° to 78° (Table 4-2). Such grey areas, with fluids oozing at temperatures > 40°C out of sandy sulfide and sulfate-bearing degraded volcaniclastic material, typically line the edges of the sulfide indurated slab, and the inside of the wide cracks in the slab, at both WC, where they are most developed (Figure 4-2c and 5e), and TE (Figure 4-5b). Being grey, these slow venting areas are not visible in the black and white photomosaics of the vent field (Barreyre et al., 2012). Their cumulated surface imprint at WC, estimated from ROV snapshots (Figure 4-5e), is ~6 m^2. They are spatially associated with white patches that have been mapped by Barreyre et al., 2012: 16 m^2 at TE and ~14 m^2 at WC (Table 4-3). Some of these patches correspond to bacterial mats only (for example the TE white patch in brownish sandy material that was monitored by (Sarrazin et al., 2009), other white patches correspond to zones of white barite (for example next to WC-3), and grey anhydrite and sulfide precipitates, that locally evolve to form a crust over the substratum of degraded volcaniclastics, and may then be fractured (for example at TE-3).

Grey patches at both TE (Figure 4-5b) and WC (Figure 4-5e) are surrounded by brownish sandy domains. These brownish domains display sinuous fissures hosting orange bulbous bacterial mats and ferruginous crust (Figure 4-3e, 3d, 5d and 6a). TE-5 is located in such a fissure, 20m to the north of the most northerly smoker of the TE sulfide mound. It vents fluids at nearly constant temperature (55 to 58°C), with no tidal variations, and a variable proportion of end-member fluid (0.04% in 2019, to 4.1% in 2018; Table 4-2). The 2019 samples are therefore conductively heated seawater, while mixed end-member fluids vented out of the same location in 2017 and 2018 (Table 4-2).

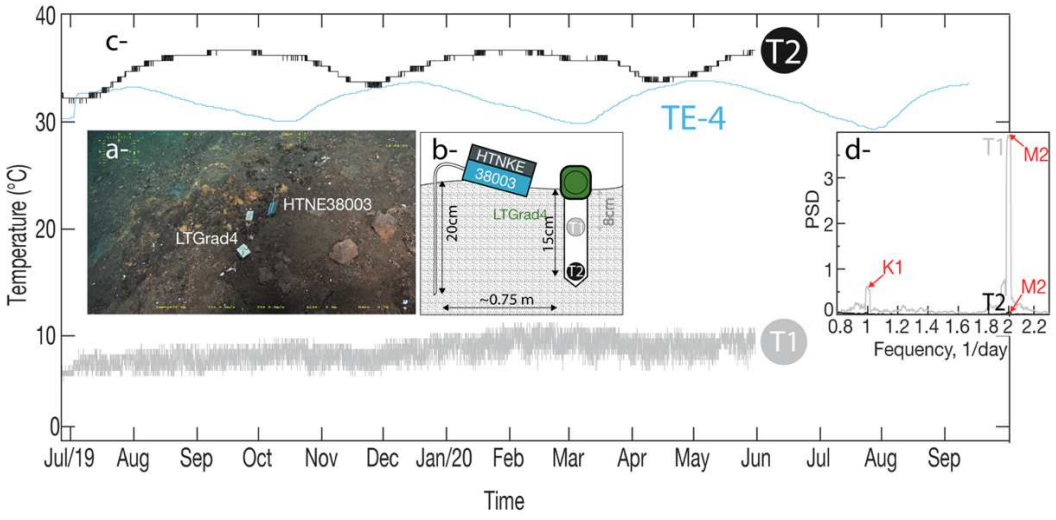

Figure 4-16 – Temperature variations recorded with a 2 probes experimental setup at and near monitoring location TE-4 in 2019-2020. (a) ROV snapshot and sketch showing the HTNKE38003 and LTgrad4 temperature probes. (b) Diagram of probes position at TE-4 with their corresponding depth. (c)Temperature variations recorded by HTNKE38003 and by the 2 iButton sensors of LTGrad4 (T1 and T2). (d) Power spectral density of temperature at diurnal and semi-diurnal frequencies for T1 and T2.

TE-4 is our reference monitoring location for brownish sandy material. It is 3.4 m away from TE-3 (Figure 4-6a), and about 30 cm from a fissure lined with orange bacterial mats (Figure 4-3d). Temperatures recorded at TE-4 have been > 30°C over the monitoring period, with no variations at tidal frequencies, but intriguing ~140 days variations (Figure 4-13a). There being no visible evidence of venting at TE-4 (no macro or meiofauna, no shimmering waters), the significance of such high temperatures in the near seafloor (20 cm bsf at the most, based on the length of the probes) may mean that there is a very high conductive heat flux out of such brownish sandy areas. We do not have constraints on the thermal conductivity of the sandy material, but for comparison, the largest conductive temperature gradient measured on the TAG mound is 157°C/m (Becker et al., 1996). The alternative is that warm fluids are oozing out very slowly through these brownish areas. In order to further investigate this issue, we deployed an additional probe at the TE-4 location in 2019-2020. LTgrad4, ~75 cm away from the other probe (HTNKE38003; Figure 4-16a and b) is made of 2 iButton temperature sensors spaced by 7 cm. The shallowest iButton sensor (T1) is about 8 cm into the ground; the deeper one (T2), is about 5 cm shallower than the tip of the HTNKE38003 probe (Figure 4-16b). T2 recorded temperatures of 31.6 to 36.6°C, with variations over the same 141 to 143 days period (from low to low), as at the nearby HTNKE38003 probe (Figure 4-16c). While we do not have a ready explanation for these ~140 days variations, them being offset between two probes that are less than 1 m apart, indicates significant lateral variability in near seafloor temperatures, that requires a variable nearby shallow heat or fluid source, possibly changes in fluid flux and/or temperature in the fissures lined by orange bacterial mats less than 1 m away (Figure 4-6a). Temperatures recorded by the shallower (~8 cm) T1 iButton of probe LTgrad4 (Figure 4-16b) vary between 6 and 11°C, with a strong semi-diurnal periodicity (Figure 4-16d) that is not recovered by probes buried deeper into the sandy venting area. It is therefore safe to propose that this periodicity is due to tidally modulated mixing with seawater in the upper decimeter of the seabed. It is, as explained above, not clear if the shallow T1 probe was maintained at temperatures up to 11°C by a very high local conductive heat flux, or by a very slow upflow of warm fluids, or both. Further studies of the brownish sandy material domains are needed to answer this question. Whatever the answer, the very shallow seawater circulation identified here would keep seabed temperatures relatively cool in brownish sandy domains, even in cases where, as at TE-4, temperatures rise to > 30°C at depths of only 15 cm into the seafloor (Figure 4-16).

4.7.2. Implications for fluid circulation at the hydrothermal site scale

Our study emphasizes the role of the thin volcaniclastic formation on the characteristics of Lucky Strike diffuse vents (Langmuir et al., 1997; Cooper et al., 2000; Humphris et al., 2002). It is irregular in thickness, up to 1.5 m at TE (Figure 4-5c), perhaps locally thicker at WC. It degrades into a sandy, porous material in the distal parts of both the TE and WC sites, and forms an impermeable cap (the slab formation) in domains that are closer to the sulfide mounds (Figure 4-4). In both cases, it is an intermediate layer, either porous, or impermeable, between the fluids that flow out of the brecciated basalt substratum (Figure 4-5c and 5e), and the vents at the seabed.

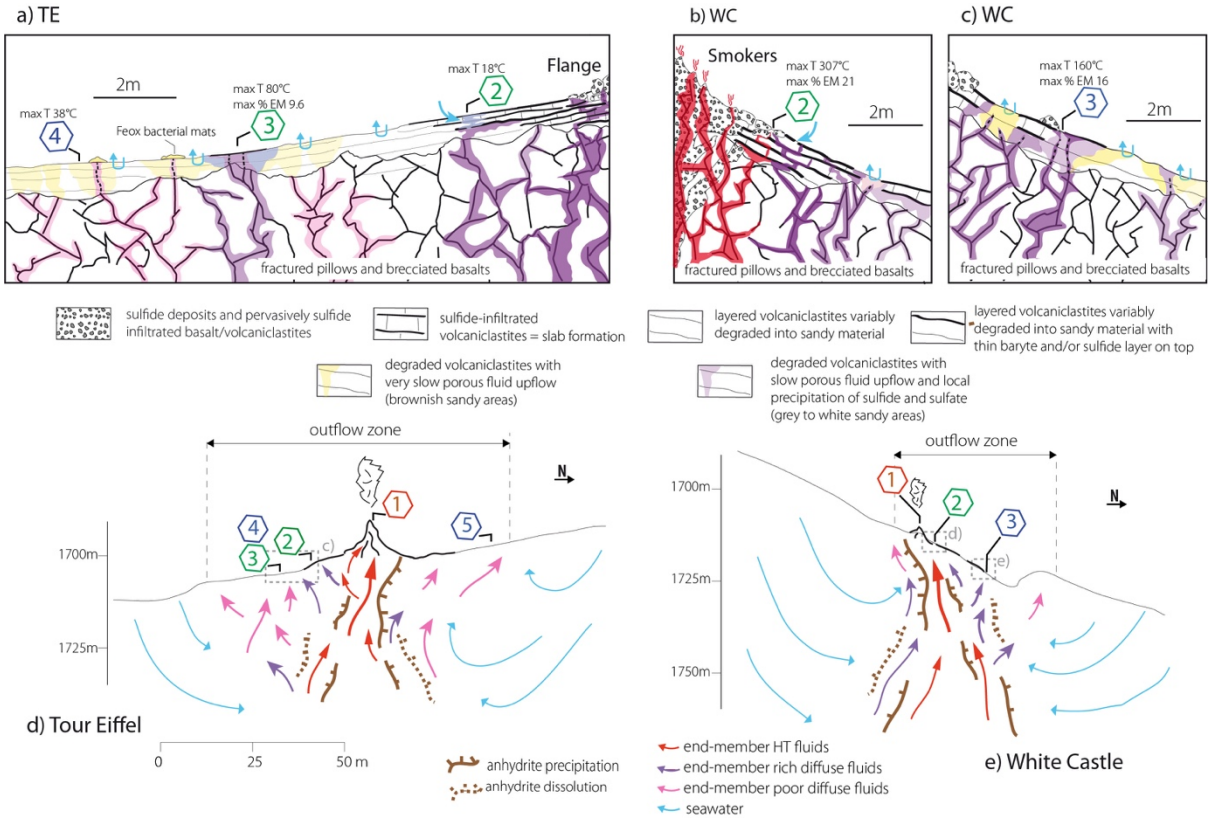

Figure 4-17 – Conceptual sketches of near seafloor fluid circulation at the Tour Eiffel and White Castle sites. (a), (b) and (c) Geological sketches at monitoring locations TE-2, TE-3 and TE-4 (a), WC-2 (b), and WC-3 (c). Same scale, no vertical exaggeration, location in (d) and (e), maximum recorded temperature and estimated % of end-member fluid (% EM; Table 4-2) shown for each location. (d) and (e) cross-sections, same scale, no vertical exaggeration of topography. Diffuse venting fluids are produced by subseafloor mixing of seawater and end-member fluids, with sulfide and anhydrite precipitation, and anhydrite dissolution.

The impermeable slab forms a cap that confines hot fluids and might allow for conductive heat exchange with seawater entrained in cavities of the slab, as proposed by Cooper et al. (2000). Seawater heating in or beneath the slab, conductively or by mixing, could cause anhydrite precipitation, which would be dissolved if hydrothermal outflow and the associated heating diminishes. Dissolution of such shallow precipitates could explain the elliptical

depressions observed for example in the extinct site to the west of TE (Figure 4-4a). Seawater entrainment in and beneath the slab also explains the low temperatures (<20°C) recorded at cracks such as TE-2 (Figure 4-17a), in close proximity to higher temperature vents, such as the flange next to TE-2 (Figure 4-5a). Venting of high and low temperature fluids successively at the same location of the same crack, as seen at WC-2 in late 2018 (Figure 4-12b), is also explained by shallow seawater entrainment. Thus, while fluids that vent in cracks of the slab may indeed be low temperature, this is best explained by very shallow mixing with seawater and there is substantial evidence that fluids venting out of the basalt basement beneath the slab are in most cases hotter (> 130°C), including near the southern edge of the slab domain at TE (the flanges near TE-2 and the TEMPO diffuse venting patch; Laes-Huon et al., 2019), and in the outer regions of the slab at WC (WC-3; Figure 4-17c).

The sandy degraded volcaniclastic layers, on the other hand, form a porous cover through which hydrothermal fluids ooze slowly, forming diffuse venting patches, some of which (such as TE-3; Figure 4-3c and 17a) are capped by a few cm-thick crust of volcaniclastic sand indurated by sulfides and anhydrite; fluids flow out of cracks in this thin crust. At WC-3 (Figure 4-3h and 17c), the venting patch became similarly capped, in the first year of monitoring, by a mm-thick crust of barite. The formation of such sulfate crusts indicates that fluids did reach sufficiently high temperatures at some point to heat near seabed seawater over sulfate precipitation temperatures (> 130°C). Disseminated sulfide may also precipitate in the sandy substrate from cooling hydrothermal fluids, ultimately leading to the formation of sulfide and sulfate indurated slab material. Anhydrite found disseminated in the grey sandy substratum could, on the other hand, precipitate from seawater in the porous matrix next to hot upflow, then dissolve back into lower temperature upflow. At least part of the variable anhydrite precipitation/dissolution signatures found in the fluid chemistry at WC-3, TE-3 and TE-5 (Figure 4-7b) could thus originate in the volcaniclastic layer, and thus do not necessarily reflect anhydrite precipitation/dissolution in the basalt basement (Figure 4-17, d and e).

Temperatures measured by our probes at both TE-3 and WC-3, at depths of 15-20 cm into the sandy seabed, are relatively hot (up to 80°C and 160°C respectively), and the fluids that ooze out contain > 9% endmember fluids. Yet, Mittelstaedt et al. (2012) report temperatures of only 11°C (and outflow velocities 0.5 to 1.4 mm/s) for fluids oozing out of the TE-3 crack just a few meters from the emplacement of our probe. More than a temporal change between the 2 experiments, this probably results from lateral variability in the temperature of the fluids that ooze through the porous volcaniclastics beneath the cracked crust. Further work (modelling and the acquisition of new monitoring data) is needed to document and explain this lateral

variability, and also the variability observed between the two probes at TE-4 (Figure 4-16). Our working hypothesis is shown in Figure 4-17a and c. It involves a decimeter to meter scale, fracture-controlled, permeable network in the brecciated basalts, which we propose based on crack distribution in basalt outcrops (for example in Figure 4-5e). Porous advection of the fluids that come out of these permeable fractured basalts, into the smaller scale and more homogeneous permeability of the volcaniclastic layer would lead to a widening of the upflow, with smaller upflow velocities that decrease laterally, and would translate into laterally decreasing venting temperatures at the seabed. In the outer domains of this meter-scale upflow, the dominant mechanism of heat transfer would be conductive. Based on this conceptual sketch, we propose that fluids at TE-3 and WC-3, where there are visible shimmering waters, are probably venting at velocities of several mm/s (Mittelstaedt et al., 2012), and that their maximum temperatures and minimum degrees of mixing are least modified from those of fluids that come out of the basalts underneath (Figure 4-17a and c).

The grey to white venting patches at both TE and WC are typically 1 to 5 m^2, and pass laterally to brownish seabed, in which there are sinuous cracks lined with orange bulbous bacterial mats and ferruginous crust (Figure 4-17a). These sinuous cracks show no visible evidence for fluid venting, which again, could mean very slow venting, or no current venting. Our type monitoring location for fluids coming out of such cracks is TE-5 (Figure 4-3e), where we do observe shimmering waters, and thus relatively fast venting velocities. The temperature and mixing degree of the TE-5 fluids (up to 58°C and variable between 0.04% and 4% end-member fluid) could thus be close to those of fluids coming out of the basalts underneath the orange cracks.

Temperatures recorded at TE-5 have no semi-diurnal variations, and semi-diurnal temperature variations recorded at WC-3 have amplitudes < 0.6°C (Figure 4-13a). By contrast, semi-diurnal venting temperatures variations at TE-3 have amplitudes up to 8°C (Figure 4-12a) and are most likely due to local seawater entrainment in the crack. More generally, while semi-diurnal temperature variations with amplitudes of a few degrees (°C) are recorded at several diffuse vents, they can be linked to very local (meter scale or less) seawater entrainment, in cracks (TE-2, TE-3), or in the upper decimeter of the sandy seabed. There is therefore no evidence for tidally modulated temperature variations of several degrees (°C) in the fluids flowing out of the basalt basement. If such large amplitude variations exist, however, in fluids that come out under the porous volcaniclastics, they will likely be damped during slow upflow through the porous layer.

Based on seafloor observations, fluid chemistry and monitoring of vents at the seabed, we therefore get a picture of the fluids that come out of the basalts beneath the slab and beneath the non-indurated volcaniclastic layer domains at both TE and WC. We constrain their range of temperatures (from 304°C at WC-2 to 58°C at TE-5; Figure 4-17a and b), estimated minimum degrees of mixing (21% at WC-2 to 0.04% in 2019 at TE-5), and spatial distribution (significant lateral variations at meter-scale). We find that high amplitude temperature variations at semi-diurnal tidal frequencies recorded at several diffuse TE vents likely originate in the thin slab/volcaniclastic layer and thus do not require complex poroelastic configurations in the basalts underneath (Crone & Wilcock, 2005). We also find that lateral and temporal changes in fluid temperature and flow in this thin layer may produce at least part of the chemical signatures for anhydrite precipitation or dissolution at both TE and WC. Thus, while anhydrite precipitation is probably required (Guo et al., 2020; Larson et al., 2015; Lowell et al., 2003; Lowell & Yao, 2002) to help focus the end-member upflow beneath vent sites (Figures 17d and e), it is not clear that we see its signature in present-day diffuse effluents. On the other hand, mixing with a conductively heated seawater component, as identified from fluid chemistry for at least some samples at most diffuse vents in this study (Figure 4-8), most clearly at TE-5 in 2019 (Table 4-2), and in several samples reported by Cooper et al. (2000), must occur in the basaltic substratum beneath both vent sites.

Conceptual sketches in Figure 4-17d and e are drawn to scale based on these constraints, and on the overall circulation pattern that is expected in the basaltic substratum from models of near site seawater entrainment due to hot and rapidly flowing end-member fluids (Guo et al., 2020; Larson et al., 2015; Lowell et al., 2003; Lowell & Yao, 2002). End-member fluids are found at (TE-1 and WC-1), and within meters (WC-2) of the sulfide mound. Hot (> 80°C) and end member rich (> 9%) fluids vent out of the basalts up to at least 25 m of the top of the sulfide mound at TE (TE-3), and at least 20 m at WC (WC-3). They form grey and white patches at the seabed that are typically 1 to 5 m2, and spaced by a few meters (Figure 4-5e), which, based on our interpretation of the role of the porous volcaniclastic layer, suggests that venting out of the underlying basalts is more localized, faster, and also spaced by a few meters (Figure 4-17a and c). End member poor fluids are associated with the sinuous cracks lined by bulbous orange bacterial mats and ferruginous crust, and our results at TE-5 suggest that they are relatively hot (50-60°C), and have variable proportions of end-member fluids (0.04 to 4%). These orange cracks are found within meters of end-member rich vents in the south of TE (Figure 4-6a), up to 30 m to the north of the top of the sulfide mound at TE (TE-5), and up to 37 m to the north

of the top of the sulfide mound at WC (Figure 4-5d), although we do not have evidence for active venting there.

4.7.3. Tour Eiffel and White Castle: maturation of site scale hydrothermal circulation and diffuse venting at two Lucky Strike vent sites

Based on the horizontal extent (168 m^2; Table 4-3) and height (more than 10 m above the surrounding slab, and 15 m above the non-indurated volcaniclastic outer domains), of the TE sulfide mound, it is clear that TE is a more mature site than WC (horizontal extent of sulfide mound only 8 m^2). Maturation is clearly a factor for the evolution of the near mound regions of WC: over a 3 years monitoring period we have documented a 2 m northward growth of the mound's horizontal imprint (Figure 4-6b), although its height has not changed. At WC, due to the local topography, the mound is not centered and diffuse vents only extend to the north (Figure 4-17). This slope effect is also visible, to a lesser extent, at TE, where most diffuse vents are mapped in the southern and lower slopes, while the northern, upper slopes are vent-free, except for the network of sinuous cracks monitored at TE-5 (Figure 4-17d).

The maximum horizontal distance from the top of the mound to the edge of the slab (~22 m) is actually similar at the two sites, with relatively high temperature fluids (up to 160°C at WC-3 and 148°C at the TEMPO flange at TE) coming out near the outer edge in both cases. But the slab surface is dominantly flat, with lots of wide cracks, at WC (Figure 4-5e), and rough, with several meter-high flanges and other sulfide constructions, and only a few cracks at TE (Barreyre et al., 2012; Girard et al., 2020). The abundance of cracks at WC may be partly a response to local slopes, but it is also clear that the slab there is thinner and therefore that site maturation at TE also caused a thickening of the slab by sulfide constructions, making it less easy to crack, hence more impermeable, and possibly focusing more hot fluids toward the mound (Figure 4-17d). End member rich fluids also come out in the sandy volcaniclastic material up to 24 m (TE) and 22 m (WC) from the top of the sulfide mound. Thus, the domain of end-member fluid upflow (i.e. the sulfide mound) is currently growing at WC, and the slab there may be getting thicker in the future, but the domain of end member rich fluid outflow has a similar along strike extent at the two sites.

The surface imprint of WC, however, is smaller: it is shaped as a flat ellipse, with very little venting beyond the outer edge of the slab (Figure 4-4d), except in the northeast, with several sinuous cracks that may actually not be currently active (Figure 4-5d). The domain of documented end member rich fluid upflow at WC is thus only 8 to 10 m-wide, and elongated in the dominant direction of the local faults (Figure 4-4d). The domain of end member rich fluid

upflow documented at TE, is also elongated in the dominant faulting direction, but significantly wider, 20 m based on the distribution of active flanges around the slab edges, and 25 m based on the outer contours of the slab. This difference in across-strike extent may result from an intrinsic difference in the geometry of the upflow zone between the two sites, with a more circular upflow beneath TE, or from a topographic control on vents distribution at WC. It might also be that the upflow is also a flat, fault-controlled ellipse at some depth beneath TE, but that the near seafloor hydrothermal system there grew through time in the across strike direction (possibly as a result of stockwork growth, or of growing a more impermeable slab domain). There could also be a link between site maturation and the greater extent of end member poor diffuse vents at TE (Figure 4-17a): these vents, associated with orange bacterial mats and ferruginous crust, are found near the outer limit of the site, and require a broad domain of secondary seawater circulation (Figure 4-17d).

4.8. Should we revisit estimates of diffuse hydrothermal heat fluxes at Lucky Strike vent sites?

Estimates of field scale (187 to 1036 MW; Barreyre et al., 2012) and vent site scale (18.75±2.22 MW for TE; Mittelstaedt et al., 2012), diffuse heat fluxes at Lucky Strike, are based on mapping the horizontal imprint of mounds, patches, flanges, and cracks (Table 4-3), and estimating corresponding heat fluxes per m^2 (Table 4-4), using available in situ fluid temperature and venting velocity measurements (Cooper et al., 2000; Mittelstaedt et al., 2012; Sarrazin et al., 2009). These estimates carry large uncertainties, because diffuse vents are complex, with large variations in venting temperature and velocity along a given crack (Mittelstaedt et al., 2012), or patch (this study), and also between diffuse vents of the same category (Table 4-4). Most of the energy flux in these estimates comes from the large surface imprint of mounds, patches and flanges, that are grouped in the calculation in spite of obvious differences in venting modes (for example fluids venting at mounds and flanges are commonly hot enough to cause sulfate precipitation from seawater, but clearly do not vent out of the entire surface, while fluids at patches do). While this is clearly a rough approach, overestimates of venting surfaces at mounds and flanges are balanced by using low heat flux per m^2 values derived from a monitoring experiment led on TE patches (Sarrazin et al., 2009)

.

Site	Mound (m^2)	Flanges (m^2)	Ligth grey to white patches (m^2)	Grey patches (m^2)	Cracks (m)	Cracks (m^2)	Q_{min}/Q_{max} (1) (W)	Slab (m^2)	Q_{min}/Q_{max} (slab) (W)
TE	168	22	16	2	74	3.0	6.72/75.63	540	28.88/57.76
WC	8	0	14	6	26	1.0	1.62/11.71	141	7.54/15.08

Table 4-3 – Diffuse venting surfaces at TE and WC measured from seafloor photomosaics, adapted after original contours from Barreyre et al. (2012). Cracks surfaces are calculated for an average crack opening of 4 cm (Barreyre et al., 2012). Slab as in Figure 4-4c and d. $Q_{min,max}$ (1) is the diffuse heat flux calculated as in Barreyre et al. (2012); see parameters in Table 4-4. $Q_{min, max}$(slab) is the heat flux for cracks representing 1/100 of the slab surface, venting 140°C end-member rich fluids at 10 to 20 mm/s (see text and Table 4-4).

We propose a different, independent, yet also quite rough approach, based on our interpretation of the various types of diffuse vents documented at the seabed in terms of what fluids could actually vent out of the basalts beneath the slab, or beneath the non-indurated volcaniclastic domains (Figure 4-17a, b and c). Our study points to end member rich fluids coming out of this basalt basement over an area that is about that of the slab domain at both TE and WC, through fissures and cracks that are spaced by a few meters (based on the distribution of venting patches). We propose an average temperature of 140°C (average for WC-3), and venting velocities of 10 mm/s to 20 mm/s (average for seabed cracks; Cooper et al., 2000; Mittelstaedt et al., 2012) for these fluids, and propose that their total surface is about 1/100 the slab surface. With an average crack opening of 4 cm, this would translate into a total length of basement venting cracks of 135 m at TE and 35 m at WC. Although there is not necessarily a coincidence between this basement cracking and the cracks mapped at the seabed, we see as indirect support that the lengths of seabed cracks at TE and WC are lower but of the same order (Table 4-3). Diffuse heat fluxes estimated with this approach (28.88 to 57.76 MW at TE and 7.54 to 15.08 MW at WC), are in the middle (TE) to upper (WC) range of the Barreyre et al. (2012) estimates (Table 4-3), also an indirect indication that in spite of all the approximations, two independent approaches point to diffuse heat fluxes at the Lucky Strike vent sites in the range of several MW, to a few 10s of MW, depending on the size of the sites.

	Fluid T °C	Fluid v mm/s	min max heat flux W/m2	
mound+flanges+patches (1)	8 to 20	1 to 5	0.017	0.329
cracks (1)	17.5 to 33	20	1.113	2.384
mound+flanges+patches (2)			0.078	
crack TEMPO (2)	38.5	15	2.124	
patch WC-3	140	1 to 5	0.535	2.674
crack/patch TE-3	80	1 to 5	0.308	1.539
grey patch	50	1 to 5	0.188	0.941
cracks beneath slab	140	5 to 20	2.674	10.696

Table 4-4 – Fluid temperature, fluid venting velocity and corresponding range of diffuse heat flux per m^2, calculated using Bischoff & Rosenbauer (1985) seawater equation of state at 200 bars to obtain fluid density and thermal capacity values. (1) range of values used in Barreyre et al. (2012) and in Table 4-3; (2) average heat flux per m^2 value used for patches, flanges and mound in Mittelstaedt et al. (2012), based on a value proposed in Sarrazin et al. (2009), and temperature and fluid velocity measured at the TEMPO crack, also in Mittelstaedt et al. (2012). For WC-3, TE-3, and a generic grey patch, temperatures are maximum (TE-3), or average values from monitoring reported on in this study; venting velocities are based on monitoring of TE patches by Sarrazin et al. (2009). For the "cracks beneath the slab" category, the temperature is for end-member rich fluids that could vent out of the basalt substratum beneath slab domains, as sketched in Figure 4-17a, b and c.

4.9. Time and space variability of hydrothermal habitats at Lucky Strike vents.

This study bears on fluids as they come out beneath hydrothermal seabed habitats. Our probes recorded temperatures at least 8 cm and up to 20 cm into the seabed, and the fluids we sampled are distinct from the mix of hydrothermal effluent and bottom seawater that actually surrounds the fauna. Our results thus bear on the hydrothermal effluent component of the system, not on how it may be modified for example by currents washing effluents away and displacing bottom seawater (Scheirer et al., 2006; Tivey et al., 2002).

Our results suggest that relatively hot (>80°C) and end-member rich (> 9%) fluids actually do come out up to 25 m from the top of the hydrothermal mounds at both TE and WC. These high temperature fluids come out in grey to white patches that are well developed in WC, and host a rich meiofauna that has yet to be studied. We also show that hydrothermal fluid temperatures measured in cracks, or in sandy patches with low venting velocities, are affected by very shallow seawater entrainment. In cracks, this entrainment appears to be occasionally enhanced by currents (TE-2). In sandy patches, it occurs through porous advection in the upper decimeter of the seabed (Figure 4-17a). In both cases, this shallow seawater entrainment results in venting temperatures that are substantially lower than the temperature of the fluids that actually come out of the basaltic basement underneath.

Shallow seawater entrainment is modulated by semi-diurnal tides and results in temperature variations of several degrees (°C) (TE-2, TE-3). This must also affect oxygen concentrations, and the content in end member smoker-type fluid. Our results document these semi-diurnal variations, with periods of low or high coherence between temperature, seafloor pressure, and current velocities, the complex and time variable effects of spring, neap, and equinox tides, occasional similarities at nearby monitoring locations, and the more general lack of correlation. While we do not explain these complexities, they could prove useful for future studies of tidal forcing at TE or WC habitats.

In the sandy brownish domains outside the slab formation, where there is no visible evidence for fluid venting, probes that monitor temperature at 15-20 cm depth record lower amplitude tidal variations than shallower probes, and relatively high temperatures (> 30°C), that could indicate that there is extremely slow venting in at least a portion of these brownish areas. In patches that do produce well visible shimmering waters (i.e. relatively high venting velocities; WC-3, TE-5), tidal variations are faint to absent. This is probably because higher upflow velocities prevent the porous advection of seawater in the seabed and therefore the acquisition of a strong tidally modulated temperature signal by the venting fluids.

4.10. Conclusions

Our results from a 3 year monitoring experiment emphasize the complexity of diffuse venting at both Tour Eiffel and White Castle: at least three types of vents, not counting the flanges, with characteristics that are largely controlled by local geology (cracks in the slab, cracks and patches in non-indurated volcaniclastics); variations between nearby vents and in some cases at a given vent, in fluid temperature, degree of mixing, chemical indicators for the precipitation or dissolution of sulfates, and local evidence for conductive heating of the seawater component; vent temperature variations that are uncorrelated between vents only a few decimeters apart, and reveal tidal forcing effects that vary in energy and phase lag, again between nearby vents, and also at a given vent through time. While we leave the cause of many of these complexities unresolved, we propose a geologically consistent conceptual framework, in which to interpret diffuse venting diversity, and the characteristics of the associated habitats. The thin layer of volcaniclastics that covers the basalts in the Lucky Strike field area, plays a key role in this framework, as an intermediate layer, either porous or impermeable depending on whether it has been indurated by hydrothermal precipitates, between the fluids that come out of the basalt basement, and the vents at the seafloor. Our reconstructed picture of the fluids that come out of the basalt points to temperatures and degrees of mixing between 300°C and 21%

next to the sulfide mounds, and 60°C with 0 to 4% mixing in distal parts of the Tour Eiffel site. We find that hot (>80°C) and end member rich (> 9%) fluids likely come out of the basalts up to 25 m from the smokers at both Tour Eiffel and White Castle. High amplitude temperature variations at semi-diurnal tidal frequencies recorded at several diffuse TE vents likely originate in the thin slab/volcaniclastic layer, as could for a significant part, the chemical signature for sulfate dissolution or precipitation. Mixing with a conductively heated seawater component on the other hand, probably occurs in the basaltic basement. Based on the distribution and diversity of diffuse vents at the seabed, we propose rough estimates of minimum diffuse energy fluxes at Tour Eiffel (28.9 MW) and White Castle (7.5 MW) that fall in the median to upper range of previous estimates based on seabed venting temperatures and velocities.

Appendix – Supplementary material

In this section we provide supplementary material submitted with the manuscript includes the following six supplementary figures:

- Figures S1 and S2 provide additional information on fluid chemistry.
- Figure S3 shows the seafloor pressure data used in the paper.
- Figure S4 compiles data that are also plotted in Figures 9, 12 and 13. Its purpose is to facilitate the intercomparison of fluid temperature variations recorded at the Tour Eiffel and White castle hydrothermal sites.
- Figure S5 show the time variation of the coherence at the M2 tidal frequency calculated over the 3 years of survey between vent temperatures and current velocity.
- Figure S6 compares coherence values at the M2 frequency between venting temperatures and current velocity between venting temperatures and seafloor pressure.

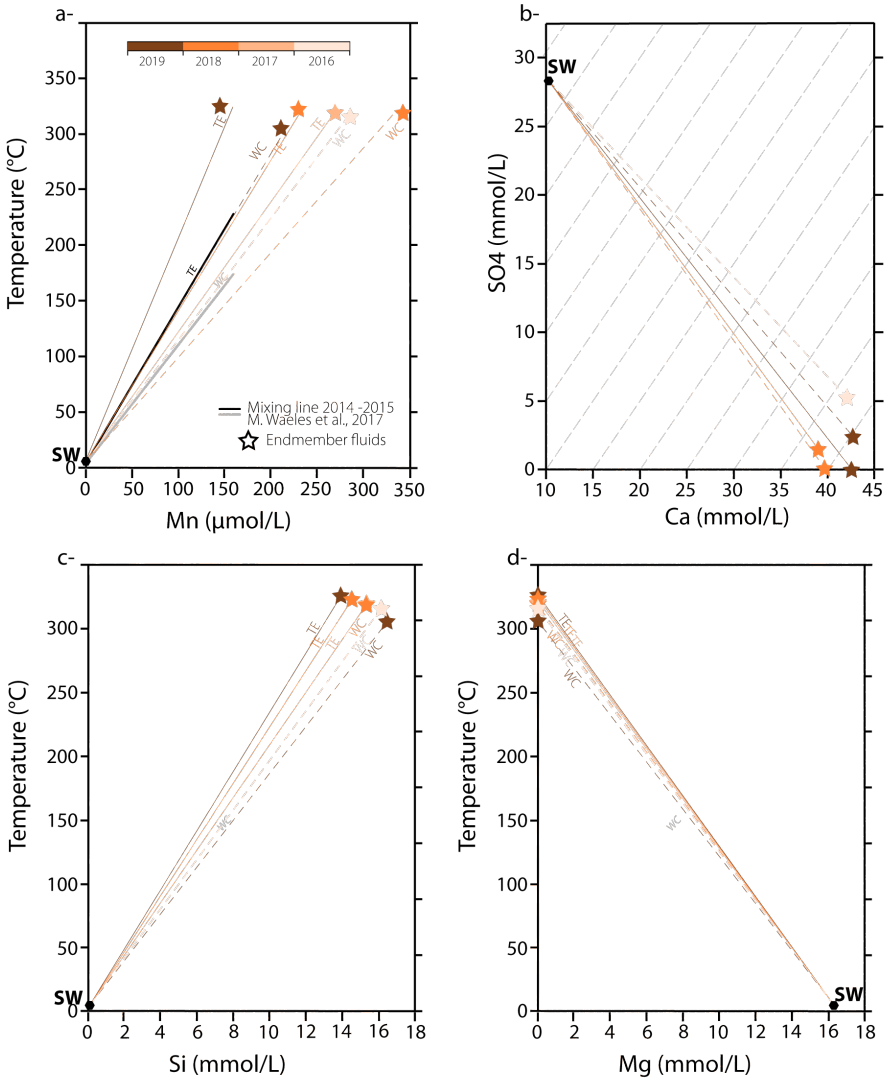

Figure S4-1 – (a) Total manganese and fluid temperature measured by the ROV or manned submersible for focused end member fluids sampled at monitoring locations TE-1 and WC-1 in 2016-2019, with linear trends to seawater composition (SW; Millero et al., 2008). Mixing trendlines measured in the corresponding black smoker plumes in 2014-2015 (Waeles et al., 2017) are also plotted (black and grey lines). (b) Calcium and sulfate ion contents for focused end member fluids sampled at monitoring locations TE-1 and WC-1 in 2016-2019, with linear trends to seawater composition (SW; Millero et al., 2008). Dashed grey lines trace the concentrations expected for anhydrite dissolution or precipitation. (c) Silica and measured fluid temperature for focused end member fluids sampled at monitoring locations TE-1 and WC-1 in 2016-2019, with linear trends to seawater composition (SW; Millero et al., 2008). (d) Magnesium and measured fluid temperature for focused end member fluids sampled at monitoring locations TE-1 and WC-1 in 2016-2019, with linear trends to seawater composition (SW; Millero et al., 2008).

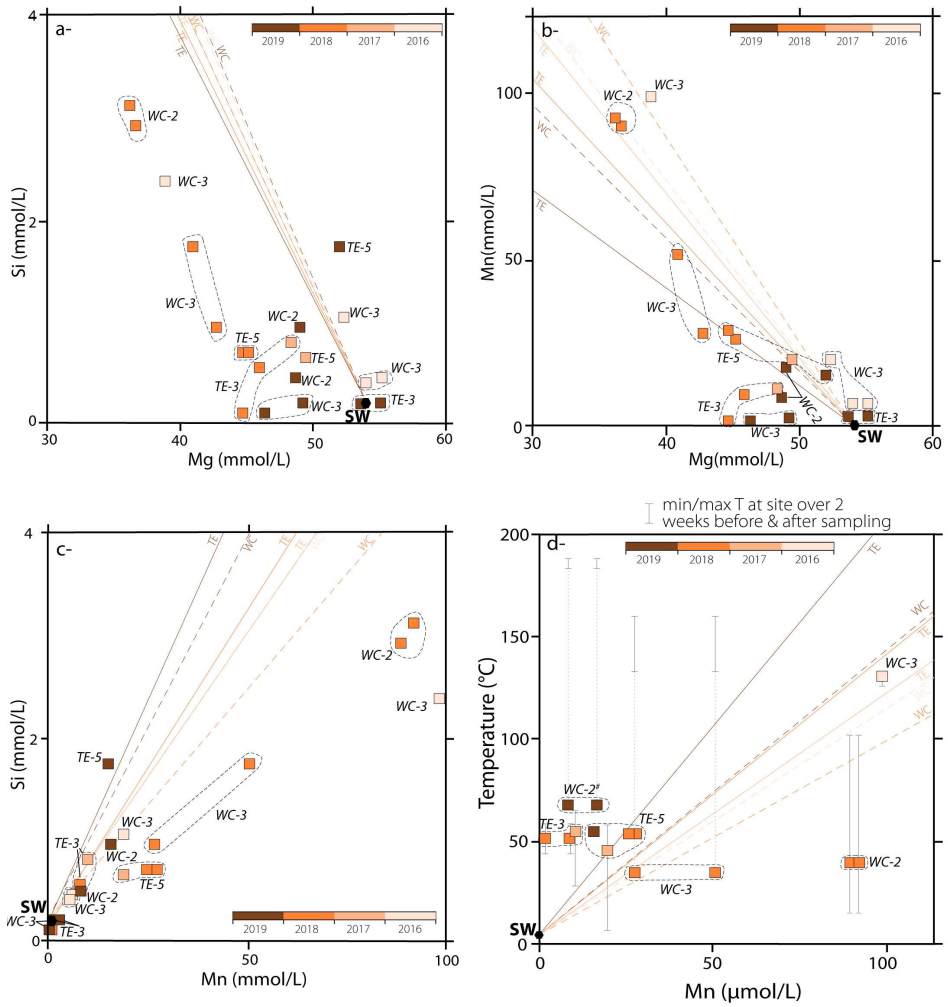

Figure S4-2 – Composition and/or temperature of diffuse fluids sampled at or near the Tour Eiffel (TE) and White Castle (WC) monitoring locations in 2016, 2017, 2018 and 2019 (see color scale and Table 4-2). Solid and dotted lines labelled WC or TE join the measured focused end-member fluid compositions and/or temperature, to seawater composition (SW) from Millero et al. (2008). (a) Magnesium and silica contents. (b) Magnesium and manganese contents. (c) Manganese and silica contents. (d) Total manganese and fluid temperature. Temperature values (Table 4-2) were measured by the ROV or manned submersible prior to fluid sampling. Grey error bars show the min and max temperature measured by autonomous temperature probes deployed at corresponding monitoring location for a period of a week before and after fluid sampling.

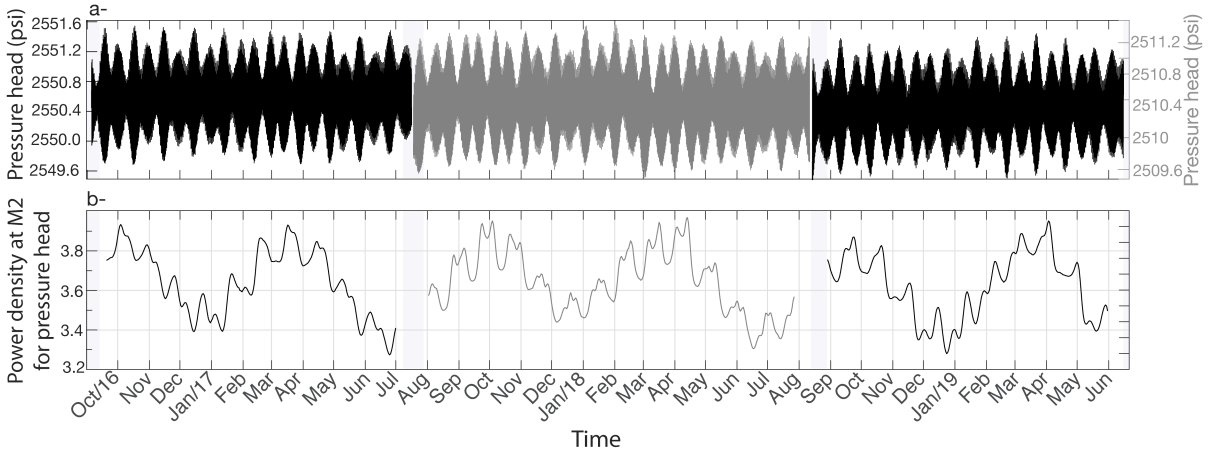

Figure S4-3 – Time variation of seafloor pressure (a) and of the power spectrum density (PSD) of seafloor pressure at the M2 frequency (b) over the 3 years of the experiment. Values for deployment years 2016-2017 and 2018-2019 are shown in black, values for deployment year 2017-2018 in grey (different location; see Figure 4-1). PSD values in b are calculated for a 30 days sliding window, 1 day sliding time.

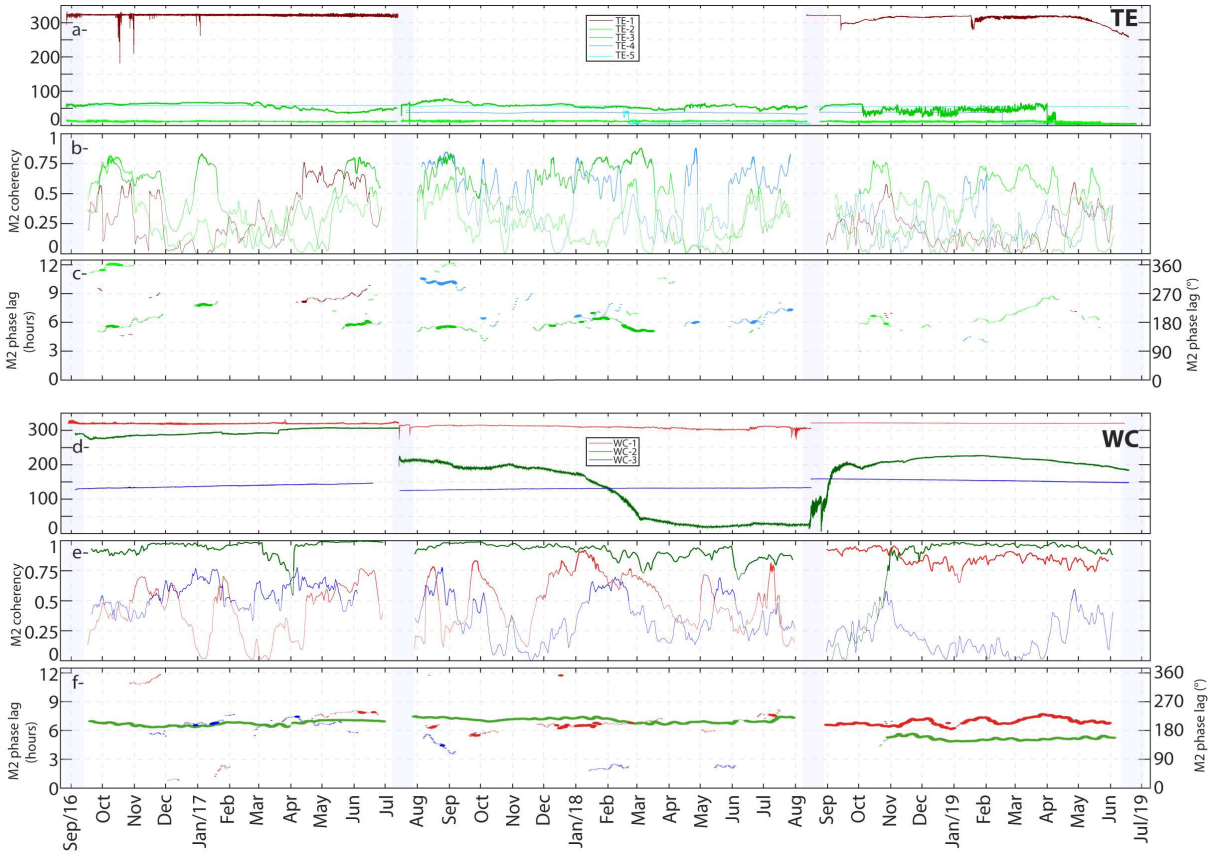

Figure S4-4 – Temperatures recorded over the 3 years of survey at focused and diffuse vents at TE and WC, and time variations of the coherence and phase lag with seafloor pressure at the M2 tidal frequency (30 days sliding window, 1 day sliding time). Light grey intervals correspond to maintenance cruises. This figure compiles data plotted in Figure 4-9, 12 and 13 using the same color codes. Its purpose is to facilitate intercomparison of time variations recorded at several monitoring locations of the same hydrothermal site. (a) and (d) Temperature time-series for monitoring locations at TE and WC respectively. (b) and (e) Time variation of the coherence calculated between temperature and seafloor pressure at the M2 tidal frequency at TE and WC respectively. (c) and (f) Time variation of the phase lag calculated between temperature and seafloor pressure at the M2 tidal frequency for M2 coherence > 0.75 (thicker lines), or > 0.5 (thin lines) at TE and WC respectively. Light grey intervals correspond to maintenance cruises.

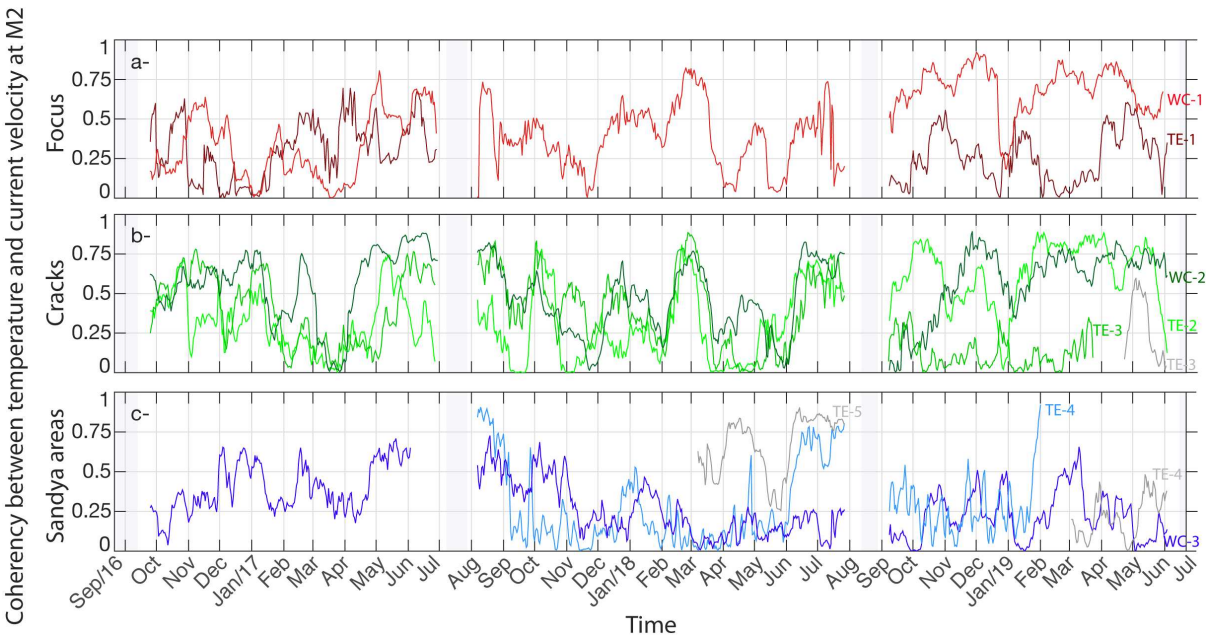

Figure S4-5 – Time variation of the coherence calculated over the 3 years of survey at focused and diffuse vents at TE and WC between vent temperatures and current velocity at the M2 tidal frequency (30 days sliding window, 1 day sliding time). Light grey intervals correspond to maintenance cruises. (a) focused vents TE-1 (dark red) and WC-1 (red). (b) at diffuse vents in cracks TE-2 (pale green), TE-3 (bright green), and WC-2 (dark green); (c) at diffuse vents in sandy areas TE-4 (pale blue), TE-5 (electric blue), and WC-3 (dark blue).

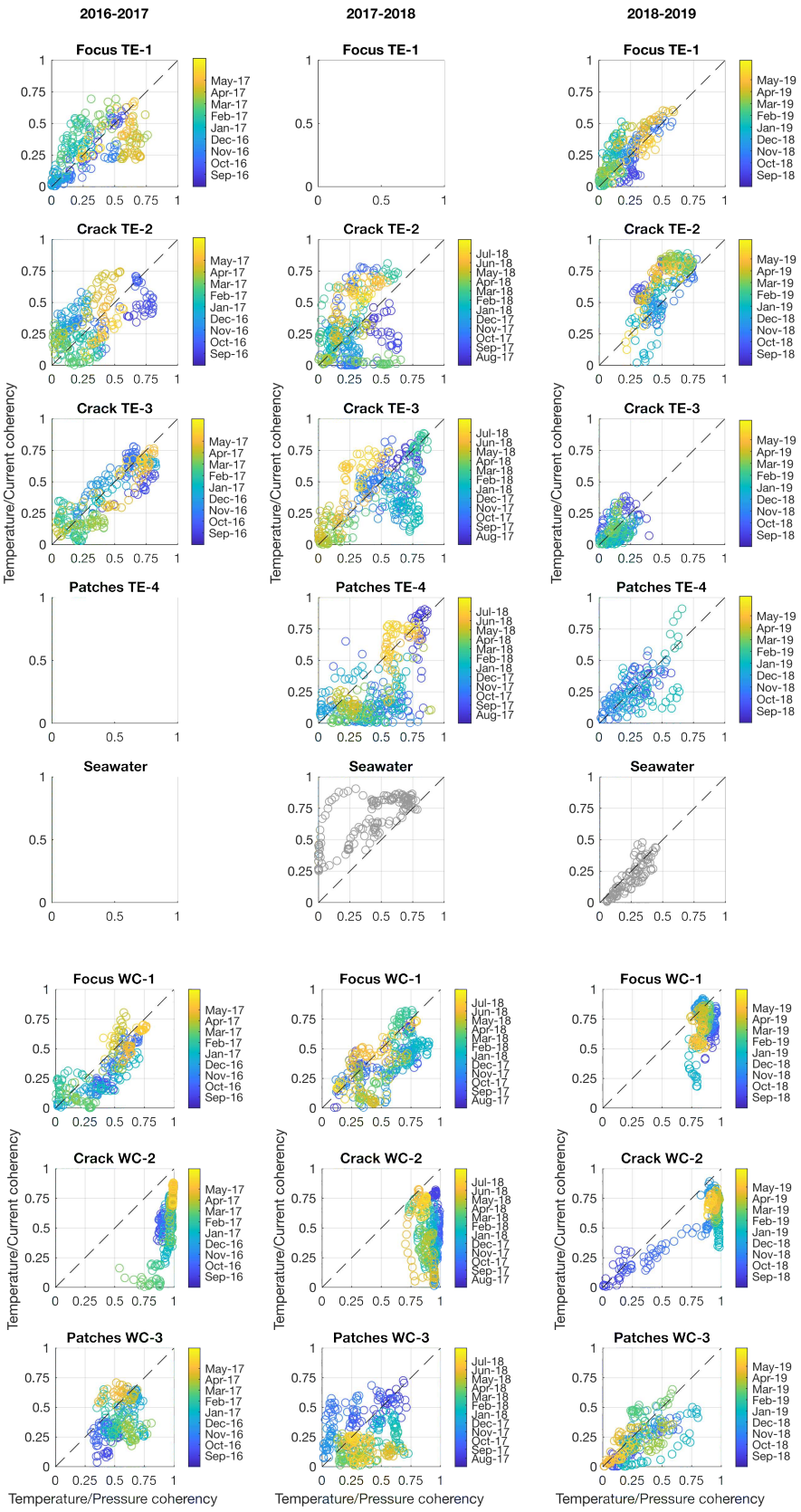

Figure S4-6 – Plots showing coherence values at the M2 frequency between venting temperatures recorded over the 3 years of the experiment at the TE and WC monitoring locations and current velocity as a function of coherence values at the M2 frequency between the same venting temperatures and seafloor pressure. Coherence values calculated for a 30 days sliding window, with a 1 day sliding time. Each dot represents 1 day (dates indicated by color scale). Panels with grey dots correspond to temperature data recorded when probe had fallen off the TE-5 vent (in 2018) or the TE-4 vent (in 2019; Figure 4-13a).

Part III

Modelling diffuse flow dynamics at the hydrothermal site scale

Foreword

In this chapter, we present our ongoing work on numerical modeling of diffuse flow formation and circulation at the site scale, allowing diffuse flow at temperatures <80°C at only a few meters away of the focus high-temperature fluids venting at black smokers. This work was conducted in collaboration with Fabrice J. Fontaine, of the Observatoire Volcanologique du Piton de la Fournaise and from the Institut de Physique du Globe de Paris, and with my advisor Mathilde Cannat. A stay of 5 weeks at the Observatoire Volcanologique du Piton de la Fournaise at La Réunion was completed in November 2019 to initiate our work on numerical models with the COMSOL software.

This project started from numerical models developed by Fabrice J. Fontaine that we studied to explain the formation of diffuse flow through shallow secondary circulation in the subseafloor below hydrothermal sites at MORs. This model includes zone of impermeability in the domain of 150-250°C, preventing heat exchange by advection. This leads to the formation of low temperature flow close to the main hot discharge zone, equivalent to low-temperature diffuse fluids observed close to high-temperature focused vents. Our goal was to adapt this model using interactive modeling software to make numerical simulations more accessible to me as a novice in numerical modelling.

We opted for the COMSOL numerical interface whose purchase was supported by the Luckyscales ANR project. I first conducted several simple models to teach myself about the COMSOL interface and to test the different parameters impacting the circulation of hot fluids in a porous media. Then we added anhydrite precipitation following Fontaine et al. (2001). We then selected the key geophysical and physical parameters to vary, coupled to possible mineral precipitation, to test the formation of diffuse flow in a temperature range of 10-80°C close to a main discharge zone >300°C. The results of these simulations are compared with in situ observations from the Lucky Strike hydrothermal field (chapter 4 of this thesis).

Chapter 5.
Modelling diffuse flow dynamics at the hydrothermal site scale

Benjamin Wheeler[1], Fabrice Fontaine[1 and 2], Mathilde Cannat[1]

[1] Université de Paris, Institut de Physique du Globe de Paris (IPGP), UMR 7154 CNRS, 1 rue Jussieu, 75238 Paris cedex 05, France (cannat@ipgp.fr)

Université de Toulouse, 14 Avenue Edouard Belin, 31400 Toulouse

[2] Observatoire Volcanologique du Piton de la Fournaise (OVPF), 14RN3 - km 27, 97418 La Plaine des Cafres, La Réunion

5.1. Introduction

This chapter presents the numerical part of our study on diffuse flows formation at black smoker type hydrothermal vent sites based on in-situ observations derived from the physical and chemical study of hydrothermal fluids at the Tour Eiffel and White Castle sites. Processes controlling the circulation and physical/chemical characteristics of hot hydrothermal fluids and related diffuse fluids have been interpreted from surveys and direct measurements at hydrothermal fields at the seafloor of mid-ocean ridges for decades but cannot be easily observed directly in the underlying substratum. Estimation of complex subsurface processes rely on modeling to link in-situ observations to the geometry of the circulation of fluids under a hydrothermal site and the related dynamics of formation of diffuse flow. In-situ observations discussed in chapter 4 allow us to constrain these numerical models. The main goal of these models is to understand under what conditions the concomitant formation of smokers with fluid temperatures above 300°C and of diffuse venting zones with fluid temperature <80 °C, just a few meters away, is possible.

Two main regimes of diffuse flow at the seafloor are observed at MOR basalt-hosted hydrothermal fields: large areas of low-temperature and low velocity venting, 30 to 100 m in diameter, along cracks in pillow lavas, with no coexisting black smokers (e.g., at the Galapagos Spreading Center at 86°W with only fluids with low velocity and low temperature below 13°C (Corliss et al., 1979)); or diffuse vents spatially associated to black smokers, as at Lucky Strike. The first regime with large diffuse venting zones develops when deep-sourced high-temperature hydrothermal fluids mix with rapidly inflowing colder seawater into high permeability pillow lavas (Lowell et al., 2003). It has been proposed that this regime corresponds to an early stage in the evolution of hydrothermal sites (Pascoe & Cann, 1995). For the second regime, the presence of diffuse fluids within ~10m of a focused discharge zone has been modelled by Larson et al. (2015) and Lowell et al. (2007) . They consider conductive cooling and mixing of a rising hot jet with cold seawater, but their simulations predict diffuse discharge zones over large areas (~100m), with large temperature gradients around the hot upflowing plume and temperatures >150°C for the diffuse vents, not matching observations. For example, these models cannot predict low-temperature ~10°C venting in the ~10m surrounding high-temperature discharge zones. A possible additional mechanism favoring more complex and

lower temperature diffuse venting is porosity/permeability clogging by mineral precipitation in regions where hot hydrothermal fluids and cold seawater interact. These porosity/permeability variations may allow for secondary circulations around the upflowing plume (see chapter 3). Consequences of porosity-permeability/precipitation feedbacks have been studied for high-temperature venting (e.g., Fontaine et al., 2001; Guo et al., 2020), but not for diffuse flow formation. To investigate this problem of concomitant diffuse and focused flow formation, we present here numerical simulations following the same kind of numerical approach as previous models (chapter 3), i.e., cellular convection models. These involve 2D transient hydrothermal circulation, Darcy-based, heat and mass transport in porous media, coupled with mineral/anhydrite precipitation-induced porosity/permeability variations.

As a first step, we used the Fontaine et al. (2011) numerical formalation to simulate in 2D the thermal evolution of an initially cold (4°C), permeable layer at the base of which hot, 350°C fluids are locally injected (figure 5-1). A hot hydrothermal upflow jet forms, crossing the porous layer, generating a forced circulation, with recharge zones on both sides of the jet (figure 5-1). To mimic, at first-order, the effects of mineral/anhydrite precipitation, these initial simulations simply consider that at the boundary between the upflowing hot jet and warm/cold recharges, no flow occurs in the 150°C-250°C temperature range (i.e., heat transfer is controlled only by diffusion), as if the permeability of the porous medium was zero, a situation that would happen if mineral precipitation completely filled the rock porosity. These preliminary simulations show that when the jet reaches the near surface, low-temperature venting areas and very shallow secondary circulation cells develop.

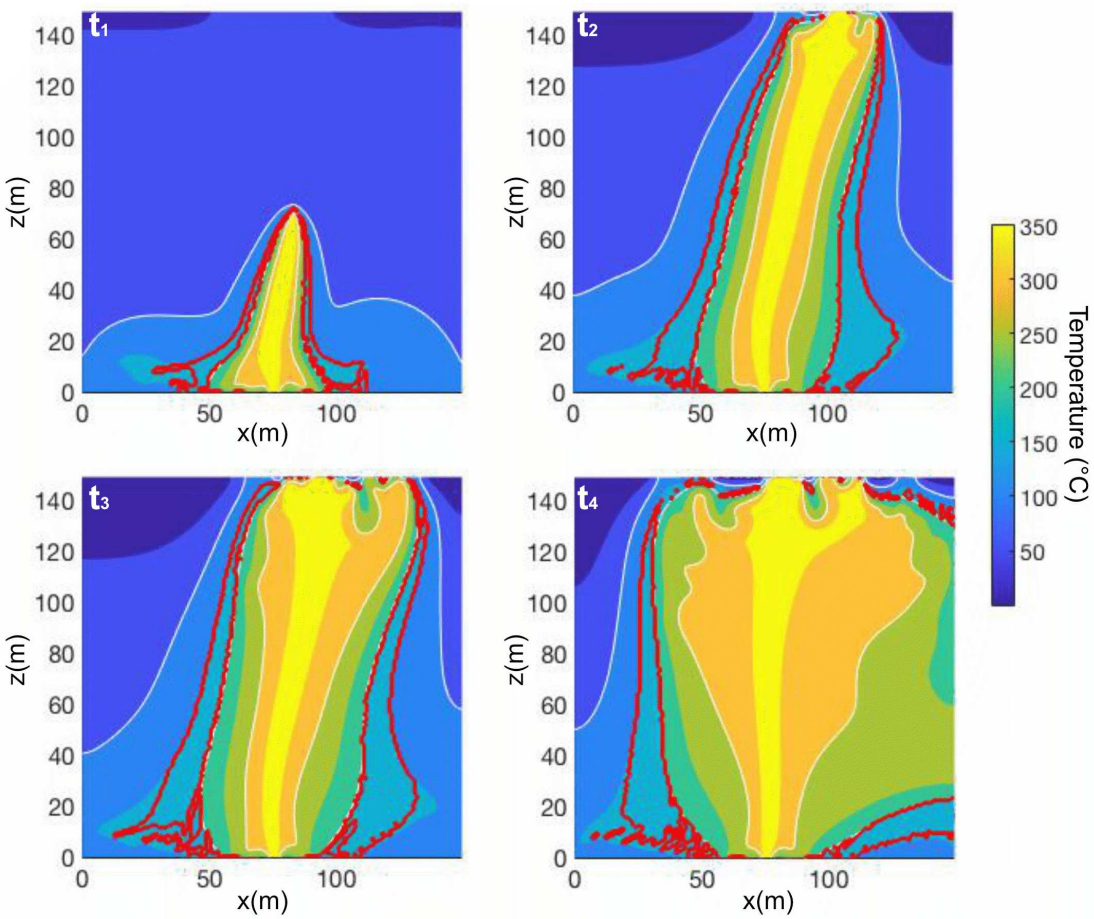

Figure 5-1– 2D 150x150m porous-flow model with inflow of 350°C hydrothermal fluid at different time during its evolution for a period of ~750 years. Red lines correspond to impermeable walls at 150°C and 250°C. Note the formation of second shallow circulations around the high-temperature focus flow.

The numerical modeling developed in this study is based largely on Fontaine et al. (2001) formulation, but is developed in the technical framework of the COMSOL Inc. commercial software. The use of this software was motivated by the versatility of its interactive interface, making it possible for the novice in numerical modeling to focus on the physics of hydrothermal flow, and not on numerical aspects as COMSOL has already demonstrated its accuracy in simulating hydrothermal processes in various geological settings (Eldursi et al., 2009; Emmanuel & Berkowitz, 2005; Guillou-Frottier et al., 2020; Schmeling & Marquart, 2014; Taillefer et al., 2017, 2018; Titarenko & McCaig, 2016). The COMSOL graphical modeling interface makes it possible to couple several "modules" comprising several fields of physics and chemistry. In our case, we are using the "heat transfer" and "subsurface fluid flow" modules. By coupling these modules, we can produce models of hot fluid circulation within a porous medium, equivalent to hydrothermal circulation in the shallow subsurface of the oceanic crust. The basic model setup involves simulating the thermal regime induced by the local injection of hot (350°C) fluid at the base of an initially cold rectangular domain. As a first step

we test parameters enabling the formation of a high-temperature focused discharge zone at the top of the domain, and describe the corresponding fluid flow. The tested parameters are the permeability of the porous medium, the width of the injection zone at the base of the rectangular domain, the initial injection velocity of these fluids, the depth of the 2D domain and the temperature at its base (outside of the injection domain). The second step consists in simulating the impact of mineral/anhydrite precipitation and induced porosity/permeability variations on the fluid flow pattern and on the resulting venting fluids. The method used in this study is based on Fontaine et al. (2001) to precipitate anhydrite at specific conditions of temperature to create porosity/permeability variations. This first-order physical method is simplified compared to models incorporating reactive transport like Guo et al. (2020).

Our models are designed with a geometry discretized by a triangular mesh with a resolution of 10m, shown in Figure 5-2a. The 2D porous box has a thickness of several hundred meters and a larger width of 1000m (Figure 5-2a). At its base, an impermeable boundary layer, at a given temperature, represents the temperature of the underlying porous medium already impacted by the hydrothermal circulation. We define an injection inlet zone at the center (x=500m) of this basal boundary where fluids at 350°C enter the domain (Figure 5-2a). Lateral boundaries of the model, which are far from the injection zone to avoid boundary effects, are impermeable and adiabatic. The top boundary is open (fluids are free to enter and exit), at constant pressure (170 bar), and its temperature verifies:

$$\begin{cases} \frac{\partial T}{\partial z} = 0, fluid\ flowing\ out\ (n.u \geq 0) \\ T = 5°C, fluid\ flowing\ in\ (n.u < 0) \end{cases} \quad (1)$$

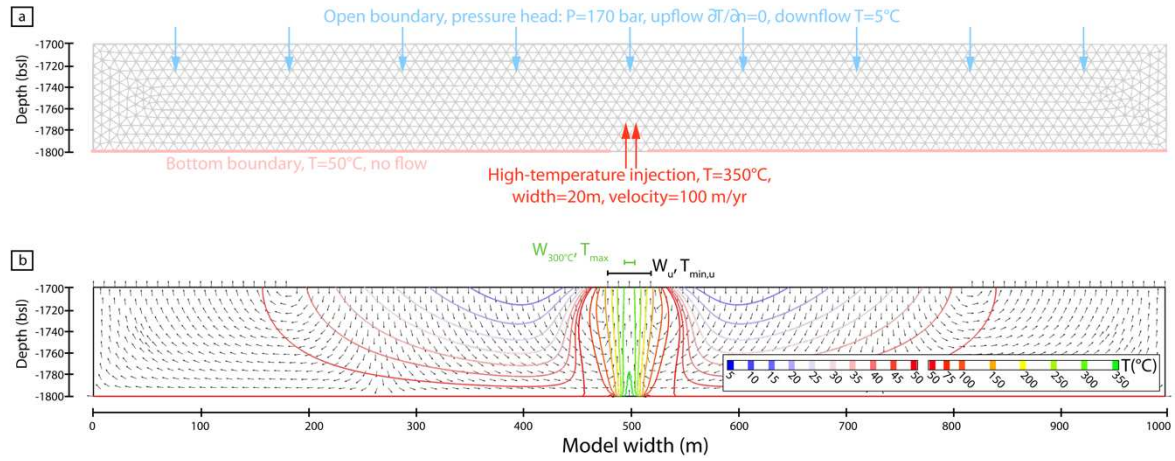

Figure 5-2 – (a) Geometry of 2D models with corresponding boundary conditions and a triangular mesh with a 10m maximum resolution. (b) Example of results of model with a permeability of 10^{-13} m^2 and the corresponding output of temperature (T_{max} and $T_{min,u}$ for respectively the maximum and minimum temperature at the top boundary.) and width ($W_{300°C}$ and W_u for respectively the width of upflowing. Fluids >300°C and for all temperature.) of the discharge zone used to constrain models.

The following physical parameters are then tested to measure their impact on the hydrothermal circulation: the permeability of the porous medium is set at 10^{-12}, 10^{-13}, or 10^{-14} m^2 which agrees with previous modeling studies (e.g. Guo et al., 2020; Wilcock & McNabb, 1996; Lowell et al. 2007). The injection velocity and width of the basal injection zone are set so as to be consistent with (i) typical heat flux values estimated for individual hydrothermal sites (a few MW to a few tens of MW; see Chapter 2) and (ii) the geographical extension of black smoker type sites, typically of the order of a few hundreds of square meters (diffuse+focused vents). The diameter of the hot upflowing conduit beneath vent sites is also constrained to be on the order of a few tens of meters based on magnetization anomalies mapped at the Endeavour field, Juan de Fuca Ridge (Tivey & Johnson, 2002). These magnetic lows are interpreted as due to hydrothermal alteration of magnetic minerals at high temperature (>300°C). Here, we run simulations with hot fluids basal inlet diameters of 20, 30, 40 or 50 meters.

The heat flux due to this basal fluid injection ($W.m^{-2}$) is $q_{inlet} = \rho C_p v(T_{fluid} - T_{ambient})$ (Table 5-1). Our model being 2D, we assume that the upflow zone is a pipe with a circular section, then given the range of injection zone width above, the basal injection velocity in our model has to range between 10 to 1000 m/yr in order to have vent heat flux of a few MW to a few tens of MW (table 5-1).

The height of the model is tested over a range of 100, 200, or 300m. It is a free parameter that is difficult to constrain and should be understood as linked to our choice of the hot fluid temperature at the base of the model. As we keep this value constant, a greater model height allows for upflowing fluids to cool over a larger distance.

The basal temperature at the bottom of our model, outside of the injection zone domain, is also not directly constrained by observations at the seafloor. One indirect constraint comes from the distribution of alteration mineral assemblages in vertical sections of the oceanic crust not impacted by high-T venting. Alt (1995) study the alteration of the oceanic crust through samples from ODP Hole 504B. Celadonite (formation temperature 30-60°C) is present down to ~300 mbsf, and saponite (formation temperature 15-170°C) down to 600 mbsf (Alt, 1995). Another constraint on this basal temperature can be derived for a case with no hydrothermal cooling from a simple calculation assuming a linear temperature gradient from seafloor to the magma body. With magmatic temperatures (1000-1200°C) at 1500m (i.e., fast spreading ridges) to 3000-4000m (i.e., magma rich slow-spreading segment such as Lucky Strike), the temperature at 100 m depth should be 25° to 80°C. Yet another approach is to use plausible

conductive heat flow values away from the venting areas. Using a range of 50 to 500 mW/m^2, values measured away from smokers at the Endeavour (Johnson et al., 2010; Salmi et al., 2014) and TAG (Becker et al., 1996) fields, a thermal conductivity k of basaltic rocks of 2.5 W/m/°C, T_{top} $(4°C)$ the temperature at the seafloor, and L the model height (100-300m), the temperature at the base of the model (T_{base}) should range between 6 and 64°C:

$$T_{base} = q/k.L + T_{top} \qquad (2)$$

Finally, yet another way to constraint the basal temperature of our model box is to use a "large-scale", km-wide, numerical model of hot hydrothermal flow in a layered system typical of the oceanic crust, i.e., a high-permeability layer above a lower-permeability one. We show in figure 5-3 such a model developed with COMSOL, which predict that, outside of the upflow zone, temperatures down to 5-10°C are possible at depths of a few 100 meters.

Based on these 3 indirect constraints, we choose to test a large range of basal temperatures: 5, 25, 50, 100, and 150°C.

To facilitate comparison between the results of the simulations, we define a set of reference values for each parameter: a fluid injection Darcy velocity of 100 m/year, an injection width of 20m, a basal temperature at the bottom boundary of 50°C and a model height of 100m.

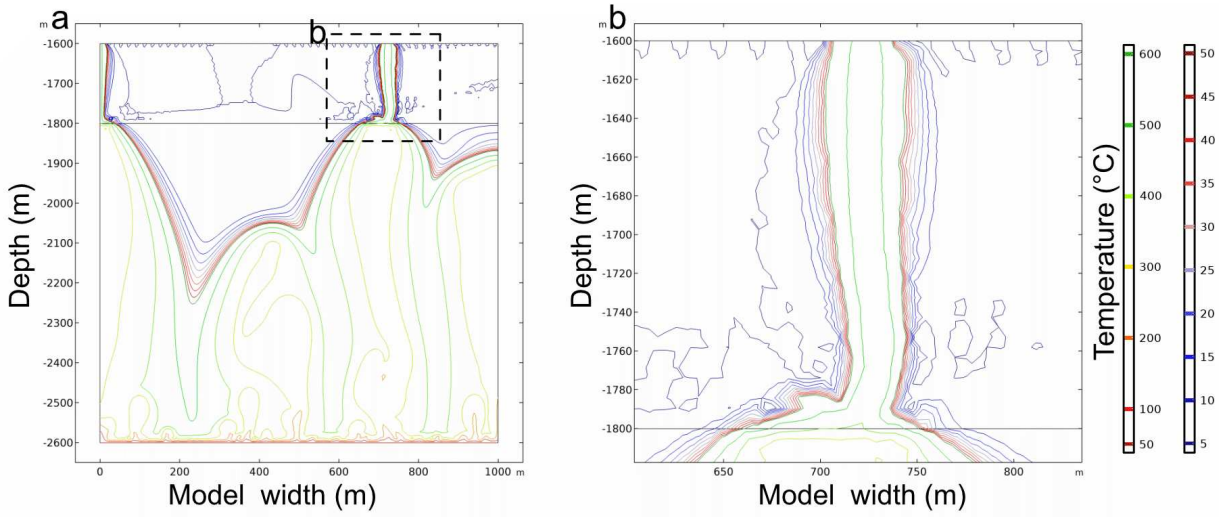

Figure 5-3 – (a) 1x1 km numerical 2D model of hydrothermal circulation with 2 permeable layers (layer height ratio of 1:5) corresponding to Lucky Strike configuration: a 600m-thick extrusive layer 2A (Seher, Crawford, Singh, & Cannat, 2010) and a ~3km-thick domain of hydrothermal downflow above the melt lens (Crawford et al., 2013). Bottom temperature is 600°C, permeabilities are 10^{-12} m^2 for layer 2A and 10^{-14} m^2. (b) Zoom on one of the plumes. Note the focalization of the fluid in layer 2A and the high temperature gradient at the edge of the plume.

Key model outputs are considered for comparison with geographical or physical parameters measured at the Tour Eiffel and White Castle hydrothermal sites (see chapter 4). The maximum temperature at the upper boundary T_{max} at any time, i.e., the highest upflow temperature is taken as representative of the temperature of the black smokers. The length of the discharge zone with temperature >300°C $W_{300°C}$ is an approximative equivalent to the domain where a sulfide mound can form. The minimum temperature $T_{min,u}$ and the total length of the discharge zone W_u at the upper boundary are measured as representative of the minimum temperature of diffuse vents. In some simulations, several upflow pathways may be present. Only the upflow pathway that rises from the fluid inlet location at the base of the model box is considered for these measurements.

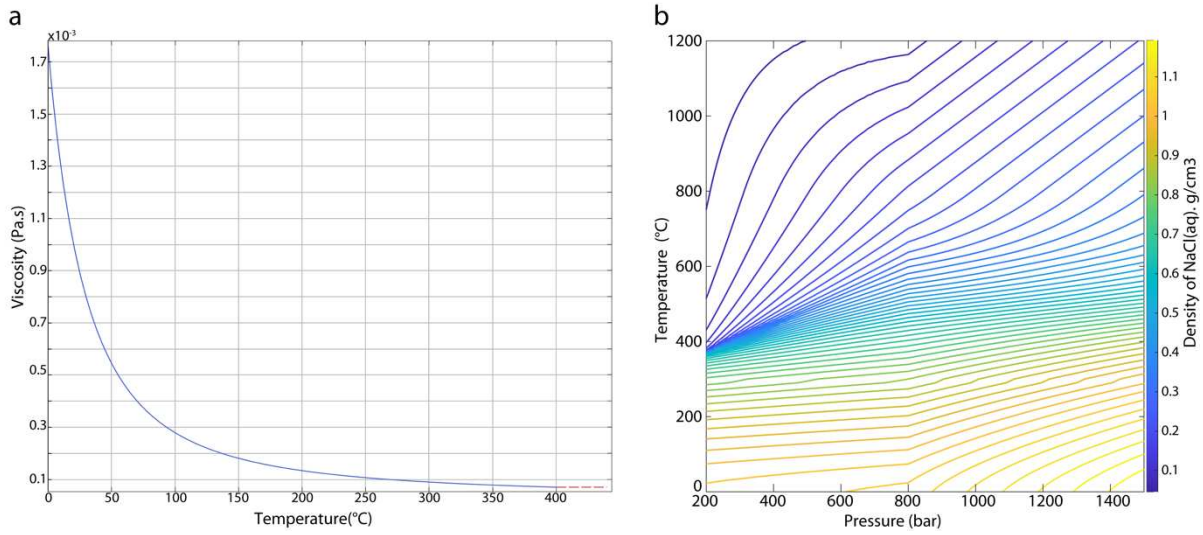

Figure 5-4 – (a)Viscosity of pure water as a function of temperature (equation 5). (b) Density of aqueous NaCl solution as a function of temperature and pressure.

For simplicity, we consider the flow of a single-phase fluid into the porous media. The governing equations are solved using the Heat Transfer and Subsurface Flow Modules of COMSOL Multiphysics with the fluid velocity following Darcy's flow law:

$$\boldsymbol{u} = -\frac{\kappa}{\mu_f(T)}(\nabla p + \rho_f(T,p)g) \qquad (3)$$

where $\boldsymbol{u}$ is the Darcy velocity (m.s^{-1}), κ is the permeability (m^2), ∇p the pressure gradient vector (Pa.m^{-1}) completed by the gravity acceleration g. μ_f is the dynamic viscosity (Pa.s^{-1}) of the fluid calculated by:

$$\mu_f = 2.414 \times 10^{-5} \times 10^{\frac{247.8}{T+133}} \qquad (4)$$

with T for the local temperature from Rabinowicz et al. (1999) for pure water (Figure 5-4a), with no pressure dependence regarding the limited (100-300 m) vertical extent of the models (Kestin et al., 1978). ρ_f is the density of the fluid and depends on pressure and temperature. To estimate ρ_f we used the relationships from Pitzer et al. (1984) (Figure 5-4b).

In simulations that take mineral precipitation into account, we derive porosity from the permeability of the basaltic substratum, using the porosity-dependent equation from Mavko & Nur (1997) completed by Marjanović et al. (2019):

$$\kappa = (\varepsilon - 0.005)^3 \times 1.2 \times 10^{-10.35} \quad (5)$$

and vice versa:

$$\varepsilon = \frac{\kappa}{\sqrt[3]{1.2\times10^{-10.35}}+0.005} \quad (6)$$

With ε being the porosity of the porous media. The Mavko & Nur (1997) equation is based on the Kozeny-Carman equation and compared with data measured for sandstone, glass beads, or calcite. Marjanović et al. (2019) compared several permeability-porosity relationships available in the literature and adapted this equation for the case of the basaltic layer 2A. The value of 0.05 represents the threshold porosity below which no fluid flow is possible, here corresponding to the lowest porosity measured in boreholes (Carlson, 2011) and $1.2\text{x}10^{-10.35}$ m^2 (Marjanović et al., 2019) resulting from the square product of 2 parameters describing the geometry of pores: the geometric factor and the effective "grain size" both describing the widths of the cracks or pore spaces, the space between them and the degree of interconnection between pores.

The mass conservation equation of fluids is written as:

$$\frac{\partial}{\partial \mathrm{t}}\Big(\varepsilon(\kappa)\rho_f(T,p)\Big) + \nabla.(\mathbf{u}(T,p)\rho_f(T,p))=0 \quad (7)$$

And we express the energy conservation for a single-phase fluid using the heat equation:

$$\big(\rho C_p(1-\varepsilon(\kappa)) + \rho_f(T,p)C_{p,f}(T)\varepsilon\big)\frac{\partial \mathrm{T}}{\partial \mathrm{t}}(x,y,t) + \rho_f(T,p)C_{p,f}(T)\boldsymbol{u}.\nabla \mathrm{T}(\mathrm{x},\mathrm{y},\mathrm{t}) = -\nabla.((1-\varepsilon(\kappa))k + \varepsilon(\kappa)k_f)\nabla \mathrm{T}(\mathrm{x},\mathrm{y},\mathrm{t})) \quad (8)$$

C_p and $C_{p,f}$ are the specific heat capacity ($J.kg^{-1}.K^{-1}$) of the porous media and the fluid, respectively; ρ is the density of the porous media, k and k_f are the thermal conductivity ($W.m^{-}$

^{1}.K^{-1}) of the porous media and the fluid, respectively. We assume that the fluids and the surrounding porous media are in local thermal equilibrium in all simulations.

In simulations that take mineral precipitation into account, pore filling due to precipitation (coupled to precipitated mineral volume, equation 10) changes the local porosity. The porosity field and the related permeability (equation 6) are therefore recalculated at each iteration. Following Fontaine et al. (2001), we used the temperature-dependent rate of variation of porosity based on the anhydrite solubility calculated from concentration in seawater:

$$\frac{\partial \varepsilon}{\partial t} = \frac{\rho_f}{\rho}\left(\lambda(\rho)\nabla^2 T \frac{\partial c}{\partial T}(T)\right) \qquad (9)$$

with $\lambda = \frac{k}{\rho C_p}$ the thermal diffusivity of the porous media (m^2.s^{-1}) and c the concentration of the chemical species for the studied minerals. Unlike Fontaine et al. (2001), the solubility rate corresponding to $\frac{\partial c}{\partial T}$ is taken as dependent of the temperature: i.e. the concentration of anhydrite components in the fluid varies with temperature (Figure 5-5). Anhydrite is formed by heating seawater, i.e., when the Laplacian of temperature $\nabla^2 T$ is >0. A limitation of our approach is that it considers only one fluid and assumes that the species needed to precipitate anhydrite are available in this fluid at all time. The model also allows for anhydrite dissolution if $\nabla^2 T$ is <0 in computing grids where anhydrite is present.

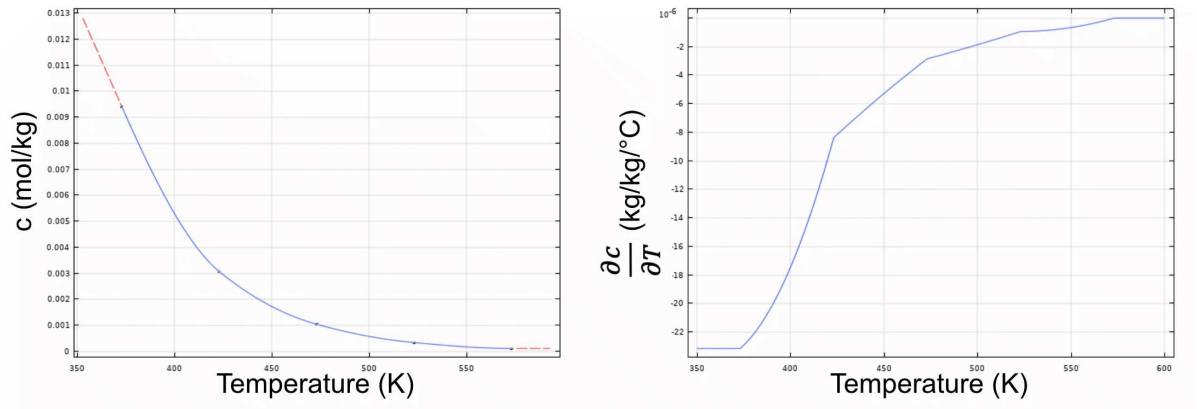

Figure 5-5 – (Left) Concentration of anhydrite components in seawater as a function of temperature estimated from Blounot & Dickson (1969) (Right) Corresponding solubility rate of anhydrite.

5.2. Results

We ran a total of 39 different simulations to test the impact of different geophysical and physical parameters on the venting temperature and the discharge zone extent. Results and parameters for each simulation are presented in table 5-1. Models 1 to 5 are based on the simple assumption of circulation of a single-phase fluid into a porous media, each model test a different parameter while other parameters keep their reference values. Each model is then run a second time (Table 5-1), but with the addition of anhydrite precipitation (Figure 5-5). We focused our observations on the control of venting temperature and discharge zone extent but also on the geometric evolution of the upflowing plume during time. These results are plotted in figures 5-6 and 5-13.

5.2.1. Controls on maximum/minimum venting temperature

The main parameter that controls the dynamics of fluids in the porous media is the permeability. This is illustrated in Figure 5-6 for the 3 simulations of model 1. The sensitivity of all simulations to permeability is further illustrated in the plots of Figure 5-7.

All models with the lowest permeability (10^{-14} m^2) have an upflow zone significantly wider than the injection zone, forming a "candelabra" shaped area (Figure 5-6). In these low permeability simulations, the injected fluids push the small (6%) volume of seawater initially present in the models upwards, displacing the downflow of cold seawater away from the center of the model (Figure 5-6). In runs with a high injection velocity (>100m/yr) at 10^{-14} m^2, the flow is essentially upwards in all the nodes, fed only by fluids from the injection, without any recharge of cold water at the model top. At higher permeability, the upflowing fluids are localized and recharge area develop near the center of the models (Figure 5-6).

Table 5-1 – Tested geophysical and physical parameters for the 5 model configurations, and 39 simulations (initial permeability, fluid velocity, basal temperature, injection width and model height) and corresponding output values for : maximum temperature T_{max}, minimum temperature of the upflow zone $T_{min,u}$, width of the upflow zone W_u and width of the discharge zone with fluid >300°C $W_{300°C}$. Tested parameter for each simulation is highlighted in bold text. Outputs are given for simulation with or without precipitation of anhydrite. Evolution of the plume geometry is indicated by the color code presented just below. Green: "Candelabra" plume shape corresponding to a wider upflow zone than the injection inlet; yellow: tilted plumes due to a lateral offsetting; orange: unstable plume with a changing position and regime during time; red: plume with a main discharge zone involving several venting areas separated by low-permeability zones.

"Candelabra" | Tilted plume | Unstable plume | Several discharge zones

								No precipitation				Anhydrite precipitation			
N° model	Initial perm. [m^2]	Calculated initial por.	Injection velocity [m/y]	Basal temp. [°C]	Injec. width [m]	Height [m]	Heat flux [MW]	T_{max} [°C]	$T_{min,u}$ [°C]	W_u [m]	$W_{300°C}$ [m]	T_{max} [°C]	$T_{min,u}$ [°C]	W_u [m]	$W_{300°C}$ [m]
1	**1.10^{-12}**	0.27	100	50	20	100	3.1	274	158	17	0	271	141	24	0
	1.10^{-13}	0.13	100	50	20	100	3.1	316	116	54	6	326	68	144	20
	1.10^{-14}	0.06	100	50	20	100	3.1	350	57	506	66	348	62	460	66
2	**1.10^{-12}**	0.27	**10**	50	20	100	0.3	244	120	16	0	224	109	17	0
	1.10^{-12}	0.27	**100**	50	20	100	3.1	274	158	17	0	271	141	24	0
	1.10^{-12}	0.27	**500**	50	20	100	15.6	329	87	24	6	325	24	67	7
	1.10^{-12}	0.27	**1000**	50	20	100	31.1	356	71	34	14	355	23	142	10
	1.10^{-13}	0.13	**10**	50	20	100	0.3	201	116	46	0	218	43	122	0
	1.10^{-13}	0.13	**100**	50	20	100	3.1	316	116	54	6	326	68	144	20
	1.10^{-13}	0.13	**500**	50	20	100	15.6	363	60	234	46	363	54	300	46
	1.10^{-13}	0.13	**1000**	50	20	100	31.1	363	59	400	74	366	53	403	86
	1.10^{-14}	0.06	**10**	50	20	100	0.3	208	107	154	0	211	108	154	0
	1.10^{-14}	0.06	**100**	50	20	100	3.1	350	57	506	66	348	62	460	66
	1.10^{-14}	0.06	**500**	50	20	100	15.6	363	51	1000	126	363	60	883	120
	1.10^{-14}	0.06	**1000**	50	20	100	31.1	368	51	1000	146	364	51	1000	146
3	**1.10^{-12}**	0.27	100	**5**	20	100	3.1	277	133	16	0	267	141	14	0
	1.10^{-12}	0.27	100	**25**	20	100	3.1	277	134	16	0	310	9	17	0
	1.10^{-12}	0.27	100	**50**	20	100	3.1	274	158	17	0	260	84	24	0
	1.10^{-12}	0.27	100	**100**	20	100	3.1	247	89	20	0	259	31	129	0
	1.10^{-12}	0.27	100	**150**	20	100	3.1	235	81	17	0	252	38	163	0
	1.10^{-13}	0.13	100	**5**	20	100	3.1	311	113	54	6	317	75	129	14
	1.10^{-13}	0.13	100	**25**	20	100	3.1	313	114	54	6	322	67	130	17
	1.10^{-13}	0.13	100	**50**	20	100	3.1	316	116	54	6	326	68	144	20
	1.10^{-13}	0.13	100	**100**	20	100	3.1	321	117	54	14	332	54	274	26
	1.10^{-13}	0.13	100	**150**	20	100	3.1	325	115	54	14	336	70	247	26
	1.10^{-14}	0.06	100	**5**	20	100	3.1	347	8	654	54	345	10	706	54
	1.10^{-14}	0.06	100	**25**	20	100	3.1	348	31	546	60	347	33	523	66
	1.10^{-14}	0.06	100	**50**	20	100	3.1	350	57	506	66	348	62	460	66
	1.10^{-14}	0.06	100	**100**	20	100	3.1	352	104	486	80	351	107	446	86
	1.10^{-14}	0.06	100	**150**	20	100	3.1	352	132	434	94	351	139	440	100
4	**1.10^{-12}**	0.27	100	50	**20**	100	3.1	274	158	17	0	242	23	40	0
	1.10^{-12}	0.27	100	50	**30**	100	7.0	274	134	20	0	275	20	80	0
	1.10^{-12}	0.27	100	50	**40**	100	12.4	273	142	20	0	297	183	17	0
	1.10^{-12}	0.27	100	50	**50**	100	19.4	298	102	20	0	307	23	60	4
	1.10^{-13}	0.13	100	50	**20**	100	3.1	316	116	54	6	325	68	144	20
	1.10^{-13}	0.13	100	50	**30**	100	7.0	343	117	66	20	346	72	174	30
	1.10^{-13}	0.13	100	50	**40**	100	12.4	350	115	74	26	350	71	172	40
	1.10^{-13}	0.13	100	50	**50**	100	19.4	351	112	80	34	350	70	186	50
	1.10^{-14}	0.06	100	50	**20**	100	3.1	350	57	506	66	348	62	460	66
	1.10^{-14}	0.06	100	50	**30**	100	7.0	351	55	580	106	352	58	546	106
	1.10^{-14}	0.06	100	50	**40**	100	12.4	351	54	640	134	351	56	597	134
	1.10^{-14}	0.06	100	50	**50**	100	19.4	350	53	686	154	350	55	640	154
5	**1.10^{-12}**	0.27	100	50	20	**100**	3.1	274	158	17	0	271	141	24	0
	1.10^{-12}	0.27	100	50	20	**200**	3.1	248	110	24	0	232	80	34	0
	1.10^{-12}	0.27	100	50	20	**300**	3.1	231	79	33	0	218	101	34	0
	1.10^{-13}	0.13	100	50	20	**100**	3.1	316	116	54	6	326	68	144	20
	1.10^{-13}	0.13	100	50	20	**200**	3.1	288	100	74	0	310	68	180	17
	1.10^{-13}	0.13	100	50	20	**300**	3.1	271	98	90	0	300	64	172	0
	1.10^{-14}	0.06	100	50	20	**100**	3.1	350	57	506	66	348	62	460	66
	1.10^{-14}	0.06	100	50	20	**200**	3.1	342	77	527	86	340	81	514	94
	1.10^{-14}	0.06	100	50	20	**300**	3.1	336	87	520	94	335	90	526	100

At low permeabilities (10^{-14} m^2), maximum venting temperatures stay close to the initial temperature of injection (350°C; Figure 5-7), and the minimum temperature of the upflow zone varies between >120°C and < 40°C depending primarily on the basal temperature. High basal temperature heats the seawater in the pores and thus limits the cooling of the injected fluids. Maximum temperature <200°C obtained at low injection velocities (10 m/yr) are due to the fact that the fluid has more time to cool, isotherms of 200-250°C cannot reach the surface (Supplementary Figure S5-1).

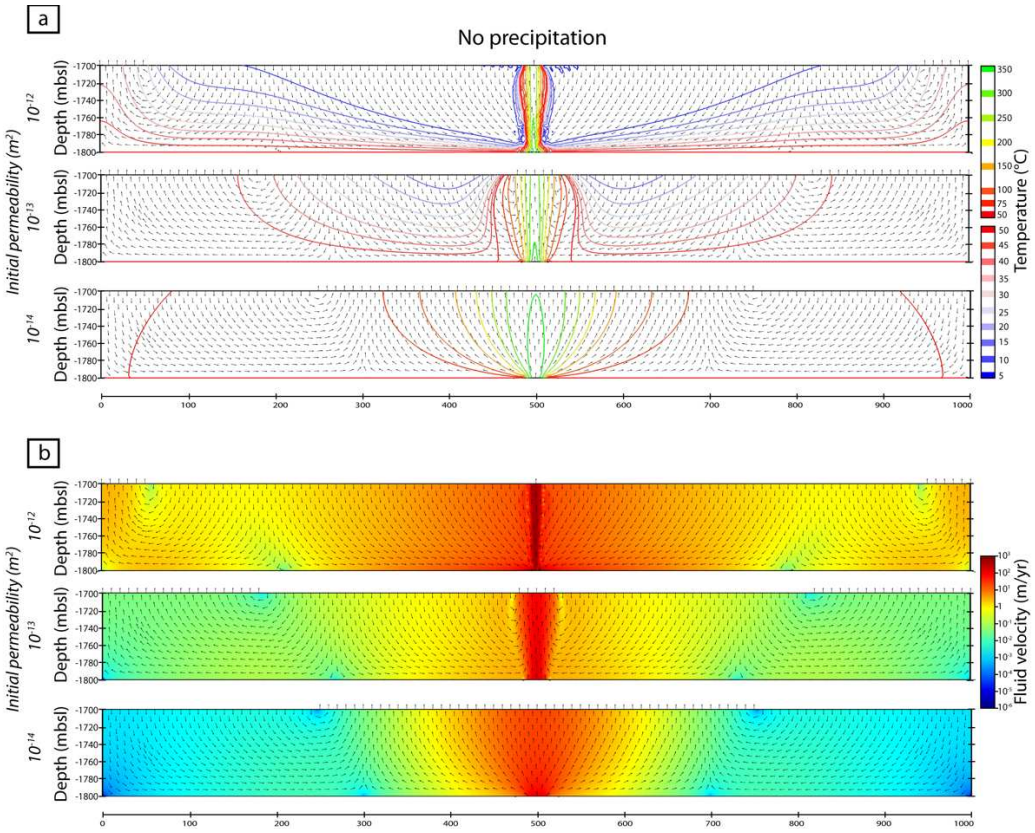

Figure 5-6 – Model 1. Simulation of an injection of a single-phase fluid in a porous media for 3 different permeabilities and for the reference parameters: fluid injection Darcy velocity of 100 m/year, injection width of 20m, basal temperature at the bottom boundary of 50°C and model height of 100m (Table 5-1). (a) Temperature field indicated by isotherms and modulus of the fluid velocity indicated by arrows. (b) Log of the velocity field in color and modulus of the fluid velocity indicated by arrows. Equivalent results with anhydrite precipitation are shown in Supplementary Figure S5-2. Note the "candelabra" shape of upflowing fluids for a permeability of 10^{-14} m^2.

High permeability models (10^{-12} m^2) have lower maximum venting temperature except if the fluid injection velocity is high (Figure 5-7). In these models, the porosity is much higher (up to 27%) so that the model contains a larger volume of seawater at the initial stages, and a larger amount of seawater can flow in and circulate in the porous media during the simulations. The injected fluid focuses in areas immediately above the injection zone (Figure 5-6). The ranges of both maximum and minimum venting temperatures are wide in these high

permeability simulations. Maximum venting temperatures increase and minimum venting temperatures decrease with injection velocity; in other words, the higher the injection velocity, the larger the range in venting temperature.

In figure 5-8, we compare 4 cases for permeability of $10^{-12}m^2$, varying the velocity of injected fluids, the basal temperature, the injection width, and the model height, and keeping the other parameters at reference values. High basal temperature (100°C) and large injection width (40m) both induce a specific geometry with a tilted plume (Table 5-1 and Figure 5-8). The tilt in the plume favors the formation of secondary, small scale cells, with fluid inflowing at the top moving along the tilt back to the top. This promotes a decrease of the minimum venting temperatures, while maximum venting temperatures can stay > 300°C if the injection velocity is high (>100m/yr).

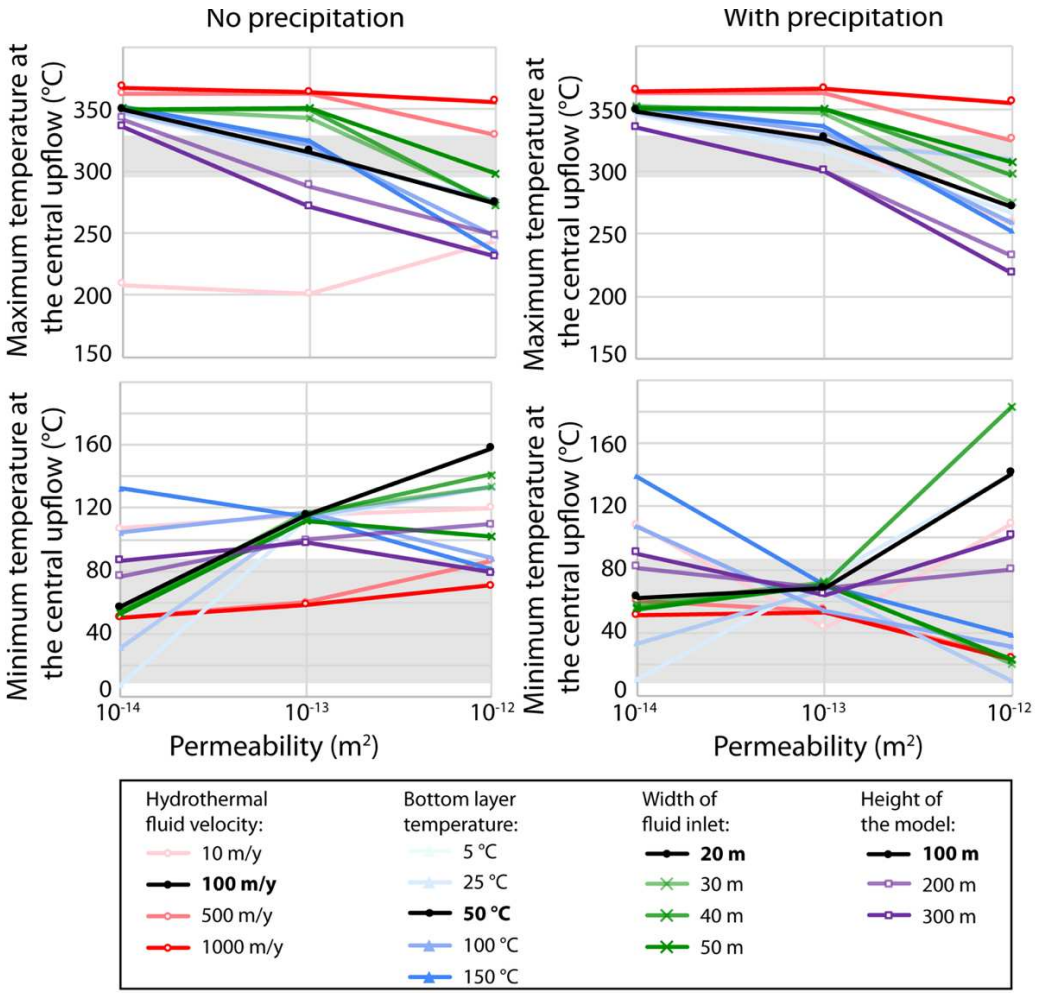

Figure 5-7 – Maximum temperature T_{max} and minimum temperature $T_{min,u}$ of the upflowing fluids at the top boundary of each of the 39 simulations (Table 5-1) for the different parameters (red: injection velocity; blue: basal temperature, green: width of injection inlet; purple: height of the model; black: reference parameters) at different permeabilities, with no precipitation (left) and with anhydrite precipitation (right). Grey area corresponds to measurements realized at TE hydrothermal sites at the LSHF (see chapter 4) to constrain the model.

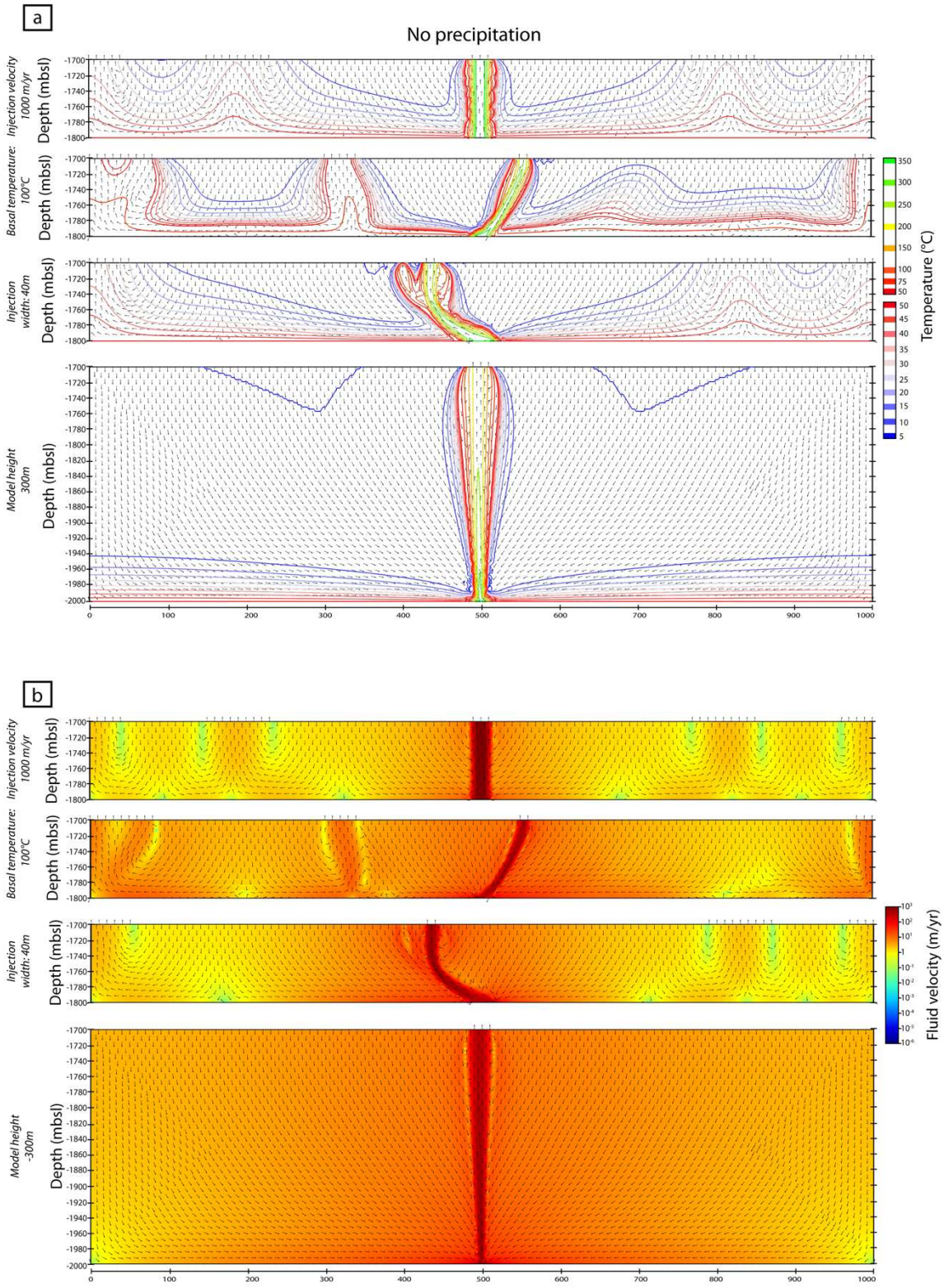

Figure 5-8 – Simulation of an injection of a single-phase fluid in a porous media for a permeability of 10^{-12} m^2 and with (i) an injection velocity of 1000 m/yr, (ii) a basal temperature of 100°C, (iii) an injection width of 40m and (iv) a model height of 300m. Other parameters in each run are kept at reference value (fluid injection Darcy velocity of 100 m/year, injection width of 20m, basal temperature at the bottom boundary of 50°C and model height of 100m). (a) temperature field indicated by isotherms and modulus of the fluid velocity indicated by arrows. (b) log of the velocity field in color and modulus of the fluid velocity indicated by arrows.

Simulations with a permeability of 10^{-13} m^2 show an intermediate regime: downflowing seawater helps focus the injected fluid as observed at the higher permeability runs, but the plume has a wider lateral extension than the injection zone (Figure 5-6). The range of maximum venting temperatures is also intermediate (Figure 5-7), and the minimum temperature of the upflow zone is near 100°C in all simulations, except those runs with high inlet fluid velocity (500-1000 m/yr).

Including anhydrite precipitation (Figure 5-7) does not greatly impact the maximum venting temperatures: they are similar to those observed for simulations without anhydrite precipitation in runs with high (10^{-12} m^2) and low (10^{-14} m^2) permeability, and they are a bit hotter in runs with intermediate (10^{-13} m^2) permeability, except for runs with low injection velocity (10 m/yr). This is because anhydrite precipitation tends to insulate the upflow to domains with T°>250°C, it therefore promotes maximum venting temperature close to the injection temperature, even in low injection velocity runs. The minimum venting temperature is more impacted by anhydrite precipitation for all permeabilities. At 10^{-13} m^2, the minimum venting temperatures are restricted in all runs to a small range between 40 and 70°C.

At higher permeabilities (10^{-12} m^2), the minimum venting temperature is by contrast more variable than in runs without precipitation, with values <40°C in several runs. Minimum venting temperatures >70°C are obtained in runs with reference values no matter the model depth, for low inlet fluid velocity (10 m/y), and for an injection width of 40m (in this case minimum venting temperatures are >160°C). For an injection width of 40m, anhydrite low-permeability “walls” seem more permeable and the plume temperature is higher than in other simulations (Figure 5-9). Equivalent zone of higher permeability that let cold fluid interact with the hot plume are seen in other simulation (e.g. reference model; Supplementary Figure S5-2) but this phenomenon is not systematically linked to minimum temperature >70°C (e.g. not observable for a model depth of 300m; Figure 5-9). These “exotic” simulations uncorrelated to lower venting temperature due to anhydrite precipitation highlight the non-linearity of processes between anhydrite precipitation and the circulation of fluids in the media.

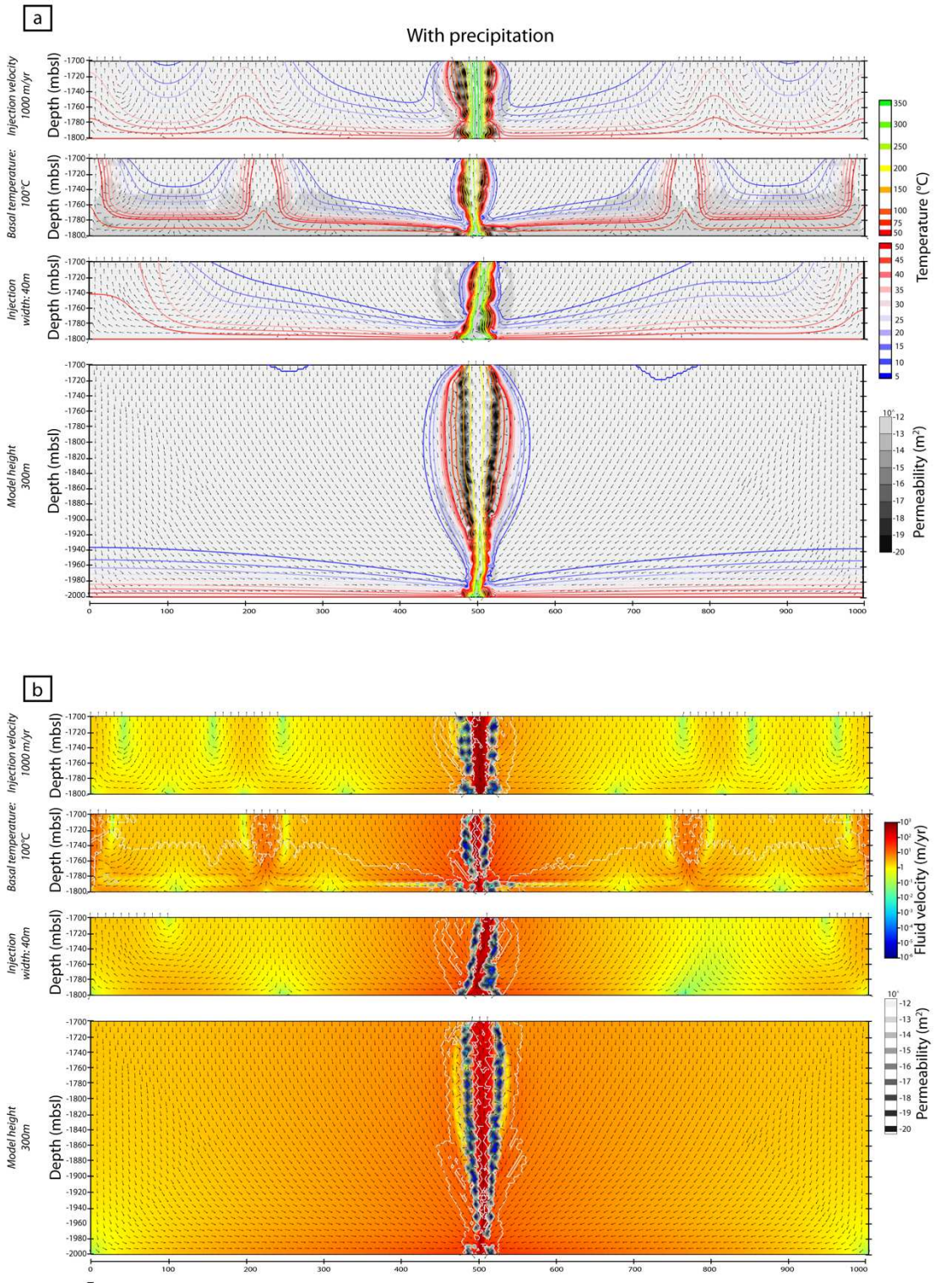

Figure 5-9 – Simulation of an injection of a single-phase fluid in a porous media for a permeability of 10^{-12} m^2, same as Figure 5-8 but with anhydrite precipitation: (i) injection velocity of 1000 m/yr, (ii) basal temperature of 100°C, (iii) injection width of 40m and (iv) model height of 300m. Other parameters in each run are kept at reference value (fluid injection Darcy velocity of 100 m/year, injection width of 20m, basal temperature at the bottom boundary of 50°C and model height of 100m). (a) temperature field indicated by isotherms and modulus of the fluid velocity indicated by arrows, completed by the permeability field (greyscale). (b) log of the velocity field in color and modulus of the fluid velocity indicated by arrows, completed by the permeability field (greyscale).

5.2.2. Time evolution of the geometry of the upflow zone

The geometry of the upflowing plume has a big impact on the simulation outputs. Several plume geometries are observed, from "candelabra-like" upflow zones to tilted or unstable plumes (Table 5-1). Figure 5-10 shows the time evolution of the maximum venting temperature for the 3 tested permeabilities and the reference parameters (fluid injection Darcy velocity of 100 m/year, injection width of 20m, basal temperature at the bottom boundary of 50°C and model height of 100m). In simulations without anhydrite precipitation, maximum venting temperature stabilizes after a rapid initial increase. For the simulation with precipitation, we observe different behaviors depending on the initial permeability: at 10^{-14} m^2, the evolution during time is similar to that with no precipitation; at 10^{-13} m^2, after the initial increase, maximum venting temperatures increase slowly by ~20°C over ~3000 years. Similar observations were made by Guo et al. (2020) but over only 3°C for a period of 5000 years. For an initial permeability of 10^{-12} m^2, maximum temperatures first increase to ~270°C, then decrease slowly and show episodic variations. Each episodic event corresponds to a reorganization of the local permeability related to anhydrite precipitation/dissolution in the shallow subsurface.

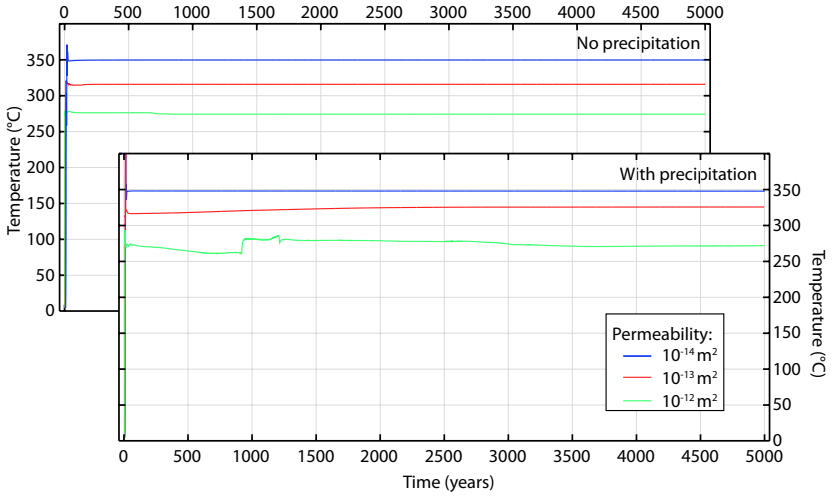

Figure 5-10 – Time evolution of the maximum venting temperature for 3 permeabilities with or without anhydrite precipitation, for the reference parameters (fluid injection Darcy velocity of 100 m/year, injection width of 20m, basal temperature at the bottom boundary of 50°C and model height of 100m).

Tilted plumes are observed in several simulations (Table 5-1; Figure 5-8 and 5-11a). They develop for different conditions with anhydrite precipitation or not: (i) for high basal temperatures, (ii) for wide fluid injection zones, or (iii) for high velocity of injected fluids. They can result from "splitting plumes", a phenomenon observed by Coumou et al. (2006) and interpreted as instabilities at the interface between the low viscosity hot fluid and the high

viscosity cold seawater. Splitting plumes can form a tilted plume or just fuse again and evolve into a vertical upflowing plume. The dynamics of formation of a tilted plume from plume splitting is shown in figure 5-11b: the split plume reaches the surface 5 years into the run, one branch being of lower temperature. This lower temperature branch is weaker and quickly resorbs, while the other branch remains tilted untill the end of the run.

Tilted plumes can also be created when neighboring plumes rise at the base of the model layer. We observed this phenomenon for simulations with a high (150°C) basal temperature.

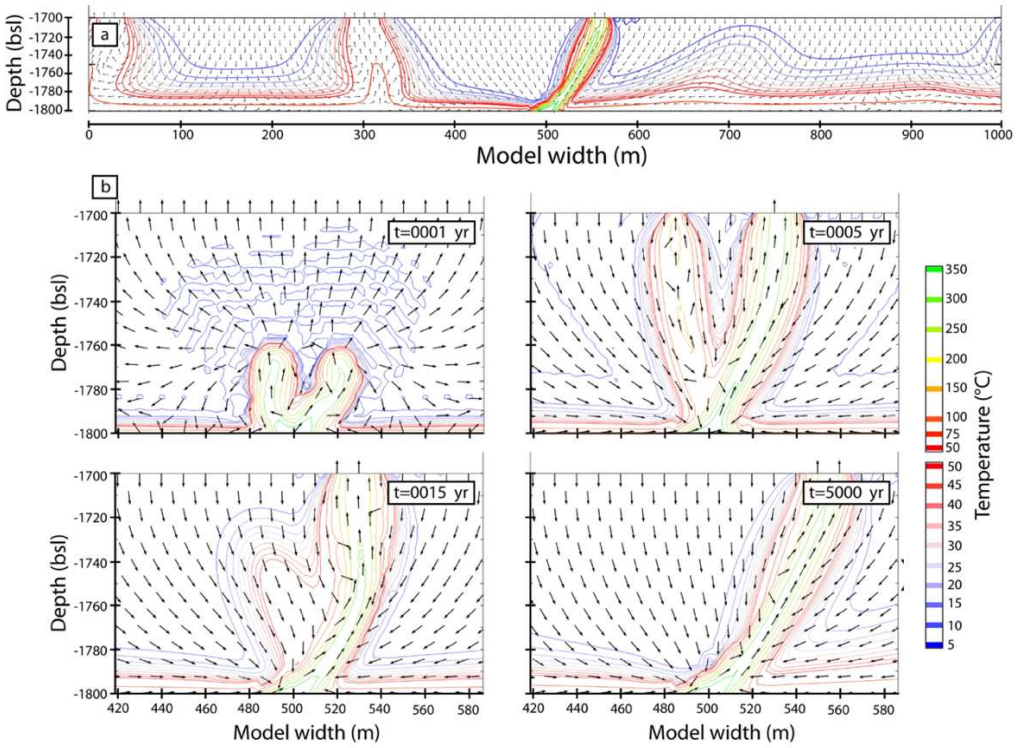

Figure 5-11 – (a) Simulation of an injection of a single-phase fluid in a porous media for a permeability of 10^{-12} m^2, without anhydrite precipitation, for a basal temperature of 100°C and other parameters kept at reference value (fluid injection Darcy velocity of 100 m/year, injection width of 20m, and model height of 100m). Temperature field indicated by isotherms and modulus of the fluid velocity indicated by arrows at the end of the run (5000 years). (b) Zooms on the main upflowing plume at different times in the run represented in (a)showing the formation of a titled plume from an initial split plume geometry.

In a few simulations, the plume geometry is not stable in time (Table 5-1): plume splitting occurs repeatedly. In the run shown in Figure 5-12, this appears to occur periodically (with period of ~100 years; Figure 5-12a) from a main tilted plume. This unstable geometry results in changes in the width of the outflow zone at the top of the model (i.e. the width of the hydrothermal venting area).

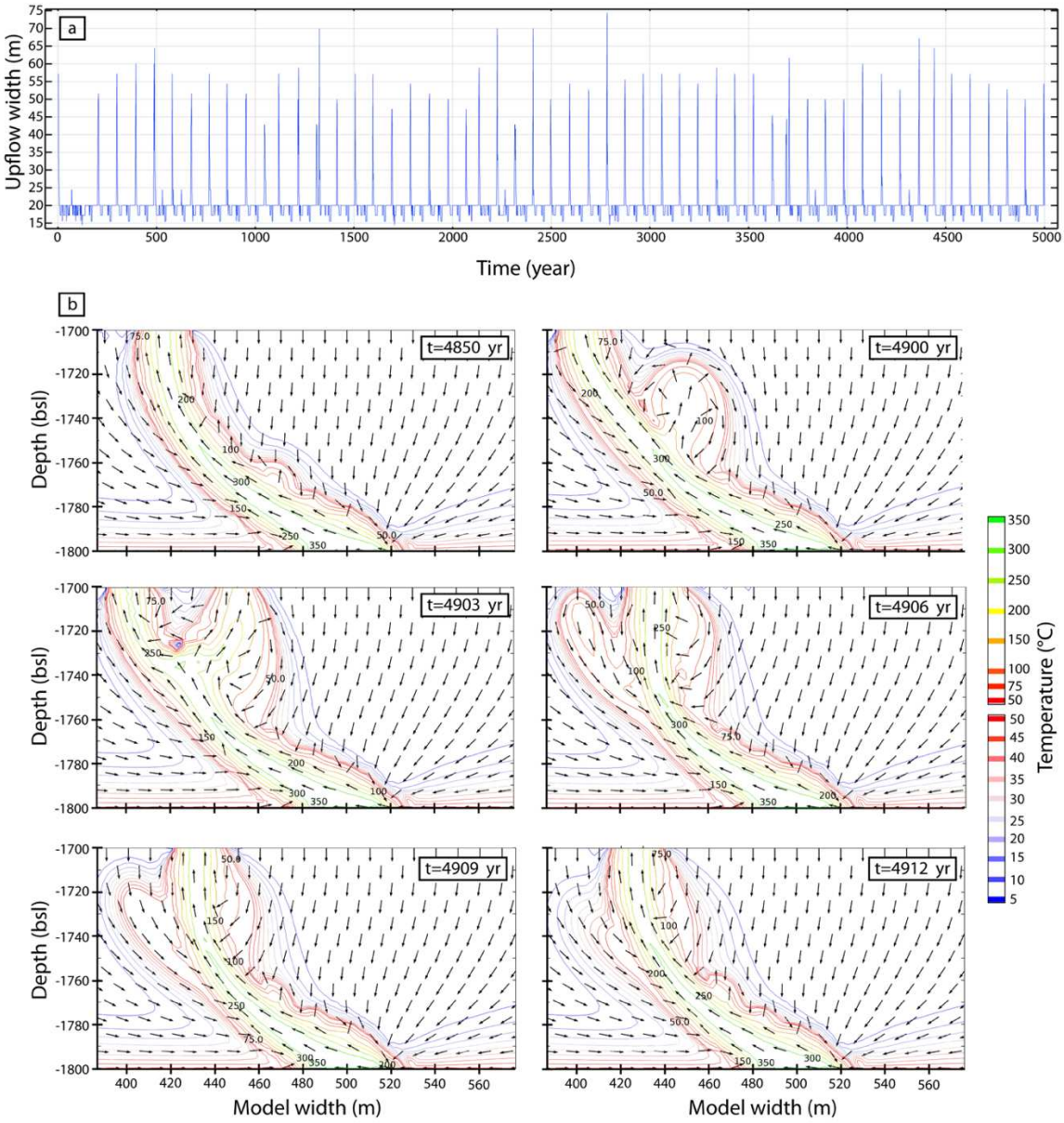

Figure 5-12 – (a) Width of the main outflow zone measured for a simulation that generated unstable plume geometries. Simulation parameters are: a permeability of 10^{-12} m^2, an injection width of 40m and reference values for fluid injection Darcy velocity (100 m/year) and model height (100m). (b) Zooms on the main upflowing plumes at different times in the run represented in (a), showing the formation of split plumes from a titled plume. The measured outflow width (a) is larger when plume splitting occurs, smaller when only the main tilted plume is present.

5.2.3. Controls on the width of the main upflow zone

In runs that result in stable plume geometries (i.e. the majority of the runs; Table 5-1), the width of the main outflow zone is mainly impacted by initial permeability (Figure 5-13). For simulations with no anhydrite precipitation, the injection velocity also has a small impact, especially at lower basal temperatures. The width of the zone where outflowing fluids have temperatures >300°C (i.e. the domain where black smokers may form) does not change for

different parameters at high permeabilities (10^{-12} m^2). At lower permeabilities, the width and fluid velocity of injection zone are the main parameters promoting larger upflowing zones with fluids >300°C.

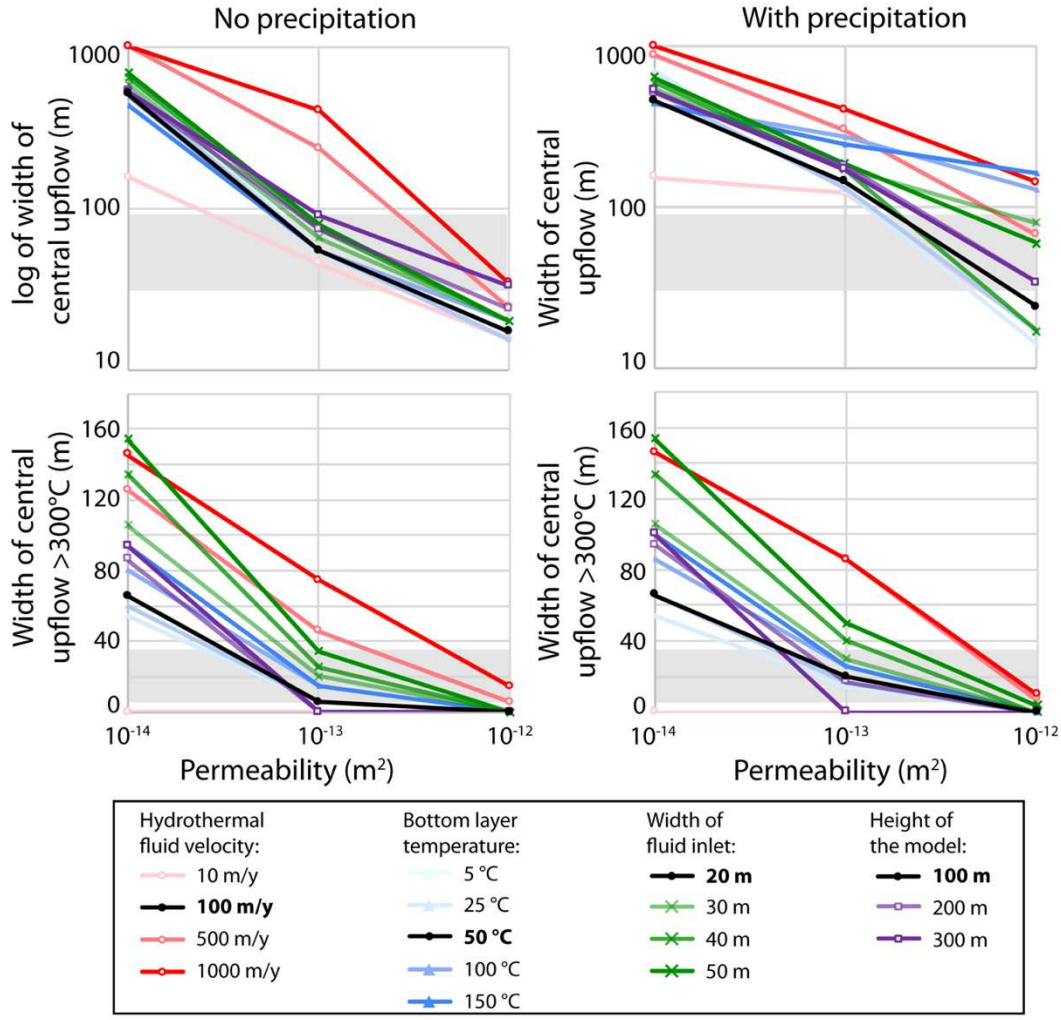

Figure 5-13 – Width of the main upflow zone W_u and of the upflow zone for fluids >300°C $W_{300°C}$ at the top boundary of each of the 39 simulations (Table 5-1) for the different parameters (red: injection velocity; blue: basal temperature, green: width of injection inlet; purple: height of the model; black: reference parameters) at different permeabilities, with no precipitation (left) and with anhydrite precipitation (right). Grey area corresponds to measurements realized at TE hydrothermal sites at the LSHF (see chapter 4) to constrain the model.

Simulations with anhydrite precipitation yield similar results in terms of the width of the upflow zone >300°C, but change significantly the results for the total width of the main upflow zone (i.e. the whole venting domain diffuse vents included). For an initial permeability of 10^{-12} m^2, simulations with anhydrite precipitation result in a wider range of width for the main discharge zone. Anhydrite precipitation also appears to result in a larger range of minimum venting temperatures (figure 5-7). The presence of lower permeability zones due to precipitation also complicates the discharge zone with several zones of fluid emission and local

shallow circulation. Lower permeability zones present at few meters below the surface favor low-temperature fluid (seawater) inlets in the shallow surface close to the upflowing plume, increasing the gradient of temperature (Figure 5-14a) or making possible the formation of small-scale secondary circulation.

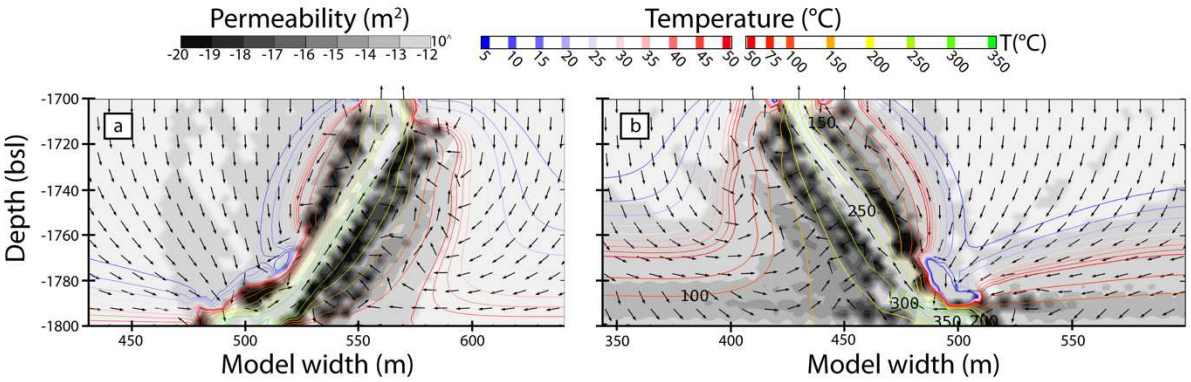

Figure 5-14 – Simulations of an injection of a single-phase fluid in a porous media for a permeability of 10^{-12} m^2 and with (a) an injection with of 30m and (b) a basal temperature of 100°C. Other parameters at reference value (fluid injection Darcy velocity of 100 m/year, injection width of 20m, and model height of 100m). Temperature field indicated by isotherms and modulus of the fluid velocity indicated by arrows, completed by the permeability field (greyscale).

5.3. Discussion

Our objective in this chapter is to explain the concomitant formation of smokers with fluid temperature above 300°C and of diffuse venting zones with fluid temperature <80 °C, just a few meters away. Using the COMSOL commercial software, we develop a numerical model of hot fluid circulation within a porous medium, equivalent to hydrothermal circulation in the shallow subsurface of the oceanic crust. Our simulations show that: (i) the permeability of the porous media is a major parameter controlling the venting temperatures and the surface extent of hydrothermal sites: high permeability (10^{-12} m^2) does not allow the formation of hot (>300°C) vents, except in simulations with a fluid injection Darcy velocity >500 m/yr; (ii) the formation of low permeability zones by mineral precipitation impacts the geometry of fluid flow in the shallow subseafloor, allowing the diffuse venting of fluids at temperatures <80°C over regions a few hundreds of square meters wide; (iii) the presence of low permeability zones a few meters below the surface of the model also favors the formation of small scale secondary cells, a mechanism that helps to obtain locally very low venting temperatures (~10°C); (iv) the plume geometry is in most cases stable after an initial period of < 100 yrs. In a few simulations, however, plume geometry is unstable, which has a direct impact on the characteristics of the

resulting discharge zone(s). In this discussion, we examine the relevance of these simulations for the near seafloor dynamics of fluid flow at hydrothermal sites like the Lucky Strike TE or WC sites, and at black smoker type hydrothermal vent sites in general. We then discuss the limitations of our modelling approach and how they might impact our conclusions.

5.1.1. What are the possible characteristics of shallow subseafloor fluid circulations below the Tour Eiffel or White Castle hydrothermal sites?

A key component of our study is the possibility to compare the outputs of our simulations with observables from in-situ measurements made at the Lucky Strike TE and WC vent sites (Figure 5-7 and 5-13). We use four observables, two relate to venting temperatures (Figure 5-7), and two relate to the spatial extent of the venting area (Figure 5-13). Simulations with a permeability of 10^{-14} m^2 predict the observed range of maximum venting temperatures (Figure 5-7), except for runs with no anhydrite precipitation and the lowest fluid injection Darcy velocity (10 m/yr). However, the spatial extent of the upflow zone in all runs is up to 10 times greater than the size of the TE or WC sites (Figure 5-13), or than the size of other MOR vent sites. This is due to the "candelabra" shape of fluid upflow.

Models with a permeability of 10^{-13} m^2 also predict the observed range of maximum venting temperatures, except for runs with no anhydrite precipitation and either the lowest fluid injection Darcy velocity (10 m/yr), or a model height ≥ 200 m (Figure 5-7). Runs without anhydrite precipitation also predict the observed range of spatial extent for the upflow zone (Figure 5-13), except for runs with fluid injection Darcy velocity ≥ 500 m/yr. Intermediate permeability runs that do include anhydrite precipitation, however, predict upflow zones that are systematically too wide (Figure 5-13).

If we now consider models with a permeability of 10^{-12} m^2, we see that a primary effect of increasing the permeability, is to reduce the extent of the venting area (Figure 5-13). However, higher injection velocities (>500m/an), or a broader injection zone (50 m; Figure 5-7), are then required in order to obtain smoker-like maximum venting temperatures. According to these different arguments, we infer that permeabilities intermediate between 10^{-13}-10^{-12} m^2 best account for the observations at Lucky Strike, and in general at other MOR vent sites, provided that the fluid flux through the basal inlet is relatively high (through larger inlet width and/or higher fluid velocity), in order to produce the good range of maximum venting temperatures. The size of black smoker fluids outflow ($W_{300°C}$ in Figure 5-13). is also adequately predicted in these rather high permeability conditions.

Based on this, we now examine the predictions of simulations that fit these conditions in terms of the minimum temperature of the upflow, i.e. the minimum predicted temperature for diffuse vents. The range (7-80°C) shown in Figure 5-7 for the TE and WC sites corresponds to actual measured temperatures at venting cracks and patches (Chapter 4). In our interpretation of possible seawater mixing dynamics in the upper few decimeters to meters of the substratum at these vents, we proposed that fluids could actually come out of the underlying fractured basalts at temperatures > 50°C. We also showed evidence for fluids hotter than 140°C venting at distances up to 25 m from the black smokers (Chapter 4). Field observations therefore leave room for interpretation and a wide range of possible minimum diffuse venting temperatures. Here, modelling results can help us identify what factors would promote higher, or lower miniuml temperatures (Figure 5-7). In this respect, introducing anhydrite precipitation has the greatest impact: in the 10^{-13}-10^{-12} m^2 permeability range, predicted minimum venting temperatures are higher than 60°C in all runs when no precipitation is allowed, and can be lowered to < 20°C when precipitation occurs (Figure 5-7).

In the high permeability runs (10^{-12} m^2), the width of the domain of high temperature (>300°C) venting is very small, below the observed width of the TE and WC sulfide mounds (5-35 m; Figure 5-13) in some runs. Combined with anhydrite precipitation that allows for low minimum diffuse venting temperatures (Figure 5-7), this could account for the formation of black smoker-less sites such as those described at the Galapagos spreading center (Corliss et al., 1979).

Finally, in some of our anhydrite precipitation models, areas of low permeability form at the edge of the upflow zone, and favor the development of small, meter-wide hydrothermal loops at very shallow depths below the seafloor, with cold fluids inflowing on one side of the low-permeability areas, flowing around, and ascending to the seafloor at some distance (Figure 5-14) from the focused high-T vent. These models are very similar to the benchmark model presented at the beginning of this chapter in Figure 5-1, where impermeable walls were able to divert the hot flow from the central plume, to promote the formation of diffuse vents by mixing and cooling with inflowing seawater. Such low temperature diffuse vents may prevail at "mature" sites such as TE where such low-permeability areas may be widely distributed, eventually controlling the local shallow hydrology. By contrast, the higher temperature of diffuse venting at less mature sites such as WC, could be due to their less complex shallow permeability structure.

5.1.2. Limitations of our modelling approach of sub-seafloor dynamics at the scale of hydrothermal sites

We use a small-scale model of hot fluid circulation in a porous media with a fixed basal source of fluid based on geophysical/geological constraints obtained at the Lucky Strike hydrothermal field at the MAR (Chapter 4). Theses simulations fit in certain cases the expected temperature and surface for the focused and diffuse domains at a typical hydrothermal site. Our model is based on local permeability variations by precipitation of anhydrite upon heating of seawater to temperatures in the range 50-250°C (Bischoff & Seyfried, 1978), without any tracking of the chemical species involved in the precipitation mechanisms. Therefore, our model considers that at all times, there are the necessary species in the fluid circulating and being heated in the 50-250°C range, to precipitate anhydrite. The case of SO_4^{2-}, whose source is seawater, is particularly sensitive as our approximation does not allow to distinguish whether mineral precipitation proceeds from (i) the hot endmember-like fluids that we continuously inject at the base of the model (ii) seawater-like fluids initially present or recharging at the model top, or (iii) "intermediate" fluids resulting from the mixing between the seawater and hot endmember fluids. Therefore, one need to pay attention to the position of the zones of reduced permeability predicted in our simulations with respect to up and downflowing fluids. In candelabra-like flow geometry for example, our approximation is probably valid only during the initial stage of the model, when the hot injected fluids expel the cold seawater initially present in the model nodes. However, as discussed above, candelabra-like geometries are probably not realistic for MOR black smoker sites, where diffuse flow areas concentrate within meters of black smoker structures. More relevant flow geometries develop in runs where steep horizontal temperature gradients are established through time between hot, vertically rising, endmember-like fluids from the injection, and warm/cold downwelling loops of seawater-like recharging fluids (figure 5-8 and 5-9). We carefully observed the pattern and dynamics of formation of the low-permeability zones/walls in this context and we noticed that they systematically grow towards the outside, i.e., that fluids from the seawater branch of the local circulation are always involved in the precipitation mechanism. We thus posit that our approach is relevant and the necessary conditions for anhydrite precipitation are met. Models that display the formation of low-permeability regions immediately below the model top, favoring secondary, small-scale circulation and low-T venting are also relevant to MOR hydrothermal sites. Here again, the formation of these regions is clearly linked to heated seawater in the close vicinity (a few meters) of the model top, and our formal approach is warranted.

However, to test and validate our precipitation model it would be good to use the particle tracing module available in the COMSOL software and to integrate a chemical model with reactive transport. This is a prerequisite to be able to evaluate the mixing proportion of diffuse fluid, a model output that could be tested against vent chemistry data (Chapter 4). It would also allow us to constrain the precipitation/dissolution rate of anhydrite and the possible amount of anhydrite that may have precipitated.

5.2. Conclusion

The presence of diffuse fluids within ~10m of focused discharge zone is documented at several hydrothermal fields at MORs (Barreyre et al., 2012; Von Damm & Lilley, 2004; Mittelstaedt et al., 2012). We develop a numerical model of hot fluid circulation within a porous medium, equivalent to hydrothermal circulation in the shallow subsurface of the oceanic crust. We test physical and geophysical parameters enabling the formation of a high-temperature focused discharge zone at the top of the domain, and we simulate the impact of mineral/anhydrite precipitation and induced porosity/permeability variations on the fluid flow pattern, on the spatial extent of venting areas, and on the resulting venting temperatures. Our models show that:

- An initial permeability in the range 10^{-13}- 10^{-12} m^2 with relatively high influx of fluid at the base of the model (i.e. an adequate combination of a relatively wide fluid inlet zone, and of a relatively high fluid velocity), combined with anhydrite precipitation is the best match to obtain venting temperatures and spatial extent of venting areas, that fit those measured at the Lucky Strike TE and WC sites, and more generally at MOR black smoker type hydrothermal sites.
- Incremental mineral precipitation and pore clogging may lead to various degrees of site "maturity", including the formation of very shallow (a few meters) low-permeability zones that can develop below venting sites, creating complex flow channelization, with mixing and cooling processes between hot fluid effluents from the black smoker plume and cold inflowing seawater. This would impact diffuse venting temperature, with "juvenile" sites like WC venting at higher T° (>60°C) than mature site like TE (<60°C).

Supplementary figures

In this section we provide supplementary figures of numerical simulations that give further support for the results presented in this chapter:

- Figure S5-1 show numerical results for fluid flow in a porous media with a permeability of 10^{-12} m^2 and with an injection velocity of 10 m/yr.
- Figure S5-2 show numerical results for fluid flow at different permeabilities like in figure 5-7 but with mineral precipitation.

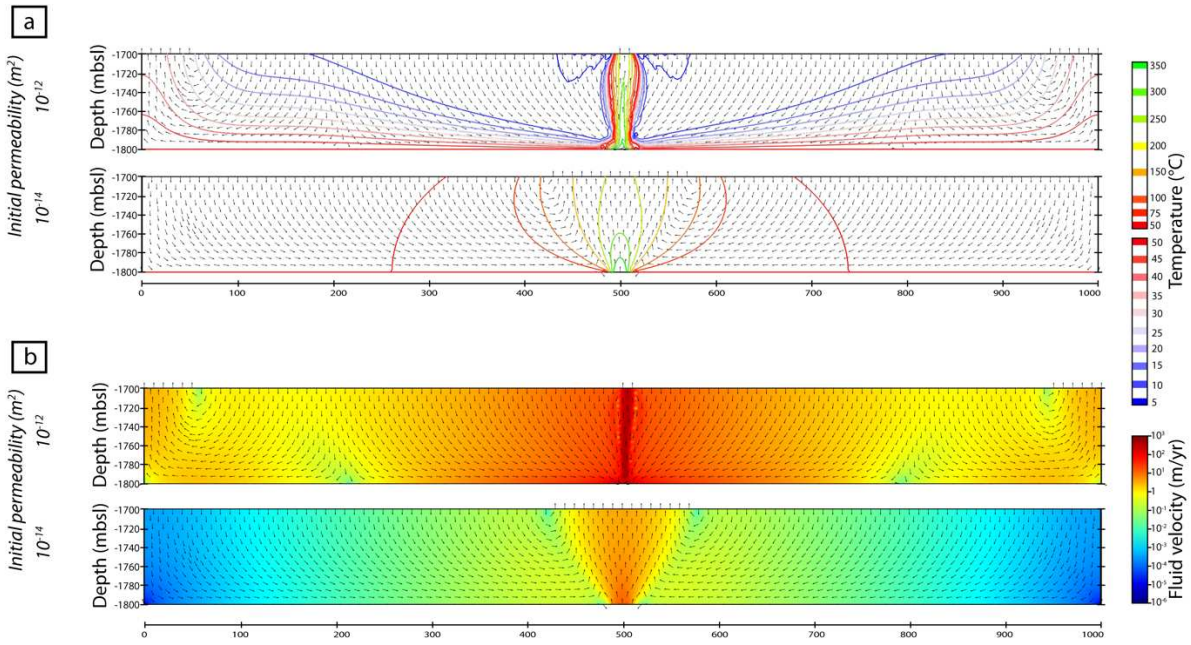

Figure S5-1 – Simulation of an injection of a single-phase fluid in a porous media for a permeability of 10^{-12} m^2 and 10^{-14} m^2 with an injection velocity of 10 m/yr. (a) temperature field indicated by isotherms and modulus of the fluid velocity indicated by arrows. (b) log of the velocity field in color and modulus of the fluid velocity indicated by arrows.

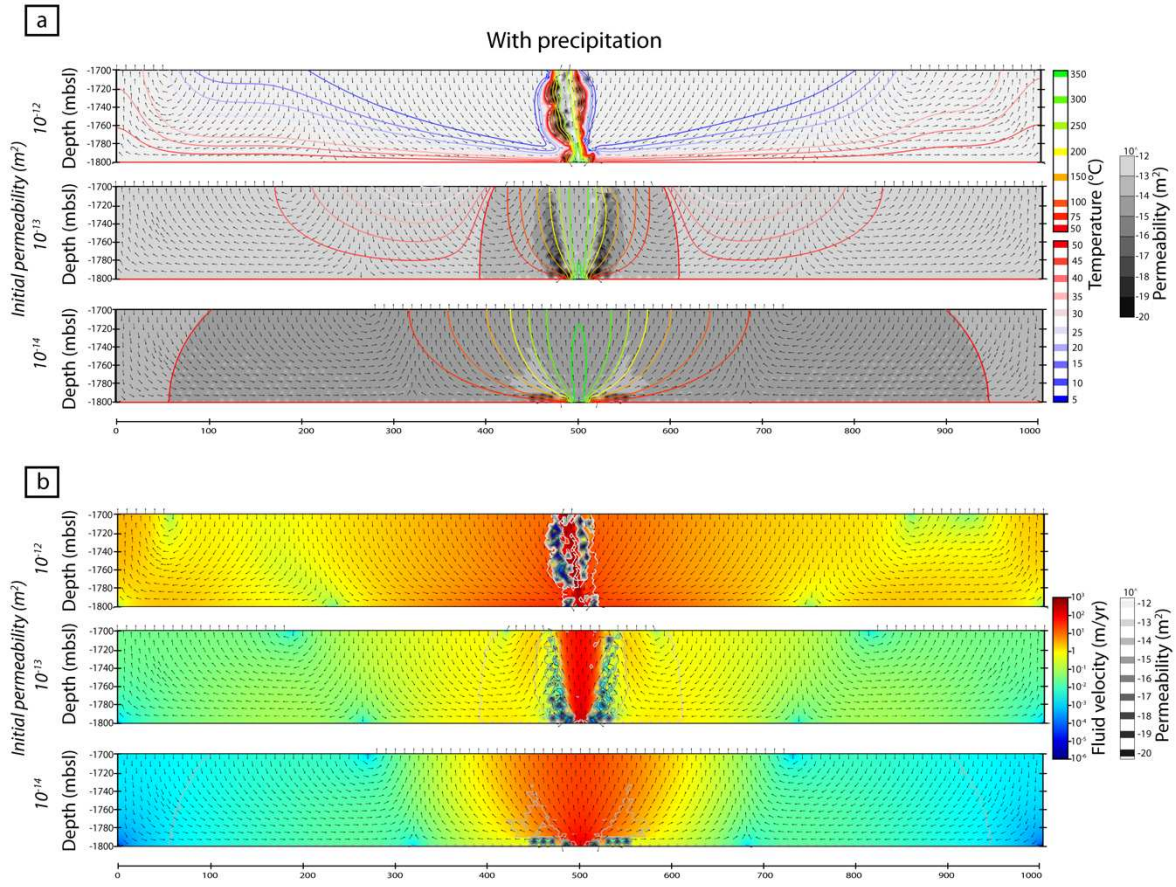

Figure S5-2– Simulation of an injection of a single-phase fluid in a porous media with anhydrite precipitations for 3 different permeabilities and for reference parameters. (a) temperature field indicated by isotherms and modulus of the fluid velocity indicated by arrows. (b) log of the velocity field and modulus of the fluid velocity indicated by arrows.

Part IV

GENERAL CONCLUSIONS

General conclusion & Perspectives

Geological observations and mapping show that the two hydrothermal sites TE and WC have several types of diffuse vents with a comparable concentric distribution in the two sites. This nature of the venting depends on the geological formation from which they emanate. A layer of thin volcaniclastic deposits (<1.5 m) deposited on basalts throughout the Lucky Strike hydrothermal field area acts as a cover when indurated by hydrothermal precipitates (it is then called the slab) and as a porous medium when it has not been indurated. Three types of diffuse vent result: (i) cracks in the indurated slab, (ii) cracks in volcaniclastic deposits and (iii) patches in the volcaniclastic deposits.

Fluid chemistry shows that the chemistry of diffuse fluids at the two sites results from the mixing of seawater with end-member hydrothermal fluids. The chemistry of these fluids also suggests a local and temporal variability of several processes such as heating of the sea water and / or cooling of the hydrothermal fluid before mixing, or the precipitation and dissolution of anhydrite in the subsurface. These signals for precipitation and dissolution of anhydrite in several fluid samples result from chemical and temperature gradients, in or below the slab. We were also able to show that these processes do not have the same intensity at the two sites. White Castle exhibits fluids with a greater proportion of end-member hydrothermal fluids and frequent evidence of anhydrite precipitation. This difference can be interpreted in the context of a difference in maturation between the two sites.

The time series of temperatures show that the different types of diffuse vents have different dynamics even for very close vents (less than a few meters). Our interpretation involves a meter-scale permeable network controlling the flow of fluids through numerous fractures present in the underlying basalt. The fluids then percolate at the interface between the basalt and the volcaniclastic deposits, and are modified before reaching the ocean floor: during advection in the porous volcaniclastic layer; or by mixing with sea water entrained in cavities under the slab. Semi-diurnal temperature variations with an amplitude of up to 8°C are recorded in the time series of fluids emerging from cracks; these variations seem to be also linked to local and very shallow entrainment of sea water. The fluids which exit at diffuse “patches” in the volcaniclastic deposits do not show tidal variations of such amplitude, which implies either that the fluids which percolate out of the basaltic basement do not have significant temperature

variations at tidal frequencies, or that these variations are damped during passage through the porous volcaniclastic layer. In any case, our study shows that the tidal modulations of the temperatures of the diffuse fluids at the TE and WC sites are essentially acquired very close to the bottom, in the slab or the volcaniclastics.

Based on our results on diffuse vents, we propose that the fluids exiting the underlying basalts have temperatures between 58°C and 304°C and are made of up to 21% end-member hydrothermal fluids. We find that hot (> 80°C) and rich in end-member hydrothermal fluids (> 9%) fluids come out of the fractured basalt basement up to 25m from the black smokers at both TE and WC. We also document meter-scale variability between the outflow of diffuse fluids, some of which may result from processes in the volcaniclastic layer or under the indurated slab, while others may reflect lateral variability of circulations in the basaltic basement. From this new characterization of the diffuse fluids of the TE and WC sites, we propose a new approach to estimate diffuse heat fluxes at the site scale, which considers not the vents observed on the bottom, but the distribution and the temperature of the corresponding fluid outlets in the basalts, under the surface layer of indurated (slab) or non-indurated volcaniclastics. The diffuse heat fluxes obtained with this method are in the range of the average to upper values of previous studies (Barreyre et al., 2012; Mittelstaedt et al., 2012). These values confirm that the heat fluxes carried by the diffuse vents at Lucky Strike hydrothermal sites are of the order of several MW to a few tens of MW.

All these observations allow us to constrain numerical models aimed at predicting the geometry of the circulation of fluids under a hydrothermal site and the dynamics of diffuse fluid formation. These models are not intended to reproduce reality but to understand under what conditions it is possible to obtain smokers at >300°C and lateral diffuse exits at <80°C up to more than 25 m from smokers. We use the multiphysical and versatile modeling software COMSOL©. This graphical modeling interface makes it possible to couple several “modules” covering several fields of physics and chemistry. In our case, we are using the modules of heat transfer and fluid flow in the subsurface. By coupling these modules, we can produce models of hot fluid circulation within a porous medium, equivalent to the basaltic substratum under the Lucky Strike hydrothermal sites.

We test several parameters: the permeability of the porous medium, the hydrothermal fluid inlet velocity, the width of the hydrothermal fluid inlet zone, the temperature of the impermeable base of the model, and the height of the model. The effect on the circulation of fluids is evaluated using model predictions which correspond to observables such as the maximum venting temperature, the minimum temperature of the fluids in the outflow zone, the width of the outflow zone, in general and for fluids with temperatures >300°C. The precipitation of anhydrite upon heating of seawater to temperatures > 50-150°C (Bischoff & Seyfried, 1978) is also approximated and leads to a decrease in porosity, resulting in a decrease in permeability, in areas where seawater entrained in the bedrock attains these temperatures.

The models confirm that the significant permeabilities ($\geq 10^{-12}$ m^2) which were estimated for the upper basaltic crust at MOR by geophysical methods (e.g. Barreyre et al., 2018; Barreyre & Sohn, 2016; Evans, 1994; Marjanović et al., 2019) allow black smokers to form only if the upflow velocity of the hot fluids at the base of the model are high, and if the height of the model remains small. For lower input speeds, and higher boxes, smokers are only formed for lower permeabilities (10^{-14} m^2). Permeability is also a major parameter for controlling the width of hydrothermal fluid outflow at the seabed (i.e. the size of hydrothermal sites). Anhydrite precipitation simulations result in a reduction in the range of minimum bottom fluid venting temperatures, allowing fluid vents at temperatures >50°C for the various conditions previously tested.

This thesis therefore makes it possible to identify: (i) different types of diffuse fluids with different dynamics depending on the geological formations that constrain their circulation; (ii) the role of the thin layer of indurated or non-indurated volcaniclastics above the basalts which modifies the characteristics (temperature, speed and exit surface, chemistry) of the fluids leaving the underlying basalts at Lucky Strike vent sites. Taking this effect into account allows us to propose an independent estimate of the energy fluxes carried by the diffuse vents of Lucky Strike; (iii) fluid circulation dynamics and the mechanics that accompany this circulation, and which depend on the maturity of the site where the hydrothermal fluids are discharged; and (iv) various parameters constraining the formation of diffuse fluids close to high temperature vents using numerical modeling at the scale of the hydrothermal site.

The immediate perspectives gained from this work are summarized below:

(i) A better consideration of the heat and material fluxes carried by diffuse vents in the formation of porous volcaniclastics of Lucky Strike. The conceptual model proposed at the end of part II, predicts a lateral passage of such very slow vents, to zones of conductive flow. This configuration, with lateral variations on the meter scale, and temporal variations documented over a few months, remains to be studied. For this, I participated in the in-house construction of a probe with two temperature sensors (LTgrad), allowing the measurement of a temperature gradient in loose and porous surface deposits. A network of ten of these probes was deployed for the first time at the TE site in 2018 and will be maintained until 2022. Analysis of these temperature data will make it possible to better identify areas warmed by slow circulation of fluids or by conduction. This analysis, coupled with better mapping of diffuse areas using OTUS2 color image mosaics, will allow a better assessment of chemical and heat fluxes at the scale of the TE hydrothermal site.

(ii) Diffuse fluids play an important role for the growth and distribution of the hydrothermal fauna. The study of temperature, and several physicochemical parameters within these biological communities at Lucky Strike has been carried out for more than ten years by fellow biologists and ecologists. The in-depth analysis of the temporal temperature and chemistry data in this thesis will serve to a better understanding of the contribution of hydrothermal fluids to the conditions of these seafloor habitats, that are located on the bottom, and therefore also affected by the dynamics and variations in the temperature and chemistry of the bottom water. To make the link between these two contributions, a temperature sensor chain was deployed on the TE site in 2016-2017 (Girard et al., 2020), then again in 2020.

(iii) Our numerical models do not consider the transport of chemical species, not allowing us to predict chemical reactions or to constrain precipitation/dissolution rates as a function of the species available in the fluids. This constraint prevents us from predicting the amounts of mixing between the so-called end-member hydrothermal fluids and seawater in the diffuse outlets. An improvement of our model would therefore be relevant, first via the monitoring of particles to follow fluid mixing, then by the integration of a chemical model for reactive transport of chemical species. The models in this thesis are also limited by their resolution (10m) which is not sufficient to predict variations at the scale of the meter as observed in-situ. An increase in the density of the model mesh in the near seafloor regions and therefore a longer computation time would be pertinent.

(iv) Finally, the important role played by the layer of volcaniclastic deposits for the dynamics of circulations of diffuse fluids at the scale of a hydrothermal site makes it relevant to study the circulation in this upper deposit and at the interface between the fractured basaltic substratum and porous deposits. Small-scale models (1x1 m) have been initiated to study these circulations. Constrained by temperature measurements made via the new network of LTgrad probes, these models could help us better understand the very superficial processes that modify the diffuse fluids leaving the basaltic bedrock

Bibliographical references

Alt, J. C. (1995). Subseafloor Processes in Mod-Ocean Ridge Hydrothermal Systems.

Alt, J. C., Anderson, T. F., & Bonnell, L. (1989). The geochemistry of sulfur in a 1.3 km section of hydrothermally altered oceanic crust, DSDP Hole 504B. *Geochimica et Cosmochimica Acta*, *53*(5), 1011–1023. https://doi.org/10.1016/0016-7037(89)90206-8

Andersen, C., Rüpke, L., Hasenclever, J., Grevemeyer, I., & Petersen, S. (2015). Fault geometry and permeability contrast control vent temperatures at the Logatchev 1 hydrothermal field, Mid-Atlantic Ridge. *Geology*, *43*(1), 51–54. https://doi.org/10.1130/g36113.1

Ark, E. M. V., Detrick, R. S., Canales, J. P., Carbotte, S. M., Harding, A. J., Kent, G. M., et al. (2007). Seismic structure of the Endeavour Segment, Juan de Fuca Ridge: Correlations with seismicity and hydrothermal activity. *Journal of Geophysical Research: Solid Earth (1978–2012)*, *112*(B2). https://doi.org/10.1029/2005jb004210

Arnulf, A. F., Harding, A. J., Singh, S. C., Kent, G. M., & Crawford, W. C. (2014). Nature of upper crust beneath the Lucky Strike volcano using elastic full waveform inversion of streamer data. *Geophysical Journal International*, *196*(3), 1471–1491. https://doi.org/10.1093/gji/ggt461

Backer, H., & Schoell, M. (1972). New Deeps with Brines and Metalliferous Sediments in the Red Sea. *Nature Physical Science*, *240*(103), 153. https://doi.org/10.1038/physci240153a0

Baker, E. T., Massoth, G. J., Walker, S. L., & Embley, R. W. (1993). A method for quantitatively estimating diffuse and discrete hydrothermal discharge. *Earth and Planetary Science Letters*, *118*(1–4), 235–249. https://doi.org/10.1016/0012-821x(93)90170-e

Baker, E. T., Massoth, G. J., Feely, R. A., Embley, R. W., Thomson, R. E., & Burd, B. J. (1995). Hydrothermal event plumes from the coaxial seafloor eruption site, Juan de Fuca Ridge. *Geophysical Research Letters*, *22*(2), 147–150. https://doi.org/10.1029/94gl02403

Baker, E. T., Fox, C. G., & Cowen, J. P. (1999). In situ observations of the onset of hydrothermal discharge during the 1998 Submarine Eruption of Axial Volcano, Juan de Fuca Ridge. *Geophysical Research Letters*, *26*(23), 3445–3448. https://doi.org/10.1029/1999gl002331

Baker, E. T., Resing, J. A., Haymon, R. M., Tunnicliffe, V., Lavelle, J. W., Martinez, F., et al. (2016). How many vent fields? New estimates of vent field populations on ocean ridges from precise mapping of hydrothermal discharge locations. *Earth and Planetary Science Letters*, *449*(FEMS Microbiol. Ecol. 91 1 2015), 186–196. https://doi.org/10.1016/j.epsl.2016.05.031

Ballu, V., Cannat, M., Wheeler, B., Legrand, J., & Sarradin, P.-M. (2021). Seafloor pressure data from two SBE53 pressure gauges on EMSO-Azores observatory, 2019-2020. *SEANOE*. https://doi.org/10.17882/80573

Baross, J. A., & Hoffman, S. E. (1985). Submarine hydrothermal vents and associated gradient environments as sites for the origin and evolution of life. *Origins of Life and Evolution of the Biosphere*, *15*(4), 327–345. https://doi.org/10.1007/bf01808177

Barreyre, T., & Sohn, R. A. (2016). Poroelastic response of mid-ocean ridge hydrothermal systems to ocean tidal loading: Implications for shallow permeability structure. *Geophysical Research Letters*, *43*(4), 1660–1668. https://doi.org/10.1002/2015gl066479

Barreyre, T., Escartín, J., Garcia, R., Cannat, M., Mittelstaedt, E., & Prados, R. (2012). Structure, temporal evolution, and heat flux estimates from the Lucky Strike deep-sea hydrothermal field derived from seafloor image mosaics. *Geochemistry, Geophysics, Geosystems*, *13*(4), n/a-n/a. https://doi.org/10.1029/2011gc003990

Barreyre, T., Escartin, J., Sohn, R., & Cannat, M. (2014a). Permeability of the Lucky Strike deep-sea hydrothermal system: Constraints from the poroelastic response to ocean tidal loading. *Earth and Planetary Science Letters*, *408*, 146–154. https://doi.org/10.1016/j.epsl.2014.09.049

Barreyre, T., Escartín, J., Sohn, R. A., Cannat, M., Ballu, V., & Crawford, W. C. (2014b). Temporal variability and tidal modulation of hydrothermal exit-fluid temperatures at the Lucky Strike deep-sea vent field, Mid-Atlantic Ridge. *Journal of Geophysical Research: Solid Earth*, *119*(4), 2543–2566. https://doi.org/10.1002/2013jb010478

Barreyre, T., Olive, J., Crone, T. J., & Sohn, R. A. (2018). Depth-Dependent Permeability and Heat Output at Basalt-Hosted Hydrothermal Systems Across Mid-Ocean Ridge Spreading Rates. *Geochemistry, Geophysics, Geosystems*, *19*(4), 1259–1281. https://doi.org/10.1002/2017gc007152

Beaulieu, S. E., & Szafrański, K. M. (2020). InterRidge Global Database of Active Submarine Hydrothermal Vent Fields Version 3.4. PANGAEA. Retrieved from https://doi.org/10.1594/PANGAEA.917894

Beaulieu, S. E., Baker, E. T., & German, C. R. (2015). Where are the undiscovered hydrothermal vents on oceanic spreading ridges? *Deep Sea Research Part II: Topical Studies in Oceanography*, *121*, 202–212. https://doi.org/10.1016/j.dsr2.2015.05.001

Becker, K. (1985). Initial Reports of the Deep Sea Drilling Project, 83. *Initial Reports of the Deep Sea Drilling Project*. https://doi.org/10.2973/dsdp.proc.83.124.1985

Becker, K. (1989). Proceedings of the Ocean Drilling Program, 111 Scientific Reports. https://doi.org/10.2973/odp.proc.sr.111.156.1989

Becker, K. (1990). Proceedings of the Ocean Drilling Program, 106/109 Scientific Results. *Proceedings of the Ocean Drilling Program*. https://doi.org/10.2973/odp.proc.sr.106109.146.1990

Becker, K., & Fisher, A. T. (2008). Borehole packer tests at multiple depths resolve distinct hydrologic intervals in 3.5-Ma upper oceanic crust on the eastern flank of Juan de Fuca Ridge. *Journal of Geophysical Research: Solid Earth (1978–2012)*, *113*(B7). https://doi.org/10.1029/2007jb005446

Becker, K., Herzen, R. V., Kirklin, J., Evans, R., Kadko, D., Kinoshita, M., et al. (1996). Conductive heat flow at the TAG Active Hydrothermal Mound: Results from 1993–1995 submersible surveys. *Geophysical Research Letters*, *23*(23), 3463–3466. https://doi.org/10.1029/96gl00969

Becker, K., & Davis, E. E. (2003). New evidence for age variation and scale effects of permeabilities of young oceanic crust from borehole thermal and pressure measurements. *Earth and Planetary Science Letters*, *210*(3–4), 499–508. https://doi.org/10.1016/s0012-821x(03)00160-2

Becker, K., Langseth, M. G., Herzen, R. P. V., & Anderson, R. N. (1983). Deep crustal geothermal measurements, hole 504B, Costa Rica Rift. *Journal of Geophysical Research: Solid Earth*, *88*(B4), 3447–3457. https://doi.org/10.1029/jb088ib04p03447

Bemis, K., Lowell, R., & Farough, A. (2012). Diffuse Flow On and Around Hydrothermal Vents at Mid-Ocean Ridges. *Oceanography*, *25*(1), 182–191. https://doi.org/10.5670/oceanog.2012.16

Besson, P., Degboe, J., Berge, B., Chavagnac, V., Fabre, S., & Berger, G. (2014). Calcium, Na, K and Mg Concentrations in Seawater by Inductively Coupled Plasma-Atomic Emission Spectrometry: Applications to IAPSO Seawater Reference Material, Hydrothermal Fluids and Synthetic Seawater Solutions. *Geostandards and Geoanalytical Research*, *38*(3), 355–362. https://doi.org/10.1111/j.1751-908x.2013.00269.x

Best, M. M. R., Favali, P., Beranzoli, L., Blandin, J., Çağatay, N. M., Cannat, M., et al. (2016). The EMSO-ERIC Pan-European Consortium: Data Benefits and Lessons Learned as the Legal Entity Forms. *Marine Technology Society Journal*, *50*(3), 8-15(8). https://doi.org/10.4031/mtsj.50.3.13

Biot, M. A. (1941). General Theory of Three-Dimensional Consolidation. *Journal of Applied Physics*, *12*(2), 155–164. https://doi.org/10.1063/1.1712886

Bischoff, J L, & Rosenbauer, R. J. (1985). An empirical equation of state for hydrothermal seawater (3.2 percent NaCl). *American Journal of Science*, *285*(8), 725–763. https://doi.org/10.2475/ajs.285.8.725

Bischoff, J L, & Seyfried, W. E. (1978). Hydrothermal chemistry of seawater from 25 degrees to 350 degrees C. *American Journal of Science*, *278*(6), 838–860. https://doi.org/10.2475/ajs.278.6.838

Bischoff, J L, & Rosenbauer, R. J. (1988). Liquid-vapor relations in the critical region of the system NaCl-H2O from 380 to 415°C: A refined determination of the critical point and two-phase boundary of seawater. *Geochimica et Cosmochimica Acta*, *52*(8), 2121–2126. https://doi.org/10.1016/0016-7037(88)90192-5

Blandin, J., Colaço, A., Legrand, J., Cannat, M., Sarradin, P. M., Sarrazin, J., & participants, and the project. (2010). The MoMAR-D project: a challenge to monitor in real time the Lucky Strike hydrothermal vent field.

Blöchl, E., Rachel, R., Burggraf, S., Hafenbradl, D., Jannasch, H. W., & Stetter, K. O. (1997). Pyrolobus fumarii, gen. and sp. nov., represents a novel group of archaea, extending the upper temperature limit for life to 113°C. *Extremophiles*, *1*(1), 14–21. https://doi.org/10.1007/s007920050010

Blounot, C. W., & Dickson, F. W. (1969). The solubility of anhydrite (CaSO4) in NaCl-H2O from 100 to 450°C and 1 to 1000 bars. *Geochimica et Cosmochimica Acta*, *33*(2), 227–245. https://doi.org/10.1016/0016-7037(69)90140-9

Blount, C. W. (1977). Barite solubilities and thermodynamic quantities up to 300°C and 1400 bars.

Bodvarsson, G., & Lowell, R. P. (1972). Ocean-floor heat flow and the circulation of interstitial waters. *Journal of Geophysical Research*, *77*(23), 4472–4475. https://doi.org/10.1029/jb077i023p04472

Bostrom, K., & Peterson, M. N. A. (1966). Precipitates from hydrothermal exhalations on the East Pacific rise. *Economic Geology*, *61*(7), 1258–1265. https://doi.org/10.2113/gsecongeo.61.7.1258

Buck, W. R., Lavier, L. L., & Poliakov, A. N. B. (2005). Modes of faulting at mid-ocean ridges. *Nature*, *434*(7034), 719–723. https://doi.org/10.1038/nature03358

Butterfield, D. A., Roe, K. K., Lilley, M. D., Huber, J. A., Baross, J. A., Embley, R. W., & Massoth, G. J. (2004). Mixing, Reaction and Microbial Activity in the Sub-seafloor Revealed by Temporal and Spatial Variation in Diffuse Flow Vents at Axial Volcano. *Geophysical Monograph Series*. https://doi.org/10.1029/144gm17

Cann, J. R., & Strens, M. R. (1989). Modeling periodic megaplume emission by black smoker systems. *Journal of Geophysical Research: Solid Earth*, *94*(B9), 12227–12237. https://doi.org/10.1029/jb094ib09p12227

Cann, J. R., Strens, M. R., & Rice, A. (1985). A simple magma-driven thermal balance model for the formation of volcanogenic massive sulphides. *Earth and Planetary Science Letters*, *76*(1–2), 123–134. https://doi.org/10.1016/0012-821x(85)90153-0

Cannat, M., Wheeler, B., Barreyre, T., & Sarradin, P.-M. (2017). Array of Ocean Bottom Tilt Current Meters: data from the EMSO-Azores observatory, 2016-2017. *SEANOE*. https://doi.org/https://doi.org/10.17882/74195

Cannat, M., Wheeler, B., Rouméjon, S., Sarradin, P.-M., & Legrand, J. (2018a). Array of Ocean Bottom Tilt Current Meters: data from the EMSO-Azores observatory, 2017-2018. *SEANOE*. https://doi.org/https://doi.org/10.17882/57005

Cannat, M., Wheeler, B., Chen, J., Sarradin, P.-M., & Legrand, J. (2020a). Array of Ocean Bottom Tilt Current Meters: data from the EMSO-Azores observatory, 2018-2019. *SEANOE*. https://doi.org/https://doi.org/10.17882/74378

Cannat, M. (1993). Emplacement of mantle rocks in the seafloor at mid-ocean ridges. *Journal of Geophysical Research: Solid Earth*, *98*(B3), 4163–4172. https://doi.org/10.1029/92jb02221

Cannat, M., Mevel, C., Maia, M., Deplus, C., Durand, C., Gente, P., et al. (1995). Thin crust, ultramafic exposures, and rugged faulting patterns at the Mid-Atlantic Ridge (22°–24°N). *Geology*, *23*(1), 49–52. https://doi.org/10.1130/0091-7613(1995)023<0049:tcuear>2.3.co;2

Cannat, M., Briais, A., Deplus, C., Escartín, J., Georgen, J., Lin, J., et al. (1999). Mid-Atlantic Ridge–Azores hotspot interactions: along-axis migration of a hotspot-derived event of enhanced magmatism 10 to 4 Ma ago. *Earth and Planetary Science Letters*, *173*(3), 257–269. https://doi.org/10.1016/s0012-821x(99)00234-4

Cannat, M., Cann, J., & Maclennan, J. (2004). Mid-Ocean Ridges. *Geophysical Monograph Series*, 111–149. https://doi.org/10.1029/148gm05

Cannat, M., Fontaine, F. J., Barreyre, T., Wheeler, B., Escartin, J., & Sarradin, P.-M. (2018b). Autonomous temperature probes, data from the EMSO-Azores observatory, 2016-2017. (Vol. SEANOE). https://doi.org/https://doi.org/10.17882/56428

Cannat, M., Wheeler, B., Fontaine, F. J., Rouméjon, S., Sarradin, P.-M., & Legrand, J. (2020b). Autonomous temperature probes, data from the EMSO-Azores observatory, 2017-2018. *SEANOE*. https://doi.org/https://doi.org/10.17882/75412

Cannat, M., Wheeler, B., Fontaine, F., Chen, J., Sarradin, P.-M., & Legrand, J. (2021a). Autonomous temperature probes, data from the EMSO-Azores observatory, 2018-2019. *SEANOE*. https://doi.org/10.17882/79527

Cannat, M., Wheeler, B., Fontaine, F., Chen, J., & Sarradin, P.-M. (2021b). Autonomous temperature probes, data from the EMSO-Azores observatory, 2019-2020. *SEANOE*. https://doi.org/10.17882/79528

Cannon, G. A., & Thomson, R. E. (1996). Characteristics of 4-day oscillations trapped by the Juan De Fuca Ridge. *Geophysical Research Letters*, *23*(13), 1613–1616. https://doi.org/10.1029/96gl01370

Carlson, R. L. (2011). The effect of hydrothermal alteration on the seismic structure of the upper oceanic crust: Evidence from Holes 504B and 1256D. *Geochemistry, Geophysics, Geosystems*, *12*(9), n/a-n/a. https://doi.org/10.1029/2011gc003624

Carlson, R. L. (2014). The influence of porosity and crack morphology on seismic velocity and permeability in the upper oceanic crust. *Geochemistry, Geophysics, Geosystems*, *15*(1), 10–27. https://doi.org/10.1002/2013gc004965

Charlou, J. L., Donval, J. P., Douville, E., Jean-Baptiste, P., Radford-Knoery, J., Fouquet, Y., et al. (2000). Compared geochemical signatures and the evolution of Menez Gwen (37°50′N) and Lucky Strike (37°17′N) hydrothermal fluids, south of the Azores Triple Junction on the Mid-Atlantic Ridge. *Chemical Geology*, *171*(1–2), 49–75. https://doi.org/10.1016/s0009-2541(00)00244-8

Charnock, H. (1964). Anomalous Bottom Water in the Red Sea. *Nature*, *203*(4945), 591. https://doi.org/10.1038/203591a0

Chavagnac, V., Leleu, T., Fontaine, F., Cannat, M., Ceuleneer, G., & Castillo, A. (2018). Spatial Variations in Vent Chemistry at the Lucky Strike Hydrothermal Field, Mid-Atlantic Ridge (37°N): Updates for Subseafloor Flow Geometry From the Newly Discovered Capelinhos Vent. *Geochemistry, Geophysics, Geosystems*, *19*(11), 4444–4458. https://doi.org/10.1029/2018gc007765

Chen, X.-G., Yu, M.-Z., Loh, P. S., Garbe-Schönberg, D., Qiu, Z., Schmidt, M., et al. (2020). A tidal-influenced hydrothermal system temporarily cooled by a tropical storm. *Journal of Volcanology and Geothermal Research*, *393*, 106792. https://doi.org/10.1016/j.jvolgeores.2020.106792

Chen, Y., & Morgan, W. J. (1990). A nonlinear rheology model for mid-ocean ridge axis topography. *Journal of Geophysical Research: Solid Earth*, *95*(B11), 17583–17604. https://doi.org/10.1029/jb095ib11p17583

Chen, Y. J. (1992). Oceanic crustal thickness versus spreading rate. *Geophysical Research Letters*, *19*(8), 753–756. https://doi.org/10.1029/92gl00161

Chevaldonné, P., Desbruyères, D., & Haître, M. L. (1991). Time-series of temperature from three deep-sea hydrothermal vent sites. *Deep Sea Research Part A. Oceanographic Research Papers*, *38*(11), 1417–1430. https://doi.org/10.1016/0198-0149(91)90014-7

Christeson, G. L., McIntosh, K. D., & Karson, J. A. (2007). Inconsistent correlation of seismic layer 2a and lava layer thickness in oceanic crust. *Nature*, *445*(7126), 418. https://doi.org/10.1038/nature05517

Colaço, A., Blandin, J., Cannat, M., Carval, T., Chavagnac, V., Connelly, D., et al. (2011). MoMAR-D: a technological challenge to monitor the dynamics of the Lucky Strike vent ecosystem. *ICES Journal of Marine Science*, *68*(2), 416–424. https://doi.org/10.1093/icesjms/fsq075

Combier, V., Seher, T., SIngh, S. C., Crawford, W., Cannat, M., Escartin, J., & carton, H. (2007). Three-dimensional Geometry of Magma Chamber Roof and Faults from 3D Seismic Reflection Data at the Lucky Strike Volcano, Mid-Atlantic Ridge. American Geophysical Union, Fall Meeting 2007, abstract id. T23B-1408.

Combier, V., Seher, T., Singh, S. C., Crawford, W. C., Cannat, M., Escartín, J., & Dusunur, D. (2015). Three-dimensional geometry of axial magma chamber roof and faults at Lucky Strike volcano on the Mid-Atlantic Ridge. *Journal of Geophysical Research: Solid Earth*, *120*(8), 5379–5400. https://doi.org/10.1002/2015jb012365

Converse, D. R., Holland, H. D., & Edmond, J. M. (1984). Flow rates in the axial hot springs of the East Pacific Rise (21°N): Implications for the heat budget and the formation of massive sulfide deposits. *Earth and Planetary Science Letters*, *69*(1), 159–175. https://doi.org/10.1016/0012-821x(84)90080-3

Cooper, M. J., Elderfield, H., & Schultz, A. (2000). Diffuse hydrothermal fluids from Lucky Strike hydrothermal vent field: Evidence for a shallow conductively heated system. *Journal of Geophysical Research: Solid Earth*, *105*(B8), 19369–19375. https://doi.org/10.1029/2000jb900138

Corliss, J. B., Dymond, J., Gordon, L. I., Edmond, J. M., Herzen, R. P. von, Ballard, R. D., et al. (1979). Submarine Thermal Sprirngs on the Galápagos Rift. *Science*, *203*(4385), 1073–1083. https://doi.org/10.1126/science.203.4385.1073

Costa, I. (2014). *Genesis of the brecciated rocks from mid atlantic ridge hydrothermal systems : Lucky Strike (37º50'N) and Menez Gwen (37º50'N)*.

Coumou, D., Driesner, T., & Heinrich, C. A. (2008). The Structure and Dynamics of Mid-Ocean Ridge Hydrothermal Systems. *Science*, *321*(5897), 1825–1828. https://doi.org/10.1126/science.1159582

Coumou, D., Driesner, T., Geiger, S., Heinrich, C. A., & Matthäi, S. (2006). The dynamics of mid-ocean ridge hydrothermal systems: Splitting plumes and fluctuating vent temperatures. *Earth and Planetary Science Letters*, *245*(1–2), 218–231. https://doi.org/10.1016/j.epsl.2006.02.044

Cowen, J. P., Massoth, G. J., & Feely, R. A. (1990). Scavenging rates of dissolved manganese in a hydrothermal vent plume. *Deep Sea Research Part A. Oceanographic Research Papers*, *37*(10), 1619–1637. https://doi.org/10.1016/0198-0149(90)90065-4

Crawford, W. C., Singh, S. C., Seher, T., Combier, V., Dogan, D. D., & Cannat, M. (2010). Crustal Structure, Magma Chamber, and Faulting Beneath the Lucky Strike Hydrothermal Vent Field. *Washington DC American Geophysical Union Geophysical Monograph Series*. https://doi.org/10.1029/2008gm000726

Crawford, W. C., Rai, A., Singh, S. C., Cannat, M., Escartin, J., Wang, H., et al. (2013). Hydrothermal seismicity beneath the summit of Lucky Strike volcano, Mid-Atlantic Ridge. *Earth and Planetary Science Letters*, *373*, 118–128. https://doi.org/10.1016/j.epsl.2013.04.028

Crépeau, V., Bonavita, M. C., Lesongeur, F., Randrianalivelo, H., Sarradin, P., Sarrazin, J., & Godfroy, A. (2011). Diversity and function in microbial mats from the Lucky Strike hydrothermal vent field. *FEMS Microbiology Ecology*, *76*(3), 524–540. https://doi.org/10.1111/j.1574-6941.2011.01070.x

Crone, T. J., & Wilcock, W. S. D. (2005). Modeling the effects of tidal loading on mid-ocean ridge hydrothermal systems. *Geochemistry, Geophysics, Geosystems*, *6*(7), n/a-n/a. https://doi.org/10.1029/2004gc000905

Crone, T. J., Wilcock, W. S. D., & McDuff, R. E. (2010). Flow rate perturbations in a black smoker hydrothermal vent in response to a mid-ocean ridge earthquake swarm. *Geochemistry, Geophysics, Geosystems*, *11*(3), n/a-n/a. https://doi.org/10.1029/2009gc002926

Crone, T. J., Tolstoy, M., & Stroup, D. F. (2011). Permeability structure of young ocean crust from poroelastically triggered earthquakes. *Geophysical Research Letters*, *38*(5), n/a-n/a. https://doi.org/10.1029/2011gl046820

Curewitz, D., & Karson, J. A. (1997). Structural settings of hydrothermal outflow: Fracture permeability maintained by fault propagation and interaction. *Journal of Volcanology and Geothermal Research*, *79*(3–4), 149–168. https://doi.org/10.1016/s0377-0273(97)00027-9

Cuvelier, D., Sarrazin, J., Colaço, A., Copley, J., Desbruyères, D., Glover, A. G., et al. (2009). Distribution and spatial variation of hydrothermal faunal assemblages at Lucky Strike (Mid-Atlantic Ridge) revealed by high-resolution video image analysis. *Deep Sea Research Part I: Oceanographic Research Papers*, *56*(11), 2026–2040. https://doi.org/10.1016/j.dsr.2009.06.006

Cuvelier, D., Legendre, P., Laes, A., Sarradin, P.-M., & Sarrazin, J. (2014). Rhythms and Community Dynamics of a Hydrothermal Tubeworm Assemblage at Main Endeavour Field – A Multidisciplinary Deep-Sea Observatory Approach. *PLoS ONE*, *9*(5), e96924. https://doi.org/10.1371/journal.pone.0096924

Von Damm, K. L. (1988). Systematics of and postulated controls on submarine hydrothermal solution chemistry. *Journal of Geophysical Research: Solid Earth*, *93*(B5), 4551–4561. https://doi.org/10.1029/jb093ib05p04551

Von Damm, K. L. (1995). Geophysical Monograph Series, 222–247. https://doi.org/10.1029/gm091p0222

Von Damm, K. L. (2000). Chemistry of hydrothermal vent fluids from 9°–10°N, East Pacific Rise: "Time zero," the immediate posteruptive period. *Journal of Geophysical Research: Solid Earth*, *105*(B5), 11203–11222. https://doi.org/10.1029/1999jb900414

Von Damm, K. V., Bray, A. M., Buttermore, L. G., & Oosting, S. E. (1998). The geochemical controls on vent fluids from the Lucky Strike vent field, Mid-Atlantic Ridge. *Earth and Planetary Science Letters*, *160*(3–4), 521–536. https://doi.org/10.1016/s0012-821x(98)00108-3

Von Damm, K. L., & Lilley, M. D. (2004). Diffuse Flow Hydrothermal Fluids from 9° 50′ N East Pacific Rise: Origin, Evolution and Biogeochemical Controls. In W. S. D. Wilcock (Ed.).

Davis, E., & Becker, K. (1999). Tidal pumping of fluids within and from the oceanic crust: new observations and opportunities for sampling the crustal hydrosphere. *Earth and Planetary Science Letters*, *172*(1–2), 141–149. https://doi.org/10.1016/s0012-821x(99)00197-1

Davis, E., Becker, K., Dziak, R., Cassidy, J., Wang, K., & Lilley, M. (2004). Hydrological response to a seafloor spreading episode on the Juan de Fuca ridge. *Nature*, *430*(6997), 335. https://doi.org/10.1038/nature02755

Davis, E. E., Wang, K., Becker, K., & Thomson, R. E. (2000). Formation-scale hydraulic and mechanical properties of oceanic crust inferred from pore pressure response to periodic seafloor loading. *Journal of Geophysical Research: Solid Earth*, *105*(B6), 13423–13435. https://doi.org/10.1029/2000jb900084

Davis, E. E., Chapman, D. S., & Forster, C. B. (1996). Observations concerning the vigor of hydrothermal circulation in young oceanic crust. *Journal of Geophysical Research: Solid Earth*, *101*(B2), 2927–2942. https://doi.org/10.1029/95jb02997

Davis, E. E., LaBonte, A., He, J., Becker, K., & Fisher, A. (2010). Thermally stimulated "runaway" downhole flow in a superhydrostatic ocean crustal borehole: Observations, simulations, and inferences regarding crustal permeability. *Journal of Geophysical Research: Solid Earth (1978–2012)*, *115*(B7). https://doi.org/10.1029/2009jb006986

Davis, E. E., & Lister, C. R. B. (1974). Fundamentals of ridge crest topography. *Earth and Planetary Science Letters*, *21*(4), 405–413. https://doi.org/10.1016/0012-821x(74)90180-0

Delaney, J. R., Robigou, V., McDuff, R. E., & Tivey, M. K. (1992). Geology of a vigorous hydrothermal system on the Endeavour Segment, Juan de Fuca Ridge. *Journal of Geophysical Research: Solid Earth*, *97*(B13), 19663–19682. https://doi.org/10.1029/92jb00174

DeMets, C., Gordon, R. G., Argus, D. F., & Stein, S. (1990). Current plate motions. *Geophysical Journal International*, *101*(2), 425–478. https://doi.org/10.1111/j.1365-246x.1990.tb06579.x

Detrick, R. S., Buhl, P., Vera, E., Mutter, J., Orcutt, J., Madsen, J., & Brocher, T. (1987). Multi-channel seismic imaging of a crustal magma chamber along the East Pacific Rise. *Nature*, *326*(6108), 35–41. https://doi.org/10.1038/326035a0

Dias, Á. S., Mills, R. A., Taylor, R. N., Ferreira, P., & Barriga, F. J. A. S. (2008). Geochemistry of a sediment push-core from the Lucky Strike hydrothermal field, Mid-Atlantic Ridge. *Chemical Geology*, *247*(3–4), 339–351. https://doi.org/10.1016/j.chemgeo.2007.10.015

Dick, H., Thompson, G., & Bryan, W. (1981). Low-angle faulting and steady-state emplacement of plutonic rocks at ridge-transform intersections. *Eos Trans. AGU*, *62*(17), 406.

Dover, C. L. V., Desbruyères, D., Segonzac, M., Comtet, T., Saldanha, L., Fiala-Medioni, A., & Langmuir, C. (1996). Biology of the Lucky Strike hydrothermal field. *Deep Sea Research Part I: Oceanographic Research Papers*, *43*(9), 1509–1529. https://doi.org/10.1016/s0967-0637(96)00051-9

Driesner, T. (2010). The interplay of permeability and fluid properties as a first order control of heat transport, venting temperatures and venting salinities at mid-ocean ridge hydrothermal systems. *Geofluids*, *10*(1-2), 132–141. https://doi.org/10.1111/j.1468-8123.2009.00273.x

Driesner, T., & Heinrich, C. A. (2007). The system H2O–NaCl. Part I: Correlation formulae for phase relations in temperature–pressure–composition space from 0 to 1000°C, 0 to 5000bar, and 0 to 1 XNaCl. *Geochimica et Cosmochimica Acta*, *71*(20), 4880–4901. https://doi.org/10.1016/j.gca.2006.01.033

Dunn, R. A., Toomey, D. R., & Solomon, S. C. (2000). Three-dimensional seismic structure and physical properties of the crust and shallow mantle beneath the East Pacific Rise at 9°30'N. *Journal of Geophysical Research: Solid Earth*, *105*(B10), 23537–23555. https://doi.org/10.1029/2000jb900210

Edmond, J. M., Measures, C., Mangum, B., Grant, B., Sclater, F. R., Collier, R., et al. (1979a). On the formation of metal-rich deposits at ridge crests. *Earth and Planetary Science Letters*, *46*(1), 19–30. https://doi.org/10.1016/0012-821x(79)90062-1

Edmond, J. M., Measures, C., McDuff, R. E., Chan, L. H., Collier, R., Grant, B., et al. (1979b). Ridge crest hydrothermal activity and the balances of the major and minor elements in the ocean: The Galapagos data. *Earth and Planetary Science Letters*, *46*(1), 1–18. https://doi.org/10.1016/0012-821x(79)90061-x

Edmond, J. M., Campbell, A. C., Palmer, M. R., Klinkhammer, G. P., German, C. R., Edmonds, H. N., et al. (1995). Time series studies of vent fluids from the TAG and MARK sites (1986, 1990) Mid-Atlantic Ridge: a new solution chemistry model and a mechanism for Cu/Zn zonation in massive sulphide orebodies. *Geological Society, London, Special Publications*, *87*(1), 77–86. https://doi.org/10.1144/gsl.sp.1995.087.01.07

Eissen, J., Fouquet, Y., Hardy, D., & Ondréas, H. (2003). Recent MORB Volcaniclastic Explosive Deposits Formed Between 500 and 1750 m.b.s.l. on the Axis of the Mid-Atlantic Ridge, South of the Azores. https://doi.org/10.1029/140gm09

Elderfield, H., & Schultz, A. (1996). MID-OCEAN RIDGE HYDROTHERMAL FLUXES AND THE CHEMICAL COMPOSITION OF THE OCEAN. *Earth and Planetary Sciences*, *24*(1), 191–224. https://doi.org/10.1146/annurev.earth.24.1.191

Eldursi, K., Branquet, Y., Guillou-Frottier, L., & Marcoux, E. (2009). Numerical investigation of transient hydrothermal processes around intrusions: Heat-transfer and fluid-circulation controlled mineralization patterns. *Earth and Planetary Science Letters*, *288*(1–2), 70–83. https://doi.org/10.1016/j.epsl.2009.09.009

Embley, R. W., Jonasson, I. R., Perfit, M., Franklin, J. M., Tivey, M. A., Malahoff, A., et al. (1988). Submersible investigation of an extinct hydrothermal system on the Galapagos Ridge; sulfide mounds, stockwork zone, and differentiated lavas. *Canadian Mineralogist*, *26*, 517–539.

Embley, R. W., Murphy, K. M., & Fox, C. G. (1990). High-resolution studies of the summit of Axial Volcano. *Journal of Geophysical Research: Solid Earth*, *95*(B8), 12785–12812. https://doi.org/10.1029/jb095ib08p12785

Emmanuel, S., & Berkowitz, B. (2005). Mixing-induced precipitation and porosity evolution in porous media. *Advances in Water Resources*, *28*(4), 337–344. https://doi.org/10.1016/j.advwatres.2004.11.010

Escartín, J., Soule, S. A., Cannat, M., Fornari, D. J., Düşünür, D., & Garcia, R. (2014). Lucky Strike seamount: Implications for the emplacement and rifting of segment-centered volcanoes at slow spreading mid-ocean ridges. *Geochemistry, Geophysics, Geosystems*, *15*(11), 4157–4179. https://doi.org/10.1002/2014gc005477

Escartin, J., Barreyre, T., Cannat, M., Garcia, R., Gracias, N., Deschamps, A., et al. (2015). Hydrothermal activity along the slow-spreading Lucky Strike ridge segment (Mid-Atlantic Ridge): Distribution, heatflux, and geological controls. *Earth and Planetary Science Letters*, *431*(Earth Planet. Sci. Lett. 263 2007), 173–185. https://doi.org/10.1016/j.epsl.2015.09.025

Evans, R. L. (1994). Constraints On the Large-Scale Porosity and Permeability Structure of Young Oceanic Crust From Velocity and Resistivity Data. *Geophysical Journal International*, *119*(3), 869–879. https://doi.org/10.1111/j.1365-246x.1994.tb04023.x

Fehn, U., & Cathles, L. M. (1979). Hydrothermal convection at slow-spreading mid-ocean ridges. *Tectonophysics*, *55*(1–2), 239–260. https://doi.org/10.1016/0040-1951(79)90343-3

Field, M. P., & Sherrell, R. M. (2000). Dissolved and particulate Fe in a hydrothermal plume at 9°45′N, East Pacific Rise: Slow Fe (II) oxidation kinetics in Pacific plumes. *Geochimica et Cosmochimica Acta*, *64*(4), 619–628. https://doi.org/10.1016/s0016-7037(99)00333-6

Fisher, A. T., Becker, K., & Davis, E. E. (1997). The permeability of young oceanic crust east of Juan de Fuca Ridge Determined using borehole thermal measurements. *Geophysical Research Letters*, *24*(11), 1311–1314. https://doi.org/10.1029/97gl01286

Fisher, A. T., Davis, E. E., & Becker, K. (2008). Borehole-to-borehole hydrologic response across 2.4 km in the upper oceanic crust: Implications for crustal-scale properties. *Journal of Geophysical Research: Solid Earth (1978–2012)*, *113*(B7). https://doi.org/10.1029/2007jb005447

Fisher, A. T. (1998). Permeability within basaltic oceanic crust. *Reviews of Geophysics*, *36*(2), 143–182. https://doi.org/10.1029/97rg02916

Fontaine, F. J., & Wilcock, W. S. D. (2006). Dynamics and storage of brine in mid-ocean ridge hydrothermal systems. *Journal of Geophysical Research: Solid Earth (1978–2012)*, *111*(B6), n/a-n/a. https://doi.org/10.1029/2005jb003866

Fontaine, F. J., & Wilcock, W. S. D. (2007a). Two-dimensional numerical models of open-top hydrothermal convection at high Rayleigh and Nusselt numbers: Implications for mid-ocean ridge hydrothermal circulation. *Geochemistry, Geophysics, Geosystems*, *8*(7), n/a-n/a. https://doi.org/10.1029/2007gc001601

Fontaine, F. J., Wilcock, W. S. D., & Butterfield, D. A. (2007b). Physical controls on the salinity of mid-ocean ridge hydrothermal vent fluids. *Earth and Planetary Science Letters*, *257*(1–2), 132–145. https://doi.org/10.1016/j.epsl.2007.02.027

Fontaine, F. J., Wilcock, W. S. D., Foustoukos, D. E., & Butterfield, D. A. (2009). A Si-Cl geothermobarometer for the reaction zone of high-temperature, basaltic-hosted mid-ocean ridge hydrothermal systems. *Geochemistry, Geophysics, Geosystems*, *10*(5), n/a-n/a. https://doi.org/10.1029/2009gc002407

Fontaine, F. J., Olive, J., Cannat, M., Escartin, J., & Perol, T. (2011). Hydrothermally-induced melt lens cooling and segmentation along the axis of fast- and intermediate-spreading centers. *Geophysical Research Letters*, *38*(14), n/a-n/a. https://doi.org/10.1029/2011gl047798

Fontaine, F. J., Cannat, M., Escartin, J., & Crawford, W. C. (2014). Along-axis hydrothermal flow at the axis of slow spreading Mid-Ocean Ridges: Insights from numerical models of the Lucky Strike vent field (MAR). *Geochemistry, Geophysics, Geosystems*, *15*(7), 2918–2931. https://doi.org/10.1002/2014gc005372

Fontaine, F. J., Rabinowicz, M., & Boulègue, J. (2001). Permeability changes due to mineral diagenesis in fractured crust: implications for hydrothermal circulation at mid-ocean ridges. *Earth and Planetary Science Letters*, *184*(2), 407–425. https://doi.org/10.1016/s0012-821x(00)00332-0

Fornari, D., Tivey, M., Schouten, H., Perfit, M., Yoerger, D., Bradley, A., et al. (2004). Mid-Ocean Ridges, 187–217. https://doi.org/10.1029/148gm08

Fornari, D. J., Shank, T., Damm, K. L. V., Gregg, T. K. P., Lilley, M., Levai, G., et al. (1998). Time-series temperature measurements at high-temperature hydrothermal vents, East Pacific Rise 9°49′–51′N: evidence for monitoring a crustal cracking event. *Earth and Planetary Science Letters*, *160*(3–4), 419–431. https://doi.org/10.1016/s0012-821x(98)00101-0

Fouquet, Y, Henry, K., Knott, R., & Cambon, P. (1998). Proceedings of the Ocean Drilling Program, 158 Scientific Results. *Proceedings of the Ocean Drilling Program*. https://doi.org/10.2973/odp.proc.sr.158.216.1998

Fouquet, Y, Wafik, A., Cambon, P., Mevel, C., Meyer, G., & Gente, P. (1993). Tectonic setting and mineralogical and geochemical zonation in the Snake Pit sulfide deposit (Mid-Atlantic Ridge at 23 degrees N). *Economic Geology*, *88*(8), 2018–2036. https://doi.org/10.2113/gsecongeo.88.8.2018

Fouquet, Y, Charlou, J.-L., Costa, I., Donval, J.-P., Radford-Knoery, J., Pellé, H., et al. (1994). A Detailed Study of the Lucky Strike Hydrothermal Site and Discovery of a New Hydrothermal Site: Menez Gwen ; Preliminary Results of the DIVA1 Cruise (5-29 May, 1994). *InterRidge News*.

Foustoukos, D. I., Pester, N. J., Ding, K., & Seyfried, W. E. (2009). Dissolved carbon species in associated diffuse and focused flow hydrothermal vents at the Main Endeavour Field, Juan de Fuca Ridge: Phase equilibria and kinetic constraints. *Geochemistry, Geophysics, Geosystems*, *10*(10), n/a-n/a. https://doi.org/10.1029/2009gc002472

Gamberi, F., Marani, M., & Savelli, C. (1997). Tectonic, volcanic and hydrothermal features of a submarine portion of the Aeolian arc (Tyrrhenian Sea). *Marine Geology*, *140*(1–2), 167–181. https://doi.org/10.1016/s0025-3227(97)00020-0

Gamo, T., Chiba, H., Masuda, H., Edmonds, H. N., Fujioka, K., Kodama, Y., et al. (1996). Chemical characteristics of hydrothermal fluids from the TAG Mound of the Mid-Atlantic Ridge in August 1994: Implications for spatial and temporal variability of hydrothermal activity. *Geophysical Research Letters*, *23*(23), 3483–3486. https://doi.org/10.1029/96gl02521

German, C. R., Yoerger, D. R., Jakuba, M., Shank, T. M., Langmuir, C. H., & Nakamura, K. (2008). Hydrothermal exploration with the Autonomous Benthic Explorer. *Deep Sea Research Part I: Oceanographic Research Papers*, *55*(2), 203–219. https://doi.org/10.1016/j.dsr.2007.11.004

German, C.R., Thurnherr, A. M., Knoery, J., Charlou, J.-L., Jean-Baptiste, P., & Edmonds, H. N. (2010). Heat, volume and chemical fluxes from submarine venting: A synthesis of results from the Rainbow hydrothermal field, 36°N MAR. *Deep Sea Research Part I: Oceanographic Research Papers*, *57*(4), 518–527. https://doi.org/10.1016/j.dsr.2009.12.011

Ginster, U., Mottl, M. J., & Herzen, R. P. V. (1994). Heat flux from black smokers on the Endeavour and Cleft segments, Juan de Fuca Ridge. *Journal of Geophysical Research: Solid Earth*, *99*(B3), 4937–4950. https://doi.org/10.1029/93jb02800

Girard, F., Sarrazin, J., Arnaubec, A., Cannat, M., Sarradin, P.-M., Wheeler, B., & Matabos, M. (2020). Currents and topography drive assemblage distribution on an active hydrothermal edifice. *Progress in Oceanography*, *187*, 102397. https://doi.org/10.1016/j.pocean.2020.102397

Glickson, D. A., Kelley, D. S., & Delaney, J. R. (2007). Geology and hydrothermal evolution of the Mothra Hydrothermal Field, Endeavour Segment, Juan de Fuca Ridge. *Geochemistry, Geophysics, Geosystems*, *8*(6), n/a-n/a. https://doi.org/10.1029/2007gc001588

Goto, S., Kinoshita, M., Schultz, A., & Herzen, R. P. V. (2003). Estimate of heat flux and its temporal variation at the TAG hydrothermal mound, Mid-Atlantic Ridge 26°N. *Journal of Geophysical Research: Solid Earth (1978–2012)*, *108*(B9). https://doi.org/10.1029/2001jb000703

Guillou-Frottier, L., Duwiquet, H., Launay, G., Taillefer, A., Roche, V., & Link, G. (2020). On the morphology and amplitude of 2D and 3D thermal anomalies induced by buoyancy-driven flow within and around fault zones. *Solid Earth*, *11*(4), 1571–1595. https://doi.org/10.5194/se-11-1571-2020

Guo, Z., Rüpke, L. H., Fuchs, S., Iyer, K., Hannington, M. D., Chen, C., et al. (2020). Anhydrite-Assisted Hydrothermal Metal Transport to the Ocean Floor—Insights From Thermo-Hydro-Chemical Modeling. *Journal of Geophysical Research: Solid Earth*, *125*(7). https://doi.org/10.1029/2019jb019035

Hannington, M. D., & Scott, S. D. (1988). Mineralogy and geochemistry of a hydrothermal silica-sulfide-sulfate spire in the caldera of Axial Seamount, Juan De Fuca Ridge. *The Canadian Mineralogist (1988) 26 (3): 603-625.*

Hannington, M. D., Jonasson, I. R., Herzig, P. M., & Petersen, S. (1995). Geophysical Monograph Series, 115–157. https://doi.org/10.1029/gm091p0115

Hawkes, J. A., Connelly, D. P., Gledhill, M., & Achterberg, E. P. (2013). The stabilisation and transportation of dissolved iron from high temperature hydrothermal vent systems. *Earth and Planetary Science Letters*, *375*, 280–290. https://doi.org/10.1016/j.epsl.2013.05.047

Haymon, R. M., Fornari, D. J., Damm, K. L. V., Lilley, M. D., Perfit, M. R., Edmond, J. M., et al. (1993). Volcanic eruption of the mid-ocean ridge along the East Pacific Rise crest at 9°45–52′N: Direct submersible observations of seafloor phenomena associated with an eruption event in April, 1991. *Earth and Planetary Science Letters*, *119*(1–2), 85–101. https://doi.org/10.1016/0012-821x(93)90008-w

Hendershott, M. (2005). Lecture1: Introduction to ocean tides. In N. J. Balmforth, S. Llewellyn-Smith, M. Hendershott, & C. Garrett, *2004 Program of Study: Tides*. Retrieved from https://apps.dtic.mil/sti/citations/ADA437377

Hicks, S. D. (2006). *Understanding tides.* (NOAA, Ed.). https://doi.org/10.25607/obp-157

Holden, J. F., & Daniel, R. M. (2004). The Upper Temperature Limit for Life Based on Hyperthermophile Culture Experiments and Field Observations, 13–24. https://doi.org/10.1029/144gm02

Humphris, S E. (1998). Proceedings of the Ocean Drilling Program, 158 Scientific Results. https://doi.org/10.2973/odp.proc.sr.158.213.1998

Humphris, S E, Alt, J. C., Teagle, D. A. H., & Honnorez, J. J. (1998). Proceedings of the Ocean Drilling Program, 158 Scientific Results. https://doi.org/10.2973/odp.proc.sr.158.220.1998

Humphris, S E., & Cann, J. R. (2000). Constraints on the energy and chemical balances of the modern TAG and ancient Cyprus seafloor sulfide deposits. *Journal of Geophysical Research: Solid Earth*, *105*(B12), 28477–28488. https://doi.org/10.1029/2000jb900289

Humphris, S. E., & Tivey, M. K. (2000). A synthesis of geological and geochemical investigations of the TAG hydrothermal field: Insights into fluid-flow and mixing processes in a hydrothermal system. *Special Papers-Geological Society of America*, 213–236.

Humphris, S. E., Herzig, P., & Miller, D. (1995a). *Proceedings of the Ocean Drilling Program, Initial Reports. Vol. 158. TAG: Drilling an Active Hydrothermal System on a Sediment-free Slow Spreading Ridge: Covering Leg 158 of the Cruise of the Drilling Vessel" JOIDES Resolution", Las Palmas, Gran Canaria, to Las Palmas, Gran Canaria, Site 957, 23 September-22 November 1994*. Texas A & M University Ocean Drilling Program.

Humphris, S. E., Herzig, P. M., Miller, D. J., Alt, J. C., Becker, K., Brown, D., et al. (1995b). The internal structure of an active sea-floor massive sulphide deposit. *Nature*, *377*(6551), 713–716. https://doi.org/10.1038/377713a0

Humphris, S. E., Fornari, D. J., Scheirer, D. S., German, C. R., & Parson, L. M. (2002). Geotectonic setting of hydrothermal activity on the summit of Lucky Strike Seamount (37°17′N, Mid-Atlantic Ridge). *Geochemistry, Geophysics, Geosystems*, *3*(8), 1–25. https://doi.org/10.1029/2001gc000284

Humphris, S. E., Tivey, M. K., & Tivey, M. A. (2015). The Trans-Atlantic Geotraverse hydrothermal field: A hydrothermal system on an active detachment fault. *Deep Sea Research Part II: Topical Studies in Oceanography*, *121*, 8–16. https://doi.org/10.1016/j.dsr2.2015.02.015

James, R. H., & Elderfield, H. (1996). Chemistry of ore-forming fluids and mineral formation rates in an active hydrothermal sulfide deposit on the Mid-Atlantic Ridge. *Geology*, *24*(12), 1147–1150. https://doi.org/10.1130/0091-7613(1996)024<1147:cooffa>2.3.co;2

Jannasch, H. W., & Mottl, M. J. (1985). Geomicrobiology of Deep-Sea Hydrothermal Vents. *Science*, *229*(4715), 717–725. https://doi.org/10.1126/science.229.4715.717

Johnson, H. P., & Tunnicliffe, V. (1985). Time-series measurements of hydrothermal activity on northern Juan De Fuca Ridge. *Geophysical Research Letters*, *12*(10), 685–688. https://doi.org/10.1029/gl012i010p00685

Johnson, H. P., Hutnak, M., Dziak, R. P., Fox, C. G., Urcuyo, I., Cowen, J. P., et al. (2000). Earthquake-induced changes in a hydrothermal system on the Juan de Fuca mid-ocean ridge. *Nature*, *407*(6801), 174. https://doi.org/10.1038/35025040

Johnson, H. P., Tivey, M. A., Bjorklund, T. A., & Salmi, M. S. (2010). Hydrothermal circulation within the Endeavour Segment, Juan de Fuca Ridge. *Geochemistry, Geophysics, Geosystems*, *11*(5), n/a-n/a. https://doi.org/10.1029/2009gc002957

Johnson, K. S., Childress, J. J., & Beehler, C. L. (1988). Short-term temperature variability in the Rose Garden hydrothermal vent field: an unstable deep-sea environment. *Deep Sea Research Part A. Oceanographic Research Papers*, *35*(10–11), 1711–1721. https://doi.org/10.1016/0198-0149(88)90045-3

Juniper, S. K., Martineu, P., Sarrazin, J., & Gélinas, Y. (1995). Microbial-mineral floc associated with nascent hydrothermal activity on CoAxial Segment, Juan de Fuca Ridge. *Geophysical Research Letters*, *22*(2), 179–182. https://doi.org/10.1029/94gl02436

Jupp, T., & Schultz, A. (2000). A thermodynamic explanation for black smoker temperatures. *Nature*, *403*(6772), 880–883. https://doi.org/10.1038/35002552

Jupp, T. E., & Schultz, A. (2004). A poroelastic model for the tidal modulation of seafloor hydrothermal systems. *Journal of Geophysical Research: Solid Earth (1978–2012)*, *109*(B3). https://doi.org/10.1029/2003jb002583

Karson, J. A., & Rona, P. A. (1990). Block-tilting, transfer faults, and structural control of magmatic and hydrothermal processes in the TAG area, Mid-Atlantic Ridge 26°N. *GSA Bulletin*, *102*(12), 1635-1645.

Karson, J. A., Kelly, D. S., Fornari, D. J., Perfit, M. R., & Shank, T. M. (2015). *Discovering the Deep: A Photographic Atlas of the Seafloor and the Ocean Crust*. (C. U. Press, Ed.).

Kashefi, K., & Lovley, D. R. (2003). Extending the Upper Temperature Limit for Life. *Science*, *301*(5635), 934–934. https://doi.org/10.1126/science.1086823

Kelley, D., Carbotte, S., Caress, D., Clague, D., Delaney, J., Gill, J., et al. (2012). Endeavour Segment of the Juan de Fuca Ridge: One of the Most Remarkable Places on Earth. *Oceanography*, *25*(1), 44–61. https://doi.org/10.5670/oceanog.2012.03

Kelley, D. S., Karson, J. A., Blackman, D. K., Früh-Green, G. L., Butterfield, D. A., Lilley, M. D., et al. (2001). An off-axis hydrothermal vent field near the Mid-Atlantic Ridge at 30° N. *Nature*, *412*(6843), 145. https://doi.org/10.1038/35084000

Kent, G. M., Harding, A. J., & Orcutt, J. A. (1993). Distribution of magma beneath the East Pacific Rise between the Clipperton Transform and the 9°17′N Deval from forward modeling of common depth point data. *Journal of Geophysical Research: Solid Earth*, *98*(B8), 13945–13969. https://doi.org/10.1029/93jb00705

Kestin, J., Sokolov, M., & Wakeham, W. A. (1978). Viscosity of liquid water in the range −8 °C to 150 °C. *Journal of Physical and Chemical Reference Data*, *7*(3), 941–948. https://doi.org/10.1063/1.555581

Kimura, M., Uyeda, S., Kato, Y., Tanaka, T., Yamano, M., Gamo, T., et al. (1988). Active hydrothermal mounds in the Okinawa Trough backarc basin, Japan. *Tectonophysics*, *145*(3–4), 319–324. https://doi.org/10.1016/0040-1951(88)90203-x

Kinoshita, M., Matsubayashi, O., & Herzen, R. P. V. (1996). Sub-bottom temperature anomalies detected by long-term temperature monitoring at the TAG Hydrothermal Mound. *Geophysical Research Letters*, *23*(23), 3467–3470. https://doi.org/10.1029/96gl02150

Kinoshita, M., Herzen, R. P. V., Matsubayashi, O., & Fujioka, K. (1998). Tidally-driven effluent detected by long-term temperature monitoring at the TAG hydrothermal mound, Mid-Atlantic Ridge. *Physics of the Earth and Planetary Interiors*, *108*(2), 143–154. https://doi.org/10.1016/s0031-9201(98)00092-2

Koschinsky, A., Seifert, R., Halbach, P., Bau, M., Brasse, S., Carvalho, L. M. de, & Fonseca, N. M. (2002). Geochemistry of diffuse low-temperature hydrothermal fluids in the North Fiji basin. *Geochimica et Cosmochimica Acta*, *66*(8), 1409–1427. https://doi.org/10.1016/s0016-7037(01)00855-9

Koschinsky, A., Garbe-Schönberg, D., Sander, S., Schmidt, K., Gennerich, H.-H., & Strauss, H. (2008). Hydrothermal venting at pressure-temperature conditions above the critical point of seawater, 5°S on the Mid-Atlantic Ridge. *Geology*, *36*(8), 615–618. https://doi.org/10.1130/g24726a.1

Koski, R. A., Jonasson, I. R., Kadko, D. C., Smith, V. K., & Wong, F. L. (1994). Compositions, growth mechanisms, and temporal relations of hydrothermal sulfide-sulfate-silica chimneys at the northern Cleft segment, Juan de Fuca Ridge. *Journal of Geophysical Research: Solid Earth*, *99*(B3), 4813–4832. https://doi.org/10.1029/93jb02871

Kuo, B.-Y., & Forsyth, D. W. (1988). Gravity anomalies of the ridge-transform system in the South Atlantic between 31 and 34.5° S: Upwelling centers and variations in crustal thickness. *Marine Geophysical Researches*, *10*(3–4), 205–232. https://doi.org/10.1007/bf00310065

Laes-Huon, A., Sarradin, P.-M., & Cannat, M. (2019). CHEMINI total dissolved iron concentrations from the EMSO-Azores observatory, 2018-2019. *SEANOE*. https://doi.org/10.17882/69883

Langmuir, C. H., Humphris, S., Fornari, D., Dover, C. V., Damm, K. V., Tivey, M. K., et al. (1997). Hydrothermal vents near a mantle hot spot: the Lucky Strike vent field at 37°N on the Mid-Atlantic Ridge. *Earth and Planetary Science Letters*, *148*(1–2), 69–91. https://doi.org/10.1016/s0012-821x(97)00027-7

Langmuir, C. H., Fornari, D., Colodner, D., Charlou, J., Costa, I., Desbruyeres, D., et al. (1993). Geological setting and characteristics of the Lucky Strike vent field at 37 17'N on the Mid-Atlantic Ridge. *Eos Trans. AGU*, *74*(43 Supplement), 99.

Larson, B. I., Olson, E. J., & Lilley, M. D. (2007). In situ measurement of dissolved chloride in high temperature hydrothermal fluids. *Geochimica et Cosmochimica Acta*, *71*(10), 2510–2523. https://doi.org/10.1016/j.gca.2007.02.013

Larson, B. I., Lilley, M. D., & Olson, E. J. (2009). Parameters of subsurface brines and hydrothermal processes 12–15 months after the 1999 magmatic event at the Main Endeavor Field as inferred from in situ time series measurements of chloride and temperature. *Journal of Geophysical Research: Solid Earth*, *114*(B1). https://doi.org/10.1029/2008jb005627

Larson, B. I., Houghton, J. L., Lowell, R. P., Farough, A., & Meile, C. D. (2015). Subsurface conditions in hydrothermal vents inferred from diffuse flow composition, and models of reaction and transport. *Earth and Planetary Science Letters*, *424*(Proc. Natl. Acad. Sci. USA 110 2013), 245–255. https://doi.org/10.1016/j.epsl.2015.05.033

Lee, R. W., Robert, K., Matabos, M., Bates, A. E., & Juniper, S. K. (2015). Temporal and spatial variation in temperature experienced by macrofauna at Main Endeavour hydrothermal vent field. *Deep Sea Research Part I: Oceanographic Research Papers*, *106*, 154–166. https://doi.org/10.1016/j.dsr.2015.10.004

Lelièvre, Y., Legendre, P., Matabos, M., Mihály, S., Lee, R. W., Sarradin, P.-M., et al. (2017). Astronomical and atmospheric impacts on deep-sea hydrothermal vent invertebrates. *Proceedings of the Royal Society B: Biological Sciences*, *284*(1852), 20162123. https://doi.org/10.1098/rspb.2016.2123

Lilley, M. D., Butterfield, D. A., Lupton, J. E., & Olson, E. J. (2003). Magmatic events can produce rapid changes in hydrothermal vent chemistry. *Nature*, *422*(6934), 878. https://doi.org/10.1038/nature01569

Lin, J., Purdy, G. M., Schouten, H., Sempere, J.-C., & Zervas, C. (1990). Evidence from gravity data for focusedmagmatic accretionalong the Mid-Atlantic Ridge. *Nature*, *344*(6267), 627–632. https://doi.org/10.1038/344627a0

Lister, C. R. B. (1972). On the Thermal Balance of a Mid-Ocean Ridge. *Geophysical Journal of the Royal Astronomical Society*, *26*(5), 515–535. https://doi.org/10.1111/j.1365-246x.1972.tb05766.x

Lister, C. R. B. (1974). On the Penetration of Water into Hot Rock. *Geophysical Journal International*, *39*(3), 465–509. https://doi.org/10.1111/j.1365-246x.1974.tb05468.x

Little, S. A., Stolzenbach, K. D., & Herzen, R. P. V. (1987). Measurements of plume flow from a hydrothermal vent field. *Journal of Geophysical Research: Solid Earth*, *92*(B3), 2587–2596. https://doi.org/10.1029/jb092ib03p02587

Little, S. A., Stolzenbach, K. D., & Grassle, F. J. (1988). Tidal current effects on temperature in diffuse hydrothermal flow: Guaymas Basin. *Geophysical Research Letters*, *15*(13), 1491–1494. https://doi.org/10.1029/gl015i013p01491

Lonsdale, P. (1977). Clustering of suspension-feeding macrobenthos near abyssal hydrothermal vents at oceanic spreading centers. *Deep Sea Research*, *24*(9), 857–863. https://doi.org/10.1016/0146-6291(77)90478-7

Lonsdale, P., & Becker, K. (1985). Hydrothermal plumes, hot springs, and conductive heat flow in the Southern Trough of Guaymas Basin. *Earth and Planetary Science Letters*, *73*(2–4), 211–225. https://doi.org/10.1016/0012-821x(85)90070-6

Lowell, R. P. (1975). Circulation in Fractures, Hot Springs, and Convective Heat Transport on Mid-ocean Ridge Crests. *Geophysical Journal of the Royal Astronomical Society*, *40*(3), 351–365. https://doi.org/10.1111/j.1365-246x.1975.tb04137.x

Lowell, R. P., & Burnell, D. K. (1991). Mathematical modeling of conductive heat transfer from a freezing, convecting magma chamber to a single-pass hydrothermal system: implications for seafloor black smokers. *Earth and Planetary Science Letters*, *104*(1), 59–69. https://doi.org/10.1016/0012-821x(91)90237-c

Lowell, R. P., Rona, P. A., & Herzen, R. P. V. (1995). Seafloor hydrothermal systems. *Journal of Geophysical Research: Solid Earth*, *100*(B1), 327–352. https://doi.org/10.1029/94jb02222

Lowell, R. P., Crowell, B. W., Lewis, K. C., & Liu, L. (2008). Geophysical Monograph Series, 15–44. https://doi.org/10.1029/178gm03

Lowell, R. P., & Yao, Y. (2002). Anhydrite precipitation and the extent of hydrothermal recharge zones at ocean ridge crests. *Journal of Geophysical Research: Solid Earth (1978–2012)*, *107*(B9), EPM 2-1-EPM 2-9. https://doi.org/10.1029/2001jb001289

Lowell, R. P., Yao, Y., & Germanovich, L. N. (2003). Anhydrite precipitation and the relationship between focused and diffuse flow in seafloor hydrothermal systems. *Journal of Geophysical Research: Solid Earth (1978–2012)*, *108*(B9). https://doi.org/10.1029/2002jb002371

Lowell, R. P., Gosnell, S., & Yang, Y. (2007). Numerical simulations of single-pass hydrothermal convection at mid-ocean ridges: Effects of the extrusive layer and temperature-dependent permeability. *Geochemistry, Geophysics, Geosystems*, *8*(10), n/a-n/a. https://doi.org/10.1029/2007gc001653

Lowell, R. P., Farough, A., Germanovich, L., Hebert, L., & Horne, R. (2012). A Vent-Field-Scale Model of the East Pacific Rise 9°50'N Magma-Hydrothermal System. *Oceanography*, *25*(1), 158–167. https://doi.org/10.5670/oceanog.2012.13

Lowell, R. P., Houghton, J. L., Farough, A., Craft, K. L., Larson, B. I., & Meile, C. D. (2015). Mathematical modeling of diffuse flow in seafloor hydrothermal systems: The potential extent of the subsurface biosphere at mid-ocean ridges. *Earth and Planetary Science Letters*, *425*(Geophys. Res. Lett. 38 2011), 145–153. https://doi.org/10.1016/j.epsl.2015.05.047

Lucazeau, F., Bonneville, A., Escartin, J., Herzen, R. P. V., Gouze, P., Carton, H., et al. (2006). Heat flow variations on a slowly accreting ridge: Constraints on the hydrothermal and conductive cooling for the Lucky Strike segment (Mid-Atlantic Ridge, 37°N): HEAT FLOW VARIATIONS, MAR. *Geochemistry, Geophysics, Geosystems*, *7*(7), n/a-n/a. https://doi.org/10.1029/2005gc001178

Lutz, R. A., & Kennish, M. J. (1993). Ecology of deep-sea hydrothermal vent communities: A review. *Reviews of Geophysics*, *31*(3), 211–242. https://doi.org/10.1029/93rg01280

Macdonald, K. C. (1982). Mid-Ocean Ridges: Fine Scale Tectonic, Volcanic and Hydrothermal Processes Within the Plate Boundary Zone. *Annual Review of Earth and Planetary Sciences*, *10*(1), 155–190. https://doi.org/10.1146/annurev.ea.10.050182.001103

Macdonald, K. C. (2001). Encyclopedia of Ocean Sciences. *Article Titles: M*, (Nature3221986), 1798–1813. https://doi.org/10.1006/rwos.2001.0094

Macdonald, K. C., Becker, K., Spiess, F. N., & Ballard, R. D. (1980). Hydrothermal heat flux of the "black smoker" vents on the East Pacific Rise. *Earth and Planetary Science Letters*, *48*(1), 1–7. https://doi.org/10.1016/0012-821x(80)90163-6

Madsen, J. A., Forsyth, D. W., & Detrick, R. S. (1984). A new isostatic model for the East Pacific Rise crest. *Journal of Geophysical Research: Solid Earth*, *89*(B12), 9997–10015. https://doi.org/10.1029/jb089ib12p09997

Marjanović, M., Fuji, N., Singh, S. C., Belahi, T., & Escartín, J. (2017). Seismic Signatures of Hydrothermal Pathways Along the East Pacific Rise Between 9°16′ and 9°56′N. *Journal of Geophysical Research: Solid Earth*, *122*(12), 10,241-10,262. https://doi.org/10.1002/2017jb015004

Marjanović, M., Barreyre, T., Fontaine, F. J., & Escartín, J. (2019). Investigating Fine-Scale Permeability Structure and Its Control on Hydrothermal Activity Along a Fast-Spreading Ridge (the East Pacific Rise, 9°43′–53′N) Using Seismic Velocity, Poroelastic Response, and Numerical Modeling. *Geophysical Research Letters*, *46*(21), 11799–11810. https://doi.org/10.1029/2019gl084040

Martin, W., Baross, J., Kelley, D., & Russell, M. J. (2008). Hydrothermal vents and the origin of life. *Nature Reviews Microbiology*, *6*(11), 805–814. https://doi.org/10.1038/nrmicro1991

Mat, A. M., Sarrazin, J., Markov, G. V., Apremont, V., Dubreuil, C., Eché, C., et al. (2020). Biological rhythms in the deep-sea hydrothermal mussel Bathymodiolus azoricus. *Nature Communications*, *11*(1), 3454. https://doi.org/10.1038/s41467-020-17284-4

Mavko, G., & Nur, A. (1997). The effect of a percolation threshold in the Kozeny-Carman relation. *Geophysics*, *62*(5), 1480–1482. https://doi.org/10.1190/1.1444251

McClain, J. S., Orcutt, J. A., & Burnett, M. (1985). The East Pacific Rise in cross section: A seismic model. *Journal of Geophysical Research: Solid Earth*, *90*(B10), 8627–8639. https://doi.org/10.1029/jb090ib10p08627

McCollom, T. M., & Shock, E. L. (1997). Geochemical constraints on chemolithoautotrophic metabolism by microorganisms in seafloor hydrothermal systems. *Geochimica et Cosmochimica Acta*, *61*(20), 4375–4391. https://doi.org/10.1016/s0016-7037(97)00241-x

Mével, C. (2003). Serpentinization of abyssal peridotites at mid-ocean ridges. *Comptes Rendus Geoscience*, *335*(10–11), 825–852. https://doi.org/10.1016/j.crte.2003.08.006

Miller, A. R., Densmore, C. D., Degens, E. T., Hathaway, J. C., Manheim, F. T., McFarlin, P. F., et al. (1966). Hot brines and recent iron deposits in deeps of the Red Sea. *Geochimica et Cosmochimica Acta*, *30*(3), 341–359. https://doi.org/10.1016/0016-7037(66)90007-x

Millero, F. J., Feistel, R., Wright, D. G., & McDougall, T. J. (2008). The composition of Standard Seawater and the definition of the Reference-Composition Salinity Scale. *Deep Sea Research Part I: Oceanographic Research Papers*, *55*(1), 50–72. https://doi.org/10.1016/j.dsr.2007.10.001

Mills, R. A., & Elderfield, H. (1995). Rare earth element geochemistry of hydrothermal deposits from the active TAG Mound, 26°N Mid-Atlantic Ridge. *Geochimica et Cosmochimica Acta*, *59*(17), 3511–3524. https://doi.org/10.1016/0016-7037(95)00224-n

Miranda, J. M., Luis, J. F., Lourenço, N., & Santos, F. M. (2005). Identification of the magnetization low of the Lucky Strike hydrothermal vent using surface magnetic data. *Journal of Geophysical Research: Solid Earth (1978–2012)*, *110*(B4). https://doi.org/10.1029/2004jb003085

Mittelstaedt, E., Escartín, J., Gracias, N., Olive, J., Barreyre, T., Davaille, A., et al. (2012). Quantifying diffuse and discrete venting at the Tour Eiffel vent site, Lucky Strike hydrothermal field. *Geochemistry, Geophysics, Geosystems*, *13*(4), n/a-n/a. https://doi.org/10.1029/2011gc003991

Mittelstaedt, E., Fornari, D. J., Crone, T. J., Kinsey, J., Kelley, D., & Elend, M. (2016). Diffuse venting at the ASHES hydrothermal field: Heat flux and tidally modulated flow variability derived from in situ time-series measurements. *Geochemistry, Geophysics, Geosystems*, *17*(4), 1435–1453. https://doi.org/10.1002/2015gc006144

Morin, R. H., Hess, A. E., & Becker, K. (1992). In situ measurements of fluid flow in DSDP Holes 395A and 534A: Results from the Dianaut Program. *Geophysical Research Letters*, *19*(5), 509–512. https://doi.org/10.1029/91gl02947

Murray, J., & Renard, A. F. (1891). Report on Deep-sea Deposits Based on the Specimens Collected During the Voyage of H.M.S. Challenger in the Years 1872 to 1876 (p. 525).

Nielsen, S. G., Rehkämper, M., Teagle, D. A. H., Butterfield, D. A., Alt, J. C., & Halliday, A. N. (2006). Hydrothermal fluid fluxes calculated from the isotopic mass balance of thallium in the ocean crust. *Earth and Planetary Science Letters*, *251*(1–2), 120–133. https://doi.org/10.1016/j.epsl.2006.09.002

Ondréas, H., Cannat, M., Fouquet, Y., Normand, A., Sarradin, P. M., & Sarrazin, J. (2009). Recent volcanic events and the distribution of hydrothermal venting at the Lucky Strike hydrothermal field, Mid-Atlantic Ridge. *Geochemistry, Geophysics, Geosystems*, *10*(2), n/a-n/a. https://doi.org/10.1029/2008gc002171

Parsons, B., & Sclater, J. G. (1977). An analysis of the variation of ocean floor bathymetry and heat flow with age. *Journal of Geophysical Research*, *82*(5), 803–827. https://doi.org/10.1029/jb082i005p00803

Pascoe, A. R., & Cann, J. R. (1995). Modelling diffuse hydrothermal flow in black smoker vent fields. *Geological Society, London, Special Publications*, *87*(1), 159–173. https://doi.org/10.1144/gsl.sp.1995.087.01.14

Percival, D. B., & Walden, A. T. (1993). *Spectral Analysis for Physical Applications*. Cambridge: Cambridge University Press. https://doi.org/10.1017/cbo9780511622762

Pester, N. J., Reeves, E. P., Rough, M. E., Ding, K., Seewald, J. S., & Seyfried, W. E. (2012). Subseafloor phase equilibria in high-temperature hydrothermal fluids of the Lucky Strike Seamount (Mid-Atlantic Ridge, 37°17′N). *Geochimica et Cosmochimica Acta*, *90*, 303–322. https://doi.org/10.1016/j.gca.2012.05.018

Pitzer, K. S., Peiper, J. C., & Busey, R. H. (1984). Thermodynamic Properties of Aqueous Sodium Chloride Solutions. *Journal of Physical and Chemical Reference Data*, *13*(1), 1–102. https://doi.org/10.1063/1.555709

Poincaré, H. (1910). Sur les courbes tracées sur les surfaces algébriques. In *Annales scientifiques de l'École Normale Supérieure* (Vol. 27, pp. 55–108).

Pruis, M. J., & Johnson, H. P. (2004). Tapping into the sub-seafloor: examining diffuse flow and temperature from an active seamount on the Juan de Fuca Ridge. *Earth and Planetary Science Letters*, *217*(3–4), 379–388. https://doi.org/10.1016/s0012-821x(03)00607-1

Rabinowicz, M., Sempéré, J., & Genthon, P. (1999). Thermal convection in a vertical permeable slot: Implications for hydrothermal circulation along mid-ocean ridges. *Journal of Geophysical Research: Solid Earth*, *104*(B12), 29275–29292. https://doi.org/10.1029/1999jb900259

Raitt, R. (1963). 6. THE CRUSTAL ROCKS. *The Earth Beneath the Sea: History*, *3*, 85.

Ramondenc, P., Germanovich, L. N., Damm, K. L. V., & Lowell, R. P. (2006). The first measurements of hydrothermal heat output at 9°50′N, East Pacific Rise. *Earth and Planetary Science Letters*, *245*(3–4), 487–497. https://doi.org/10.1016/j.epsl.2006.03.023

Ravizza, G., Blusztajn, J., Damm, K. L. V., Bray, A. M., Bach, W., & Hart, S. R. (2001). Sr isotope variations in vent fluids from 9°46′-9°54′N East Pacific Rise: evidence of a non-zero-Mg fluid component. *Geochimica et Cosmochimica Acta*, *65*(5), 729–739. https://doi.org/10.1016/s0016-7037(00)00590-1

Ribando, R. J., Torrance, K. E., & Turcotte, D. L. (1976). Numerical models for hydrothermal circulation in the oceanic crust. *Journal of Geophysical Research*, *81*(17), 3007–3012. https://doi.org/10.1029/jb081i017p03007

Rona, P. A. (1980). TAG Hydrothermal Field: Mid-Atlantic Ridge crest at latitude 26°N. *Journal of the Geological Society*, *137*(4), 385–402. https://doi.org/10.1144/gsjgs.137.4.0385

Rona, P. A., Widenfalk, L., & Boström, K. (1987). Serpentinized ultramafics and hydrothermal activity at the Mid-Atlantic Ridge crest near 15°N. *Journal of Geophysical Research: Solid Earth*, *92*(B2), 1417–1427. https://doi.org/10.1029/jb092ib02p01417

Rona, P. A., & Trivett, D. A. (1992). Discrete and diffuse heat transfer atashes vent field, Axial Volcano, Juan de Fuca Ridge. *Earth and Planetary Science Letters*, *109*(1–2), 57–71. https://doi.org/10.1016/0012-821x(92)90074-6

Rona, P. A., McGregor, B. A., Betzer, P. R., Bolger, G. W., & Krause, D. C. (1975). Anomalous water temperatures over Mid-Atlantic Ridge crest at 26° North latitude. *Deep Sea Research and Oceanographic Abstracts*, *22*(9), 611–618. https://doi.org/10.1016/0011-7471(75)90048-0

Rosenberg, N. D., & Spera, F. J. (1990). ROLE OF ANISOTROPIC AND/OR LAYERED PERMEABELITY IN HYDROTHERMAL CONVECTION. *Geophysical Research Letters*, *17*(3), 235–238. https://doi.org/10.1029/gl017i003p00235

Rouxel, O., Fouquet, Y., & Ludden, J. N. (2004a). Copper Isotope Systematics of the Lucky Strike, Rainbow, and Logatchev Sea-Floor Hydrothermal Fields on the Mid-Atlantic Ridge. *Economic Geology*, *99*(3), 585–600. https://doi.org/10.2113/gsecongeo.99.3.585

Rouxel, O., Fouquet, Y., & Ludden, J. N. (2004b). Subsurface processes at the lucky strike hydrothermal field, Mid-Atlantic ridge: evidence from sulfur, selenium, and iron isotopes. *Geochimica et Cosmochimica Acta*, *68*(10), 2295–2311. https://doi.org/10.1016/j.gca.2003.11.029

Salmi, M. S., Johnson, H. P., Tivey, M. A., & Hutnak, M. (2014). Quantitative estimate of heat flow from a mid-ocean ridge axial valley, Raven field, Juan de Fuca Ridge: Observations and inferences. *Journal of Geophysical Research: Solid Earth*, *119*(9), 6841–6854. https://doi.org/10.1002/2014jb011086

Sarradin, P.-M., Caprais, J.-C., Riso, R., Kerouel, R., & Aminot, A. (1999). Chemical environment of the hydrothermal mussel communities in the Lucky Strike and Menez Gwen vent fields, Mid Atlantic ridge. Retrieved from https://archimer.ifremer.fr/doc/00147/25847/

Sarradin, P.-M., Legrand, J., Moreau, B., Lanteri, N., & Cannat, M. (2018). High precision pressure, data from the EGIM deployed on EMSO-Azores observatory, 2017-2018. *SEANOE*. https://doi.org/10.17882/56522

Sarrazin, J., & Juniper, S. (1999). Biological characteristics of a hydrothermal edifice mosaic community. *Marine Ecology Progress Series*, *185*, 1–19. https://doi.org/10.3354/meps185001

Sarrazin, J., Blandin, J., Delauney, L., Dentrecolas, S., Dorval, P., Dupont, J., et al. (2007). TEMPO: a new ecological module for studying deep-sea community dynamics at hydrothermal vents. *OCEANS 2007 - Europe*, 1–4. https://doi.org/10.1109/oceanse.2007.4302310

Sarrazin, J., Rodier, P., Tivey, M. K., Singh, H., Schultz, A., & Sarradin, P. M. (2009). A dual sensor device to estimate fluid flow velocity at diffuse hydrothermal vents. *Deep Sea Research Part I: Oceanographic Research Papers*, *56*(11), 2065–2074. https://doi.org/10.1016/j.dsr.2009.06.008

Scheirer, D. S., Shank, T. M., & Fornari, D. J. (2006). Temperature variations at diffuse and focused flow hydrothermal vent sites along the northern East Pacific Rise. *Geochemistry, Geophysics, Geosystems*, *7*(3), n/a-n/a. https://doi.org/10.1029/2005gc001094

Schmeling, H., & Marquart, G. (2014). A scaling law for approximating porous hydrothermal convection by an equivalent thermal conductivity: theory and application to the cooling oceanic lithosphere. *Geophysical Journal International*, *197*(2), 645–664. https://doi.org/10.1093/gji/ggu022

Schultz, A., & Elderfield, H. . (1994). Direct measurements of the physics and chemistry of diffuse flow and high-temperature effluent at TAG and Broken Spur vent fields.

Schultz, A., Delaney, J. R., & McDuff, R. E. (1992). On the partitioning of heat flux between diffuse and point source seafloor venting. *Journal of Geophysical Research: Solid Earth*, *97*(B9), 12299–12314. https://doi.org/10.1029/92jb00889

Schultz, A., Dickson, P., & Elderfield, H. (1996). Temporal variations in diffuse hydrothermal flow at TAG. *Geophysical Research Letters*, *23*(23), 3471–3474. https://doi.org/10.1029/96gl02081

Schultz, A., & Elderfield, H. (1997). Controls on the physics and chemistry of seafloor hydrothermal circulation. *Philosophical Transactions of the Royal Society of London. Series A: Mathematical, Physical and Engineering Sciences*, *355*(1723), 387–425. https://doi.org/10.1098/rsta.1997.0014

Scott, M. R., Scott, R. B., Rona, P. A., Butler, L. W., & Nalwalk, A. J. (1974). Rapidly accumulating manganese deposit from the Median Valley of the Mid-Atlantic Ridge. *Geophysical Research Letters*, *1*(8), 355–358. https://doi.org/10.1029/gl001i008p00355

Scott, R. B., RONA, P. A., MCGREGOR, B. A., & SCOTT, M. R. (1974). The TAG hydrothermal field. *Nature*, *251*(5473), 301–302. https://doi.org/10.1038/251301a0

Seher, T., Crawford, W. C., Singh, S. C., Cannat, M., Combier, V., & Dusunur, D. (2010a). Crustal velocity structure of the Lucky Strike segment of the Mid-Atlantic Ridge at 37°N from seismic refraction measurements. *Journal of Geophysical Research: Solid Earth (1978–2012)*, *115*(B3). https://doi.org/10.1029/2009jb006650

Seher, T., Crawford, W. C., Singh, S. C., & Cannat, M. (2010b). Seismic layer 2A variations in the Lucky Strike segment at the Mid-Atlantic Ridge from reflection measurements. *Journal of Geophysical Research: Solid Earth (1978–2012)*, *115*(B7). https://doi.org/10.1029/2009jb006783

Seyfried, W., & Bischoff, J. L. (1977). Hydrothermal transport of heavy metals by seawater: The role of seawater/basalt ratio. *Earth and Planetary Science Letters*, *34*(1), 71–77. https://doi.org/10.1016/0012-821x(77)90107-8

Simeoni, P., SARRAZIN, J., NOUZE, H., SARRADIN, P.-M., ONDREAS, H., SCALABRIN, C., & SINQUIN, J.-M. (2007). Victor 6000: New High Resolution Tools for Deep Sea Research. :Module de Mesures en Route; *OCEANS 2007 - Europe*, 1–6. https://doi.org/10.1109/oceanse.2007.4302214

Singh, S. C., Crawford, W. C., Carton, H., Seher, T., Combier, V., Cannat, M., et al. (2006). Discovery of a magma chamber and faults beneath a Mid-Atlantic Ridge hydrothermal field. *Nature*, *442*(7106), 1029. https://doi.org/10.1038/nature05105

Sinton, J. M., & Detrick, R. S. (1992). Mid-ocean ridge magma chambers. *Journal of Geophysical Research: Solid Earth*, *97*(B1), 197–216. https://doi.org/10.1029/91jb02508

Sleep, N. H. (1991). Hydrothermal circulation, anhydrite precipitation, and thermal structure at ridge axes. *Journal of Geophysical Research: Solid Earth*, *96*(B2), 2375–2387. https://doi.org/10.1029/90jb02335

Sleep, N. H., & Biehler, S. (1970). Topography and tectonics at the intersections of fracture zones with central rifts. *Journal of Geophysical Research*, *75*(14), 2748–2752. https://doi.org/10.1029/jb075i014p02748

Sohn, R. A. (2007). Stochastic analysis of exit fluid temperature records from the active TAG hydrothermal mound (Mid-Atlantic Ridge, 26°N): 1. Modes of variability and implications for subsurface flow. *Journal of Geophysical Research: Solid Earth (1978–2012)*, *112*(B7). https://doi.org/10.1029/2006jb004435

Sohn, R. A., Fornari, D. J., Damm, K. L. V., Hildebrand, J. A., & Webb, S. C. (1998). Seismic and hydrothermal evidence for a cracking event on the East Pacific Rise crest at 9° 50′ N. *Nature*, *396*(6707), 24146. https://doi.org/10.1038/24146

Spiess, F. N., Macdonald, K. C., Atwater, T., Ballard, R., Carranza, A., Cordoba, D., et al. (1980). East Pacific Rise: Hot Springs and Geophysical Experiments. *Science*, *207*(4438), 1421–1433. https://doi.org/10.1126/science.207.4438.1421

Stakes, D. S., Perfit, M. R., Tivey, M. A., Caress, D. W., Ramirez, T. M., & Maher, N. (2006). The Cleft revealed: Geologic, magnetic, and morphologic evidence for construction of upper oceanic crust along the southern Juan de Fuca Ridge. *Geochemistry, Geophysics, Geosystems*, *7*(4), n/a-n/a. https://doi.org/10.1029/2005gc001038

Stein, C. A., & Stein, S. (1994). Constraints on hydrothermal heat flux through the oceanic lithosphere from global heat flow. *Journal of Geophysical Research: Solid Earth*, *99*(B2), 3081–3095. https://doi.org/10.1029/93jb02222

Stein, J. S., & Fisher, A. T. (2001). Multiple scales of hydrothermal circulation in Middle Valley, northern Juan de Fuca Ridge: Physical constraints and geologic models. *Journal of Geophysical Research: Solid Earth*, *106*(B5), 8563–8580. https://doi.org/10.1029/2000jb900395

Strens, M. R., & Cann, J. R. (1982). A model of hydrothermal circulation in fault zones at mid-ocean ridge crests. *Geophysical Journal of the Royal Astronomical Society*, *71*(1), 225–240. https://doi.org/10.1111/j.1365-246x.1982.tb04995.x

Strens, M. R., & Cann, J. R. (1986). A fracture-loop thermal balance model of black smoker circulation. *Tectonophysics*, *122*(3–4), 307–324. https://doi.org/10.1016/0040-1951(86)90149-6

Taillefer, A., Soliva, R., Guillou-Frottier, L., Goff, E. L., Martin, G., & Seranne, M. (2017). Fault-Related Controls on Upward Hydrothermal Flow: An Integrated Geological Study of the Têt Fault System, Eastern Pyrénées (France). *Geofluids*, *2017*, 1–19. https://doi.org/10.1155/2017/8190109

Taillefer, A., Guillou-Frottier, L., Soliva, R., Magri, F., Lopez, S., Courrioux, G., et al. (2018). Topographic and Faults Control of Hydrothermal Circulation Along Dormant Faults in an Orogen. *Geochemistry, Geophysics, Geosystems*, *19*(12), 4972–4995. https://doi.org/10.1029/2018gc007965

Thompson, G., Humphris, S. E., Schroeder, B., Sulanowska, M., & Rona, P. A. (1988). Active Vents and Massive Suflides at 26°N (TAG) and 23°N (Snakepit) on the Mid-Atlantic Ridge. *Canadian Mineralogist* , *26*, 697–7.

Thomson, D. J. (1982). Spectrum estimation and harmonic analysis. *Proceedings of the IEEE*, *70*(9), 1055–1096. https://doi.org/10.1109/proc.1982.12433

Titarenko, S. S., & McCaig, A. M. (2016). Modelling the Lost City hydrothermal field: influence of topography and permeability structure. *Geofluids*, *16*(2), 314–328. https://doi.org/10.1111/gfl.12151

Tivey, M. K. (2007). Generation of Seafloor Hydrothermal Vent Fluids and Associated Mineral Deposits. *Oceanography*, *20*(1), 50–65. https://doi.org/10.5670/oceanog.2007.80

Tivey, M. A., & Johnson, H. P. (2002). Crustal magnetization reveals subsurface structure of Juan de Fuca Ridge hydrothermal vent fields. *Geology*, *30*(11), 979–982. https://doi.org/10.1130/0091-7613(2002)030<0979:cmrsso>2.0.co;2

Tivey, M. K. (1995). Modeling chimney growth and associated fluid flow at seafloor hydrothermal vents sites. In S.E. Humphris, R. A. Zierenberg, L. S. Mullineaux, & R. D. Thomson, *Seafloor Hydrothermal Systems: Physical, Chemical, Biological, and Geological Interactions* (Vol. 91, pp. 158–177). Washington, DC: American Geophysical Union.

Tivey, M. K., & McDuff, R. E. (1990). Mineral precipitation in the walls of black smoker chimneys: A quantitative model of transport and chemical reaction. *Journal of Geophysical Research: Solid Earth*, *95*(B8), 12617–12637. https://doi.org/10.1029/jb095ib08p12617

Tivey, M. K. (1995). The influence of hydrothermal fluid composition and advection rates on black smoker chimney mineralogy: Insights from modeling transport and reaction. *Geochimica et Cosmochimica Acta*, *59*(10), 1933–1949. https://doi.org/10.1016/0016-7037(95)00118-2

Tivey, M. K. (2004). Environmental Conditions Within Active Seafloor Vent Structures: Sensitivity to Vent Fluid Composition and Fluid Flow. *The Subseafloor Biosphere at Mid-Ocean Ridges*, *Volume 144*.

Tivey, M. K., Humphris, S. E., Thompson, G., Hannington, M. D., & Rona, P. A. (1995). Deducing patterns of fluid flow and mixing within the TAG active hydrothermal mound using mineralogical and geochemical data. *Journal of Geophysical Research: Solid Earth*, *100*(B7), 12527–12555. https://doi.org/10.1029/95jb00610

Tivey, M. K., Bradley, A. M., Joyce, T. M., & Kadko, D. (2002). Insights into tide-related variability at seafloor hydrothermal vents from time-series temperature measurements. *Earth and Planetary Science Letters*, *202*(3–4), 693–707. https://doi.org/10.1016/s0012-821x(02)00801-4

Tolstoy, M., Waldhauser, F., Bohnenstiehl, D. R., Weekly, R. T., & Kim, W.-Y. (2008). Seismic identification of along-axis hydrothermal flow on the East Pacific Rise. *Nature*, *451*(7175), 181. https://doi.org/10.1038/nature06424

Tolstoy, M., Harding, A. J., & Orcutt, J. A. (1993). Crustal Thickness on the Mid-Atlantic Ridge: Bull's-Eye Gravity Anomalies and Focused Accretion. *Science*, *262*(5134), 726–729. https://doi.org/10.1126/science.262.5134.726

Tucholke, B. E., & Lin, J. (1994). A geological model for the structure of ridge segments in slow spreading ocean crust. *Journal of Geophysical Research: Solid Earth*, *99*(B6), 11937–11958. https://doi.org/10.1029/94jb00338

Tunnicliffe, V. (1991). The biology of hydrothermal vents: ecology and evolution. In M. Barnes (Ed.), *Oceanography And Marine Biology* (Vol. 29, pp. 319–407). https://doi.org/10.1201/9781482267297

Veirs, S. R., McDuff, R. E., & Stahr, F. R. (2006). Magnitude and variance of near-bottom horizontal heat flux at the Main Endeavour hydrothermal vent field. *Geochemistry, Geophysics, Geosystems*, *7*(2), n/a-n/a. https://doi.org/10.1029/2005gc000952

Waeles, M., Cotte, L., Pernet-Coudrier, B., Chavagnac, V., Cathalot, C., Leleu, T., et al. (2017). On the early fate of hydrothermal iron at deep-sea vents: A reassessment after in situ filtration. *Geophysical Research Letters*, *44*(9), 4233–4240. https://doi.org/10.1002/2017gl073315

Wang, K., & Davis, E. E. (1996). Theory for the propagation of tidally induced pore pressure variations in layered subseafloor formations. *Journal of Geophysical Research: Solid Earth*, *101*(B5), 11483–11495. https://doi.org/10.1029/96jb00641

Wang, X., & Cochran, J. R. (1993). Gravity anomalies, isostasy, and mantle flow at the East Pacific Rise crest. *Journal of Geophysical Research: Solid Earth*, *98*(B11), 19505–19531. https://doi.org/10.1029/93jb01551

Wankel, S. D., Germanovich, L. N., Lilley, M. D., Genc, G., DiPerna, C. J., Bradley, A. S., et al. (2011). Influence of subsurface biosphere on geochemical fluxes from diffuse hydrothermal fluids. *Nature Geoscience*, *4*(7), 461. https://doi.org/10.1038/ngeo1183

White, R. S., Detrick, R. S., Sinha, M. C., & Cormier, M. H. (1984). Anomalous seismic crustal structure of oceanic fracture zones. *Geophysical Journal of the Royal Astronomical Society*, *79*(3), 779–798. https://doi.org/10.1111/j.1365-246x.1984.tb02868.x

White, R. S., McKenzie, D., & O'Nions, R. K. (1992). Oceanic crustal thickness from seismic measurements and rare earth element inversions. *Journal of Geophysical Research: Solid Earth*, *97*(B13), 19683–19715. https://doi.org/10.1029/92jb01749

Wilcock, W. S. D. (1998). Cellular convection models of mid-ocean ridge hydrothermal circulation and the temperatures of black smoker fluids. *Journal of Geophysical Research: Solid Earth*, *103*(B2), 2585–2596. https://doi.org/10.1029/97jb03252

Wilcock, W. S. D. (2004). Physical response of mid-ocean ridge hydrothermal systems to local earthquakes. *Geochemistry, Geophysics, Geosystems*, *5*(11), n/a-n/a. https://doi.org/10.1029/2004gc000701

Wilcock, W. S. D., & Delaney, J. R. (1996). Mid-ocean ridge sulfide deposits: Evidence for heat extraction from magma chambers or cracking fronts? *Earth and Planetary Science Letters*, *145*(1–4), 49–64. https://doi.org/10.1016/s0012-821x(96)00195-1

Wilcock, W. S. D., & McNabb, A. (1996). Estimates of crustal permeability on the endeavour segment of the Juan de Fuca mid-ocean ridge. *Earth and Planetary Science Letters*, *138*(1–4), 83–91. https://doi.org/10.1016/0012-821x(95)00225-2

Wilcock, W. S. D., Solomon, S. C., Purdy, G. M., & Toomey, D. R. (1992). The Seismic Attenuation Structure of a Fast-Spreading Mid-Ocean Ridge. *Science*, *258*(5087), 1470–1474. https://doi.org/10.1126/science.258.5087.1470

Wilcock, W. S. D., Archer, S. D., & Purdy, G. M. (2002). Microearthquakes on the Endeavour segment of the Juan de Fuca Ridge. *Journal of Geophysical Research: Solid Earth (1978–2012)*, *107*(B12), EPM 4-1-EPM 4-21. https://doi.org/10.1029/2001jb000505

Wilcock, W. S. D., Delong, E. F., Kelley, D. S., Baross, J. A., & Cary, S. C. (2018). The Subseafloor Biosphere at Mid-Ocean Ridges. https://doi.org/10.1029/gm144

Wilson, C., Charlou, J.-L., Ludford, E., Klinkhammer, G., Chin, C., Bougault, H., et al. (1996). Hydrothermal anomalies in the Lucky Strike segment on the Mid-Atlantic Ridge (37°17′N). *Earth and Planetary Science Letters*, *142*(3–4), 467–477. https://doi.org/10.1016/0012-821x(96)00100-8

Winslow, D. M., Fisher, A. T., & Becker, K. (2013). Characterizing borehole fluid flow and formation permeability in the ocean crust using linked analytic models and Markov chain Monte Carlo analysis. *Geochemistry, Geophysics, Geosystems*, *14*(9), 3857–3874. https://doi.org/10.1002/ggge.20241

Woese, C. R., Kandler, O., & Wheelis, M. L. (1990). Towards a natural system of organisms: proposal for the domains Archaea, Bacteria, and Eucarya. *Proceedings of the National Academy of Sciences*, *87*(12), 4576–4579. https://doi.org/10.1073/pnas.87.12.4576

Yang, J., Edwards, R. N., Molson, J. W., & Sudicky, E. A. (1996a). Fracture-induced hydrothermal convection in the oceanic crust and the interpretation of heat-flow data. *Geophysical Research Letters*, *23*(9), 929–932. https://doi.org/10.1029/96gl00728

Yang, J., Edwards, R. N., Molson, J. W., & Sudicky, E. A. (1996b). Three-dimensional numerical simulation of the hydrothermal system within TAG-Like sulfide mounds. *Geophysical Research Letters*, *23*(23), 3475–3478. https://doi.org/10.1029/96gl03081

Yang, J., Latychev, K., & Edwards, R. N. (1998). Numerical computation of hydrothermal fluid circulation in fractured Earth structures. *Geophysical Journal International*, *135*(2), 627–649. https://doi.org/10.1046/j.1365-246x.1998.00669.x

De la chambre magmatique aux microhabitats : dynamique des circulations hydrothermales diffuses aux dorsales médio océaniques

par

Benjamin Wheeler

Résumé

L'activité hydrothermale se manifeste sous la forme de cheminées hydrothermales renommées « fumeurs noirs » mais aussi via des fluides diffus de plus basse température évacués sur de plus larges surfaces. Il existe toutefois relativement peu de données sur les différents mécanismes de formation et la dynamique de circulation des fluides diffus dans le sous-sol malgré leur rôle majeur pour la faune hydrothermale. Nous avons étudié les fluides diffus lors d'observations réalisées sur 3 ans au niveau de 2 sites du champ hydrothermal de Lucky Strike (Tour Eiffel and White Castle). Sur la base de nos observations, nous avons développé un modèle géologique conceptuel pour la dynamique de circulation hydrothermale à l'échelle de site à Lucky Strike. Ce modèle confirme le rôle joué par la fine couche volcanoclastique déposée sur la couche sous-jacente de basaltes bréchifiés pour contrôler la dynamique de circulation et l'évacuation des fluides diffus. Ces fluides génèreraient un flux de chaleur estimé à 7.5 MW à White Castle et 28.9 MW à Tour Eiffel.

Nous utilisons ces observations pour contraindre un modèle 2D thermo-hydraulique de circulation de fluides chauds dans un milieu poreux, afin de prédire la géométrie de la circulation des fluides dans le sous-sol peu profond et la formation de fluides diffus. Nous explorons également l'effet de la précipitation des sulfates à partir de l'eau de mer circulant dans la croute océanique. Nos résultats montrent qu'une faible perméabilité ou une grande vitesse pour les fluides hydrothermaux sont nécessaires afin de former des fluides à haute température > 300°C. Pour pouvoir avoir des fluides diffus latéraux >20°C, une précipitation d'anhydrite pour changer la perméabilité locale et l'écoulement du fluide est nécessaire.

Mots clés : Systèmes hydrothermaux aux dorsales océaniques, sorties diffuses, géologie, série temporelle de la température des fluides, chimie des fluides, circulation hydrothermale, modèles numériques, précipitation d'anhydrite.

Summary

The hydrothermal activity is visible at the seafloor through chimney edifices called "black smokers" but also through diffuse fluids of lower temperature that are scattered on larger surfaces. Very little is known about the different mechanisms of formation and the dynamics of circulation of diffuse fluids in the subseafloor despite their important role for the hydrothermal fauna. We studied diffuse fluids during a 3 years monitoring at 2 hydrothermal vent sites from the Lucky Strike hydrothermal field (Tour Eiffel and White Castle). Based on these results, we developed a conceptual geological model for the dynamics of vent site scale hydrothermal circulations at the Lucky Strike field. This model confirms the role of the thin volcaniclastic formation deposited on the brecciated basalt substratum of both sites to control the dynamic of circulation and of venting of diffuse fluids. These fluids would generate a diffuse heat flow estimated as about 7.5 MW at White Castle, and 28.9 MW at Tour Eiffel.

We use these observations to constrain a 2D thermo-hydraulic model of hot fluid circulation in a porous media, in order to predict the geometry of fluid circulation in the shallow subseafloor and the formation of diffuse fluids. We also explore the effect of sulfate precipitation from entrained seawater. Our results show that low permeability for the porous media or high velocity for the upflowing hydrothermal fluids are necessary in order to have high-temperature fluids >300°C vents. To be able to have close lateral diffuse fluids >20°C, anhydrite precipitation to change local permeability and fluid flow is necessary.

Key-words: Mid-oceanic hydrothermal system, diffuse venting, geology, fluid temperature time-series, fluid chemistry, near seafloor hydrothermal circulation, numerical modelling, anhydrite precipitation